REPORT DOCUMENTATION PAGE

AFRL-SR-BL-TR-02-

_0015_

1. REPORT DATE (DD-MM-YYYY)	2. REPORT TYPE	3. DATES COVERED (From - To)
December 14, 2001	Final Technical	7/01/1993 - 6/30/1997

4. TITLE AND SUBTITLE
(U) (MURI) Turbulent Reacting Flow at High Speed

5a. CONTRACT NUMBER

5b. GRANT NUMBER
F49620-93-1-0427

5c. PROGRAM ELEMENT NUMBER
61103D

6. AUTHOR(S)
Garry L. Brown, Frederick L. Dryer, Luigi Martinelli, Richard B. Miles, Alexander J. Smits

5d. PROJECT NUMBER
3484

5e. TASK NUMBER
AS

5f. WORK UNIT NUMBER

7. PERFORMING ORGANIZATION NAME(S) AND ADDRESS(ES)

Princeton University
Mechanical and Aerospace
Engineering Department
Princeton, NJ 08544-5263

8. PERFORMING ORGANIZATION REPORT NUMBER

9. SPONSORING / MONITORING AGENCY NAME(S) AND ADDRESS(ES)
AFOSR/NA
801 North Randolph Street
Room 732
Arlington, VA 22203-1977

10. SPONSOR/MONITOR'S ACRONYM(S)

20020130 268

12. DISTRIBUTION / AVAILABILITY STATEMENT
Approved for public release; distribution is unlimited

AIR FORCE OFFICE OF SCIENTIFIC RESEARCH (AFOSR)
NOTICE OF TRANSMITTAL DTIC. THIS TECHNICAL REPORT
HAS BEEN REVIEWED AND IS APPROVED FOR PUBLIC RELEASE
LAW AFR 190-12. DISTRIBUTION IS UNLIMITED.

13. SUPPLEMENTARY NOTES

14. ABSTRACT

The overall goal of the research was to establish a strong foundation for understanding and predicting the interaction of fluid mechanical processes with chemical reactions in high speed flows. To accomplish this goal, expertise in chemical kinetics, experimental fluid mechanics and combustion, and computational fluid mechanics were brought together to make a systematic attack on turbulent reacting flows at high speed. In particular, the following tasks were established

Task 1: High Speed Flow Experiments Including Mixing and Heat Release
Task 2: Fundamental Combustion Experiments and Modeling
Task 3: The Development and Application of Advanced Optical Diagnostics
Task 4: Numerical Simulation Of Reacting Flows At High Speed

The report summarizes the goals of the research and the progress made in each of these tasks.

15. SUBJECT TERMS
Reacting flow, turbulent flow, high speed flow

16. SECURITY CLASSIFICATION OF:			17. LIMITATION OF ABSTRACT	18. NUMBER OF PAGES	19a. NAME OF RESPONSIBLE PERSON
a. REPORT	**b. ABSTRACT**	**c. THIS PAGE**	UL		Julian M. Tishkoff
Unclassified	Unclassified	Unclassified		240	**19b. TELEPHONE NUMBER** (include area code) (703)696-8478

Standard Form 298 (Rev. 8-98)
Prescribed by ANSI Std. Z39.18

Princeton University   **School of Engineering and Applied Science**
Department of Mechanical and Aerospace Engineering
P.O. Box CN5263
Princeton, NJ 08544-5263

DEC 17

December 14, 2001

Dear Julian,

Further to your letter of February 2, 2001, I attach a revised final report for University Research Initiative Grant F49620-93-1-0427. I have consolidated the individual reports sent to you in a draft of the final technical report, made a number of corrections, included the work of Professor Dryer and myself and included a summary. I regret the delay in responding to your requests.

Sincerely,

Garry Brown
Robert Porter Patterson Professor

FINAL TECHNICAL REPORT

to the
Air Force Office of Scientific Research
Attn: Dr. J. M. Tishkoff

Grant No. F49620-93-1-0427

Turbulent Reacting Flows at High Speed

Covering the Period 07/1/92 through 06/30/97

Prepared by:

G.L. Brown, S.M. Bogdonoff, F.L. Dryer, A. Jameson, S.H. Lam,
C.K. Law, W.R. Lempert, L. Martinelli, R.B. Miles,
A.J. Smits, R.A. Yetter and K. Xu

Submitted by:

G. L. Brown
Principal Investigator

Summary

This report is the Technical Final Report for Grant No. F49620-93-1-0427, "Turbulent Reacting Flows at High Speed", covering the period 07/1/92 through 06/30/97.

Summary

The overall goal of the research was to establish a strong foundation for understanding and predicting the interaction of fluid mechanical processes with chemical reactions in high speed flows. To accomplish this goal, we brought together expertise in chemical kinetics, experimental fluid mechanics and combustion, and computational fluid mechanics to make a systematic attack on turbulent reacting flows at high speed. In broad terms we sought to:

- Develop and validate experimentally a reaction mechanism for $H_2/O_2/N_2$ over a wide range of pressures and equivalence ratios and establish sensitivities to impurities.

- Develop numerical schemes to compute compressible, viscous, reactive flow.

- Develop optical diagnostic for the direct measurement of reaction species in supersonic flow.

- Undertake experiments in well-defined premixed supersonic flow in which the reaction is initiated and sustained in a laminar flow, and make detailed comparisons with numerical predictions for cases where the reaction mechanism has been validated.

- Undertake experiments on mixing in a well-defined supersonic turbulent flow (boundary layer) in the absence of heat release but including the case where mixing is enhanced by the generation of longitudinal vorticity through the exploitation of the baroclinic torque.

- Undertake experiments in a well-defined reacting supersonic turbulent flow (boundary layer) including the case where heat release plays a substantial role.

- Compare turbulent mixing and reacting flow experimental results (including species measurements) with numerical predictions to develop further physical insight and to evaluate turbulence models, but after first validating the computational scheme in laminar flows, validating the reaction mechanism and establishing the accuracy of the diagnostics.

The above objectives were classified into four broad efforts:

Task 1: High Speed Flow Experiments Including Mixing and Heat Release

Task 2: Fundamental Combustion Experiments and Modeling

Task 3: The Development and Application of Advanced Optical Diagnostics

Task 4: Numerical Simulation Of Reacting Flows At High Speed

This research program concentrated on developing and applying new tools. In particular, several new experimental facilities were built, including a new hypersonic facility, a pilot combustion facility, and a pilot diagnostic facility. The pilot facilities allow testing of new concepts and techniques to support the "full-scale" experiments currently in progress in the hypersonic facility, and for future large-scale combustion experiments. The availability of the hypersonic and pilot facilities has allowed us to make substantial progress in the experimental and diagnostic parts of the program.

In task 1 the new Mach 8 facility was completed and operated with the heater to provide Mach 8 flow at a stagnation temperature of 870K. A range of experiments including mixing, injection, and boundary layer structure has been completed. The proposed extension to use the heater for a modification to the Mach 8 facility and to operate it at Mach 3 for mixing and combustion experiments was not completed. Similarly, progress was made in operating the LTVG at Mach 3 at low pressures but the planned experiments at Mach 3 in the LTVG were instead undertaken in a special purpose, smaller scale Mach 3 facility.

Amongst the important findings in Task 2, were the measurements made in a pre-mixed hydrogen-air reacting laminar flow over a wedge at a Mach number of 2.6. The experiment showed that the post-shock temperatures and pressures were not sufficiently high to allow large quantities of OH radicals to react with H_2 to form H and H_2O. Substantial heat release sufficient for a sustained reaction was not found. The results were qualitatively in agreement with the numerical predictions obtained in Task 4. Prior to the experiment and the development of the predictive models it was not known whether the catalyst would lead to substantial heat release.

In task 3 there were four particular advances made in diagnostics for aerothermochemical flows.

1. Quantitative Velocity, Temperature, and Density Imaging by Filtered Rayleigh Scattering.

2. Planar and line Raman imaging through atomic filters.

3. The development and application of an MHz rate pulse-burst laser.

4. Planar boundary layer imaging with sodium laser-induced fluorescence.

In Task 4 considerable progress was made in the development and validation of high-resolution schemes for compressible reactive flow. In particular, systematic procedures for the design of scalar discretization schemes have been developed, the development and accuracy of numerical methods designed to handle reactive flows has been advanced, ignition characteristics in laminar flows have been successfully computed, and great progress in developing a theory of catalytic surfaces and implementing it as part of the laminar flow schemes has been made.

The principal authors of the Task reports are respectively Professor A.J. Smiths (Task 1), Professor F.L. Dryer (Task 2), Professor R.B. Miles (Tasks 3) and Professor L. Martinelli (Task 4).

Task 1: High Speed Flow Experiments Including Mixing and Heat Release

The following program of research has been undertaken using the new Mach 8 facility:

- Studies of scalar diffusion and mixing in turbulent boundary layers, using sodium florescence.

- Studies of turbulent boundary layer structure, using CO_2-enhanced Filtered Rayleigh Scattering.

- Studies of boundary layer development on a 4:1 ellipsoid cone.

- Studies of boundary layer development on a double cone model, to verify computations made by Professor Candler's group at the University of Minnesota.

3.   Accomplishments/New Findings

Task 1: High Speed Flow Experiments Including Mixing and Heat Release

The new Mach 8 facility has now been made fully operational, including the heater capable of producing a maximum stagnation temperature of 870K for run times of 2 to 13 minutes. The free stream Mach number was found to be very uniform across the tunnel, at a level of 8.0± 0.10. The stagnation temperature typically falls about 8% over a 90 second run, and the stagnation pressure is constant to within 1%. The tunnel operating conditions give a Reynolds number range so that at the lowest Reynolds number the flow is laminar (even on the tunnel walls), and at the highest Reynolds number fully turbulent boundary layers are generated on a flat plate mounted in the test section.

Results from our new Mach 8 facility include:

A. Turbulent Boundary Layer Structure:

The first images of boundary layer structure have been obtained at Mach 8., and the results were reported at the AIAA Advanced Measurement and Ground Testing Technology Conference in New Orleans. Filtered Rayleigh Scattering (FRS) was used, enhanced with CO_2 seeding, to obtain plan-view images of the instantaneous density field. The images suggest that the broad structure of the boundary layer appears to be remarkably similar to that seen in incompressible flows at a similar Reynolds number (see Figures 1 and 2). This is borne out by the measured intermittency distribution (based on the Rayleigh scattering images) which agrees very closely with Klebanoff's classic curve for incompressible turbulent boundary layers.

B. Effects of Helium Injection:

Preliminary experiments have been completed using helium injection on the structure of a Mach 8 turbulent boundary layer. We have found that low levels of helium injection near the leading edge stabilizes the turbulent boundary layer, apparently causing a reverse transition to laminar flow to take place. These results have important implications for thermal insulation of hypersonic engine surfaces, controlling mixing at high Mach number and influencing shock structure in shock-wave boundary layer interactions.

Figure 3 illustrates very recent experiments at Princeton in which we have demonstrated that low levels of helium injection into a transitional boundary layer delays transition indefinitely, apparently by lowering the Reynolds number in the near-wall region and cutting off turbulent production.

Figure 3a shows a CO_2 enhanced scattering image obtained 432mm from the leading edge of a flat plate model in a Mach 8 flow. The boundary layer is turbulent, with a Reynolds number based on momentum thickness $Re_\theta = 3200$. Fig. 1b shows images obtained at the same location but with helium injected into the boundary layer through a slot located 87mm from the leading edge and at a temperature which matches the wall recovery temperature. The dramatic difference due to the helium injection is clearly evident. The mass flow rate of helium is less than 2% of the freestream mass flow rate. Interestingly, injection of air at the same location with the same momentum flow rate has no significant effects, and it produces boundary layer images similar to those shown in Figure 3a.

While the phenomenon illustrated if Figure 3b is far from understood, it appears that the injection of helium effectively reduces the Reynolds number near the wall (the kinematic viscosity of helium is a factor of 8 higher than that of air at the same temperature). Transition is delayed, and no turbulent mixing takes place. Surveys show that the low density region remains trapped near the wall (see Figure 4), apparently because mixing has been inhibited. A key question is how long this effect will persist downstream, and if a similar injection into a fully turbulent flow will cause reverse transition to a more laminar-like state. The phenomenon has important implications for heat transfer to the wall from the external flow: if the wall region is effectively laminar, the wall will be insulated to a much greater extent than if the flow is turbulent.

C. Sodium Tagging

Sodium tagging in the boundary layer to study the effects of helium injection on the structure of a Mach 8 turbulent boundary layer. The sodium diagnostic technique itself has

been the focus of an intense development effort (see also Task 3). Considerable progress has been made, in designing the sodium supply, quantifying the injection rates, and optimizing signal levels. Preliminary images demonstrate the potential of the method, especially in identifying the region of high helium concentration in the injection experiments reported in Figures 3 and 4.

D. Transition on Elliptic Cones

The transition process on a 4:1 ellipsoid at Mach 8 is under investigation. The cone is taken to be representative of a generic hypersonic vehicle shape. This cone is the same body that is being used in computational transition studies by Thorvald Herbert at Ohio State University, and experimental transition studies by Steve Schneider at Purdue University. The onset of transition is being studied as a function of unit Reynolds number.

Working with the Applied Physics Group, Filtered Rayleigh Scattering (FRS) has been used to image turbulent structure on flat-plate boundary layers and is now being applied to studies of the transitional boundary layer over elliptic cones at Mach 8.0. The flow is seeded with carbon dioxide which condenses in the freestream and enhances the Rayleigh signal. In the images which follow, the light regions represent the cold, high-density freestream while the dark regions represent the low-density boundary layer where sublimation of the carbon dioxide crystals has occurred due to aerodynamic heating.

Two elliptic cone configurations are being tested. The first has 2:1 cross section with a half-angle along the major axis of 13.8 degrees. It is the first 0.1524 m section of the 1.016 m cone which was tested in AEDC Tunnel B by Roger Kimmel and Jon Poggie of Wright Laboratory. Previous results on the 2:1 configuration include numerical computations, hot-film probes, schlieren, shadowgraphs and oil flow. FRS images were then taken in the Princeton Mach 8 facility. The second model is a 0.2416 m 4:1 elliptic cone with 17.5 degree half-angle on the major axis.

Transition in the boundary layer of both models was imaged using streamwise and spanwise laser sheet orientations.

The single-shot FRS images shown in Figure 5 are streamwise slices of the boundary layer along the centerline of the 4:1 elliptic cone at four different Reynolds numbers. Each pair of images is meant to be a representative sampling of the boundary layer behavior at those flow conditions. Frames 1 and 2 are taken at a Reynolds number of 1.1×10^6 based on free stream conditions and x-distance along the axis of the model. In most frames, the boundary layer appeared laminar. Occasionally though, traveling waves with wavelength of about 2.5δ were imaged as seen in frame 2. Frames 3 and 4 are taken at Re_x of 1.7×10^6. Here again, traveling waves were observed, but the wavelength has been decreased to a value close to delta. Frame 4 shows a series of organized structures which seem to have retained the wave-like character of 3. Frames 5 and 6 are taken at Re_x of 2.3×10^6. The behavior is similar to that observed at the previous Reynolds number, but the appearance of small scale structures is increasing. Frames 7 and 8, taken at Re_x of 2.8×10^6, show the development of small scale structures throughout the boundary layer. The traveling wave structures seen at lower Reynolds numbers have disappeared.

The single-shot FRS images shown in Figure 6 are spanwise slices of the boundary layer at five different Reynolds numbers. The centerline of the model is on the left side of the image, approximately where the laser scatter along the surface ends. Each pair of images is meant to be a representative sampling of the boundary layer behavior at those flow conditions. Frames 1 and 2 are taken at a Reynolds number of 0.7×10^6 based on free stream conditions and x-distance along the axis of the model. Frames 3 and 4 are taken at

Re_x of 1.2×10^6. Frames 5 and 6 are taken at Re_x of 1.8×10^6. Frames 7 and 8 are taken at Re_x of 2.4×10^6. Frames 9 and 10 are taken at Re_x of 3.0×10^6.

Presently, we are using CO_2-enhanced FRS at Mhz framing rates to study the time evolution of the boundary layer on the cone, at two cross-sections simultaneously. The technique uses a Mhz framing rate camera developed in conjunction with Princeton Scientific Instruments, Inc., and a Ti:Saphire pulse-burst laser (for details see Task 3).

E. Double Cone Flow Field Studies
Preliminary images have been obtained of the boundary layer development on a double-cone model, to verify the computations performed by Professor Candler and his group at the University of Minnesota. The original 3" diameter models were found to choke the tunnel, even with conical fairings, and tests are now being conducted on a 2.5" model. Schlieren images, Filtered Rayleigh images, pressure distributions and surface flow visualization was used to characterize the flowfields. These are reported in detail in Tom Magruder's MSE thesis.

The schlieren image shown in Figure 7 makes visible a Type V shock interaction on an axisymmetric 25/50 double cone. The flow conditions are air at Mach 8, Po=500 psi, To =775 K. Note that the large corner separation region significantly effects the flowfield, indicating the importance of viscous effects in this case.

The results of the computation were presented at the AIAA Aerospace Sciences Meeting in January, 1997, and they are currently being prepared for publication.

4.   Personnel Supported (7/1/96 through 6/30/97)

The work reported here was performed by:

Professors: A.J. Smits

Graduate students: M.L. Baumgartner, P. Erbland, M. Etz. M. Huntley, T. Magruder, D. Williams

Technical Specialists: W. Stokes, R. Bogart

5. Publications Acknowledging Grant F49620-93-1-0427 (7/1/94 through 6/30/97)

Baumgartner, M.L., Erbland, P.J., Etz, M.R., Yalin, A., Muzas, B., Smits, A.J., Lempert, W. and Miles, R.B., "Structure of a Mach 8 Turbulent Boundary Layer," AIAA paper #97-0765, 35th AIAA Aerospace Sciences Meeting, Reno, Nevada, January 6 - 9, 1997.

Baumgartner, M.L., Smits, A.J., Nau, T. and Rowley, C.W., "A New Hypersonic Boundary Layer Facility." AIAA Paper #95-0787, 33rd AIAA Aerospace Sciences Meeting, Reno, Nevada, January 9 - 12, 1995.

Biage, M. Harris, S.R., Lempert, W.R. and Smits, A.J., "Quantitative Velocity Measurements in Taylor-Couette Flow by PHANTOMM Flow Tagging", Proc. Eighth International Symposium on Applications of Laser Techniques to Fluid Mechanics, July 8-11 1996, Lisbon, Portugal.

Debiéve, J.F., Dupont, P., Dussauge, J.P., and Smits, A.J. "Compressibility versus Density Variations and the Structure of Turbulence: A Viewpoint from Experiments" IUTAM Symposium on Variable Density Low Speed Turbulent Flows, IRPHE, UMR CNRS/Universités d'Aix-Marseille I et II, July 8-10, 1996.

Dussauge, J.-P., Fernholz, H.H., Finley, P.J., Smith, R.W., Smits, A.J. and Spina, E.F., "Turbulent Boundary Layers in Subsonic and Supersonic Flows," NATO-Advisory Group for Aerospace Research and Development AGARDograph, #335, 1996.

Dussauge, J.P. and Smits, A.J., "Characteristic Scales for Energetic Eddies in Turbulent Supersonic Boundary Layers." Experimental Thermal and Fluid Science, Vol. 14, No. 1, 1997.

Erbland, P.J., Baumgartner, M.L., Yalin, A., Etz, M.R., Muzas, B., Lempert, W., Miles, R.B. and Smits, A.J., "Development of Planar Diagnostics for Imaging a Mach 8 Flow Fields Using CO_2 and Na Seeding," AIAA paper #97-0154, 35th AIAA Aerospace Sciences Meeting, Reno, Nevada, January 6 - 9, 1997.

Fielding, J., Yetter, R.A., Dryer, F.L. and Smits, A.J., "Reaction of Hydrgen-Oxygen Mixtures in a Laminar Supersonic Wind Tunnel," Paper No. 97S-061, Spring Technical Meeting of the Western States Section of the Combustion Institute, Sandia National Laboratories, Livermore, CA, April 14-15, 1997.

Fielding, J., Yetter, R.A., Dryer, F.L. and Smits, A.J., "Reaction of Hydrogen-Oxygen Mixtures in a Laminar Supersonic Wind Tunnel," Submitted Journal of Propulsion and Power.

Forkey, J., Cogne, S., Smits, A.J., Lempert, W. and Miles, R.B. 1993, "Time-sequenced and spectrally filtered Rayleigh imaging of shock wave and boundary layer structure for inlet characterization," AIAA/SAE/ASME/ASEE Joint Propulsion Conference, Monterey CA, June 28 - 30, 1993.

Huntley, M., Erbland, P. and Smits, A.J., "Transition Studies on Elliptic Cones in Mach 8 Flow Using Filtered Rayleigh Scattering," Supersonic Tunnel Association presentation, October 1997.

Konrad, W. and Smits, A.J., "Three-Dimensional Supersonic Turbulent Boundary Layer Generated by an Isentropic Compression." To appear Journal of Fluid Mechanics, 1997.

Magruder, T. "Flowfields on Double Cone Geometries at Mach 8," MSE Thesis, Princeton University, 1997.

Poggie, J. and Smits, A.J., "Wavelet Analysis of Intermittent Wall-Pressure Fluctuations in a Supersonic Blunt Fin Flow." AIAA Journal, Vol. 35, pp. 1597-1603.

Poggie, J. and Smits, A.J., "Large-Scale Coherent Turbulence Structures in a Compressible Mixing Layer," Submitted to AIAA Journal, 1996.

Poggie, J. and Smits, A.J., "Quantitative Visualization of Supersonic Flow Using Rayleigh Scattering," Submitted to AIAA Journal, 1996.

Smith, D.R. and Smits, A.J., "A Study of the Effects of Curvature and Pressure Gradients on the Behavior of a Supersonic Turbulent Boundary Layer." To appear Experiments in Fluids.

Smith, D.R. and Smits, A.J., "The Effects of Successive Distortions on the Behavior of a Turbulent Boundary Layer in a Supersonic Flow." Journal of Fluid Mechanics, Vol. 351, pp. 253-288, 1997.

Smits, A.J., "Mach and Reynolds Number Effects on Turbulent Boundary Layers." AIAA Paper #95-0578, 33rd AIAA Aerospace Sciences Meeting, Reno, Nevada, January 9 - 12, 1995.

Smits, A.J. "Compressible Turbulent Boundary Layers," Chapter 1, AGARD Report 819 "Turbulence in Compressible Flows," NATO, June 1997.

Wright, M.J., Olejniczak, J., Candler, G.V., Magruder, T.D. and Smits, A.J., "Numerical and Experimental Investigation of Double-Cone Shock Interactions," AIAA paper submitted, 35th AIAA Aerospace Sciences Meeting, Reno, Nevada, January 6 - 9, 1997. Also, University of Minnesota Supercomputer Institute Research Report 97/187, October 1997.

Yalin, A.P., Lempert, W., Etz, M.R., Erbland, P.J. Smits, A.J. and Miles, R.B., "Planar Imaging in a Mach 8 Flow Using Sodium Laser-Induced Fluorescence," AIAA paper #96-2270, 19th AIAA Advanced Measurement and Ground Testing Technology Conference, June 17-20, 1996.

6. Interactions/Transitions (7/1/96 through 6/30/97)

1. Under AASERT Grant F49620-93-1-0476, we have studied the flowfield generated by a generic hypersonic vehicle shape. This investigation will provide data on a complex three-dimensional flowfield which is expected to contribute new insight into the physics of shock-shock interactions, the generation of vorticity in compressible flows (by the action of pressure gradients acting on boundaries as well as by baroclinic torques, the surface pressure and heat loading, the steadiness of the flowfield and the onset of separation in high-speed three-dimensional flows. This detailed information on the flowfield behavior will also be used to generate an important test case for code validation. The particular body chosen is a 4:1 elliptical cone at Mach 8. This is the same body that is being used in computational transition studies by Thorvald Herbert at Ohio State University, and experimental transition studies by Steve Schneider at Purdue University

2. Under AASERT Grant F49620-97-1-0181, and under AFOSR Grant F49620-97-1-0484, the elliptic cone studies are continuing. We have expanded our interests to include the 2:1 ellipsoid tested by Kimmel et al. from Wright Labs., which was lent to us for investigation at Princeton. Dr. Kimmel spent three days with us supervising the tests. Our 4:1 ellipsoid will also be tested at Calspan by Dr. M. Holden.
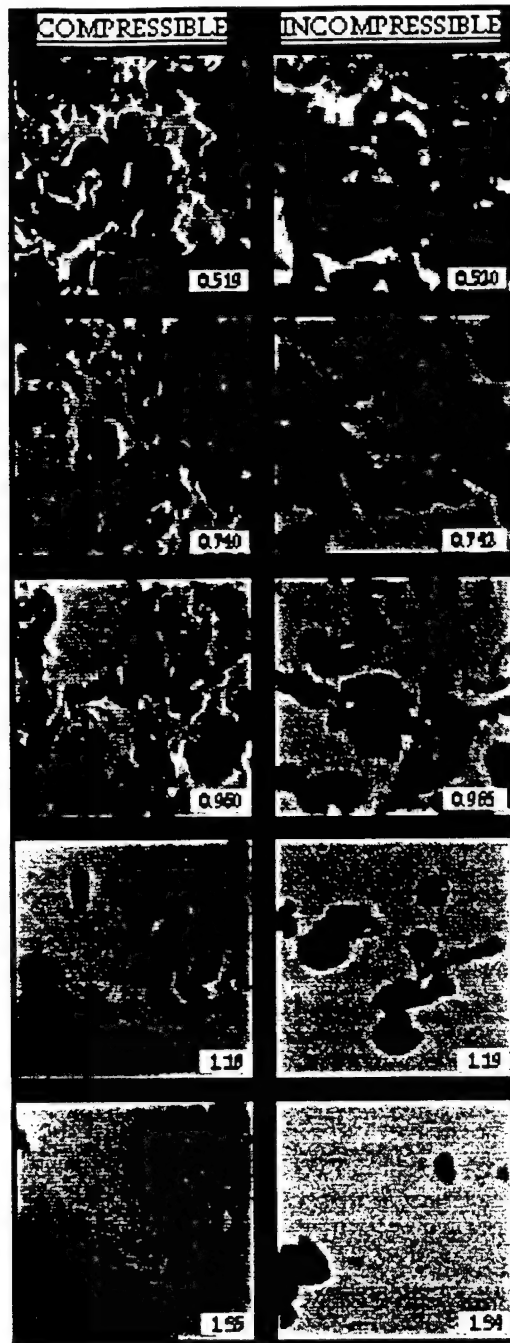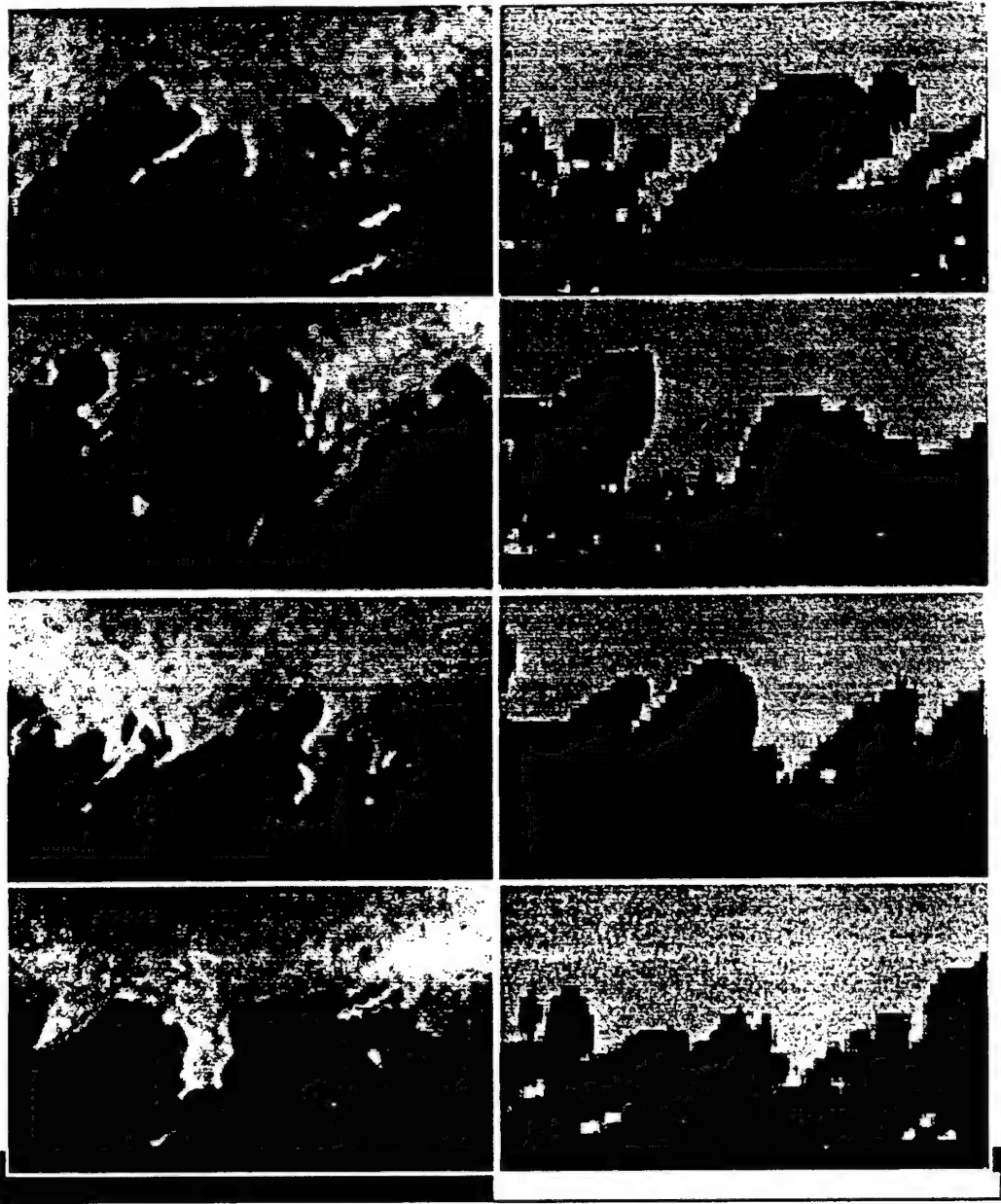
Figure 1. On the left, filtered Rayleigh side-view images of boundary layers at Mach 8. The flow is from left to right. The Reynolds number based on momentum thickness is about 3,600. On the right, side-view images of dye in a boundary layer in water flow at zero Mach number. The Reynolds number based on m

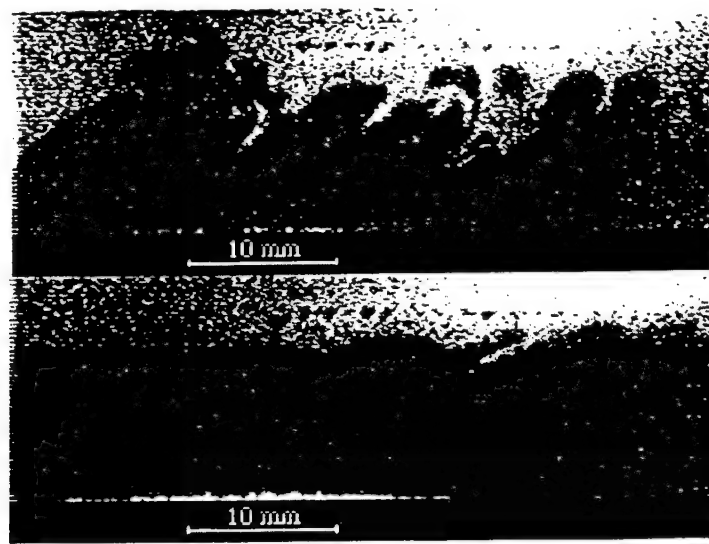Figure 2. On the left, filtered Rayleigh plan-view images of boundary layers at Mach 8. The flow is from left to right. The Reynolds number based on momentum thickness is about 3,600. On the right, plan-view images of dye in a boundary layer in water flow at zero Mach number. The Reynolds number based on momentum thickness is about 700.

Figure 3: Representative Mach 8 Boundary Layer image without (upper) and with (lower) helium injection.
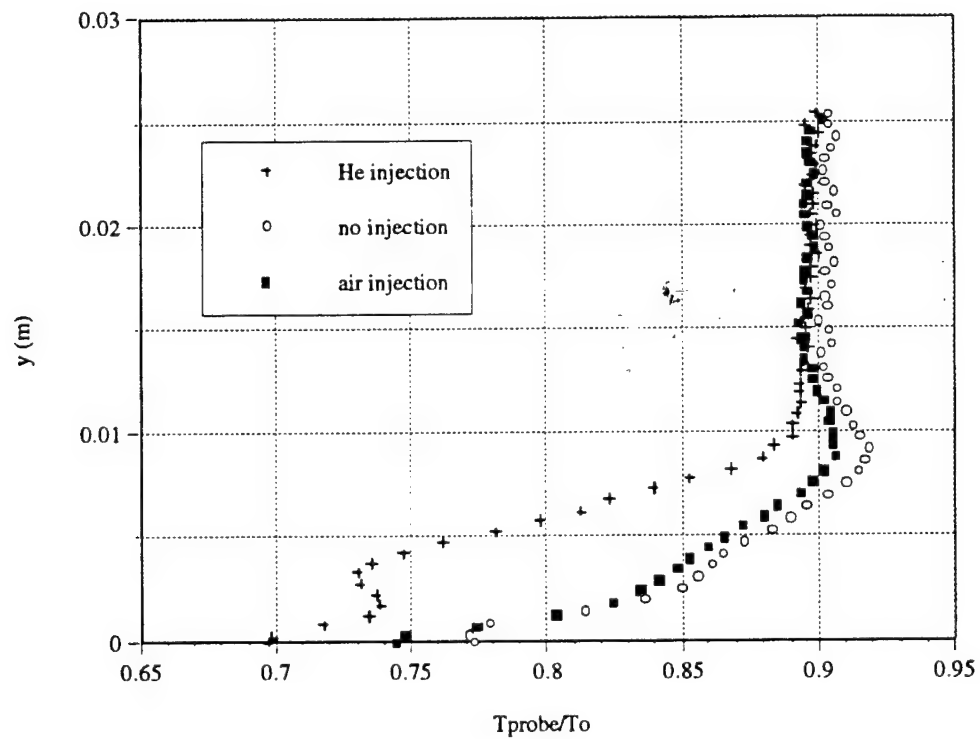
Figure 4: Total temperature surveys for the two flow cases shown in Fig. 1.
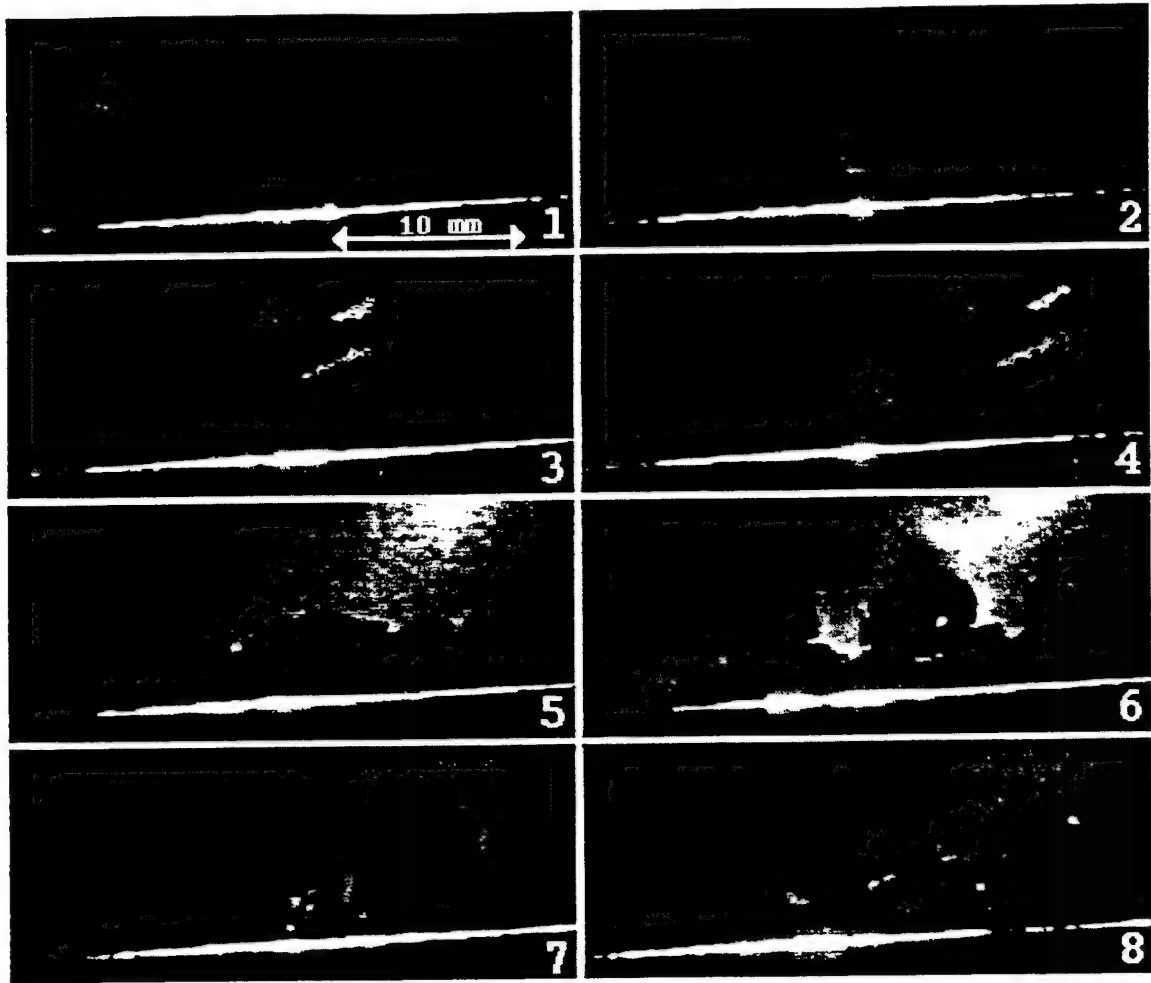
Figure 5. Filtered Rayleigh Scattering images on the 4:1 elliptic cone: Streamwise images of the boundary layer.
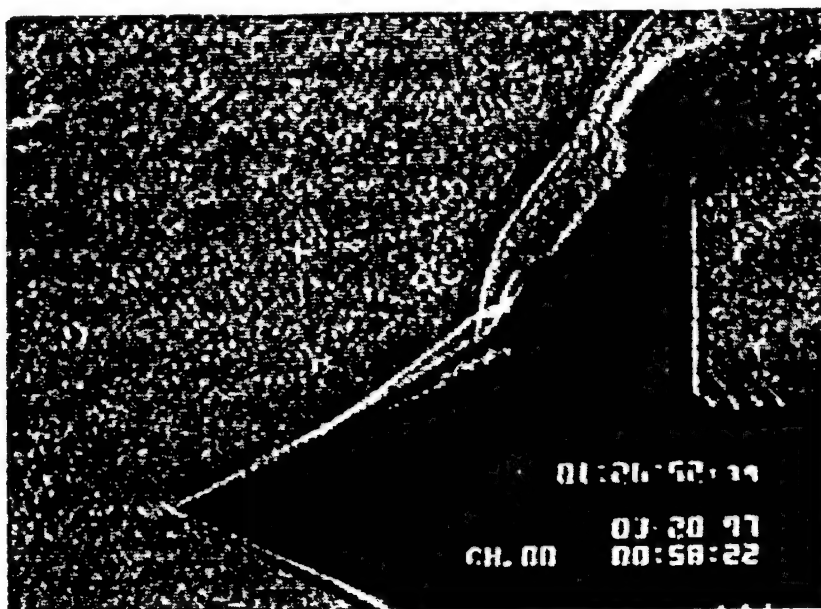
Figure 7. Schlieren images of flowfield over a double 25/50 degree circular cone at Mach 8. The flow is from left to right.
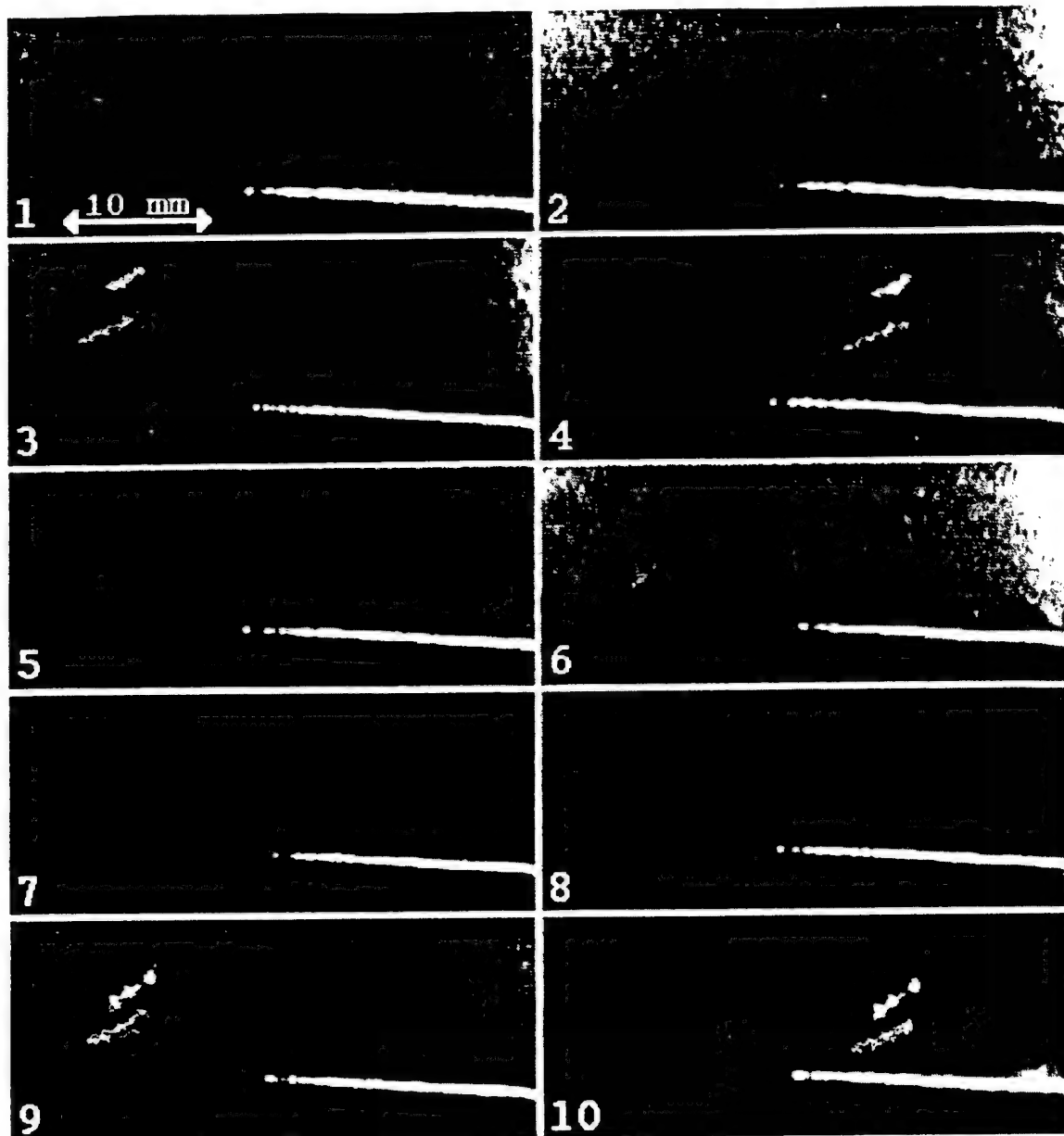
Figure 6. Filtered Rayleigh Scattering images on the 4:1 elliptic cone: Spanwise images of the boundary layer.

Task 2: Fundamental Combustion Experiments and Modelling

Abstract:

A pilot-scale supersonic combustion tunnel was designed and constructed to operate with initial stagnation temperatures up to 900 K and static pressure/stagnation temperatures of 0.01-0.1/290-900 K in the test chamber without vitiation of nitrogen/oxygen gas supply. Through addition of hydrogen in the upstream settling chamber, operating temperatures the effective operating stagnation temperature in the test section was extended to 1100 K. The tunnel facility was instrumented with a Schlieren/shadow graph system and CCD intensified imaging of chemiluminescence from excited hydroxyl radicals (OH*) to study the initiation and combustion properties of nitrogen diluted hydrogen/oxygen mixtures under about Mach 3.0 supersonic flow conditions over both flat plate and wedge-type center bodies. Reaction initiation by recovery effects on non-catalytic and catalytic surfaces as well as through seeding of the flow with radicals was investigated.

Flat plate center-body experiments at M=3.0, a stagnation temperature of 920 K, and a static pressure of 0.6 atmospheres show no conclusive evidence to support the effectiveness of platinum catalytic action at the surface for enhancing reaction initiation. Reaction initiation was achieved by seeding of the flow with radicals produced by hydrogen/oxygen reaction chemistry in the upstream subsonic nozzle inlet (followed by subsequent reaction quenching in the nozzle throat. Employing a wedge geometry and an increased stagnation temperature (to 1070 K), reaction was observed downstream of the oblique shocks generated by the wedge leading edge. While the chemiluminescence measurements showed positive indications of chemical reactions, there was only very weak indications of heat release effects in the Schlieren measurements.

Qualitative one-dimensional modeling of the hydrogen-oxygen reaction under the conditions of these experiments showed that the majority of the chemical energy potential present in the initial reactants resides in the flow as dissociated species rather than as sensible enthalpy changes, once the reaction process is initiated. Results suggested that reaction heat release and the attendant density changes on mixing are strongly coupled with the reaction conditions.

Objectives:

Supersonic combustion has received considerable attention in recent years for application to air-breathing propulsions systems at hypersonic flight speeds.   The increased intake air recovery temperatures associated with flight in the hypersonic range (beyond Mach 6) point to utilizing thermal self-ignition of fuels in supersonic ramjet combustors. Improved understanding of chemical kinetics, heat transfer, and mixing processes in high speed flows is critical to successful implementation and optimization of the engine design. These issues form the basic building blocks necessary to develop computational models of sufficient robustness to project scaling effects as different engine designs are studied. Computational fluid dynamics (CFD) has seen major breakthroughs thanks to ever-increasing computing power, speed, storage, and improved

algorithms. But the simplified and/or empirical nature of the engineering submodels makes it imperative that benchmark experiments are available for investigating various aspects of these high speed flows and to provide a primary database with which to validate the numerical modeling efforts. It is important to initially examine situations in which the flow conditions are simplified (laminar) in order to decrease the overall modeling complexity of the system. A two-dimensional, reacting, supersonic laminar flow is one such system which can be realistically studied in an experimental setting.

The objectives of the work under this AASERT Grant (Grant No. F49620-93-1-0478) were to augment efforts performed under the ongoing AFOSR URI Program "Turbulent Reacting Flows at High Speed" (Grant No. F49620-93-1-0427). Specifically, this work pursued the development and application of techniques for achieving localized, controlled ignition and heat release in supersonic, reacting flows. To accomplish these tasks, a pilot Mach 3 Combustion Tunnel facility capable of accommodating various ignition sources and characterization diagnostics was developed. Ignition processes of nitrogen diluted hydrogen/oxygen mixtures were studied near and over the surfaces of two types of center-body models (flat plate and wedge) utilizing Schlieren/shadowgraph as well as chemiluminescence imaging. Results from studies performed in the pilot scale facility provided fundamental insight into the governing physical processes of high speed reacting flows, as well as design information for the construction of a full scale combustion facility at the Forrestal campus.

In addition to providing general design background for the full scale facility, the present work was directed toward developing and analyzing methods for achieving localized, controlled ignition and heat release within a supersonic reacting flow. Specifically, the issue of ignition of hydrogen-oxygen-nitrogen mixtures in a laminar boundary layer over a flat plate or wedge in supersonic flow was addressed. Boundary layers in high speed flows can generate heat through viscous dissipation providing a mechanism for stimulating ignition. If the boundary layers are laminar rather than turbulent, the modeling complexity of the problem is substantially simplified.

Hydrogen was chosen as the test fuel because the H_2-O_2 chemistry has been extensively studied in a variety of experimental systems over a wide range of conditions, and chemical kinetic modeling efforts here at Princeton have been extensive (Yetter, et al., 1991; Kim, 1994). Under the parent grant, these kinetics have recently been studied and validated experimentally at sub-atmospheric pressures, and perturbations of the kinetics by possible contaminants such as NO_x continue to be under investigation.

The unique explosion limit behavior of the hydrogen-oxygen system provides an innovative means of potentially igniting reactive pre-mixed H_2 - O_2 - N_2 mixtures in a supersonic stream. Explosion limits of combustible mixtures are essentially mappings of the pressure and temperature conditions that separate regions of slow and explosively fast reaction for a particular equivalence ratio. The "classical" explosion limits a stoichiometric H_2 - O_2 mixture are shown in Fig. 1. Above the limits, the reaction chemistry is very fast from thermal self-heating, but more importantly from chemical chain branching. A point between the second and third limits in the non-explosive regime is used to represent initial conditions in the settling chamber of a supersonic wind tunnel. Isentropic expansion to Mach 3, and subsequent recovery in a boundary layer at near-constant pressure assuming an adiabatic wall thermal recovery factor of about 0.85

puts the system inside the second explosion limit. This diagram supports the possibility of mixing the reactants at conditions where the reaction chemistry is slow (and therefore not likely to proceed to ignition in the residence times available, and then creating (through recovery) downstream conditions in the supersonic stream where the chemistry is chain-branched and very rapid in comparison to the available residence times.

Maintaining laminar flow conditions in such experiments is desirable for several reasons. Numerical modeling for laminar flows is less computationally intensive because it eliminates the fluctuation of velocities, concentrations, and other variables. Turbulent transport and its interaction with a chemically reacting system often makes modeling problems intractable. Maintenance of laminar conditions requires that test section static pressures be very low (0.01-0.07 atm). Most combustion studies in supersonic wind tunnels to date have employed static pressures on the order of one atmosphere.

Research Activities:

Figure 2 shows the arrangement of the pilot scale supersonic facility constructed to perform this work. The test section itself was manufactured of 304 stainless steel with quartz windows on the nozzle/test section. An electrically heated packed bed, followed by heated and insulated transfer lines was utilized as the primary means of increasing the stagnation enthalpy of the nitrogen/oxygen flows to the settling chamber upstream of the nozzle/test section. For extended operation at higher stagnation temperatures, controlled quantities of hydrogen were injected at the entrance to the settling chamber and oxygen flows were supplemented to further increase the enthalpy of the stream by vitiation. Successful operation with runs as long as seven minutes or more have been achieved with flow rates around 15 g/s. An ejector was used to achieve the desired pressure ratio P_0/P_{exit} (7:1) for tunnel startup. The nitrogen motive flow was utilized to dilute the tunnel gases, resulting in reasonable exhaust temperatures and quenching any reactions downstream of the ejector. A silencer was also installed downstream of the ejector to reduce ambient operational noise.

Figure 3 is a photograph of the settling chamber, nozzle and test section, with a thermocouple and pitot probe in place where the center-body models were placed in this work. The settling chamber has a 7.62 cm diameter circular cross-section, with a smooth transition to two-dimensional conditions in the nozzle section (rectangular cross-section 7.62 cm by 2.54 cm at the inlet, 12 cm long). The nozzle contour was designed to provide a smooth and ideally isentropic transition from subsonic speeds ($M_0 \ll 1$) to a supersonic design Mach number (M_{test}) of 3. The parallel walls of the tunnel consist of removable plates with two polished optical-grade fused quartz windows 27.84 cm long and 5.00 cm high. The windows provided universal access for optical diagnostics, including ultraviolet (UV) imaging of spontaneous emission from electronically excited hydroxyl radicals (see below). A diffuser was incorporated downstream of the test section to decelerate the flow with minimal loss in total pressure. Finally, addition of trip wires to the nozzle walls was used to prevent laminar separation of the flow during startup and operation, as well as eliminate shock-induced boundary layer transition which inevitably results in an increased boundary layer thickness. Further design details are available in

the M.S.E. thesis of Mr. Fielding. Table 1 summarizes the operational characteristics of the facility.

Table 1: Summary of the Operating Characteristics

Design Mach number:	3	
Settling Chamber		
Stagnation Temperatures:	300 - 1100	K
Stagnation Pressure:	0.46 - 1.5	atm
Test Section		
Static Temperatures:	110 - 400	K
Static Pressures:	0.01 - 0.1	atm
Reynolds number:	20000 - 175000	per inch
Mass flow rates:	10 - 30	gm/sec

Because run times were short, a microcomputer-based system was developed to acquire, display, and save important variables during operation of the wind tunnel. Data were logged on an IBM PC equipped with an Analog Devices A/D board (16 analog channels with 0-10 volt input signals at a 31.2 kHz sampling rate and ± 0.02% full-scale accuracy). Pressures were measured using variable capacitance absolute pressure gauges (0.5% of reading with a temperature coefficient of 0.04% reading/°C). Flow rates of the fuel and oxidizer were measured (±0.5%) using mass flowmeters. Choked orifice calculations were used to define the primary nitrogen flow (+5%/-2%) from stagnation parameter measurements.

Static conditions inside the test section were calculated using isentropic flow relationships, the conditions upstream of the nozzle inside the settling chamber, and the test section Mach number. Total temperature (± 3 K) was measured with a type K exposed junction thermocouple located at the centerline of the settling chamber. Total pressure measurements were obtained at a static tap in the settling chamber wall at the same axial location as the total temperature thermocouple.

Nitrogen was used as the main tunnel flow (Liquid Carbonic, >99.998%). Oxygen (Airco, >99.993%) was mixed several meters upstream of the stagnation chamber and hydrogen (Matheson >99.99%) was injected into the tunnel flow at points in the settling chamber section.

Flow visualization inside the supersonic test section was achieved through the use of Schliren or shadowgraph techniques. An electronic stroboscope followed by an adjustable iris was used as a point light source for a typical two-mirror Schliren system. A high resolution video camera and video cassette recorder were used to obtain real-time and recorded Schliren images. Spontaneous emission from electronically excited hydroxyl radicals (OH*) within the nozzle and test section was also imaged using a uv-sensitive video camera. The OH* radicals which are produced in a reaction zone are de-excited by

$$OH^* + M = OH + M \qquad\qquad (quenching)$$

$$OH^* = OH + h\nu \qquad\qquad\qquad\qquad \text{(emission)}$$

producing chemiluminescence from the electronic transition $^2\Sigma^+$-$^2\Pi$ in the ultraviolet OH band at 306.4 nm. A glass uv filter assembly was used to reduce visible and infrared emission records (generated from hot metal surfaces). An analytical line filter (10 nm band width, centered at 307.1 nm), was also used in selected cases to verify that chemiluminescence arising from the (0,0) transition of the electronically excited hydroxyl radicals was indeed the source of uv emission. However, the low peak transmittance required increased gain, reducing the resolution of the video image, and thus, the glass filter assembly was utilized in a majority of the work.

Experimental Results

Numerous experiments were conducted to investigate chemical reaction of the hydrogen-oxygen system in a laminar boundary layer formed over two different test model geometries including:

- Flat plates, with and without catalytic platinum coating
- 12.7 degree (total angle) wedge

Supports for the models were typically streamlined wedge shapes positioned such that the surface of the model was at the centerline of the flow stream, and the supports were fastened to the lower wall of the test section. Disturbances to the flow stream in the form of oblique shocks and the reflected shock train remained below the model surface, leaving the boundary layer on the top surface of the model undisturbed.

In addition to implementing different test section models, increases in stagnation temperature and variation of radical concentrations in the entering flow were studied by varying the location and magnitude of hydrogen injection upstream of the nozzle throat. Operating pressures could not be varied significantly, however, due to ejector operating constraints. As the location of the hydrogen injector exit plane was moved closer to the nozzle throat, less time was provided for fuel mixing with the nitrogen and oxygen. With the injector further upstream, turbulent Reynolds numbers inside the settling chamber, combined with longer residence times due to low subsonic convective velocities provided effective mixing for the gas stream prior to entering the two-dimensional transition. For injector locations nearest the nozzle throat, the fuel was poorly mixed within the flow. Exemplar observations over the two center-body types are presented below in Figs. 4, 6-9, with conditions for Figs. 6, 7 and 9 summarized in Table 2.

Table 2: Summary of Experimental Conditions for Figs. 6, 7, and 9

Test Section Geometry	Injector Pos. (cm)	T_0 (K)	P_0 (atm)	Mole Fraction (%)		Figure	Notes
				$H_{2, inj}$	O_2		
Flate Plate	-29.8	920	0.65	5%	10%	6	a
Flate Plate	-14	930	0.66	3%	10%	7	b
Wedge	-2.54	1070	0.53	1%	20%	9	c

[a] Chemiluminescence in boundary layer and wake

[b] Emission outlines shock structure

[c] Chemiluminescence surrounds wedge

For the flat plate experiments a 0.16 cm thick stainless steel flat plate of length 5.4 cm was inserted at the centerline of the wind tunnel. In some of the experiments, the top surface of the plate was coated with a thin catalytic film of platinum, approximately 0.1 mm thick. The flow was turned along the bottom of the plate by a 14° angle, in order that the boundary layer formation along the top of the plate remain undisturbed by the

presence of an oblique shock. The tip of the flat plate was positioned 8.9 cm from the nozzle throat, at the beginning of the constant area test section.

A typical shock formation over a flat plate similar to that used in the reacting flow experiments is shown in Figure 4 for a non-reacting flow with a stagnation pressure of 0.6 atm and stagnation temperature of 420 K. Clearly visible are the oblique shock created from turning the flow beneath the plate, and the subsequent expansion fan. The shock structure seen above the plate is the weak shock created from initial formation of the boundary layer along the top surface of the plate. Measurements of the shock angles give a value for the free stream Mach number of 2.8. This is lower than the design value of Mach 3 because boundary layer growth along the contoured nozzle and windows of the test section effectively decreases the area ratio. When this effect on the area ratio is taken into account, the computed Mach number for these conditions is 2.85, in good agreement with the experimental measurement. The boundary layers are visible over both the plate and at the walls of the test section, and the shear layer formed in the wake of the test geometry is also apparent. Measurement of the boundary layer thickness over the plate gives a value of 0.6 mm, in excellent agreement with a calculated value of 0.56 mm at the end of the flat plate assuming a laminar boundary layer. The flat plate used in reacting flow experiments described below differed from that in Fig. 4 in that the rear portion of the plates was flat instead of tapered.

Several positions of hydrogen injection were investigated in both the flat plate and wedge model testing (Figure 5). A typical result for fuel injection at position #1 is documented in Fig. 6. Combustion heating was used with a hydrogen flow rate of 1% by volume to obtain the noted stagnation conditions. Chemiluminescence was observed to fill the entire converging portion of the nozzle, clearly indicating that the reaction was initiated at a location upstream of the throat. The flow was quenched in the nozzle, and gray scale images of OH chemilumenscence along with other noted flow characteristics are shown in the figure. Chemiluminescence was visible in the boundary layer on the top and bottom of the plate, as well as in the subsonic wake at the rear of the plate.

The qualitative nature of the diagnostic made it difficult to quantify how much of the fuel was consumed prior to entering the test section. However, one-dimensional calculations indicated that reaction was probably completed upstream of the nozzle. Consistent with complete mixing of the injected hydrogen, chemiluminescence did not appear preferentially over the top or bottom surface of the plate, and absolute intensities varied slightly for different trial runs. Typical boundary layer thickness over the top of the plate was measured to be 1 mm, and the luminous region within the boundary layer appeared to vary in thickness over its length.

When settling chamber total temperatures were lowered such that ignition of the hydrogen did not occur upstream of the throat, no chemiluminescence was observed in the test section. The absence of pre-reaction inside the settling chamber was identified by a decrease in total temperature during fuel injection rather than a temperature rise, and the lack of chemiluminescence in the contraction of the nozzle. Thus, high radical concentrations frozen in the flow after the expansion appear to lead principally to recombination effects inside the boundary layer.

With the injector positioned closer to the nozzle throat and at the entrance to the two-dimensional transition, ignition occurred upstream of the contraction, and test section

chemiluminescence was no longer confined to the boundary layer and the wake region of the flat plate. The emission, shown in gray scale in Fig. 7, filled the test section for hydrogen mass flow rates of 3% by volume of the total flow. Beneath the plate, the oblique shock and expansion fan are clearly outlined as a result of the chemiluminescence. The intensity of the chemiluminescence clearly increased behind the oblique shock, and then decreased in intensity as the pressure drops through the Prandtl-Meyer expansion.

Some luminosity was again present in the boundary layer on the plate surface, increasing in intensity at a distance of 1.5 cm from the plate tip. The thickness of the luminous layer was around 0.4 mm (± 0.15 mm) compared with a non-reacting laminar calculated value of 0.9 mm. Chemiluminescence did not always appear in the boundary layer, and in instances where occurred, it appeared at the start of hydrogen injection and then tended to disappear as the tip of the plate began to heat.

As with the previous injector position, unless reaction was initiated upstream of the nozzle, no chemiluminescence was observed in the test section. Test section temperatures in the wake of the flat plate were measured in excess of 1000 K for the maximum injected hydrogen flow fraction. Finally, for a fuel injection location of 2.54 cm from the throat of the nozzle, no chemiluminescence was observed anywhere in the nozzle or in the tunnel. Test section temperatures measured in the wake of the flat plate showed significant temperature drops during hydrogen injection.

A 12.7 degree (total angle) wedge geometry was designed such that oblique shocks formed over both sides of the wedge, with consequent increase in static pressure and temperature. The rear of the wedge was truncated to create a large re-circulation zone in the wake and the model thickness was increased to 3.18 mm. It was anticipated that the longer residence times associated with local subsonic velocities in the wake would make conditions more favorable for reaction. Overall length of the model is 2.7 cm.

Schlieren images of the wedge in supersonic flow is presented in Fig. 8. From the angle b of the shock emanating from the tip of the wedge and the flow deflection q, the Mach number was determined to be 2.6. The structure of the wake was visible including the corner expansion, wake shock, and re-compression shock in the downstream region. Slight asymmetry in the flow downstream of the wedge resulted from the model support (swept-back shape silhouetted in the figure) oblique shocks from the side and lower wall, and the interaction with the two-dimensional wake.

With 1% hydrogen injection located at location #3, chemiluminescence surrounded the wedge as shown in gray scale in Figure 9. The pattern clearly outlined the fluid mechanical structures such as the oblique shocks emanating from the wedge tip. The luminosity appeared to extend over the length of the nozzle expansion from the injector to the wedge location and throughout the remainder of the test section. However, luminous intensity in the wake was virtually nonexistent. Attempts to ignite the mixture in the wake using a 0.25 mm tungsten wire as a thermal source were unsuccessful.

Accomplishments/Findings:

Chemiluminescence has been observed inside the test section using the ignition techniques described above and with two different plate geometries. For the flat plate

geometry with catalytic surface, reaction was observed in the boundary layer and wake region of the plate for stagnation temperatures of 920 K and pressures of 0.6 atm. However, no differences were apparent with or without platinum coating. Thus no conclusive experimental evidence was found to support the effectiveness of the platinum surface in enhancing the reaction. Zero dimensional modeling calculations suggest that the observed chemiluminescence was primarily a result of radical recombination reactions. With a wedge geometry and increased stagnation temperatures up to 1070 K, reaction was observed in a region behind the oblique shocks generated from the leading edge of the model. In this case, reaction was stimulated through a combination of the higher free stream temperatures and radical concentrations.

Zero and one dimensional modeling calculations were utilized to assist in qualitatively interpreting observations. These calculations suggest that the noted emissions were due primarily to radical recombination conditions, with much of the radicals generated in the pre-reaction phase rather than from locally enhanced reaction of hydrogen and oxygen near the plate surface. However, the modeling work brought to light new insights both to the experimental observations and to the proposed mechanism for achieving pre-mixing and ignition discussed depicted in Fig. 1.

Using a hydrogen-oxygen kinetic mechanism experimentally validated under the parent grant to this work, zero-dimensional calculations can be performed to determine under what environmental parameters reaction will be initiated and proceed in the available observation times. The analyses are best represented in terms of a Damköhler number, Da , where

$$Da = \frac{\tau_f}{\tau_c}$$

A characteristic time, t_c, for the overall reaction can be expressed by examining the ratio

$$\tau_c = \frac{[H_2]_{in}}{\left. \dfrac{d[H_2]}{dt} \right|_{max}}$$

where $[H_2]_{in}$ is the concentration of hydrogen injected into the system, and $d[H_2]/dt_{max}$ is the maximum rate of change in hydrogen concentration. This time includes both the time for the reaction initiation and a measure of the time necessary to consume the initial reactants.

Characteristic observation time is defined using a characteristic length divided by the velocity of the stream.

$$\tau_f = \frac{L_c}{U_0}$$

In the experimental system, obvious choices for these values would be the desired characteristic reaction length scale and the free stream velocity,

$$U_0 = M_\infty \sqrt{\gamma RT}$$

where γ is the specific heat of the mixture, R the gas constant, and T the local absolute temperature. Convective times within a boundary layer formed in supersonic flow are

considerably longer than those of the free stream, approaching infinity at the surface. However, to spread the reaction into the flow above a surface, Da>1 must exist in the flow.

The effect of varying the pressure on Damköhler number is shown in Figure 10 for an equivalence ratio of 0.5. As pressure is increased from 0.01 to 3 atm, Da becomes a linear function of initial temperature). The sudden drop in Da at the low temperature limit of each curve corresponds to the explosion limit condition.

From this information, contours of Da = 1 can be constructed in the pressure-temperature plane for a Mach 3, $\phi = 0.5$, H_2 - air system, with varying characteristic lengths, as represented in Figure 11. These characteristic lengths estimate the distance over which the fuel would be consumed a supersonic free stream. Two calculations are represented corresponding to isobaric and isothermal conditions. It is significant to notice the convergence of the isobaric Da=1 contours above approximately 0.7 atm, as a result of chemical branching, delineated by the extended second limit. When the release from the reaction is included in the analysis, the pressures at which reaction can be obtained in a given characteristic length become lower. However, for a given characteristic length, the isobaric and isothermal results converge as operating pressure is reduced. At these conditions, the disappearance of initial reactants does not yield large exothermicity, but large quantities of radicals (with high heats of formation). The overall reaction rate of fuel becomes the limiting reaction time rather than the time required for reaction initiation. In the experiments presented above, the conditions were such that reaction times could not be obtained in the length scale of the models unless recovery temperatures were of the order of 1800 K (which could not be achieved within experimental constraints). These results suggested that successful operations of the pilot tunnel can be obtained with different ejector designs and operating pressures in the test section higher than about 0.5 atm. The important new finding, is that there is a limiting pressure below which exothermicity is not achieved from the reaction, and reaction rates of the fuel not chemical initiation become the limiting kinetics. The operating principles depicted in Fig. 1 appear to be achievable in a range of operating parameters where the third limit explosive condition is avoided in the mixing time, and the after initiation by recovery remains substantially exothermic. Continuing work will look at these conditions using more variable ejector/supply conditions available in the gas dynamics laboratory at the Forrestal campus.

Personnel Supported

Drs. Dryer, Smits and Yetter have been associated with the present work. A second-year graduate student (academically advised by Dr. Dryer), Mr. Joseph Fielding, has performed the research and was supported by these resources. Mr. Fielding has submitted an M.S.E. thesis describes the work in greater detail and will be approved by the University in January, 1997. The thesis is included as Appendix A.

Publications: "An Experimental Study of Supersonic Laminar Reacting Boundary Layers", J. Fielding, M.S.E. Thesis, Mechanical and Aerospace Engineering, Princeton University, Princeton, NJ, January, 1997. MAE Report No. 2090-T.

Interactions/Transitions

    a) Participation: none
    b) Consultative/Advisory Functions: none
    c) Transitions:

Discoveries, Inventions or Patent Disclosures: none

Honors/Awards: none

TASK 3: The development and Application of Advanced Optical Diagnostics

This URI program has culminated with four significant advancements to the diagnostics of aerothermochemical flows.

1. Quantitative Velocity, Temperature, and Density Imaging by Filtered Rayleigh Scattering.

2. Planar and line Raman imaging through atomic filters.

3. The development and application of an MHz rate pulse-burst laser.

4. Planar boundary layer imaging with sodium laser-induced fluorescence.

At the same time, the diagnostics group has worked in close harmony with the gas dynamics group to bring these new diagnostics to bear on the understanding of high-speed flows. This work has been primarily conducted in the new Mach 8 facility that was built as part of this program, and is reported in more detail under Task 1. A particularly useful factor has been the utilization of CO_2 vapor in small concentrations to form a dry ice vapor fog in the core of the supersonic flow. This vapor fog has permitted high contrast visualization of boundary layer structures and shock waves at Mach numbers from 2 to 8. With this technique, high-speed (500,000 frames per second) movies of shock wave boundary layers have been taken using the pulse-burst laser, and the impact of helium injection into a Mach 8 boundary layer has been observed. The introduction of sodium vapor in the boundary layer has permitted us to take instantaneous images which track the location of the injected helium or nitrogen in the outer region or mixing layer portion of the boundary layer.

A major contribution that this program has enabled is the development and application of Filtered Rayleigh Scattering. The primary work in this area was done by Joseph Forkey, who completed his Ph.D. in June 1996, and has been carried on by Noah Finkelstein, who is expected to complete his Ph.D. within the next several months, and, more recently, byAzer Yalin. Joe Forkey concentrated on the use of the iodine molecular filter in conjunction with a frequency-doubled, injection-narrowed Nd:YAG laser. He was able to measure flow velocities with uncertainties of ±5.4 meters/second, temperatures with uncertainties of ±3.2 K, and pressures with uncertainties of ±38 torr using Rayleigh scattering from air. His paper on these accuracy limits was submitted to *Experiments in Fluids* in December of 1996, has been accepted, and is pending publication. In order to achieve these accuracies, Dr. Forkey had to develop a corrected and calibrated iodine absorption model which is now widely used by others in the field. This work was published in the 20th of September 1997 issue of *Applied Optics*. Many other papers have arisen from Dr. Forkey's work, most of which have been presented at AIAA meetings and published through the *AIAA Journal*.

The extension of this work into the ultraviolet has been the focus of Noah Finkelstein's research. He has demonstrated Filtered Rayleigh Scattering using a frequency-tripled Ti:Sapphire laser together with a mercury vapor filter. The laser development part of this program has been done in conjunction with Schwartz Electro-Optics Corporation, and has led to a new ramp-and-lock technology for laser stabilization. This laser is now capable of producing ultra-narrow linewidth, high power pulses, accurately tunable throughout a wide range of the ultraviolet spectrum. This laser system has been developed to take advantage of the frequency to the fourth dependence of Rayleigh and Raman scattering, so that much stronger signals can be detected than would be possible with a similar amount of power in the visible region. Furthermore, the overlap of this frequency-tripled laser with a mercury vapor absorption spectrum at 0.254 microns not only enables Filtered Rayleigh Scattering to be performed, but also opens the door to various new mechanisms for Filtered Raman Scattering.

Filtered Raman Scattering has been conducted using two new approaches. The first is a narrow linewidth "transmission" filter, which allows imaging of the single state of a single species. This "transmission" filter is achieved by observing the refluorescence from a standard mercury vapor-

blocking filter. Since mercury is a strong absorber, this refluorescence maintains the image and can be time-gated to eliminate all background light. The second approach is a mercury vapor dispersion filter which allows line imaging of multiple species and multiple states simultaneously. In this case the mercury vapor blocks out strong Rayleigh scattering and other background scattering at the laser frequency, and passes the Raman lines while simultaneously dispersing them onto a camera. This work is published as an SPIE paper and was presented at the end of July 1997.

The pulse-burst laser is a powerful new concept that enables rapid imaging of time-evolving structure. This laser uses as its first stage a very narrow linewidth, continuous wave Nd:YAG laser which can be tuned precisely by changing the crystal temperature. This continuous laser beam is then chopped into a series of pulses with a repetition rate up to 1 M pulses/second, and a variable pulsewidth, usually on the order of 20 nsecs. The pulse train is then amplified through a series of multi-pass amplifier stages using careful isolation to eliminate backward scattering. The final output is frequency-doubled the visible and can be used in conjunction with an iodine filter. This laser source is paired with a new MHz-rate CCD camera that has been developed by Princeton Scientific Instruments, Inc. under Phase II SBIR funding from Wright Laboratory in order to take MHz rate images of shockwave/boundary layer interactions. A videotape of the dynamic interactions was presented at the 1996 APS/DFD Meeting in Syracuse, and is reported in several of the attached publications. A Phase I SBIR has just been completed with Positive Light Corporation in California, examining the possibility of using an injection-locked diode laser as a front-end for this system.

Much of the recent work on diagnostics has been included in *an Annual Review of Fluid Mechanics* paper entitled, "Quantitative Flow Visualization in Unseeded Flows" that was published in March 1997. Attached to this report are copies of papers published since June of 1996.

The following corporate liaisons were associated with this program during the contract period:

PERFORMER	CUSTOMER	RESULT	APPLICATION
Prof. R. Miles Princeton University	Leigh Bromley POSITIVE LIGHT 103 Cooper Ct. Los Gatos, CA 95030 408/399-7744	Phase I SBIR Pulse-Burst Laser	Development of diode laser front-end technology
"	David Welford SCHWARTZ ELECTRO-OPTICS 135 South Road Bedford, MA 01730 617/275-9535	Phase II SBIR Ti:Sapphire Laser	Development of ramp-and-lock scheme
"	Glen Rines IR SOURCES, INC. P.O. Box 401 28 Old Milford Road Brookline, NH 03033 603/672-0582	Ti:Sapphire Laser Pulse-Burst Laser	Optimization of laser performance. Development of next generation pulse-burst laser.
"	Moshe Lavid M.L. ENERGIA, INC. P.O. Box 470 Princeton, NJ 08542-0470 609/799-7970	Phase II SBIR RELIEF	Implementation of RELIEF in R-1D tunnel at AEDC.
"	John Lowrance PRINCETON SCIENTIFIC INSTRUMENTS 7 Deer Park Drive Monmouth Junction, NJ 08852 908/274-0774	Phase II SBIR CCD Camera	Development of high sensitivity, megahertz CCD camera.
"	Dr. Robert Barat NJ Institute of Technology Dept. of Chemical Engineering Newark, NJ 07102 201/596-5605	EPA Mercury Detector	Application of Filtered Rayleigh Scattering to environmental monitoring of mercury vapor.
"	Dr. Nikolai Koroteev International Laser Center Moscow State University Moscow, Russia	CRDF Program	Application of processes to measurement of plasma propagation.
"	Dr. Kyle Gee MOLECULAR PROBES 4849 Pitchford Ave. Eugene, OR 97402 503/465-8340	Phase I SIBR Flow Tagging	Development and optimization of dyes for tagging in water.

PUBLICATION LIST
(June 1996 to Present)

1. R.B. Miles and W.R. Lempert, "Three-Dimensional Diagnostics in Air and Water by Molecular Tagging and Molecular Scattering," Paper #AIAA 96-1963, 27th AIAA Fluid Dynamics Conference, New Orleans, LA (June 17-20, 1996).

2. A.P. Yalin, W.R. Lempert, M.R. Etz, P.J. Erbland, A.J. Smits, and R.B. Miles, "Planar Imaging in a Mach 3 Flow Using Sodium Laser-Induced Fluorescence," Paper #AIAA 96-2770, 19th AIAA Advanced Measurement and Ground Testing Technology Conference, New Orleans, LA (June 17-20, 1996).

3. N.D. Finkelstein, W.R. Lempert, and R.B. Miles, "A Narrow Passband, Imaging, Refluorescence Filter for Non-Intrusive Flow Diagnostics," Paper #AIAA 96-2269, 19th AIAA Advanced Measurement and Ground Testing Technology Conference, New Orleans, LA (June 17-20, 1996).

4. J.N. Forkey, W.R. Lempert, and R.B. Miles, "Accuracy Limits for Planar Measurements of Flow Field Velocity, Temperature, and Pressure Using Filtered Rayleigh Scattering," *Experiments in Fluids* (Manuscript Submitted December 1996--accepted for publication).

5. R.B. Miles and W.R. Lempert, "Quantitative Flow Visualization in Unseeded Flows," *Annual Review Fluid Mechanics* 29, (1997) pp. 285-326.

6. P.J. Erbland, M.L. Baumgartner, A.P. Yalin, M.R. Etz, B. Muzas, W.R. Lempert, A.J. Smits, and R.B. Miles, "Development of Planar Diagnostics for Imaging Mach 8 Flow Fields Using Carbon Dioxide and Sodium Seeding," Paper #AIAA 97-0154, 35th Aerospace Sciences Meeting & Exhibit, Reno, NV (Jan. 6-10, 1997).

7. N.D. Finkelstein, W.R. Lempert, and R.B. Miles, "Mercury Vapor Filter Technology and Ultraviolet Laser Source for Flow Field Imaging," Paper #AIAA 97-0157, 35th Aerospace Sciences Meeting & Exhibit, Reno, NV (Jan. 6-10, 1997).

8. W.R. Lempert, P-F. Wu, and R.B. Miles, "Filtered Rayleigh Scattering Measurements Using a MHz Rate Pulse-Burst Laser System," Paper #AIAA 97-0500, 35th Aerospace Sciences Meeting & Exhibit, Reno, NV (Jan. 6-10, 1997).

9. M.L. Baumgartner, P.J. Erbland, Mr.R. Etz, A. Yalin, B.K. Muzas, A.J. Smits, W.R. Lemeprt, and R.B. Miles, "Structure of a Mach 8 Turbulent Boundary Layer," Paper #AIAA 97-0765, 35th Aerospace Sciences Meeting & Exhibit, Reno, NV (Jan. 6-10 1997).

10. J.N. Forkey, W.R. Lempert, and R.B. Miles, "Observation of a 100-MHz Frequency Variation Across the Output of a Frequency-Doubled Injection-Seeded Unstable Resonator Q-Switched Nd:YAG Laser" *Optics Letters 22* (Feb. 15, 1997) pp. 230-232.

11. N.D. Finkelstein, W.R. Lempert, and R.B. Miles, "Narrow-Linewidth Passband Filter for Ultraviolet Rotational Raman Imaging," *Optics Letters 22* (Apr. 15, 1997) pp. 537-539.

12. W.R.Lempert, P. Wu, N. Finkelstein, P. Erbland, and R.B. Miles, "Imaging Fluid Phenomena with Atomic and Molecular Vapor Filters," Paper #AIAA 97-2520, AIAA 32nd Thermophysics Conference, Atlanta, GA (June 23-25, 1997).

13. J.N. Forkey, W.R. Lempert, and R.B. Miles, "Corrected and Calibrated I_2 Absorption Model at Frequency-Doubled Nd:YAG Laser Wavelengths," *Applied Optics 36* (Sept. 20,1997), pp. 6729-6738.

14. N.D. Finkelstein, W.R. Lempert, and R.B. Miles, "Narrow Linewidth Passband Filters and UV Laser Source for Rotational Raman Imaging," SPIE Paper #3172 88, SPIE Annual Meeting, San Diego, Ca (July 31, 1997).

INVENTION DISCLOSURES

Title: "Resonant Dispersion Raman Spectrometer"
Inventors: Richard B. Miles, Walter R. Lempert, and Noah Finkelstein

U.S. Patent Office
Serial No.:   60/050,320, Dated July 31, 1997.

TASK 4: Numerical Methods for Compressible Reactive Flow

Contents

1 Computational Fluid Dynamics

The combination of mathematical models for fluid flow, well-constructed numerical algorithms and high speed digital computers has made the use of computational fluid dynamics (CFD) a routine occurrence in science and engineering. Because the governing equations of fluid flow are a set of coupled non–linear partial differential equations, the analytic solution of these equations is nearly impossible except for a relatively small group of problems. Thus, in order to model and understand flow fields that cannot be simplified, either computational or experimental techniques must be explored. In essence, CFD allows the user to simulate a fluid flow on a computer system.

There are many characteristics of computational fluid dynamics that make it an attractive tool for engineering analysis and design. Computer simulations allow the user to interrogate the flow domain at any point in a non-intrusive manner. Thus, field information such as pressure, temperature, density and velocity may be obtained without altering the flow field as some experimental measurement techniques may. Numerical simulation allows the user to determine all of the variables in the flow domain as a function of time (subject to hardware memory constraints) which allows visualization of the flow in a manner similar to that of experiments. In addition, it may be possible to remove sources of experimental noise by using computational fluid dynamics, although some noise from the discretization and truncation errors of the numerical scheme may be introduced.

Numerical simulation also enables the user to separate the various processes (convection, diffusion, reaction, etc.) that occur in a flow and study the many complex interactions of these processes. For example, the role of diffusion in a reactive flow may be better understood by studying that flow without diffusion (convection and reaction alone) and then introducing diffusion to see the effect on the flow field. It would be exceptionally difficult or impossible to accomplish this decoupling and removal of processes in an experimental environment.

The numerical simulation of fluid dynamic phenomena involves several distinct steps. First, a mathematical model that adequately describes the processes in the flow must be chosen with regard to the dominant phenomena.

The next step is to develop a numerical algorithm and discretize the governing mathematical equation(s). In this step, important decisions are made about the overall spatial and temporal accuracy of the scheme. The choice of the numerical algorithm must be made in conjunction with the choice of a computing platform, as some algorithms may be incompatible with efficient implementation on some computing platforms.

After the algorithm has been implemented on a computer, the flow is then simulated. However, the process does not end here. After the simulation of the flow, an examination of the solution must be made and it must be determined if the governing equations have actually been solved. This usually involves a refinement study in space and time. Once the series of grid solutions has converged to "a" solution, the user must interpret that solution to see if the relevant physical phenomena have been simulated. This usually involves the comparison of the numerical solution to analytic, asymptotic or experimental results.

1.1 Overview of the Presentation

The work performed under Grant URI/AFOSR F49620-93-1-0427 follows the steps described quite closely. We have focused our research on

1. The development and validation of high resulution schemes for compressible reactive flow.

2. Implementation of reactive flow models on parallel computers which allows the use of detailed chemical kinetics.

In the next two sections we will examine the relevant numerical techniques which have been devised and implemented.

The numerical scheme devised for the simulation of compressible reactive flow with detailed chemistry can be seen as both a predictive tool to enable well-posed experiments to be designed and also as a scheme which can benefit from experimental data for validation.

2 Simulation of reactive flow with detailed chemistry

The simulation of high speed chemically reacting flows is a very challenging area for computational methods. The presence of shock waves necessitates good shock capturing properties, while excessive numerical dissipation must be avoided in the treatment of chemical reactions so that the solution remains uncontaminated. Viscous effects, heat conduction and species diffusion complicate reactive flow calculations, both from the increased computational work required and because of possible interactions between the chemistry and these effects. Diffusion of radical species in a boundary layer may significantly alter the resulting flowfield. Exponential increases and decreases of radical species in small spatial zones lead to large gradients that must simultaneously be captured without oscillation and without unnecessary dissipation. In addition, there is usually a great disparity between the characteristic time scales of the chemical source terms and the characteristic times of the convective and diffusive portions of the governing equations. This "stiffness" makes the integration of the governing equations very difficult and time consuming.

Stiffness may be viewed in terms of characteristic times. If two processes exist in the same system, but the first has a very short characteristic time while the second has a much longer characteristic time, then it is clear that after a short period of time, the first process will have been completed. Thus, further change in the solution is only determined by the second process and it would only be necessary to use the second mode to further advance the solution. Therefore, in terms of accuracy, only the second mode is important after the first mode has reached an "equilibrium" state. However, for the numerical solution of the system, the stability requirements of the scheme necessitate retaining both modes. The time step limitation of the scheme is based on the fastest mode, which means that the system is being simulated at an exceptionally slow rate. This conflict between acceptable accuracy and necessary stability is the heart of stiff problems [3].

Because most chemical reactions have characteristic times much less than those of the convective flow field, many explicit schemes are handicapped in computing such flows. In addition, in detailed chemical mechanisms, there is stiffness within the mechanism as some modes may decay very rapidly while others have longer lifetimes. The time step for an explicit scheme is proportional to the shortest characteristic time, so that stability restrictions require very short time steps in reactive flow simulations. This short time step leads to very long simulation times for steady state computations.

Several ways to overcome this limitation of explicit schemes for chemically reacting flows have been explored. Gear [3] recognized that treating a stiff system implicitly would remove time step limitations for stability purposes and allow the time step to be chosen on the basis of accuracy requirements. Thus, one way to remove stability limitations for the simulation of chemically reacting flow is to use a fully implicit scheme. Wilson and MacCormack [21] used such a scheme with Gauss-Seidel line relaxation to compute steady hydrogen–air combustion over high speed blunt projectiles. Shuen and Yoon [12] used a Lower–Upper Symmetric Successive Overrelaxation (LU-SSOR) implicit factorization scheme to compute premixed and non-premixed chemically reacting flow including viscous effects. Yungster [17] used an LU-SSOR scheme to compute shock-wave/boundary layer interactions in premixed combustible gas flows. Yungster and Rabinowitz [20] used the same LU-SSOR scheme to simulate high speed methane–air combustion over blunt bodies and ram accelerator configurations. Ju [6] implemented a Lower–Upper Symmetric Gauss-Seidel (LU-SGS) scheme to calculate several reactive viscous flows.

Due to the large allowable time step of an implicit scheme, all of these methods may converge to a steady state solution in fewer time steps than an explicit method. However, these implicit methods entail inverting large numbers of matrices. Most link the solution domain together in a way that may hamper efficient parallelization. For unsteady simulations, the restriction on the time step for time accuracy may be the dominant factor, removing the advantage gained by the unconditional stability of the implicit scheme. In addition, during the initial stages of a steady state simulation, growing modes (such as production of radicals) may require the time step to be set by accuracy requirements instead of stability requirements which would again lower the advantage of having a large allowable time step from stability considerations.

Another way of reducing the effect of the chemical term stiffness is to treat the source term in a point implicit manner. In this formulation, due to Bussing and Murman [2, 1], the source term at the next time level is linearized about the current time level, leading to a fully explicit equation at the cost of a matrix inversion. This action has the effect of preconditioning the species continuity equations, rescaling the chemical characteristic time so that it is of the same order as the convective characteristic time. Thus, the entire system may be advanced using a time step based on the spectral radii of the convective and diffusive portions of the governing equations. Palmer and Venkatapathy [11] performed a study of high speed dissociating air using both the fully implicit and point implicit approach. They found that, at higher Mach numbers, the fully implicit scheme would not converge unless its time step was drastically reduced while the point implicit scheme was very robust and converged at all Mach numbers at its time step limit.

With the addition of viscous effects and species diffusion to reactive flows and the use of detailed chemical models, a way to accelerate convergence is sorely needed. The use of multigrid acceleration for reactive flow calculations has not been adequately examined. Bussing and Murman [2] explored the use of multigrid, but only briefly for their one-dimensional calculations. Multigrid techniques may have been thought to be too dissipative and cause radical species to be moved to physically incorrect regions. However, proper multigrid techniques, in which the coarse grids are forced by the fine grid solution, can in fact be used to compute chemically reacting flows. While parallelization will decrease the computational time associated with a numerical simulation, multigrid techniques represent an untapped potential for convergence acceleration of steady state reactive flow calculations.

The accurate capture of shock waves and large gradients in species concentrations necessitates non-oscillatory numerical dissipation schemes that do not overly dissipate the solution. Unphysical diffusion of radical species can lead to gross errors in the prediction of reaction zones and induction times. Oscillations in temperature and pressure may lead to inaccurate production and destruction of radicals. The Total Variation Diminishing (TVD) approach has been taken by several investigators [10, 9, 19, 15, 18, 17, 20] to try to accurately capture shock waves and reaction fronts. Yee and Shinn [16] investigated several aspects of semi-implicit and fully implicit shock-capturing methods for reacting flow. Ju [6] used a fourth order MUSCL (Monotone Upwind Scheme for Conservation Laws) scheme with Steger-Warming flux vector splitting to calculate reactive flows. Jameson [4, 5] has presented a framework for Local Extremum Diminishing (LED) and Essentially Local Extremum Diminishing (ELED) schemes which have been shown to have excellent shock capturing qualities for non-reactive perfect gas flows. The LED/ELED framework includes the TVD concept but has the advantage of being equally generalizable to structured and unstructured grids, unlike TVD. One scheme, the Convective Upwind and Split Pressure (CUSP) scheme, has good shock capturing properties and has been shown to give accurate viscous solutions without spurious numerical dissipation [13, 14]. Because of its high accuracy in viscous dominated regions, it would be expected to provide the same accuracy in regions where species diffusion effects are present. Thus, the CUSP splitting combined with a flux limiter may be able to provide good resolution of inviscid and viscous reactive flow phenomena.

In this work, the point-implicit formulation of Bussing and Murman is combined with an explicit

time-stepping multigrid solver [8] using CUSP dissipation to compute inviscid and viscous high speed reactive flows with detailed chemical kinetics. The fully explicit algorithm is implemented using the MPI standard on an IBM SP-2 parallel computer and various nonreactive and reactive flows are simulated to validate the algorithm.

2.1 $M = 3.55$ Hydrogen-Oxygen Reacting Blunt Body Flow

The results of a multidimensional reacting hydrogen–oxygen supersonic flow over an axisymmetric spherical tip projectile are presented first. This corresponds to an experiment conducted by Lehr [7] which is shown in Figure 1. The diameter of this projectile is 15 mm. The fluid is stoichiometric
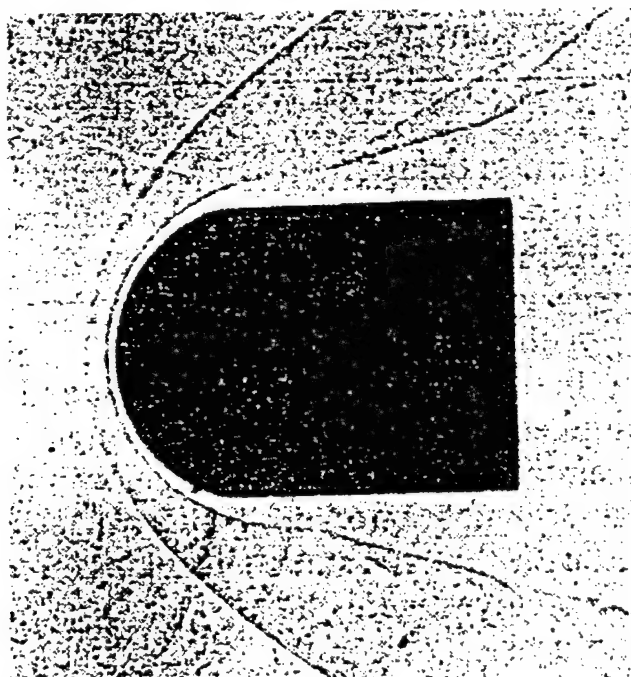
Figure 1: Experimental shockwave and reaction front: $M = 3.55$ hydrogen/oxygen, from Lehr [38].

hydrogen-oxygen. The free stream temperature is 292 K, the free stream pressure is 24800 Pa and the Mach number of the flow is 3.55. At this speed, the flow is dominated by convection and reaction processes and thus, diffusive effects may be neglected. This allows further validation of the convective and reactive portions of the algorithm using experimental data. In addition, the length of the induction zone is sufficiently large to remove any question of inadequate grid resolution in that area.

This flow was initially simulated using the reduced chemistry model of Evans and Schexnayder with six species and eight reactions [22]. This model was chosen because of its relatively low computational cost and its adequate accuracy. The computational domain for the simulation included only the region in front of the projectile and extending back to the shoulder of the projectile; the domain behind the shoulder is not of great interest and, because the flow is supersonic, does not affect the upstream region. Because the flow field should be symmetric, only half of the domain was simulated and symmetry boundary conditions were applied at the centerline of the flow. The body was assumed to have a non-catalytic, inert surface with negligible heat transfer (adiabatic wall) between the fluid and the body. The domain was discretized with equally spaced cells in the direction normal to the surface of the body. The grid in this case was 64×64 cells. As shown in Figure 2, the bow shock in front of the body raises the temperature of the flow so that, after an induction zone, the flow reacts. The temperature
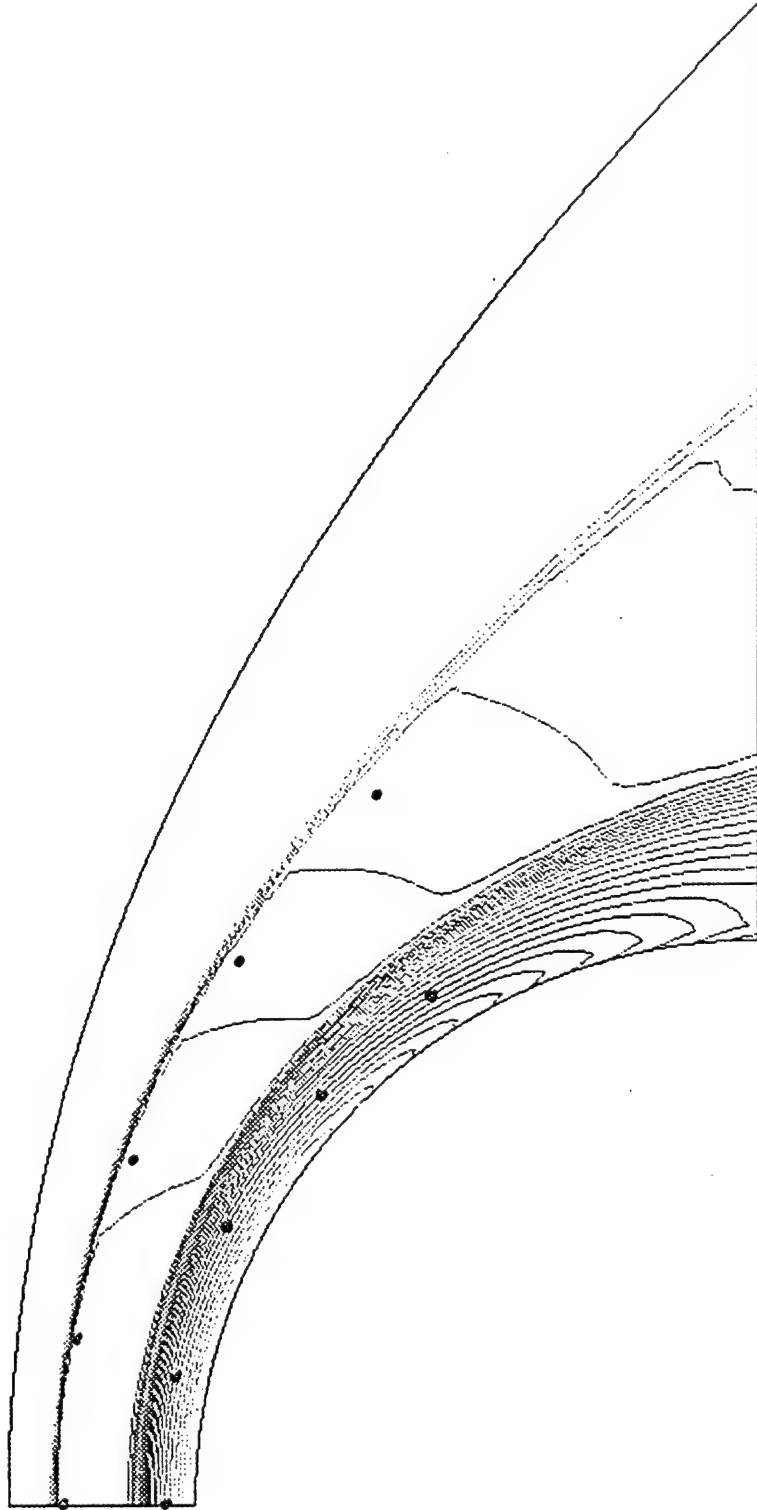
Figure 2: *Temperature contours: M = 3.55 hydrogen/oxygen. Contour levels in K: min: 250, max: 3130, inc: 93. Grid size: 64 × 64. Circles indicate experimental shock and heat release locations.*

rise across the bow shock varies with the angle, and thus the strength, of the shock. Because of the varying temperatures behind the shock, the length of the induction zone increases as the flow moves away from the centerline where the largest temperature jump occurs. Larger temperatures cause higher production rates of radicals which then build up to react in a shorter period of time. In fact, far away from the body, there is a region where the temperature jump across the shock is insufficient to cause enough radicals to form, react and release heat. Temperature is approximately constant in the induction zone as radicals build up to the necessary levels to react and produce water vapor. The production of water vapor is accompanied by heat release which raises the temperature and, because pressure is nearly constant across the reaction zone, lowers the density. Figures 3 and 4 show density and pressure contours for this simulation. Figure 5 shows the temperature along the stagnation streamline computed using the Evans and Schexnayder reaction model and also the Jachimowski eight species, nineteen reaction modified model.   The eight species, nineteen reaction model produced a slightly different shock location, while the point of heat release is close to the Evans and Schexnayder model. The only difference between these two calculations was the chemistry model used: both models used the same algorithm and grid and were converged to the same level of accuracy. Thus, even though both simulations are converged, different solutions result because the mathematical models were slightly different in the modeling of the chemistry. The difference in shock location could be explained by a difference in relaxation characteristics behind the shock due to the chemical models. In addition, the heat release profiles lead to slightly different static pressures behind the heat release region, which could result in different shock positions. Figure 5 indicates that the numerical dissipation scheme is providing the necessary dissipation in regions of steep gradients, such as the shock, to prevent oscillations and preserve monotonicity while still allowing sharp resolution.

However, upon examining Figure 2, one may notice that the numerical solution differs slightly from the experimental shock location and heat release front. Thus, another simulation was performed on a 64×128 cell grid which had twice the number of grid cells in the normal direction as the 64×64 grid had. The Evans and Schexnayder model was used for the chemistry, since it produced a shock location that was closer to the body on the 64×64 grid. Temperature contours for this finer grid simulation are presented in Figure 6 along with experimental shock and heat release front locations. As can be seen, the agreement between the experimental results and the numerical simulation is much better on this finer grid. The increased resolution has moved the shock closer to the body, increased the length of the induction zone and moved the heat release front closer to the body. Density and pressure contours are presented in Figures 7 and 8.

The temperature along the stagnation streamline for the 64×128 grid is shown in Figure 9. As in the case of the 64×64 cell grid, the flow passes through a shock which is followed by an induction zone where radicals are created due to the higher temperature. After sufficient amounts of radicals have been formed, water vapor is created, increasing the temperature and further hastening the reaction.

The mass fractions of the reactants and products for the Evans model simulation on the 64×128 grid are plotted in Figure 10. As expected, the reactants have almost constant mass fraction through the shock and only begin to be consumed in the heat release region. Water vapor is not formed in any appreciable quantity until the heat release region. It should also be noted that the mass fraction profiles are monotonic; no overshoots in the mass fraction of these primary components is observed, again indicating good performance of the CUSP dissipation scheme.

The growth and destruction of radical species is depicted in Figure 11 for the Evans model. This figure shows the logarithm of the mass fractions of the radical species. Exponential growth can be observed in the induction zone, which is to be expected. After a small region of slow growth, the radical mass fractions grow approximately nine orders of magnitude in a very short distance, which is a testament to the ability of the CUSP splitting and the flux limiter to capture large changes in the conservative variables without oscillation and without undue damping. The mass fraction of the
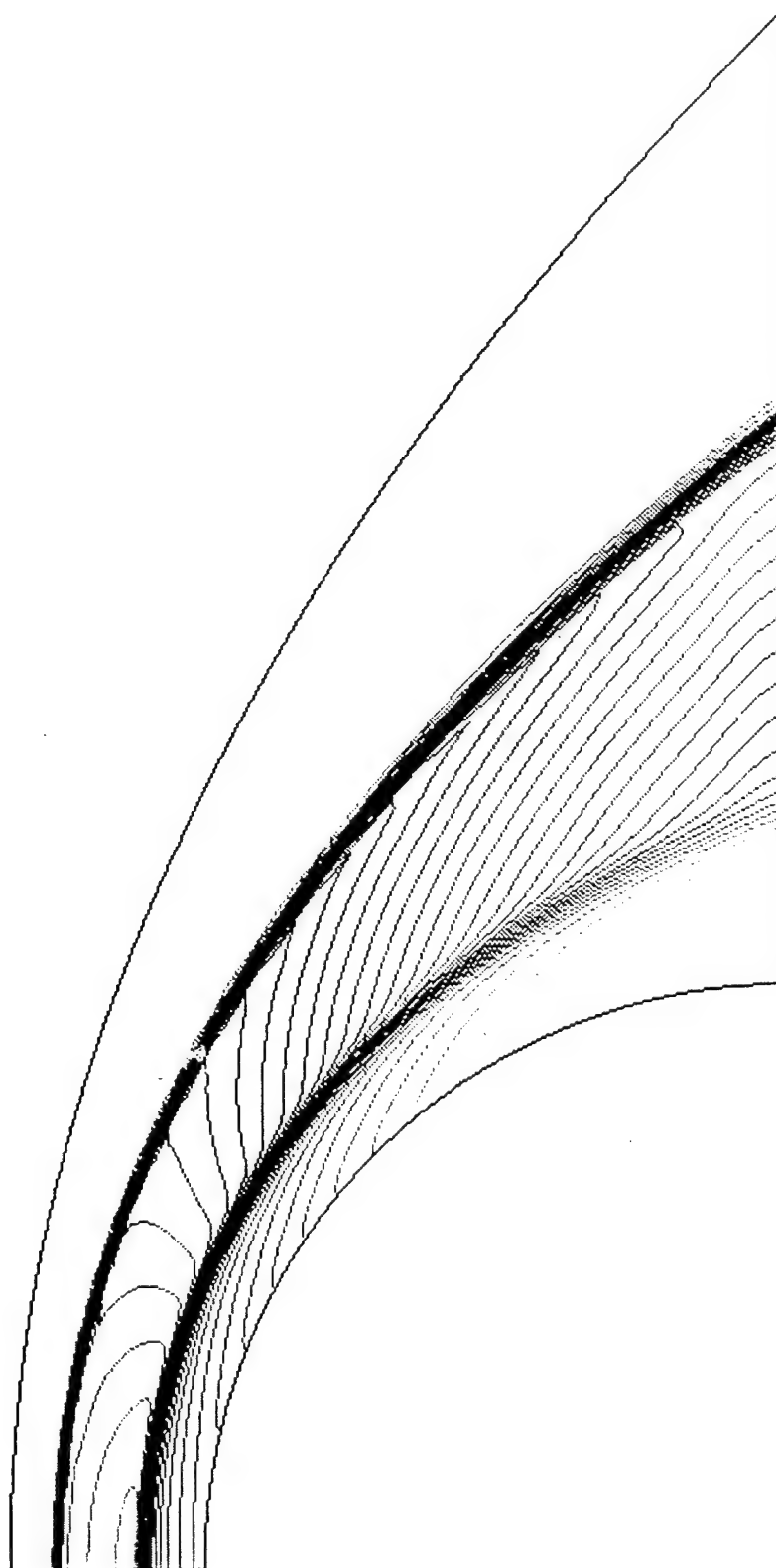
Figure 3: Density contours: $M = 3.55$ hydrogen/oxygen. Contour levels in kg/m^3: min: 0.05, max: 0.6, inc: 0.016. Grid size: 64×64.
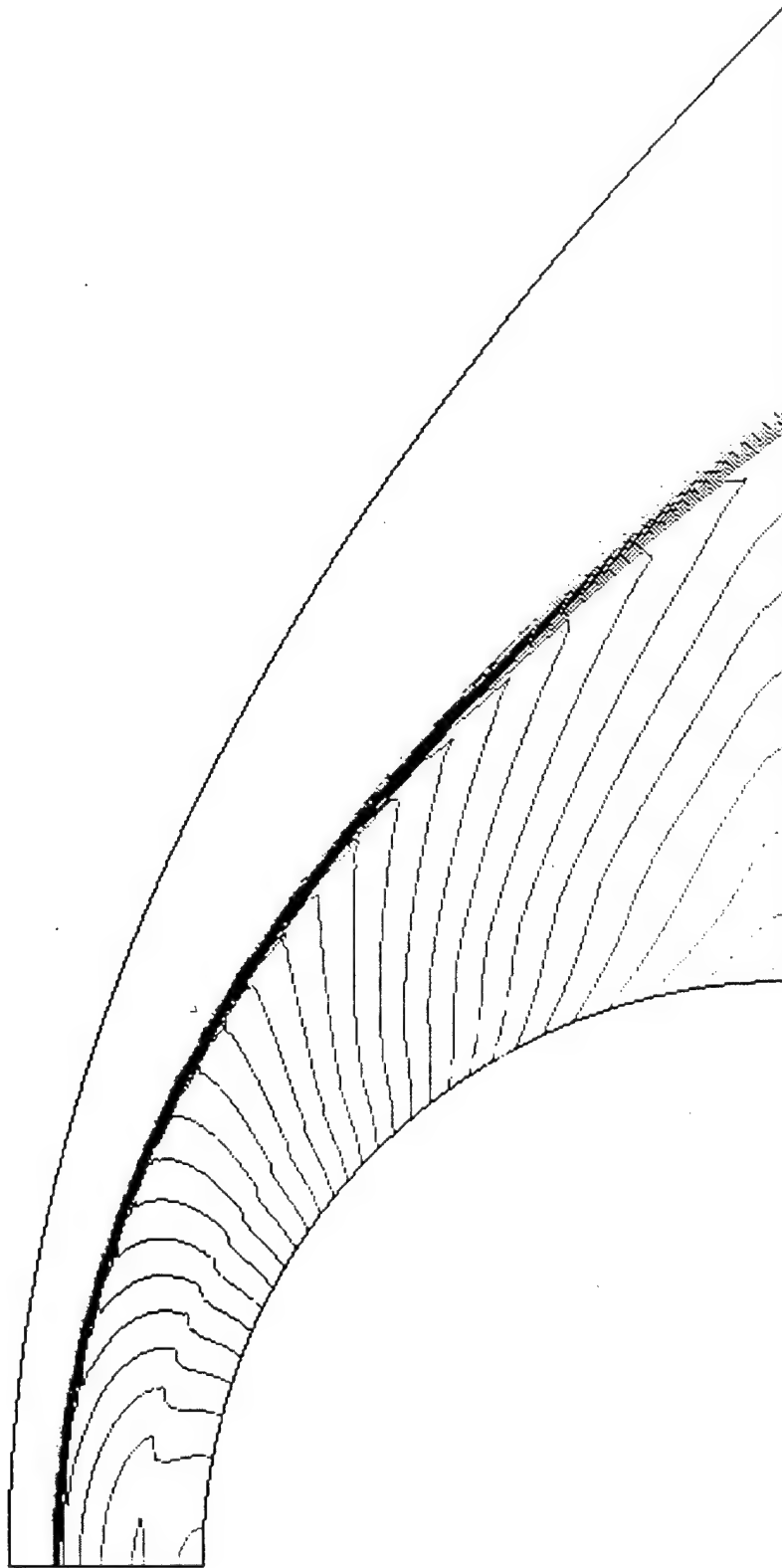
Figure 4: *Normalized pressure contours: M = 3.55 hydrogen/oxygen. Contour levels (p/p∞): min: 1.0, max: 16.5, inc: 0.5. Grid size: 64 × 64.*
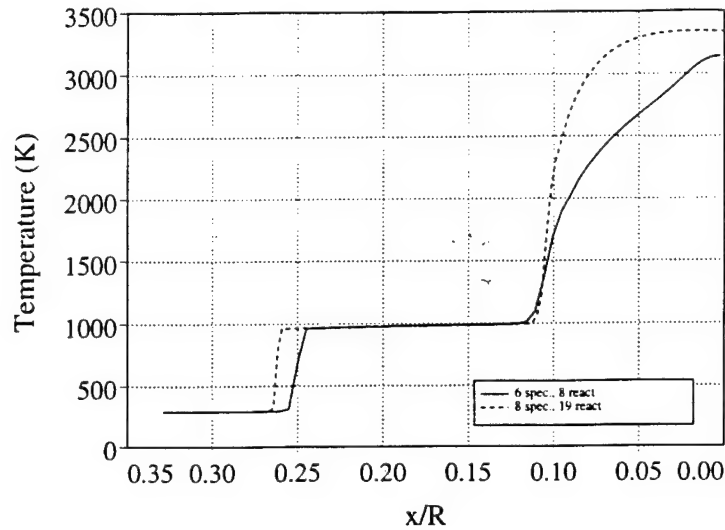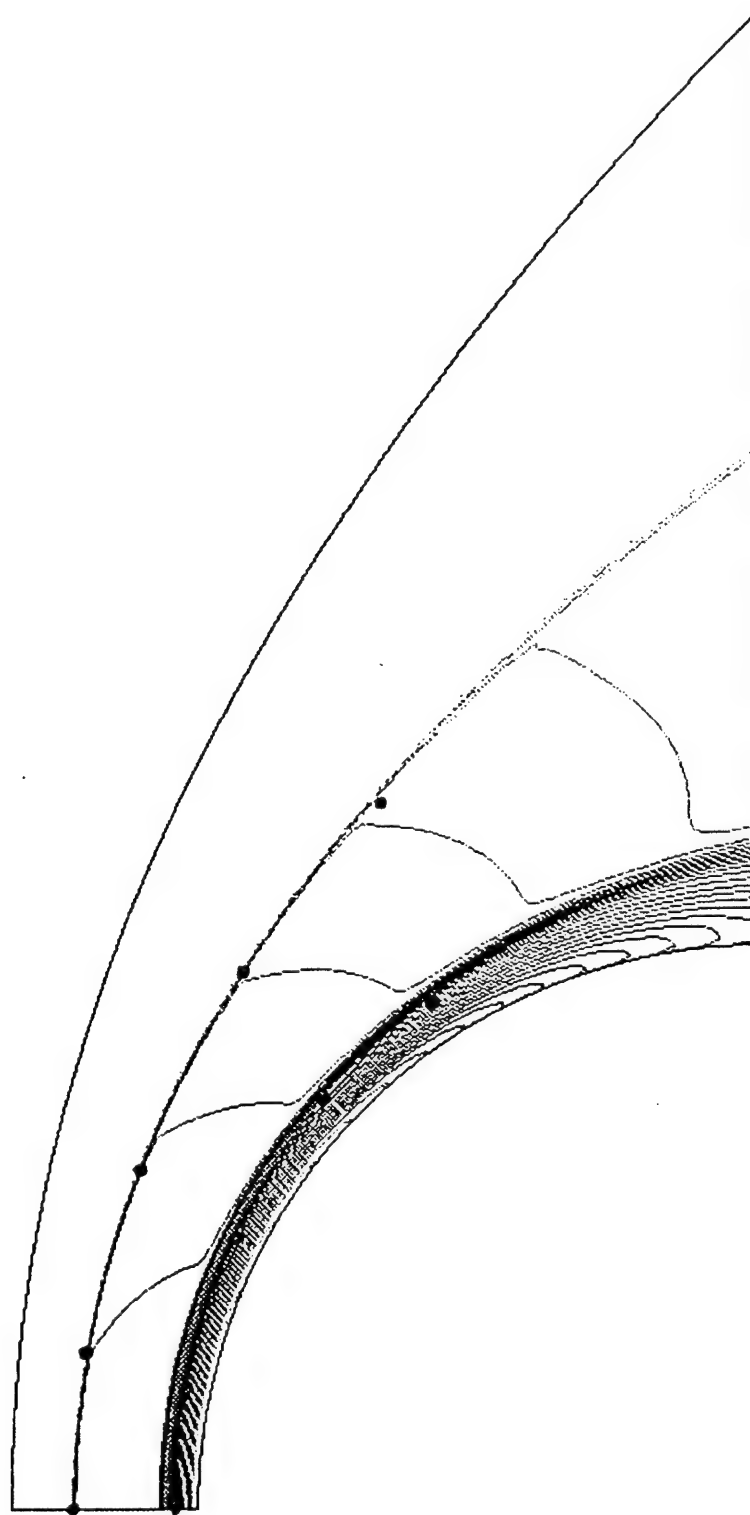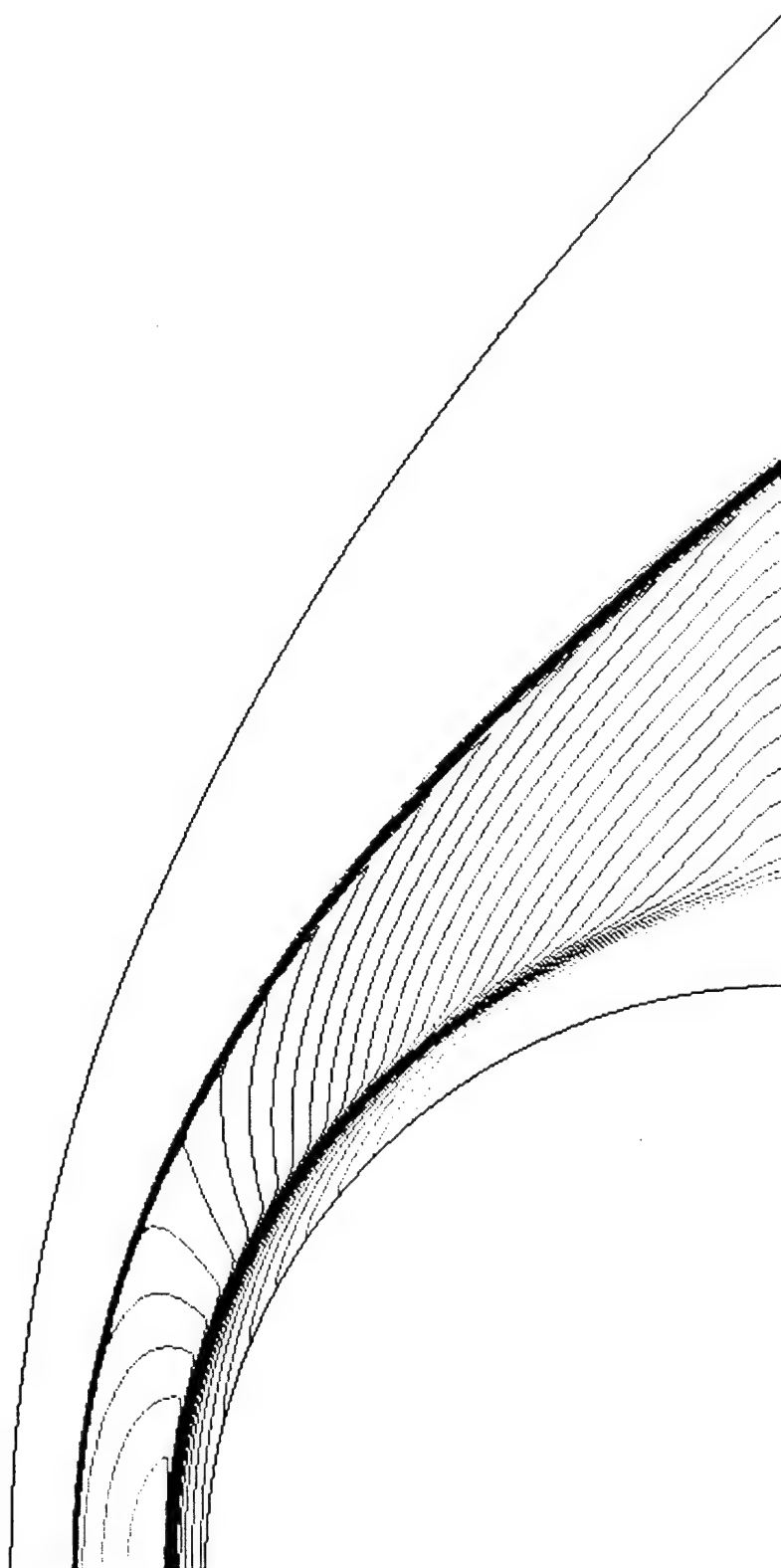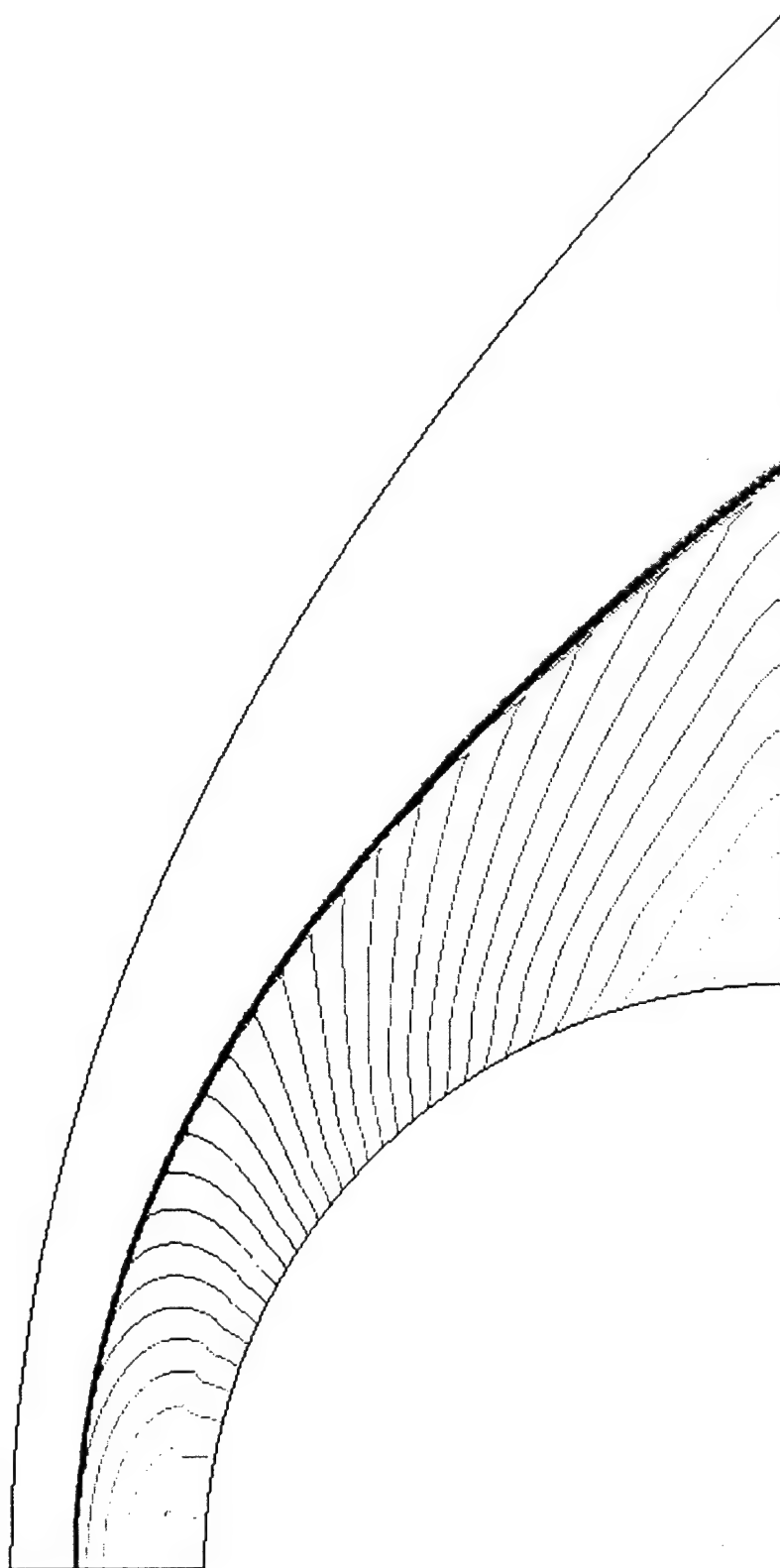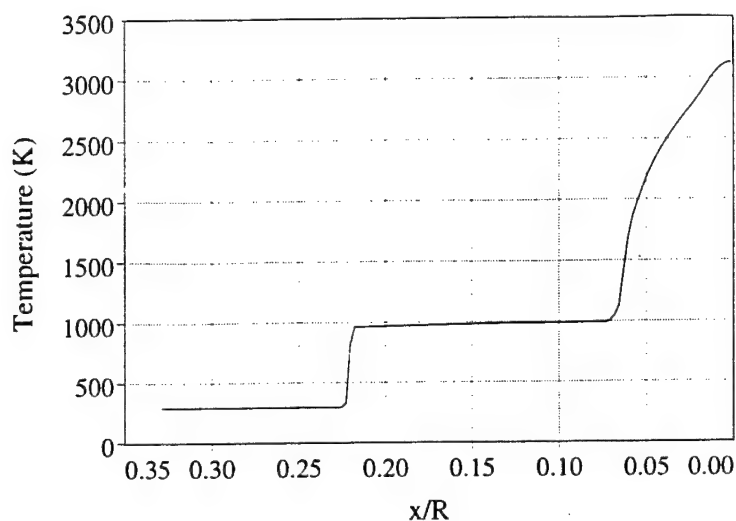
Figure 5: Temperature along stagnation streamline for two different chemical models: $M = 3.55$ hydrogen/oxygen; projectile surface at $x/R = 0.00$. Grid size: 64×64.

radicals does not decrease greatly after the heat release zone, even with the formation of a great deal of water vapor. This is due to the conversion of the reactants into radical species which then combine directly to form water.

Upon examination of Figure 6, it can be seen that the agreement between the computation and experiment is quite good. This computation also agrees favorably with the simulation of Yungster *et al.* [19] who limited the cell Damköhler number so that the heat release was spread out among two to three cells. No such limitation is necessary using the current formulation. Yungster *et al.* predicted a shock location of $x/R = 0.24$ as compared to the present prediction of $x/R = 0.22$, a difference of 8.3%. Their heat release zone began at approximately $x/R = 0.10$, compared to a location of $x/R = 0.065$ as predicted by the 64×128 simulation, a difference of 35%.

Figures 12 and 13 show the convergence histories for the six species, eight reaction 64×64 cell calculation without and with multigrid acceleration. The convergence histories present the root mean squared residual of the density of water and the number of supersonic cells in the domain versus the number of cycles. The initial increase in the density residual is due to the production of water as the flow initially reacts and the bow shock and reaction zone move outward from the body. The use of multigrid provides a significant convergence acceleration in this problem without compromising the accuracy of the solution.

The single grid calculation converged about six orders of magnitude in 2000 iterations, consuming 995 seconds (wall clock) using four processors of an IBM SP-2. The multigrid calculation, using only two levels of multigrid for this 64×64 mesh, converged fourteen orders of magnitude in 2000 iterations while requiring 1250 seconds on four processors. The same level of convergence (which results in a solution that does not change) as the single grid case using multigrid takes about 800 iterations at a cost of 500 seconds, almost halving the computational time. The converged solutions with and without multigrid acceleration are virtually identical due to the correct forcing of the coarse grid by the fine grid solution. No unphysical diffusion of radical species is seen. The convergence history for the multigrid 64×128 cell simulation is shown in Figure 14. Multigrid again provides a significant convergence

Figure 6: Temperature contours: $M = 3.55$ hydrogen/oxygen. Contour levels in K: min: 250, max: 3130, inc: 93. Grid size: 64×128. Circles indicate experimental shock and heat release locations.

Figure 7: *Density contours:* $M = 3.55$ *hydrogen/oxygen. Contour levels in* kg/m^3*: min: 0.05, max: 0.6, inc: 0.016. Grid size:* 64×128*.*

Figure 8: *Normalized pressure contours:* $M = 3.55$ *hydrogen/oxygen. Contour levels* (p/p_∞): *min: 1.0, max: 16.5, inc: 0.5. Grid size:* 64×128.

Figure 9: *Temperature along stagnation streamline: M = 3.55 hydrogen/oxygen; projectile surface at x/R = 0.00. Grid size:* 64×128.
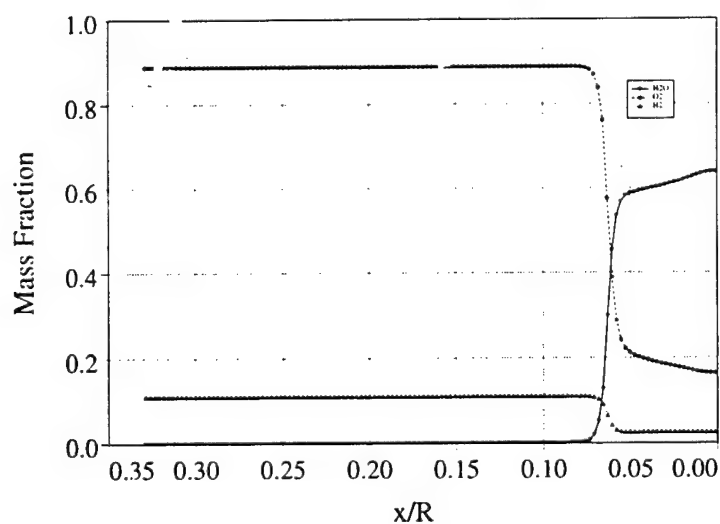
Figure 10: *Mass fractions along stagnation streamline: M = 3.55 hydrogen/oxygen. Shock location is at x/R = 0.22; heat release region begins at x/R = 0.065; projectile surface at x/R = 0.00. Grid size:* 64×128.
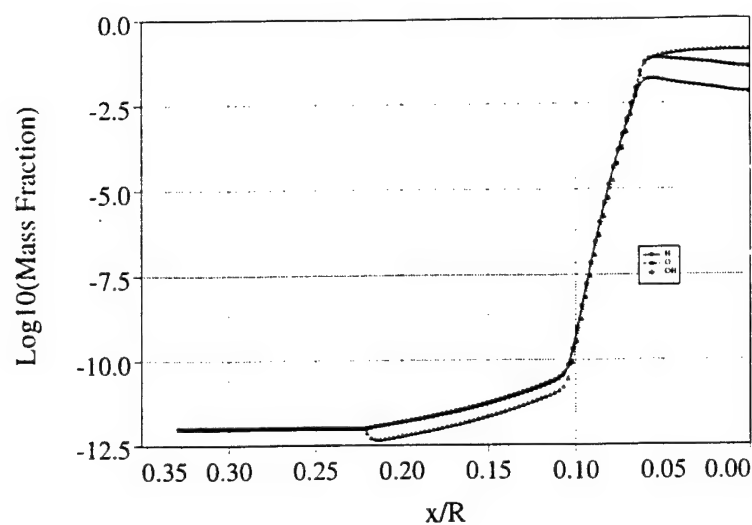
Figure 11: *Logarithm of radical mass fractions along stagnation streamline:* $M = 3.55$ *hydrogen/oxygen.* *Shock location is at* $x/R = 0.22$; *heat release region begins at* $x/R = 0.065$; *projectile surface at* $x/R = 0.00$. *Grid size:* 64×128.
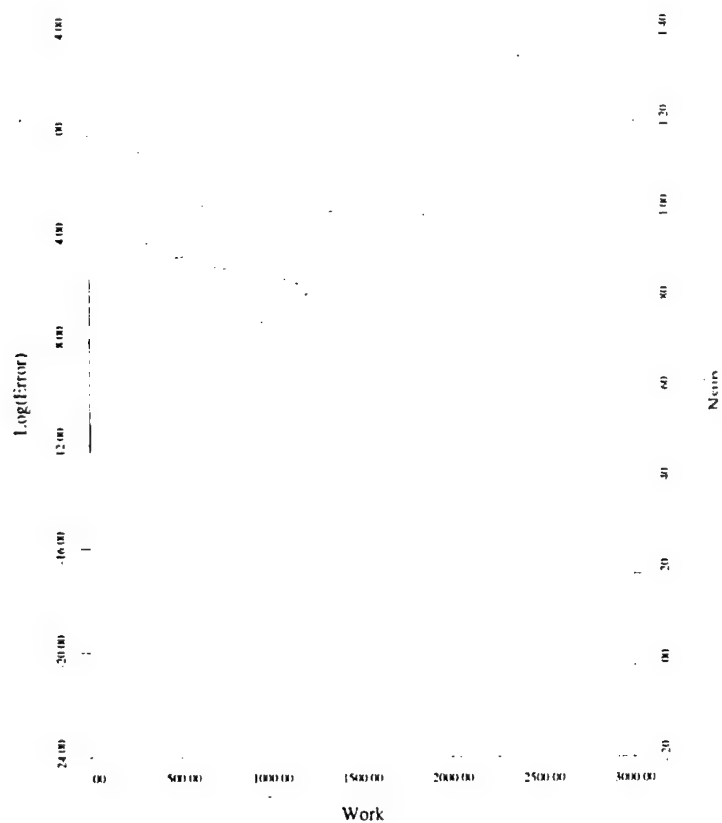
Figure 12: *Single grid convergence history:* $M = 3.55$ *hydroger/oxygen.* *Grid size:* 64×64.
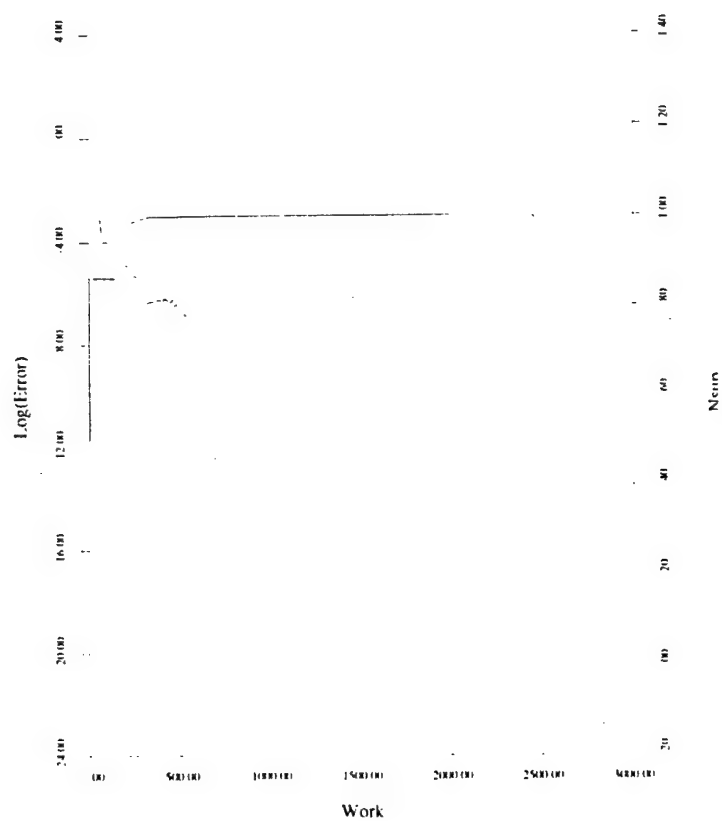
Figure 13: Multigrid convergence history: $M = 3.55$ hydrogen/oxygen. Grid size: 64×64.

acceleration.
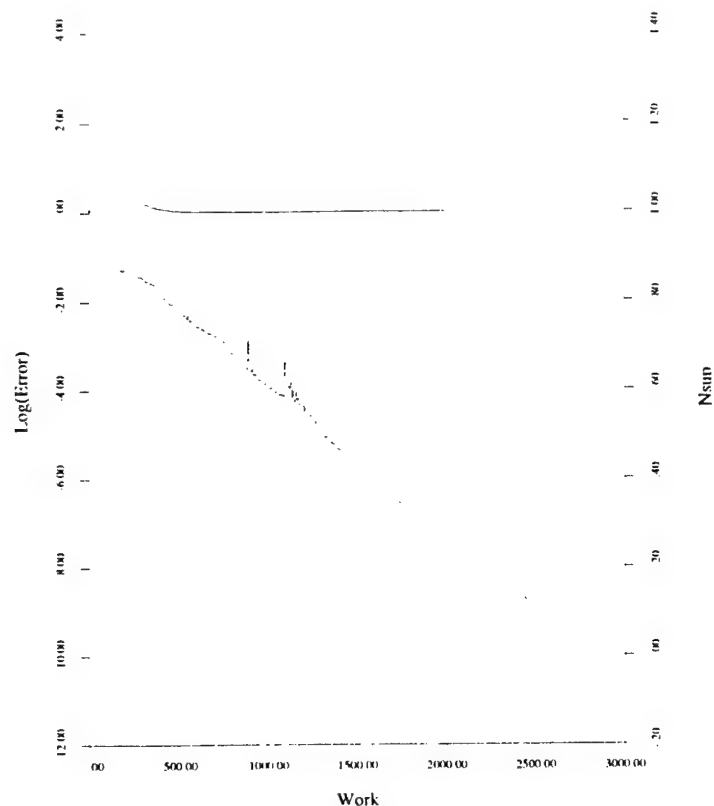
Figure 14: Multigrid convergence history: $M = 3.55$ hydrogen/oxygen. Grid size: 64×128.

2.2 $M = 4.79$ Hydrogen-Air Reacting Blunt Body Flow

Another axisymmetric flow is considered in this section. This case, computed by Matsuo *et al.* [10], is a stoichiometric hydrogen–air flow at $M = 4.79$ over an axisymmetric spherical projectile with a diameter of 2.5 mm. The free stream temperature for this case is 292 K while the pressure is 42600 Pa. Flow with these same conditions over a projectile of diameter 15 mm exhibits oscillations in temperature, pressure and density of a constant frequency. The smaller diameter projectile was found by Matsuo *et al.* to produce a steady state solution, which is useful for our validation study. Again, this flow is dominated by convection and reaction, which enables us to neglect diffusive effects and concentrate on the interaction of the convective, reactive and numerical dissipation portions of the algorithm. In addition, like the $M = 3.55$ hydrogen–oxygen case, this flow has a large induction zone relative to the diameter of the body. This will allow validation of the algorithm with the knowledge that the induction zone has been adequately resolved.

Because Matsuo *et al.* used the modified Jachimowski hydrogen–air mechanism (nine species and nineteen reactions) for their simulation, it was also chosen in this work. Nitrogen is treated as an inert diluent due to the temperature and pressure range in the region behind the bow shock. In order to be able to compare with the results of Matsuo *et al.*, it is also necessary to use the same grid resolution. Therefore, this flow was simulated using a 128×256 cell grid (128 along body, 256 in normal direction) in which the normal grid spacing along the stagnation streamline was the same as that of Matsuo *et al.* As was the case in Section 2.1, the projectile was assumed to have a non-catalytic, inert surface

with negligible heat transfer (adiabatic wall) between the fluid and the body. The simulation domain is again from the centerline of the flow to the shoulder of the projectile with symmetry boundary conditions at the centerline. Figure 15 shows contours of temperature for the steady state result while Figures 16 and 17 show the density and pressure contours in the flow field.

As was seen in the $M = 3.55$ hydrogen–oxygen case, the bow shock curves and thus causes the temperature behind the shock to vary with the angle of the shock. The varying temperature causes the length of the induction zone to vary. However, the induction zone for this case is much smaller than the case in the previous section because the higher free stream Mach number produces a larger temperature rise across the shock. This larger initial temperature in the induction zone produces radicals at a much higher rate which leads to a faster reaction. Again, the heat release and temperature increase is accompanied by a density drop because the pressure remains relatively constant through the induction and reaction zones. The CUSP scheme is seen to capture the shock and reaction front without oscillation and unnecessary dissipation.

The temperature along the stagnation streamline is depicted in Figure 18 while Figure 19 shows the results of the simulation of Matsuo et al. The temperature profiles are very similar with the current simulation predicting a shock position of 0.202 mm while a shock location of 0.195 mm is predicted by the simulation of Matsuo et al. This difference of approximately 3.6% can be explained by the difference in numerical dissipation schemes as well as the fact that Matsuo et al. used a finite difference scheme instead of the present finite volume scheme. Matsuo et al. validated their algorithm using Lehr's unsteady experimental results and achieved very good accuracy. Because of the similarity between our results and those of Matsuo et al., we have fairly high confidence that the present numerical algorithm is accurately capturing phenomena present in high speed reactive flows dominated by convection.

2.3 $M = 4.00$ Hydrogen-Air Reacting Viscous Flow Over a Wedge

With the success of the previous cases involving convection dominated reactive flows, it is appropriate now to consider simulating a reactive viscous flow involving hydrogen combustion. A common viscous reactive test case consists of a stoichiometric hydrogen–air flow over a 10° ramp. The free stream Mach number was 4.0, the free stream temperature was 1200 K and the free stream pressure was one atmosphere. The 2 cm long ramp was preceded by a 1 cm solid wall section. All solid walls were modeled as inert, non-catalytic, adiabatic surfaces. The effects of viscosity, heat conduction and species diffusion are all included in this computation. This is a common computational test case, with several published simulations available [23, 16, 12, 6] for turbulent reactive flows. However, because of the lack of concrete knowledge regarding the effect of turbulence on combustion, in this work the flow was computed assuming fully laminar flow. This will produce different results than those obtained using a turbulence model, but a grid convergence study may still be pursued to determine the robustness of the numerical model. In addition, most of the researchers who attempted this computation used grids leading to solutions that were severely underresolved, both in the boundary layer region and in the reaction zone. Thus, any results that were obtained must be viewed in this light.

This flow was computed using Westbrook's nine species, seventeen reaction hydrogen–air mechanism because other researchers have used this model for this test case. This is a very challenging flow because of the myriad of physical phenomena that must be resolved accurately. The formation of the boundary layer must be captured well, without unnecessary dissipation, so that the displacement thickness is correct. The conduction of heat must also be accurate so that the effects of viscous dissipation deep in the boundary layer are felt correctly in the sections of the boundary layer far from the wall. Proper resolution of the interaction of the shock and boundary layer and the oscillation free capture of the shock are essential, as is the correct modeling of species diffusion. The free stream temperature is not high enough to initiate a reaction, but the combination of high temperature in the boundary layer,
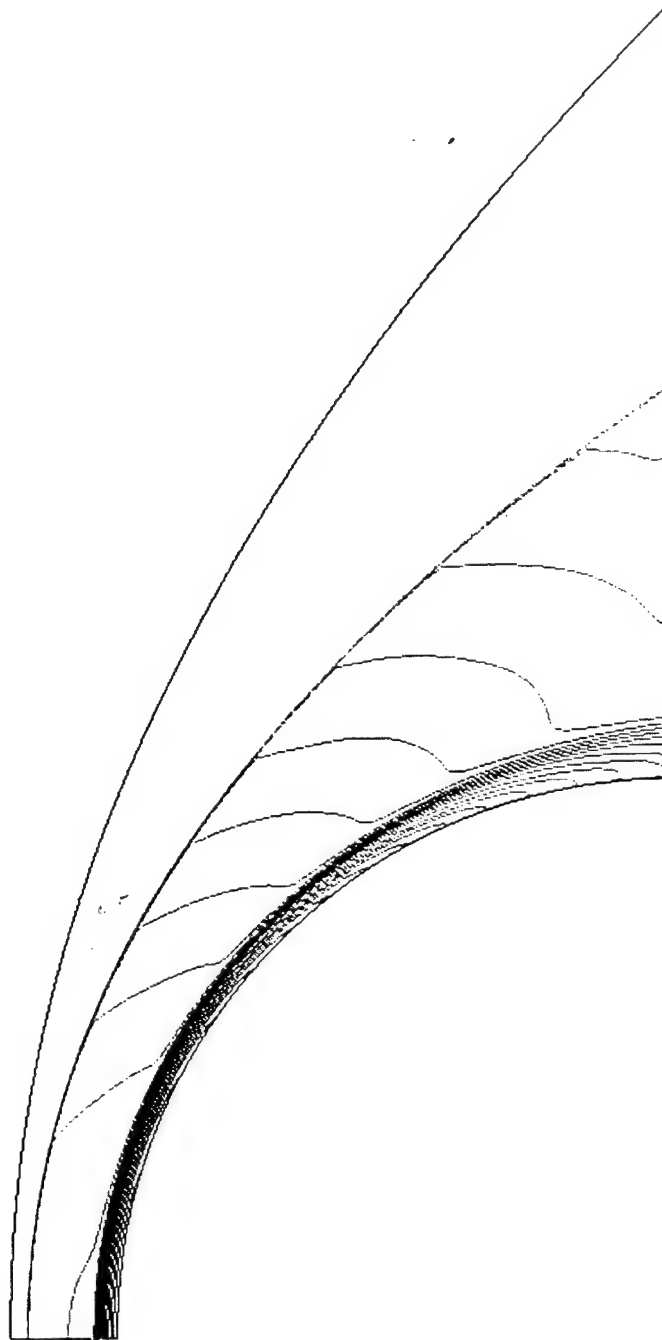
Figure 15: *Temperature contours: $M = 4.79$ hydrogen/air. Contour levels in K: min: 250, max: 2850, inc: 93.*
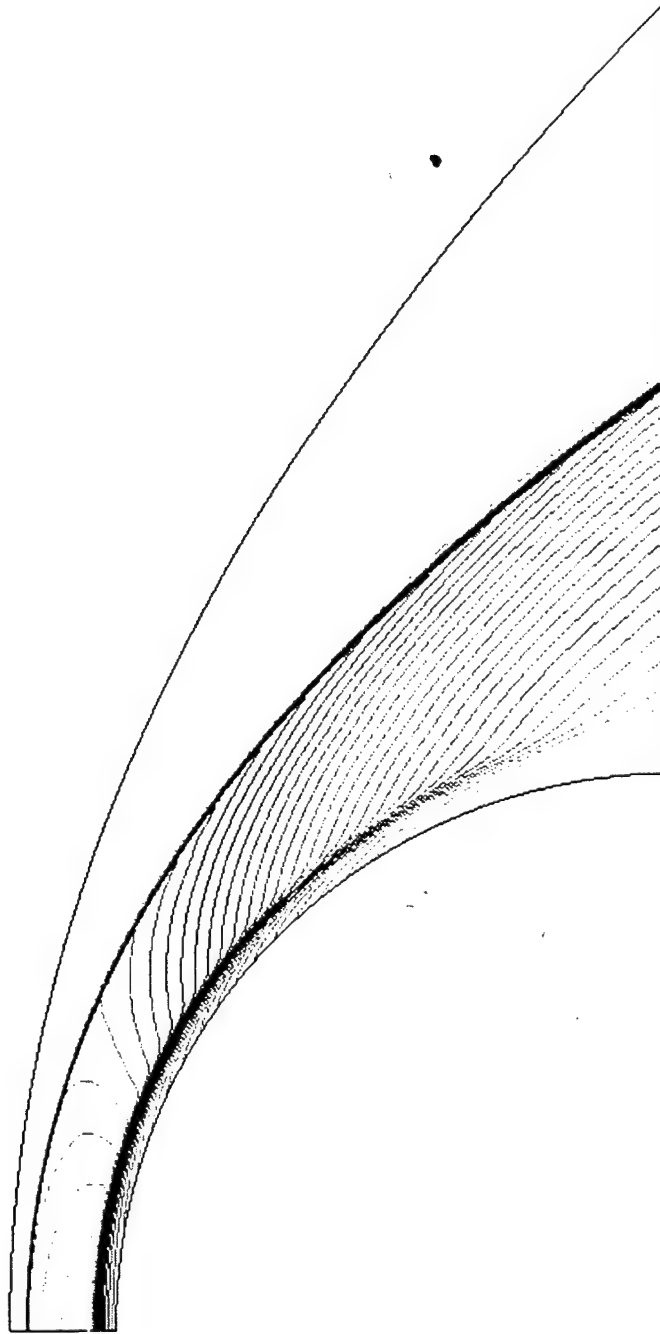
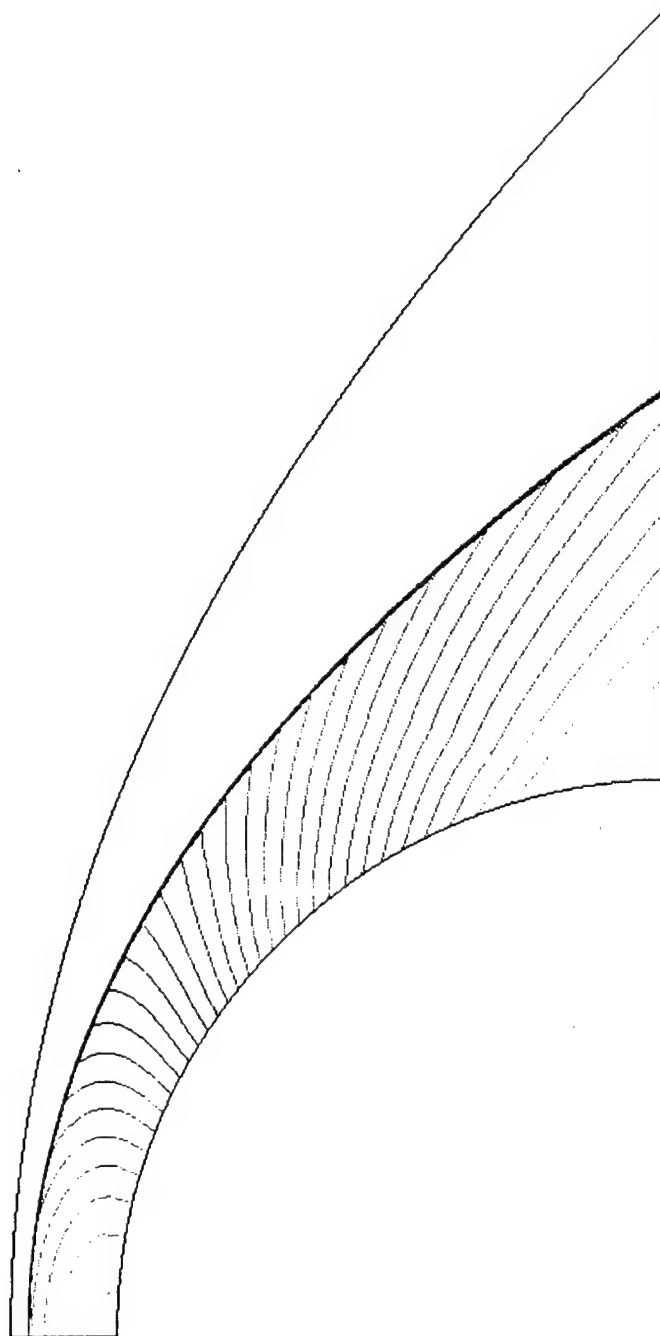Figure 16: Density contours: $M = 4.79$ hydrogen/air. Contour levels in kg/m^3: min: 0.2, max: 2.1, inc: 0.054.

Figure 17: *Normalized pressure contours:* $M = 4.79$ *hydrogen/air. Contour levels* (p/p_∞): *min: 1.0, max: 30.0, inc: 0.83.*
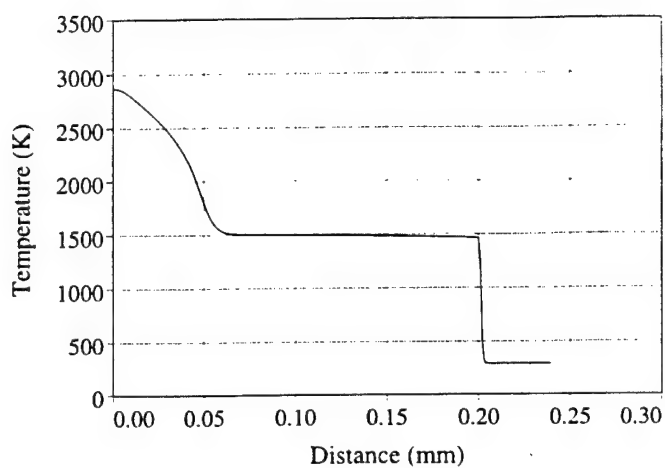
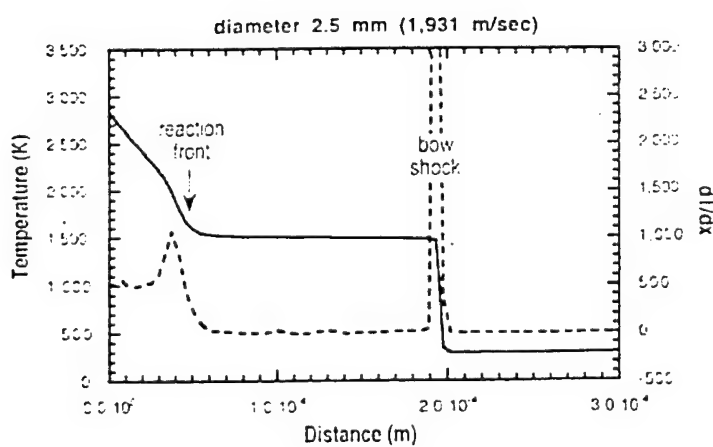Figure 18: Temperature profile along stagnation streamline: $M = 4.79$ hydrogen/air. Body surface is at 0.00 mm.

Figure 19: Temperature profile and temperature gradient along stagnation streamline from Matsuo et al. [44]: $M = 4.79$ hydrogen/air. Body surface is at 0.00 mm.

diffusion of radicals in the direction normal to the wall and the oblique shock cause a reaction front to form past the shock in the ramp region. Any inaccuracy will cause the location of the reaction front to be incorrect.

An assiduous grid convergence study was undertaken for this flow. Three grids were used to simulate this flow and to determine the robustness of the algorithm. All three grids had cells clustered near the wall to properly capture the laminar boundary layer, with approximately 32 cells within the boundary layer. In addition, cells were clustered near the start of the ramp, where shock–boundary layer interaction may lead to int..resting phenomena. We would expect any artificial diffusion of mass, momentum and energy to decrease as the grid resolution increases. In addition, the modeling of convective and diffusive transport is second order accurate and thus, the accuracy of the physical transport should increase as the grid spacing becomes smaller. Figures 20, 21 and 22 show the temperature in the flow field for three grids of size 64×96, 64×108 and 128×156, with the first number of cells along the wall and the second number of cells normal to the wall. As was expected, the formation of the
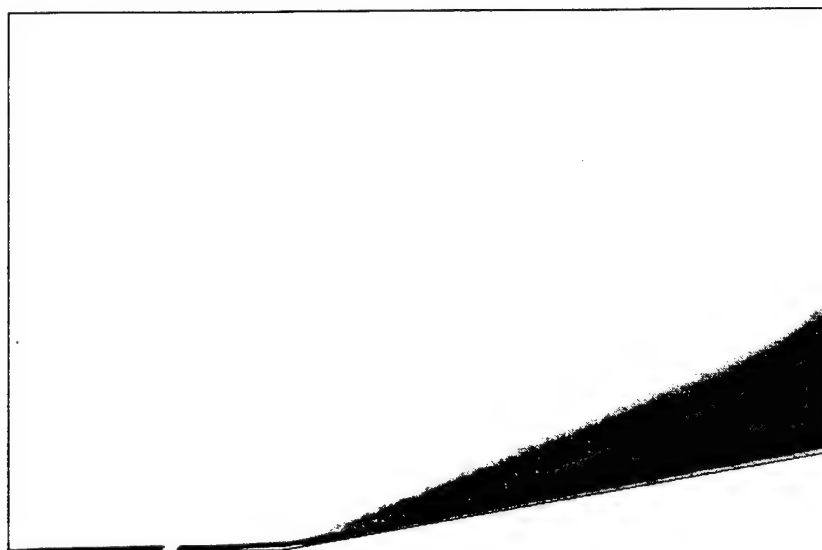
Figure 20: *Temperature:* $M = 4.0$ *hydrogen/air* $10°$ *viscous ramp,* 64×96 *grid. Temperature range: 1200–3500 K.*

boundary layer and the attendant viscous dissipation raises the temperature near the wall which causes various radical species to form. This leads to the formation of some water vapor very near the wall before the shock, but does not greatly affect the flowfield. One may also notice the formation of a weak oblique shock at the left edge of the domain due to the displacement thickness of the boundary layer. The interaction of the stronger oblique shock and the boundary layer at the ramp corner separates the boundary layer for a short distance and causes a small recirculation zone in that region. Beyond the oblique shock, the increased temperature and pressure lead to faster radical production and increased diffusion of those radicals and heat to the unreacted bulk flow behind the shock. The result is a reaction front that forms and gradually moves away from the wall. The reaction front may be seen in a different way by viewing the mass fraction of water in Figure 23 for the 128×156 grid. Comparing the results of the three grid simulations yields interesting insights into the resolution needed for this flow. The third grid (128×156) has twice the resolution of the first grid (64×96) in both the normal and streamwise directions outside of the boundary layer. The result is that the reaction front is unphysically diffused on the coarser grid (due to inadequate resolution of the reaction zone, artificial diffusion of radical

Figure 21: *Temperature:* $M = 4.0$ *hydrogen/air* $10°$ *viscous ramp,* 64×108 *grid. Temperature range:* *1200-3500 K.*
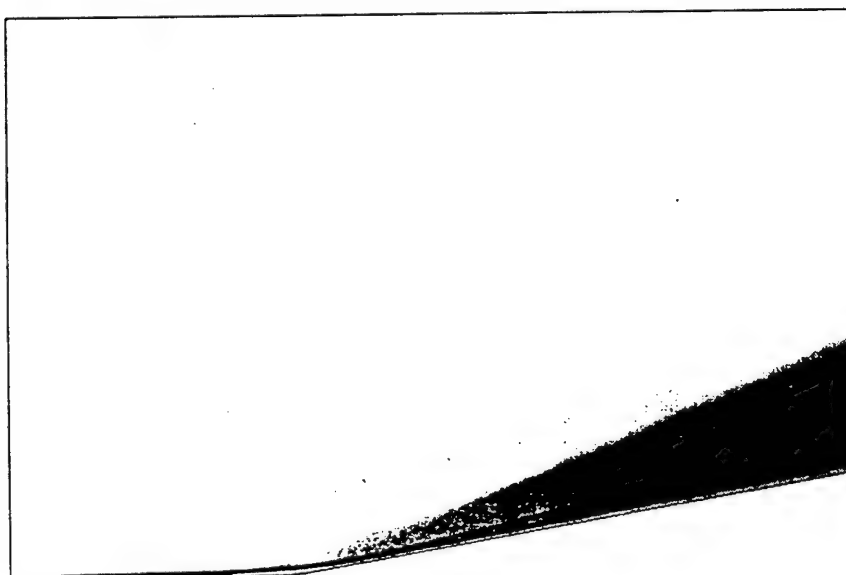

Figure 22: *Temperature:* $M = 4.0$ *hydrogen/air* $10°$ *viscous ramp,* 128×156 *grid. Temperature range:* *1200-3500 K.*
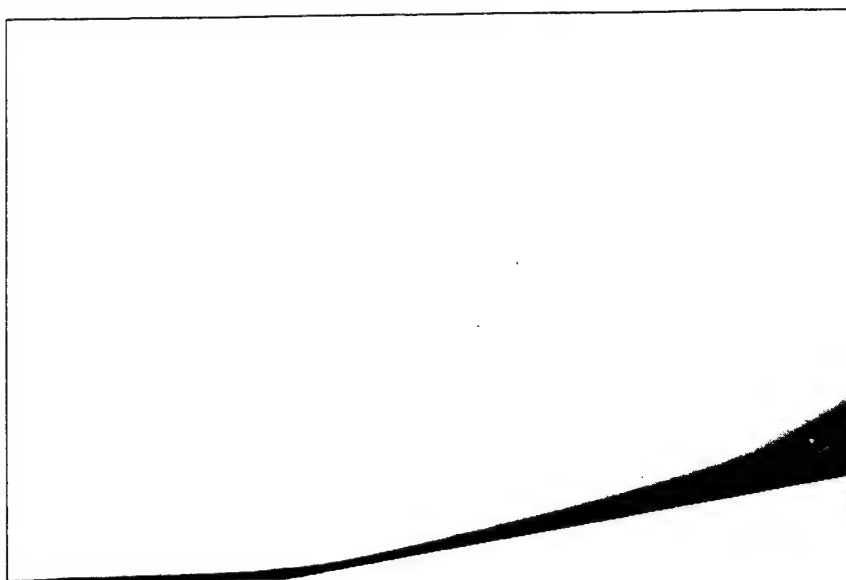
Figure 23: Water mass fraction: $M = 4.0$ hydrogen/air $10°$ viscous ramp, 128×156 grid. Mass fraction range: 0.00–0.18.

species and energy and inadequate resolution for diffusive transport) and is captured quite well on the finest grid. The curvature of the reaction front at the right edge of the domain may be an actual physical phenomenon or it may be a numerical artifact. If it is a spurious numerical phenomenon, it is probably due to one of two causes. First. it may be that the supersonic extrapolation boundary conditions at the outflow plane are contaminating the solution. Second, the numerical dissipation may be causing unphysical diffusion of radical species and heat. However, it is unlikely, given the resolution of this grid in that particular area, that the artificial dissipation is the cause. Thus, in order to test the accuracy of the boundary condition. an additional simulation was performed in which the outflow plane of the simulation domain was moved approximately 0.9 cm downstream. The computational size of this additional simulation was also 128×156 cells, with 32 cells again within the boundary layer.

The results of this extended domain simulation are presented in Figures 24 through 26. The flow field temperature is depicted in Figure 24. where the solid line within the simulation domain indicates the former outflow plane location. Comparing this figure to Figure 22. one can see that the temperature in the smaller domain and the extended domain match exceptionally well in the original computational region. Water mass fraction is shown in Figure 25. while pressure may be viewed in Figure 26. The extension of the domain makes it evidently clear that the curvature of the reaction front observed in Figures 22 and 23 is indeed a true physical phenomenon. In addition, the simulation on the extended domain indicates that the use of the supersonic extrapolation boundary conditions at the outflow plane does not compromise the accuracy of the solution in the region of the boundary. In this flow, radicals and heat in the boundary layer diffuse outward normal to the wall and eventually, along with the increased temperature and pressure behind the oblique shock, cause the reaction to proceed in the inviscid region behind the oblique shock. This reaction front couples with the shock toward the outflow plane and changes the angle of the discontinuity in the flow due to the pressure and heat release behind the shock/reaction front.

Other researchers' previously published results for this flow were calculated on grids with half as many cells in the normal direction as the finest grid presented here. These simulations show a coupled shock reaction front located much closer to the ramp corner in which the shock curves away from the
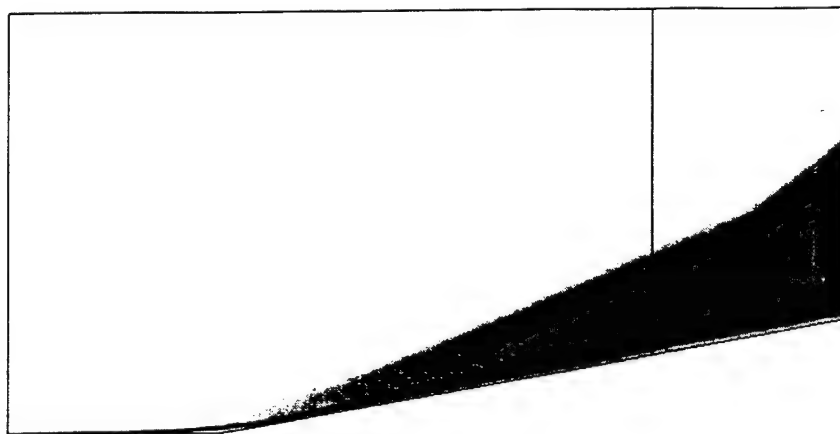
Figure 24: *Temperature for extended domain:* $M = 4.0$ *hydrogen/air* $10°$ *viscous ramp,* 128×156 *grid.* *Temperature range: 1200–3500 K. Solid line in the computational domain indicates original outflow boundary.*
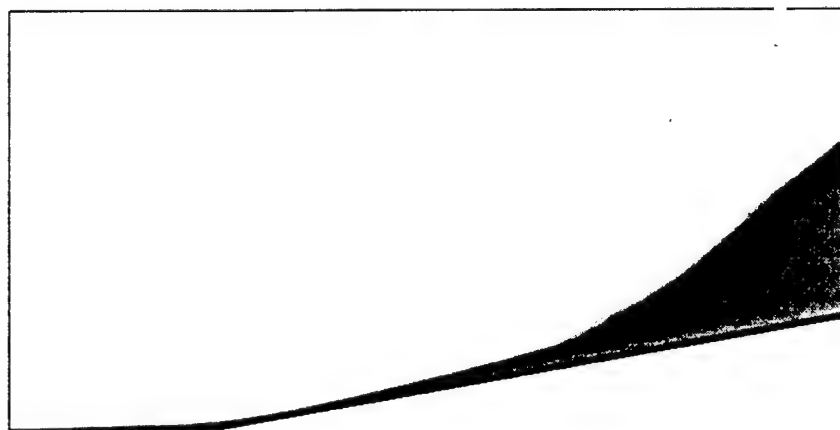

Figure 25: *Water mass fraction for extended domain:* $M = 4.0$ *hydrogen/air* $10°$ *viscous ramp,* 128×156 *grid. Mass fraction range: 0.00–0.18.*
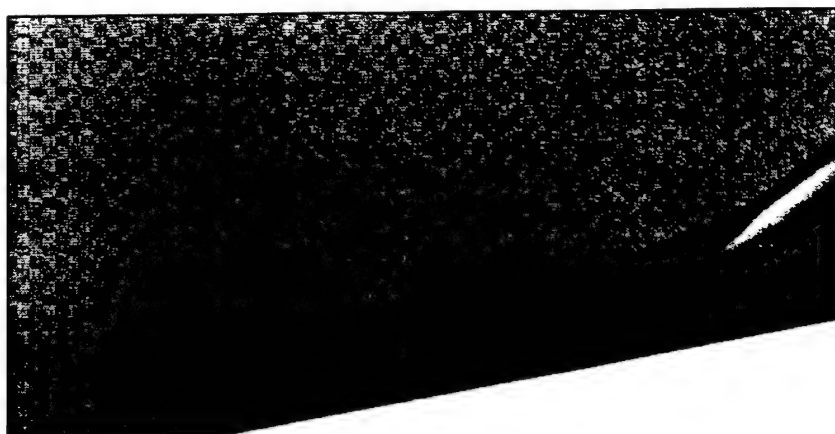
Figure 26: Normalized pressure for extended domain: $M = 4.0$ hydrogen/air $10°$ viscous ramp, 128×156 grid. Normalized pressure range: 0.00-6.00.

wall. While these other simulations were computed with turbulence models of varying complexity, it is probably the underresolution of the reaction area which leads to the greatest disparity between those results and those presented here. If the reaction area is underresolved and the numerical scheme is too dissipative, then a probable result would be for the reaction zone to move upstream to the shock position. This would be caused by unphysical diffusion of radical species and thermal energy upstream, allowing the reaction to commence earlier and thus move toward the shock. In fact, early simulations of this flow field with the current method using a very coarse grid were characterized by the reaction front moving upstream and away from the wall toward the shock location.

2.4 $M = 2.10$ Hydrogen-Air Reacting Viscous Flow Over a Wedge

As was mentioned in Section 1.1, one of the objectives of this research is to provide a computational tool for the analysis of experiments that were performed under the University Research Initiative at Princeton University while at the same time allowing the numerical scheme to be validated by comparison of converged solutions to experimental results. To that end, an experiment that has not been previously simulated was chosen as both a test for the numerical scheme and an opportunity for the numerical method to be used to illuminate the physical processes of the experiment. This two dimensional viscous reactive test case is taken from an experiment performed by Fielding [24]. In this experiment (Figure 27), a wedge of half angle $6.34°$ was placed in a free stream of partially reacted hydrogen and air. The free stream Mach number was 2.10, the free stream temperature was approximately 569 K and the pressure was 0.060 atmospheres. The object of the experiment was to see if radical-seeded hydrogen–air mixtures would react at low pressures over a wedge after passing through an oblique shock. The mass fractions of the inlet flow were determined by Fielding using a one dimensional reacting gas code and are given in Table 1. Hydrogen had been injected into the air stream upstream of the ramp, partially reacted and then expanded so that the flow constituents became frozen. It was assumed that nitrogen was an inert diluent. Due to the low pressure, the Reynolds number at the end of the ramp is approximately 33000 so that fully laminar flow may be assumed. Species diffusion and heat conduction effects are included in the simulation. The nine species, 21 reaction model of Yetter *et al.* was used because it had been the model utilized to generate the composition of the incoming flow.

The flow was simulated on a grid with 128 cells in the streamwise direction and 96 in the direction
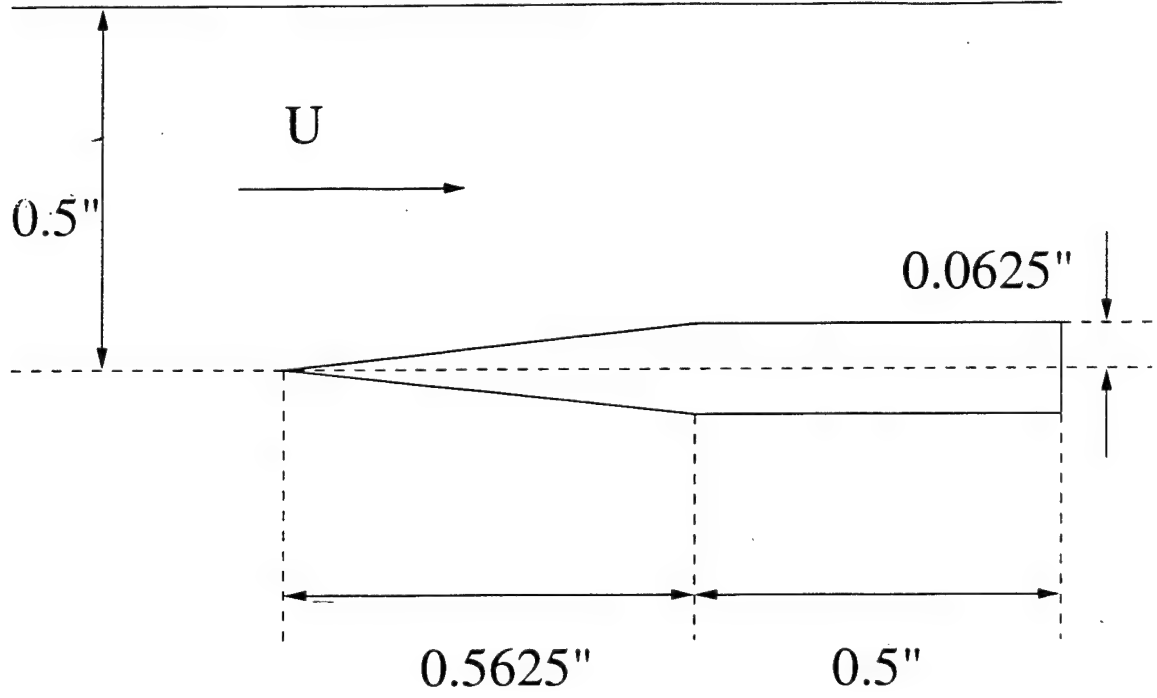
Figure 27: *Experimental setup for M = 2.10 viscous wedge.*

Species	Mass Fraction
H_2	6.86×10^{-3}
O_2	1.75×10^{-1}
H_2O	2.86×10^{-2}
N_2	7.84×10^{-1}
H	2.33×10^{-4}
O	9.66×10^{-4}
OH	1.65×10^{-4}
HO_2	3.97×10^{-3}
H_2O_2	4.76×10^{-10}

Table 1: *Free stream mass fractions for M = 2.10 hydrogen–air viscous wedge flow.*

normal to the plate. Symmetry boundary conditions were implemented along the centerline of the flow upstream of the wedge so that the governing equations were solved on only half of the experimental domain. The grid was clustered near the leading edge of the wedge to properly resolve the growth of the boundary layer and the shock attachment. Cells were also clustered near the ramp to resolve the boundary layer structure adequately; approximately 32 cells were within the boundary layer.

Figure 28 presents contours of density for this flow. The relatively thick boundary layer is immediately noticeable. Because of this thick boundary layer, the shock near the leading edge of the plate is at a much higher angle than the region away from the ramp. The growing displacement thickness from the boundary layer causes the main flow to see an effectively curved wall and thus, weak expansion waves are formed to adjust the curvature of the shock. It is also important to point out the absence of large heat release regions even though the domain near the leading edge experiences a relatively large compression. The shock angle obtained from the numerical simulation is 35.0° while the experimental shock angle is 34.5°.
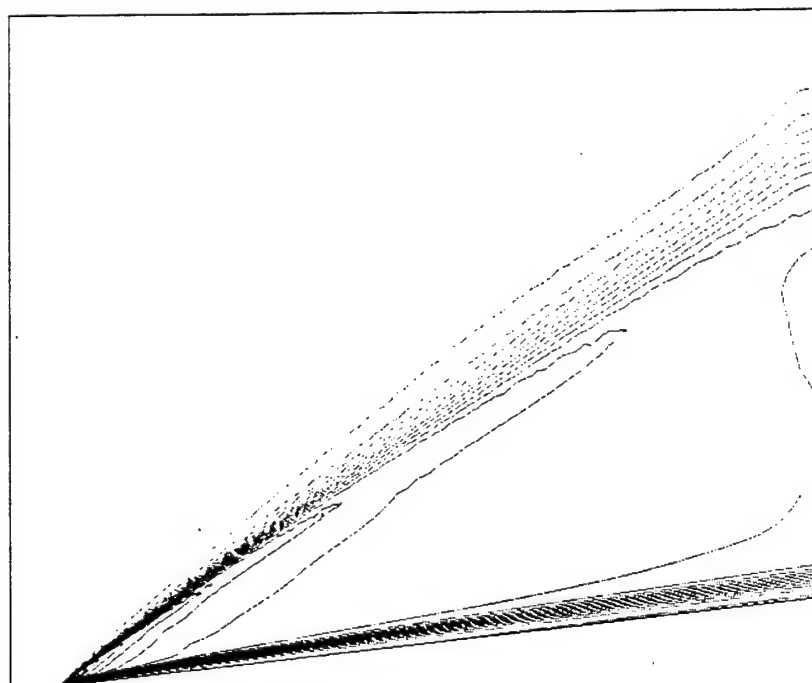
Figure 28: Density contours: $M = 2.10$ hydrogen/air 6.34° viscous ramp. Contour levels in kg/m^3: min: 0.033, max: 0.056, inc: 0.00129.

The pressure field (Figure 29) yields trends similar to the density field. There is curvature of the shock near the leading edge and expansion waves may be seen in the region behind the oblique shock. Very little change in the pressure is seen through the boundary layer.

The lack of progress of the reaction may be understood by viewing Figure 30, which shows contours of the logarithm of OH mass fraction. It is immediately obvious that the inlet mass fractions are not in an equilibrium state, as rapid reaction takes place in the free stream flow, producing more OH. Behind the shock, the increased pressure and temperature and slightly increased residence time cause faster formation of OH, but the post shock temperature and pressures are not sufficient to allow large quantities of OH to strip hydrogen atoms from H_2 molecules and form water vapor. Near the ramp surface, it can be observed that some OH is being consumed and transformed to water. This is due to the higher temperature in the boundary layer near the wall, and because the molecules in that
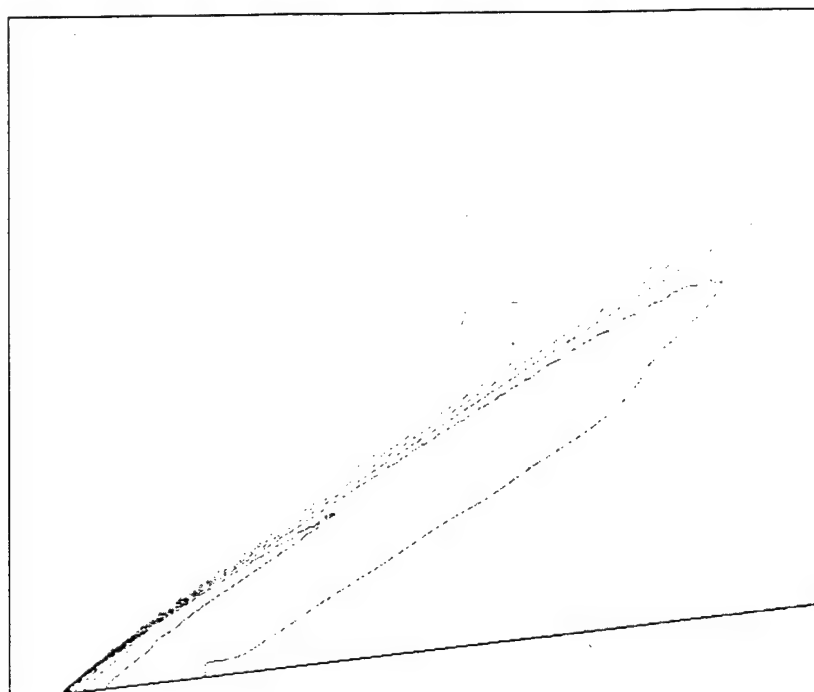
Figure 29: Normalized pressure contours: M = 2.10 hydrogen/air 6.34° viscous ramp. Contour levels (p/p_∞): min: 1.0, max: 3.06, inc: 0.0857.

region have a longer residence time at those higher temperatures due to the lower velocity near the wall. The maximum water mass fraction is approximately 3%, which is not much greater than the free stream water mass fraction from Table 1. This small amount of water production and heat release is not sufficient to cause thermal runaway, greater reaction and greater heat release. These results agree qualitatively with the experimental findings. Excited OH fluorescence was observed in the region behind the shock and near the leading edge, but large regions of heat release were absent.

The grid resolution used in this simulation was deemed to be adequate in light of the previous simulations and also upon viewing the computed results. The areas where high resolution was needed were mostly confined to the boundary layer. Examination of velocity profiles near the wall confirmed that the boundary layer was adequately resolved. However, upon viewing Figures 28 and 29, it may seem that the oblique shock is poorly resolved near the outflow plane. This poor resolution is caused by the increasing streamwise length of the computational cells in this area. Because of the nature of the conservative finite volume scheme used in this work, the correct jumps in properties across the shock are produced. In addition, in this type of reactive flow, an underresolved area would tend to lead to premature reaction and an accompanying movement of the reaction front upstream. This is not seen in this case, which lends credence to the claim that the shock is adequately resolved. Neither a sharply defined reaction zone nor any heat release region was developed at any point in the solution domain, thus removing the need to resolve them in great detail.

In order to provide greater understanding of the physical processes in a supersonic reactive flow and to assist in the design of a possible experiment, two additional simulations were performed. Due to the lack of reaction in the previous $M = 2.1$ case, the free stream Mach number was increased to $M = 2.92$. This higher Mach number will cause an increase in the temperature in the boundary layer of the flow, which could increase the Damköhler number in that region to the point where strong reaction might take place. The pressure was lowered to a value of 0.0157 atmospheres to match a one-dimensional
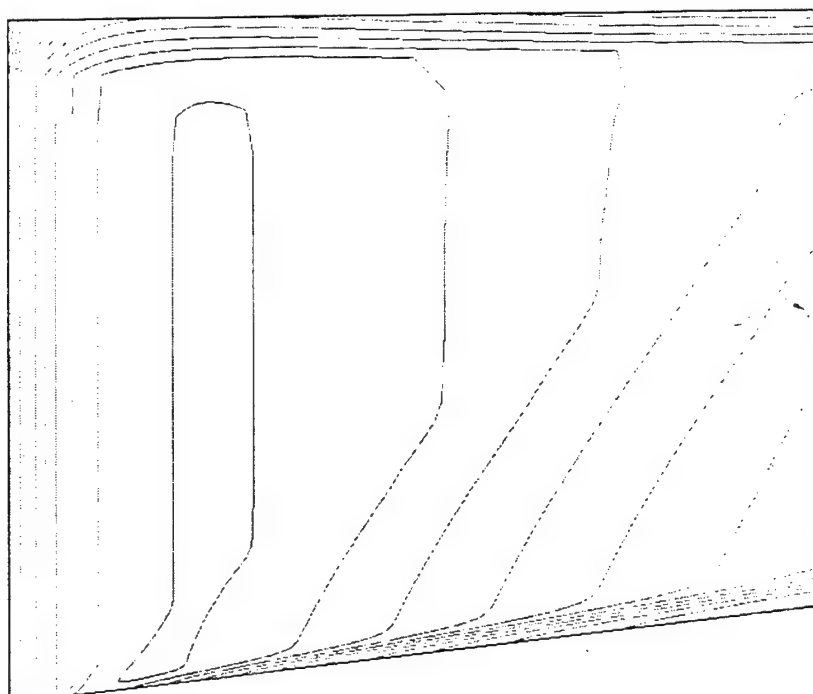
Figure 30: Logarithm of OH mass fraction contours: $M = 2.10$ hydrogen/air 6.34° viscous ramp. Contour levels: min: -3.33, max: -2.65, inc: 0.057.

prediction of Fielding [24]. The temperature in the free stream flow was changed to approximately 440 K, again to match a one-dimensional prediction.

This $M = 2.92$ flow is shown in Figures 31 and 32. Density contours are depicted in Figure 31 which, similar to Figure 28, shows a relatively thick boundary layer. The oblique shock angle is 25.9° while the exact analytic value for this Mach number and wedge angle pair is 24.5° This difference may be explained by reactions due to the nonequilibrium nature of the inlet flow at this free stream pressure and temperature which cause the Mach number to decrease in the streamwise direction. Figure 32 shows the logarithm of the mass fraction of OH. Again, similar to Figure 30, little progress is seen, with some OH forming water vapor at the end of the ramp near the exit plane. The maximum mass fraction of water is approximately 4%. In this case, the flow apparently still has a rather low Damköhler number due to the low pressure and temperature in the boundary layer.

The free stream Mach number was then increased to $M = 4.0$ and the free stream pressure was set at 0.5 atmospheres. The free stream temperature was the same as in the previous case. In addition, the free stream flow was changed to be composed of stoichiometric hydrogen/air. This condition, as determined by Fielding [24], should be sufficient to cause strong reaction at least in the boundary layer. Density contours from this simulation are shown in Figure 33, where the boundary layer can be seen to be thinner than in the two previous cases. The computed shock angle is 18.7° while the exact solution gives a shock angle of 19.0°. The close agreement in this case is because the stoichiometric hydrogen/air flow does not react before passing through the shock, so that the Mach number in the inviscid free stream is then constant until the shock. In this flow, the increased pressure and temperature do indeed cause a noticeable reaction to occur in the boundary layer as shown by contours of water vapor mass fraction in Figure 34. The maximum mass fraction of water at this condition is approximately 16%. Temperature contours are depicted in Figure 35. In this regime of flow conditions, the Damköhler number in the boundary layer is sufficiently large to cause strong
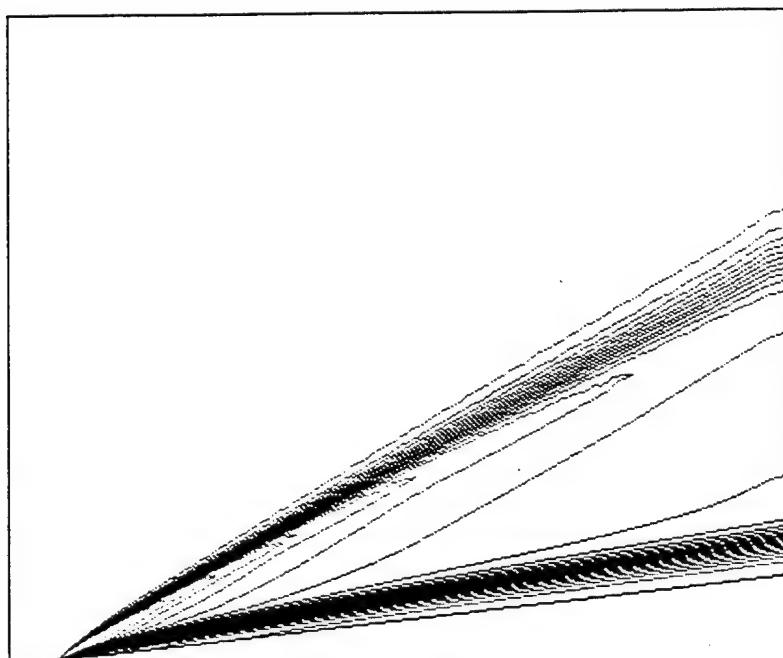
Figure 31: *Density contours: $M = 2.92$ hydrogen/air $6.34°$ viscous ramp. Contour levels in kg/m^3: min: 0.011, max: 0.022, inc: 0.0007.*
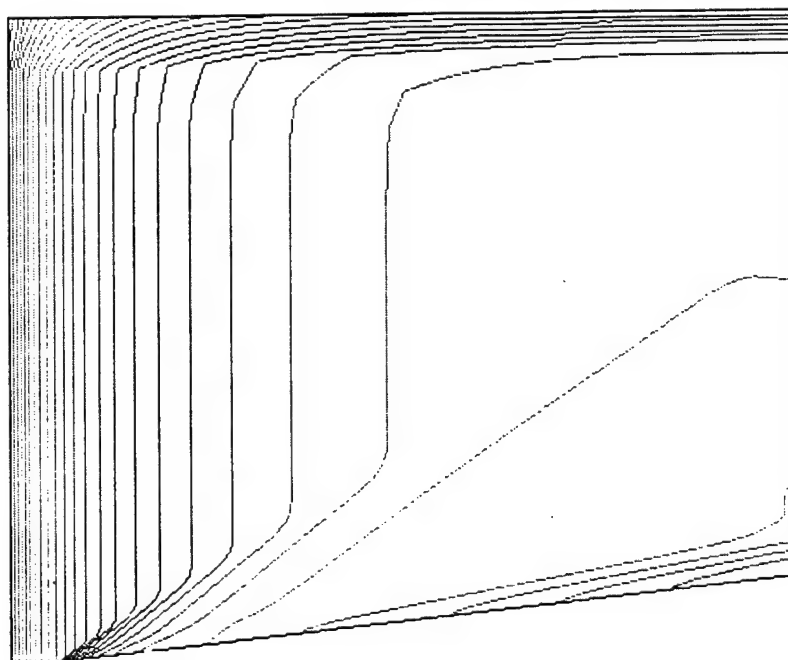
Figure 32: Logarithm of OH mass fraction contours: $M = 2.92$ *hydrogen/air* $6.34°$ *viscous ramp. Contour levels: min: -3.57, max: -2.54, inc: 0.057.*
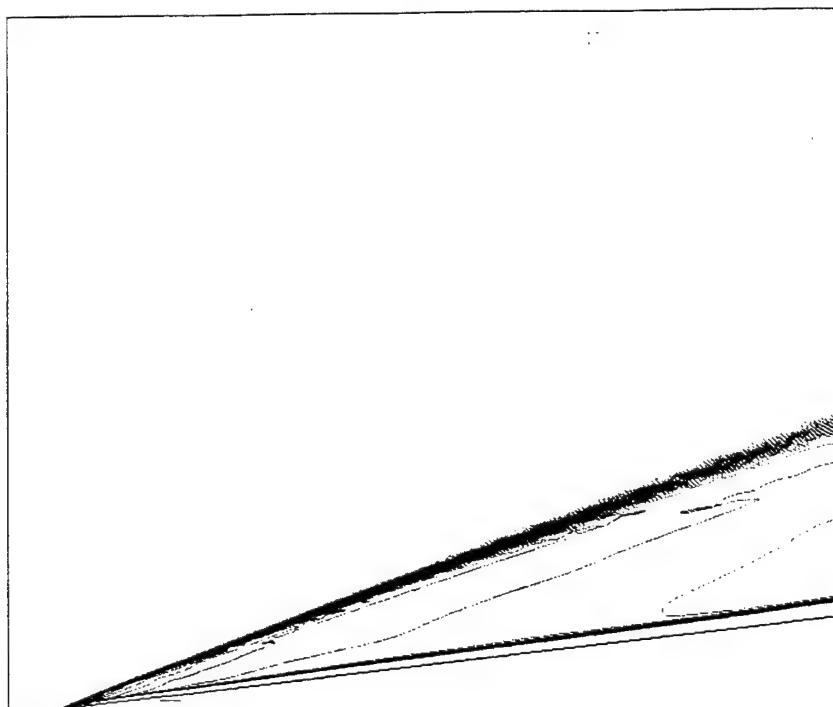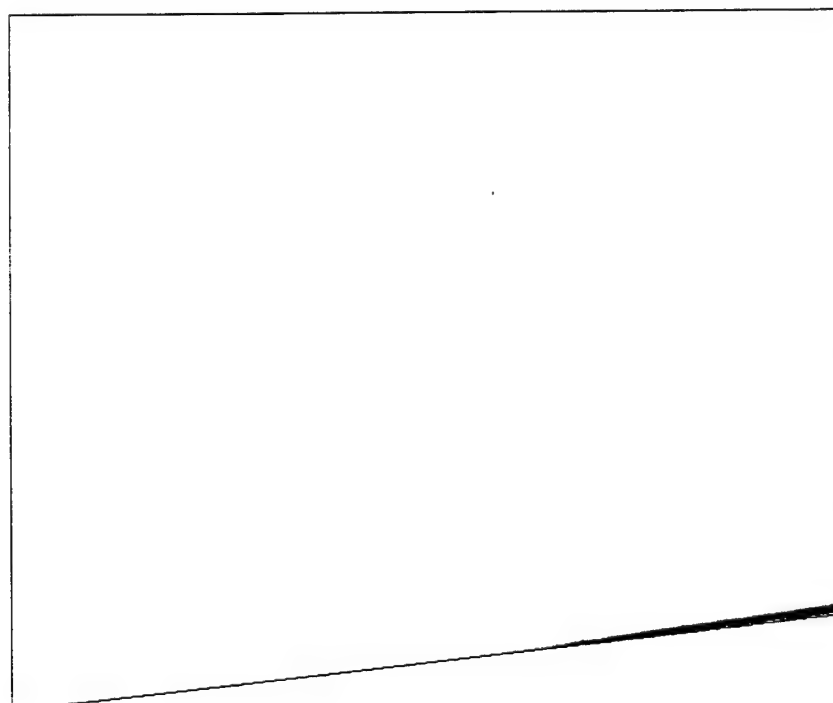
Figure 33: Density contours: $M = 4.00$ hydrogen/air 6.34° viscous ramp. Contour levels in kg/m^3: min: 0.3. max: 0.6, inc: 0.0086.

Figure 34: Water mass fraction contours: $M = 4.00$ hydrogen/air 6.34° viscous ramp. Contour levels: min: 0.0, max: 0.16, inc: 0.0073.
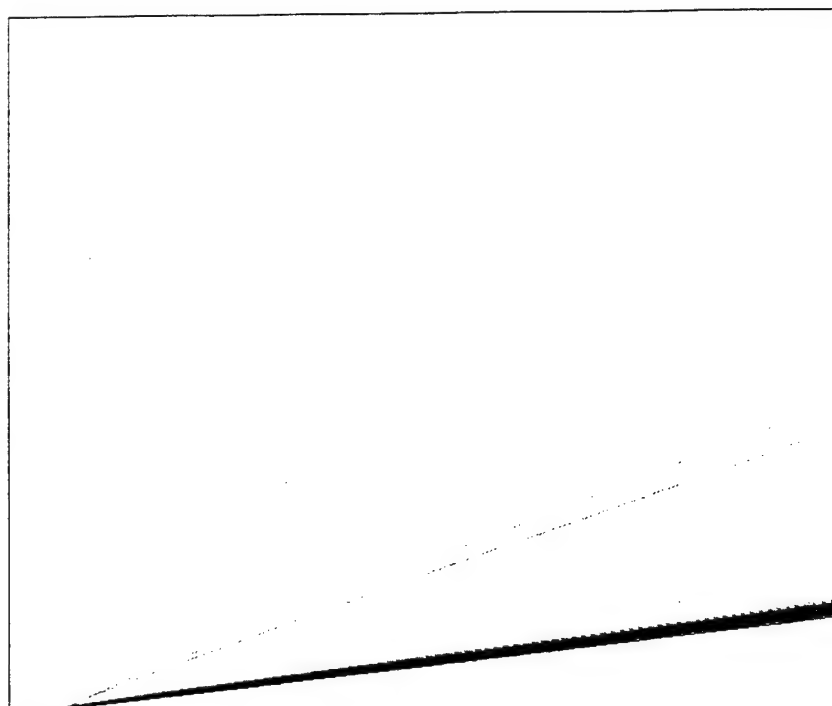
Figure 35: Temperature contours: $M = 4.00$ hydrogen/air $6.34°$ viscous ramp. Contour levels in K: min: 440. max: 2040, inc: 64.

reaction. However, strong exothermicity is not present, and the reaction does not have enough time to transition out of the boundary layer through either species diffusion or heat transfer into the main flow. Thus, in order to achieve strong reaction at the length scale dictated by the size of the experimental apparatus. the free stream Mach number and pressure must be increased appreciably from their current levels. Alternatively, if the wind tunnel conditions remain fixed, a longer distance must be allowed for the reaction to develop so that the flow in the boundary layer has sufficient residence time to achieve strong reaction.

Finally. in order to further demonstrate the capabilities and robustness of the numerical algorithm, methane–air combustion is considered. We will consider only the case of convection–reaction with no diffusive effects included (the convective velocity is much greater than the diffusive speed). Two dimensional methane–air combustion cases were computed using the mechanism of Yungster and Rabinowitz [20] which includes 19 reacting species and 52 reactions. The efficiency and scalability of the parallel implementation in addition to the robustness, accuracy and efficiency of the fully explicit numerical scheme allow calculations of such size to be performed in a reasonable amount of time.

These test cases consist of cylinders of various diameters placed in an oncoming flow of stoichiometric methane–air. The free stream temperature is 295 K, the free stream pressure is 51600 Pa and the Mach number of the flow is 6.61. Both cases were calculated on 64×72 cell grids. The first cylinder diameter was 1 mm. The oncoming flow forms a bow shock upstream of the cylinder which causes the temperature behind the shock to be about 2200 K with a pressure of 2.75 MPa. Under these conditions, the reactant species begin to break down, in small quantities, to form various radical species. Eventually, when sufficient amounts of radicals have built up, products are formed and heat is released, which causes further break down of reactants and product formation. Temperature contours for this case are shown in Figure 36. The varying strength of the shock causes the induction zone to vary in length. Eventually, at the outer regions of the flow domain, the shock is not strong enough to allow sufficient amounts of

radicals to form to cause heat release. The temperature along the stagnation streamline is depicted in Figure 37. As expected, the temperature is approximately constant in the induction zone between the shock and the heat release region. These results are in good agreement with those of Yungster and Rabinowitz [20]. The shock position predicted from Figure 37 is $x/R = 0.34$ while the result of Yungster and Rabinowitz gives a shock position of $x/R = 0.37$, a difference of 8.8%. The location of the initial heat release is predicted to be at $x/R = 0.06$; Yungster and Rabinowitz predict this point to be at $x/R = 0.10$. In this case no limitation on the cell Damköhler number is necessary, unlike the algorithm of Yungster and Rabinowitz.

Flow over a 3 mm diameter cylinder was also simulated; temperature contours (Figure 38) and stagnation streamline temperature (Figure 39) again show good agreement with the work of Yungster and Rabinowitz. In this case, Figure 39 shows a shock location of $x/R = 0.4$ while the simulation of Yungster and Rabinowitz yields a shock location of approximately $x/R = 0.46$, a difference of 13%. The location of heat release is at $x/R = 0.21$ while a location of $x/R = 0.32$ is predicted by Yungster and Rabinowitz. The differences in shock and heat release location for both the 1 mm and the 3 mm cases may be due to the dissipation scheme of Yungster and Rabinowitz being too diffusive. In general, overdissipated simulations tend to push the shock away from the body and decrease the size of the induction zone due to unphysical diffusion of radical species and energy. The chemistry results are fairly similar; for the 1 mm diameter body, Yungster and Rabinowitz predict a temperature at the stagnation point on the surface of the body of approximately 3100 K while the current simulation predicts a temperature of 3150 K. In the case of the 3 mm diameter body, Yungster and Rabinowitz predict a surface temperature of 3300 K and the current simulation predicts a temperature of 3300 K as well. Thus, the results of the chemistry are in quite good quantitative agreement.

Figures 40 through 43 depict the mass fractions of the various species along the stagnation streamline for the 3 mm diameter cylinder. As would be expected, the mass fractions of the radicals increase past the shock while the mass fractions of reactants stay approximately constant. When enough radical species have been formed, some products are created, liberating heat, which causes more radicals to form. These radicals react with the reactants, depleting their supply greatly in the heat release region and liberating more heat as more products are formed. One can also notice in Figure 41 the production and destruction of intermediate radicals between the shock and the heat release region. Higher order hydrocarbons (Figure 43) are created in the induction zone due to combination of some radical species, but these hydrocarbons are rapidly destroyed through the heat release region. In general, the CUSP scheme handles the large increases and decreases in radical species mass fraction very well. These mass fraction results compare very favorably with those of Yungster and Rabinowitz in a qualitative sense. Locations of radical growth, decay and maxima relative to the position of the shock and heat release front are similar. More quantitative comparisons cannot be made due to the different shock and heat release locations.
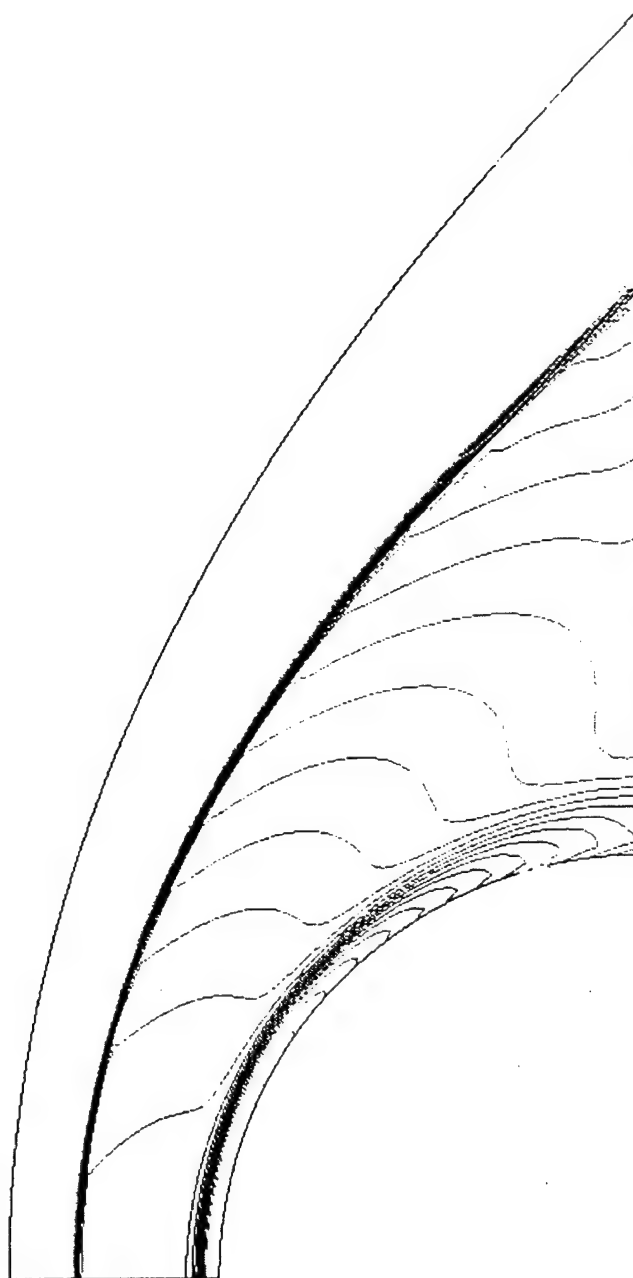
Figure 36: *Temperature contours:* $M = 6.61$ *methane/air, 1 mm diameter. Contour levels: min: 250 K, max: 3130 K, inc: 93 K.*
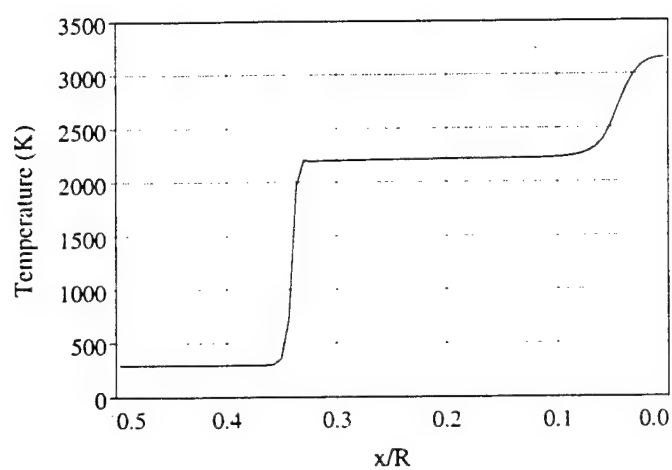
Figure 37: *Temperature along stagnation streamline:* $M = 6.61$ *methane/air, 1 mm diameter, projectile surface at $x/R = 0.00$.*
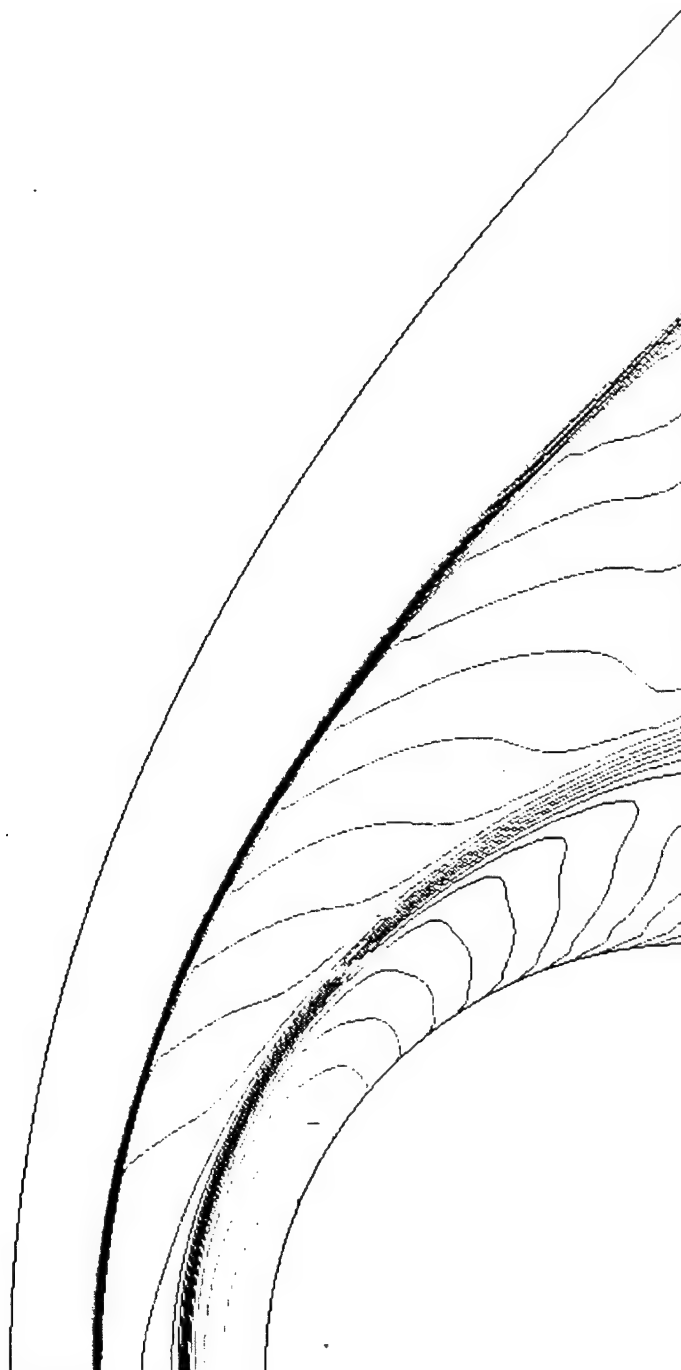
Figure 38: Temperature contours: $M = 6.61$ methane/air, 3 mm diameter. Contour levels: min: 250 K, max: 3220 K, inc: 93 K.
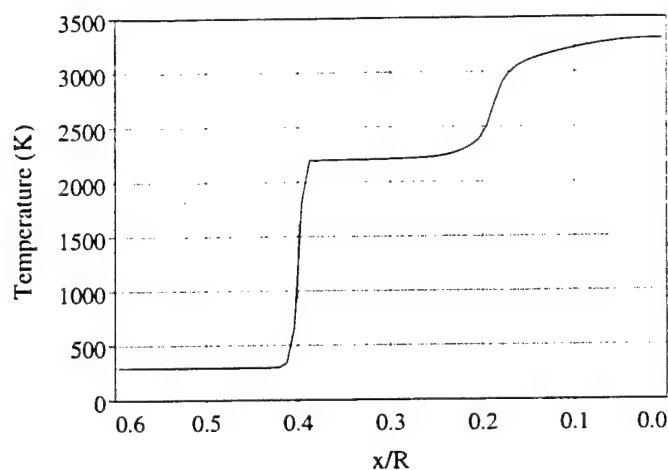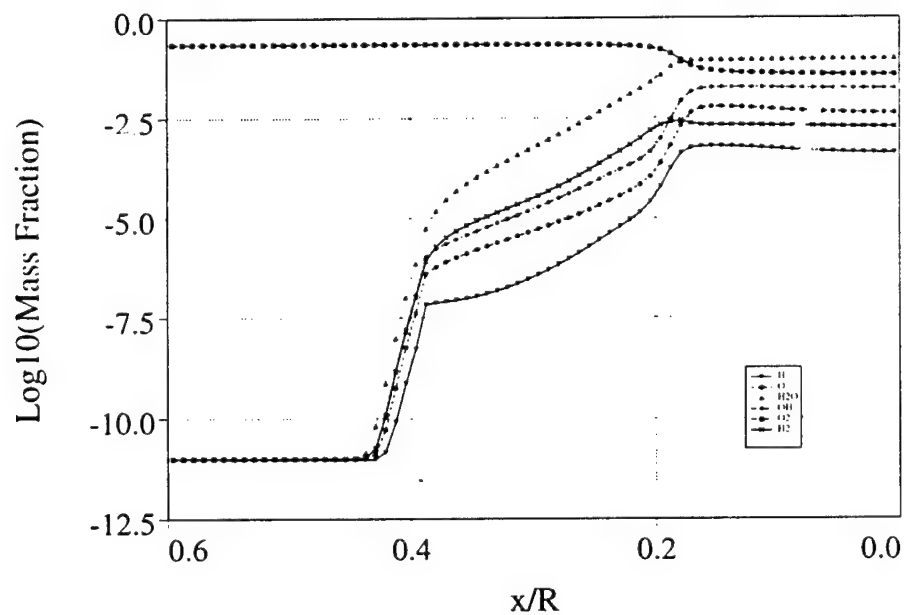
Figure 39: *Temperature along stagnation streamline: M = 6.61 methane/air, 3 mm diameter, projectile surface at x/R = 0.00.*
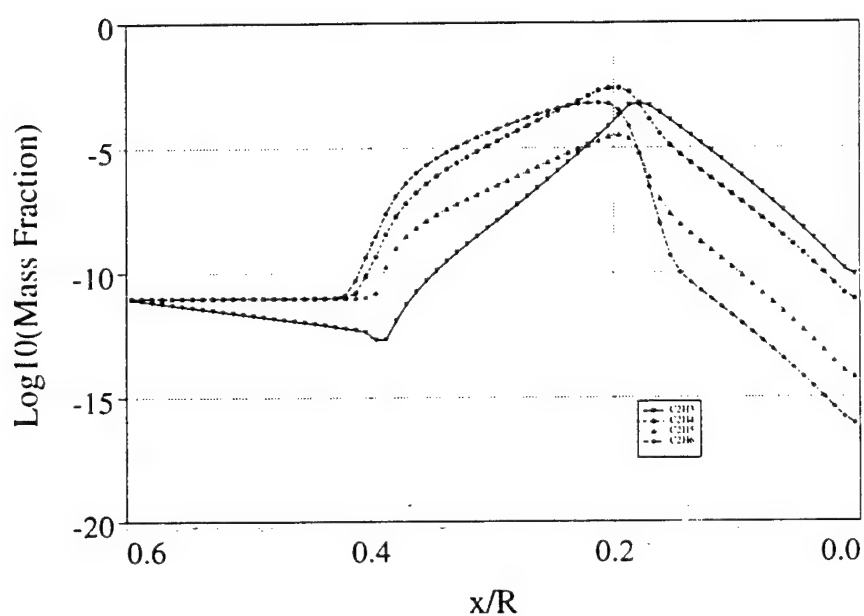

Figure 40: *Species mass fractions along stagnation streamline: M = 6.61 methane/air, 3 mm diameter. Shock location is at x/R = 0.40, heat release begins at x/R = 0.21, projectile surface at x/R = 0.00.*
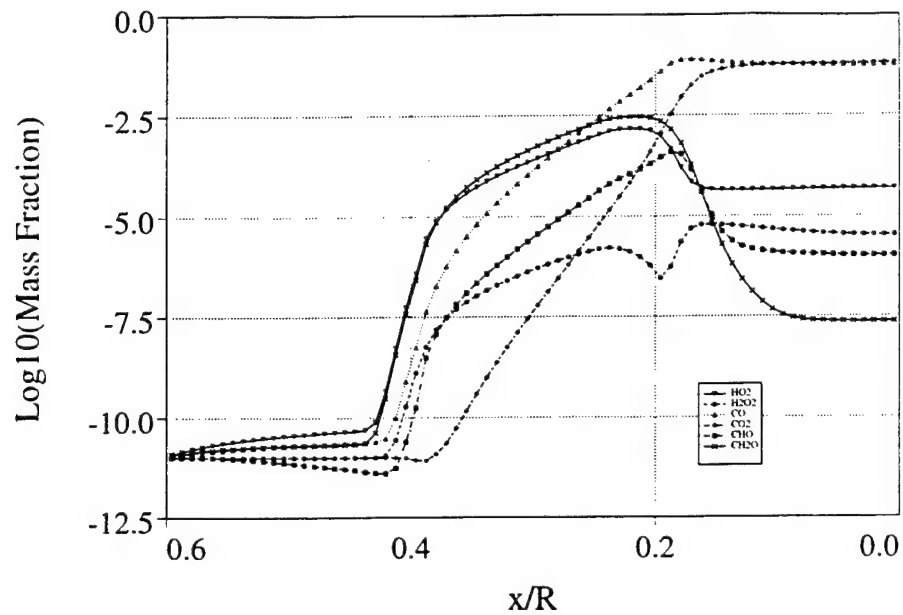
Figure 41: Species mass fractions along stagnation streamline: $M = 6.61$ methane/air, 3 mm diameter. Shock location is at $x/R = 0.40$, heat release begins at $x/R = 0.21$, projectile surface at $x/R = 0.00$.
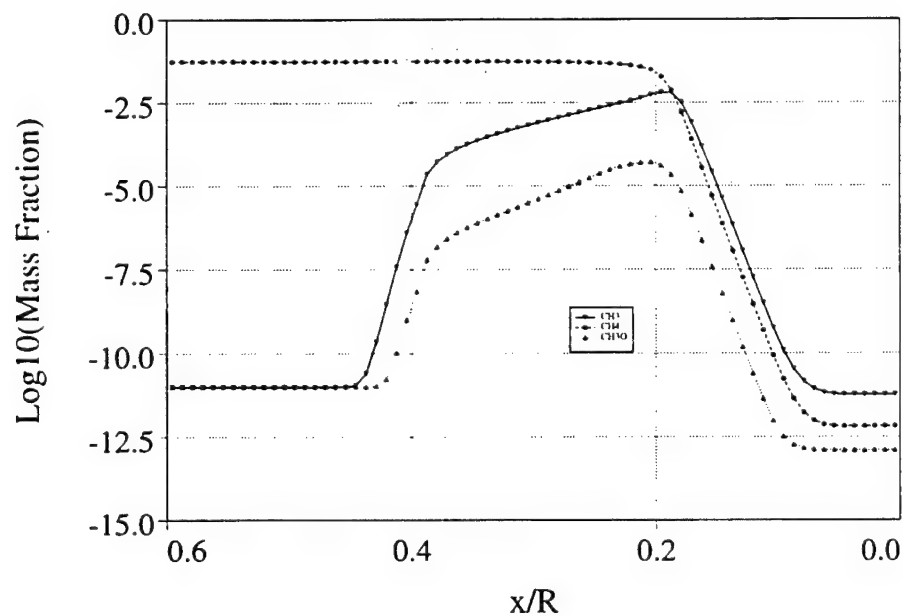
Figure 42: Species mass fractions along stagnation streamline: $M = 6.61$ methane/air, 3 mm diameter. Shock location is at $x/R = 0.40$, heat release begins at $x/R = 0.21$, projectile surface a$^+$ $x/R = 0.00$.

Figure 43: Species mass fractions along stagnation streamline: $M = 6.61$ methane/air, 3 mm diameter. Shock location is at $x/R = 0.40$, heat release begins at $x/R = 0.21$, projectile surface at $x/R = 0.00$.

3   Robust and Accurate LED-BGK Solvers

Since computational methods were first introduced as a way to simulate, analyze and predict fluid dynamics problems, considerable progress has been made in the areas of compressible flow solvers and solution strategies[39]. At the same time, we have witnessed tremendous advances in computer storage, speed and architecture. These two factors have made it possible the routine calculation of steady compressible flows over three dimensional complex bodies. In spite of these advances, accurate computations of unsteady compressible flows over complex geometry still present a challenge. This is partly due to the complex physical interactions between linear and non-linear waves. As unsteady computations of complex flows are becoming an essential tool for practical application and fundamental research, there is a need to design a low-dissipative, robust numerical scheme on unstructured triangular meshes. Quite often, the requirements of robustness and accuracy in the design of a numerical scheme are in conflict with each other: If a scheme A is robust, it is unnecessarily diffusive and, if a scheme B is accurate, it loses robustness. This suggests that intelligent control of numerical dissipation based on the physics of the flow may lead to the successful development of schemes which are both robust and accurate.

A high resolution scheme can be examined in terms of an initial reconstruction and a gas evolution procedure. Higher order(more than second order) interpolation on unstructured mesh is much more involved than that of structured mesh since neighboring cell vertices are not, in general, co-linear. Additionally, all interpolated values should be reduced to first order accuracy to exclude unphysical oscillations across local extrema. Thus it seems reasonable to keep second order accuracy in both spatial and temporal discretization, and introduce a local mesh refinement step to preserve the required accuracy. Recently, Jameson has developed the theory of non-oscillatory positive schemes in terms of the LED criteria[40]. Flux limited dissipation schemes based on the LED criteria have been implemented and validated for both inviscid and viscous flow computations on structured mesh[61], [42]. It has been observed that the LED interpolation, unlike the TVD(Total Variation Diminishing) interpolation, can be extended to unstructured mesh with maintaining the positive coefficients of the discrete form in a scalar conservation law. This can be carried out by calculating gradients of appropriate neighboring triangles or edges and applying a monotonic limiter.

Riemann solvers, approximate or exact, have gained much acceptance as a way to describe the gas evolution process[34], [59], [37]. In most test cases, Riemann solvers produce good results. Nevertheless, it has been found that Riemann solvers can produce unphysical situations such as expansion shocks, carbuncle phenomena or failure of local linearization, etc[33], [56], [42]. Although most of the problems can be cured by adding *ad hoc* fixes, the robustness of the original approach seems to be blurred as a result of incomplete remedies. After the introduction of a gas kinetic scheme based on the BGK model by Xu and Prendergast[64], [65], there has been continuous development in this area[66], [67], [43], [45]. Previous studies have unveiled interesting properties of BGK-based schemes. Firstly, they satisfy the entropy and the positivity condition which are important in the computations of high speed compressible flows. Secondly, they possess a multi-dimensional gas evolution character and the interpolation in the initial reconstruction step is quite flexible. Thirdly, the BGK model produces the Navier-Stokes equation through particle collision mechanism and describes a higher order gas evolution process. These properties can not be found in most popular Riemann solvers and are generally regarded as limitations of Riemann solver approach. Thus it is not surprising that BGK-based schemes can overcome many shortcomings of Riemann solvers and provide a good alternative to Riemann solvers for the gas evolution step.

BGK-based schemes are different from the class of schemes called Boltzmann-type schemes[55], [32],

[54]. [51]. The physical model for these schemes is the collisionless Boltzmann equation, which does not include the dynamic correlation between left and right moving particles. The missing correlation corresponds to a gas kinetic Lax-Wendroff step[66] and in BGK-based schemes, it is coupled to kinetic flux vector splitting through particle collision time[43]. In addition, Boltzmann-type schemes split the gas evolution step into a convective step and an instantaneous collision step, which makes the collision time and mean free path $O(\Delta t)$, $O(\Delta x)$, respectively. This simplification is, however, unreasonable considering the characteristic time and length scale of molecular motion, and it leads to large numerical viscosity and heat conductivity. As a way to cure this problem, Moschetta and Pullin has recently proposed a hybrid solver (EFMO) which augments the equilibrium flux method (EFM) with Osher's approximate Riemann solver in calculating fluxes for linearly degenerate subpath[53]. Unlike hybrid approach, BGK-based schemes make local use of the full integral solution of the BGK model in a finite volume framework which allows us to compute a time-dependent gas distribution function at a cell interface and to obtain the numerical fluxes. This approach provides a physical model for particle collision designed to reduce the large numerical viscosity inherently present in schemes based on the collisionless Boltzmann equation. BGK-based schemes also give Navier-Stokes solutions which follow directly from the BGK model, and the gas relaxation from an initial nonequilibrium to a final equilibrium state is associated with an increase of entropy.

In order to increase efficiently the resolution of physically important local phenomena, a mesh adaptation strategy is essential. Since unstructured triangular meshes facilitate mesh adaptation, unstructured based flow solver is very desirable. Most popular mesh adaptation strategies can be classified into two approaches : mesh movement(r-refinement) and mesh enrichment (h-refinement). The r-refinement method redistributes existing nodes at every adaptation, clustering them towards positions where the solution gradient is relatively large. An advantage of the r-refinement method is that the total number of nodes and the grid topology are conserved. Thus there is no computational overhead on a flow solver and the flow solver is amenable to parallelization. However, the possibility of edge crossing during nodes movement or the need for re-meshing make this approach cumbersome. Additionally, an accurate estimate of solution error and conservation of mesh smoothness after adaptation become difficult[27]. On the other hand, the h-refinement method alters the number of nodal points by adding or deleting nodes within the computational domain. Since only specific regions of the computational domain are altered, the node density can be locally controlled and the regularity of the initial mesh can be maintained. Another advantage of h-refinement method with respect to r-refinement method is that the error indicator only needs to be sensitive enough to trigger mesh enrichment when there is a rapid variation of flow field. In the analysis of unsteady flow with mesh adaptation strategy, it is necessary not only to refine high-gradient regions but also de-refine over-resolved regions. The adaptation routine therefore consists of mesh enrichment/coarsening steps. Starting from the BGK model of the Boltzmann equation, we have developed a family of robust and accurate finite volume gas kinetic scheme on both structured quadrilateral and unstructured triangular meshes. The proposed numerical approach is composed of two steps - an initial reconstruction step and a gas evolution step. In the initial reconstruction step, an unstructured version of the LED (Local Extremum Diminishing) interpolation is applied to the conservative variables and to compute left and right states along a node edge. In the gas evolution step, the local integral solution of the BGK model is used to compute numerical fluxes at a cell interface. This approach provides an alternative to Riemann solvers and yields numerical schemes which possess many desirable properties that may not be found in Godunov-type schemes. A classic h-refinement adaptive procedure is implemented to increase the spatial resolution of high speed unsteady flow characteristics such as shock waves, contact discontinuities or expansion waves with minimal computational costs and memory overheads. It involves mesh enrichment/coarsening steps to either insert nodes on an edge center in high-gradient regions or delete nodes in over-resolved regions. Numerical results of several test cases for unsteady compressible inviscid flows are presented.

To verify the accuracy and robustness of the current numerical approach. the computed results are compared with analytical solutions. experimental data. the results of structured mesh calculations and the results obtained by widely used flux splitting methods.

3.1   Validation Studies

Five standard test cases have been chosen to examine the accuracy and robustness of the current numerical approach. For each case, the adaptation routine is called every four iteration and the maximum level of adaptation is two. Thus one initial triangle can be divided into 16 sub-triangles. The CFL number is set to 0.75. In unsteady flow computations, most phenomena to be adapted are transient. In order to keep track of those accurately during the time intergration, two outer layers are added to adapted regions. Pressure gradient is used to detect shock waves or expansion fan while density or entropy gradient is employed to capture contact discontinuities. The threshold value for pressure and density is 0.1 and 0.015 for entropy. The computed results are compared with other LED schemes which is based on the characteristic splitting using Roe averaging(LED-Csplit scheme) and CUSP splitting(LED-CUSP scheme)[40],[42].

The first test case treats a moving shock with a speed $M_s = 1.5$ that is propagated in two-dimensional duct of $(x,y) = (1.2, 0.2)$. Although this is a relatively simple test, it provides a good way to check shock capturing properties of LED schemes augumented with mesh adaptation. Fig.44 shows density profile along $y = 0.1$ line at five different times. All schemes yield monotonic shock profiles and show an excellent agreement with exact solutions. As can be seen from Fig.45, the number of nodes remains almost uniform during the entire adaptation process.

The second test case is the forward facing step with free stream Mach number 3. Since this test shows many important phenomena which typically happen in unsteady supersonic flows. it has been widely computed. especially on structured mesh[63]. In order to resolve the behavior of the expansion fan around the step corner, no special treatment such as an entropy fix was required. Fig.46 shows a typical initial mesh distribution. We can see the mesh regularity including the boundary region. The initial mesh contained 4836 nodes. Fig.47 shows the comparison of density distribution at t = 4. The results on unstructured mesh without adaptation gives very competitive results with structured mesh calculation. There are 16140 cells in structured mesh and 18110 nodes in unstructured mesh, respectively. Fig.48 shows the effect of adaptation at t = 3. Starting from the coarser mesh(4836 nodes), a typical final adapted mesh(LED-Csplit : 16961. LED-CUSP : 16016. LED-BGK : 17649 nodes) shown in Fig.48a is nicely clustered around shock waves. a contact discontinuity and expansion regions. The corresponding computed results resolve local phenomena very clearly while keeping monotonic profiles. Especially. the inviscid instability, so called Kelvin - Helmholtz instability, of the contact discontinuity emerging from the shock triple point can be seen more clearly in the result of the LED-BGK scheme. In the case of the LED-Csplit scheme. the contact discontinuity is relatively diffused and a noticeable length of Mach step has been observed. The reason is that if the same α_2 limiter is used as in other LED schemes. the adapted mesh around the step corner produces an over-expansion leading to negative density and/or pressure. A relatively diffusive limiter such as the Minmod limiter had to be used to prevent that. This indicates the importance of robustness in designing a numerical scheme.

The third test case is the double Mach reflection with a shock speed $M_s = 10.0$. Initially a shock wave with $M_s = 10.0$ is located at the entrance of a 30 degree wedge and propagated along the wedge. The computational domain is a rectangle of length $(x,y) = (4,1)$ and the entrance of the wedge is located at $(x,y) = (1/6, 0)$. The initial mesh for this case contained 16986 nodes and the final adapted mesh 36245 nodes. Fig.49b shows the density distribution of the computed results at t = 0.25. Compared with the results of the calculation on rectangular mesh(480*120 cells, Fig.49a), the computation without adaptation gives a similar result. The number of nodes used is about one third of the number of

nodes in the rectangular mesh. Fig.49b.c show the density comparison between the uniform mesh and the adapted mesh. The adapted mesh is a result of two level adaptation on the uniform mesh. Again, the resolution of shock waves is greatly improved. The resolution of the contact discontinuity and the wall jet merits particular attention. Fig.50 - Fig.52 show local views of density. and entropy contours for the around the triple point. Due to the increased resolution. the local flow pattern can be seen in detail. Since the contact discontinuity is unstable, the wavy motion originated from the triple point is growing, leading to a non-similar Kelvin-Helmholtz rollup along the principle slip line. The normal shock reflected from the solid wall ? e slightly curved due to the shock-vortex interaction. The LED-Csplit and LED-BGK schemes yield extremely good results while the LED-CUSP scheme is slightly diffusive. Because of the orientation of local mesh, the unsteady carbuncle phenomenon of the LED-Csplit scheme which can be observed on a structured mesh is eliminated[42]. Similar numerical results on the instability of the contact discontinuity have been reported by Berger and Colella. These results are based on a PPM solver combined with AMR(Automatic Mesh Refinement) technique on rectangular mesh[30].

In the fourth test case, a moving shock interaction over a circular cylinder is examined. A moving shock with the speed $M_s = 2.81$ passes through the circular cylinder, which induces shock-shock, shock-contact discontinuity interactions and high expansions terminated by weak shocks. Fig.53 - Fig.54 show the density and mesh distribution at $t = 0.55$. The adapted mesh is slightly asymmetric with respect to the center line because of the asymmetry of the initial mesh. The LED-BGK produces equally good results compared to those of the LED-Csplit or LED-CUSP schemes.

Finally, we consider the case of a hypersonic inviscid flow around the conceptual geometry of high speed engine intake with free stream Mach number 8. The angle of the first and second cones are 25 and 35 degrees respectively. The initial mesh contains 2356 nodes and the final adapted mesh contains 12156 nodes for the LED-CUSP scheme and 12161 nodes for the LED-BGK scheme. Fig.55 shows density contours with forty levels and Fig.58 for the mesh distribution at $t = 0.4$. The interaction of two shocks originating from the nose of each cone produces a strong contact discontinuity . The density expansion fan at the exit of the second cone is partially kinked due to the interference of the contact discontinuity. All these features are well resolved by the LED-BGK and LED-CUSP schemes. However, first order characteristic splitting as well as the higher order LED-Csplit scheme fail to capture this flow pattern due to the problem of negative pressure and/or density. This failure can be observed regardless of mesh adaptation. Fig.56 shows schlieren images of the flow pattern around the same double cone, which has been taken in Princeton Gas Dynamics Laboratory[50]. The images clearly show the flow characteristics that were captured computationally.

Although the present work is mainly directed toward the design of robust and accurate numerical methods. computational efficiency is also important. This issue may be critical in the computation of large scale three-dimensional flows. Thus it is relevant to compare the CPU time required to calculate *only* the flux functions. If the CPU time of the CUSP splitting is normalized as unit, the ratio of CPU time required per mesh point per iteration is given by

$$CUSP : Csplit : BGK - I : BGK - II = 1 : 1.136 : 1.684 : 1.908$$

BGK-II stands for the full BGK scheme which takes account of both spatial and temporal slopes and BGK-I for the simplified BGK scheme which considers the temporal slope only. As can be seen from the ratio, the CUSP splitting is quite efficient while the BGK scheme is relatively expensive. The reason is that unlike the CUSP or characteristic splitting, spatial and temporal slopes have to be used in the BGK solver, which inevitably needs extra arithmetical operations. Since the spatial slopes of the BGK scheme correspond to Navier-Stokes terms, the BGK solver does not need an extra flux routine for Navier-Stokes calculations. This will reduce the computational ratio substantially in Navier-Stokes computations. This issue will be addressed in near future work. In addition, as can be judged from
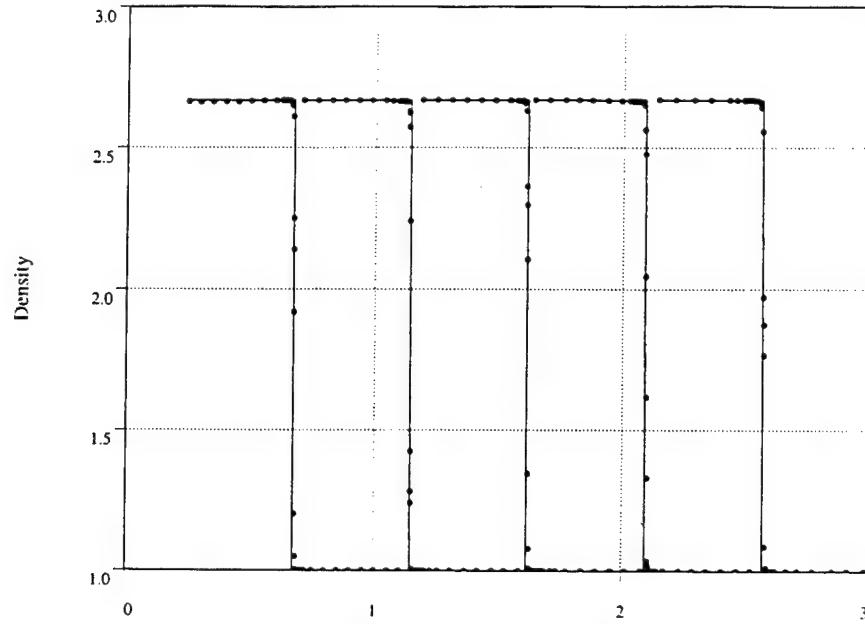
previous test cases, the superior robustness and accuracy of the LED-BGK scheme may offset the burden of extra computational costs.
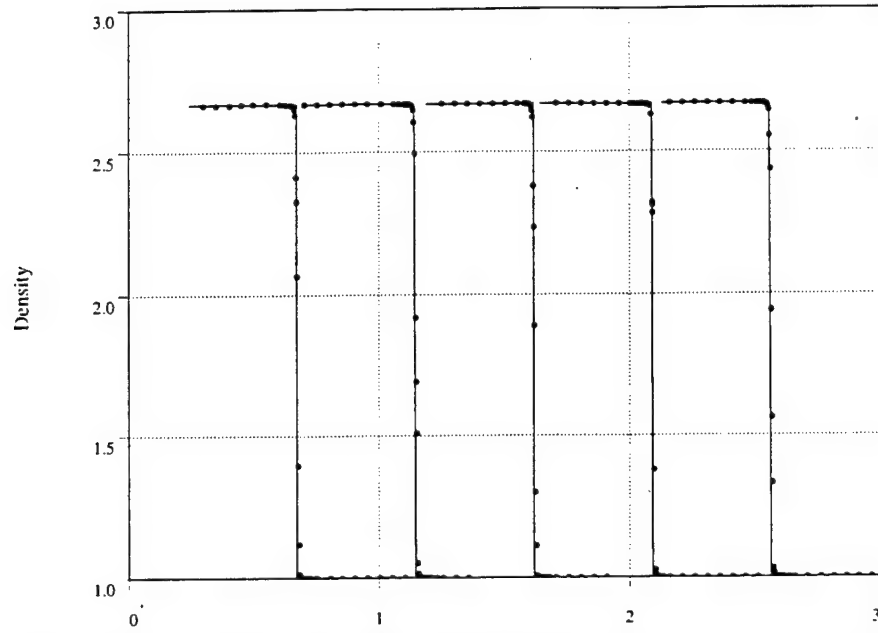
44a: Density Profile with LED-Csplit Scheme at $t = 0.2, 0.4, 0.6, 0.8, 1.0$
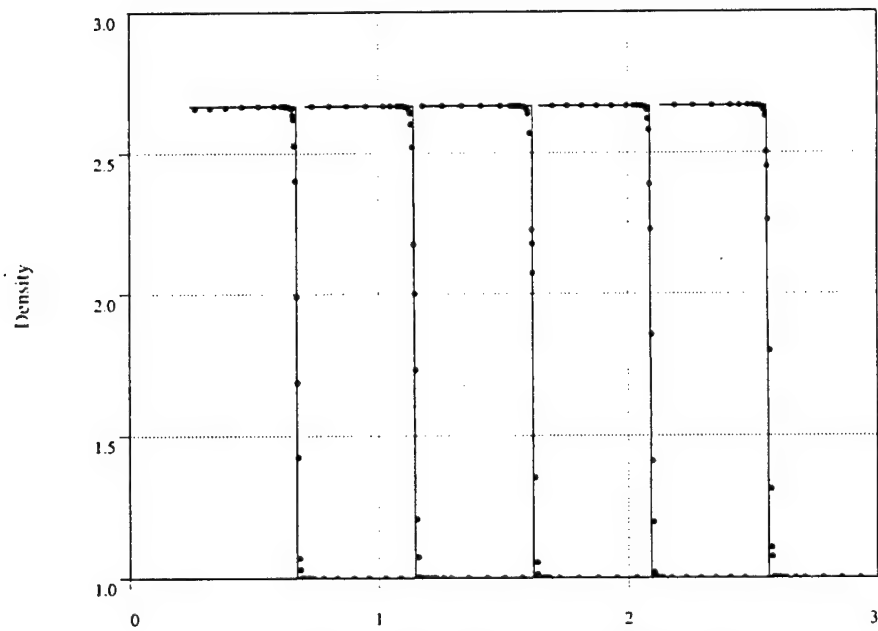
44b: Density Profile with LED-CUSP Scheme

44c: Density Profile with LED-BGK Scheme

Figure 44: *Two-Dimensional Moving Shock with* $M_s = 1.5$. *Computed Results(··) are Compared with Exact Solutions(-)*
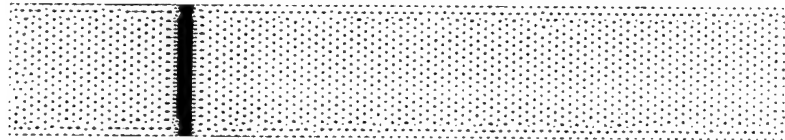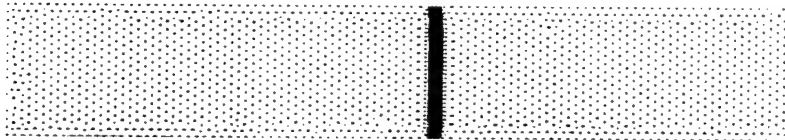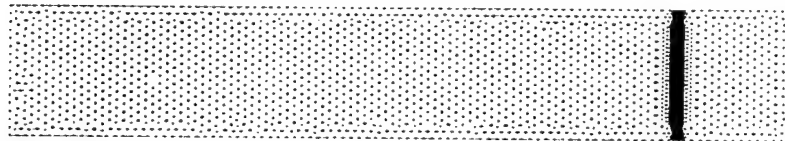

45a: $t = 0.2$. 3503 Nodes

45b: $t = 0.6$. 3474 Nodes

45c: $t = 1.0$. 3534 Nodes

Figure 45: *Adapted Mesh Distribution*
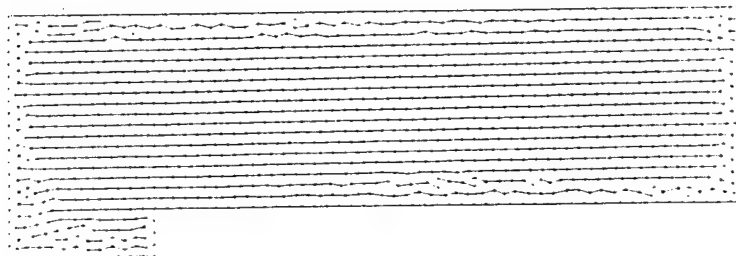
Figure 46: Typical Mesh Distribution
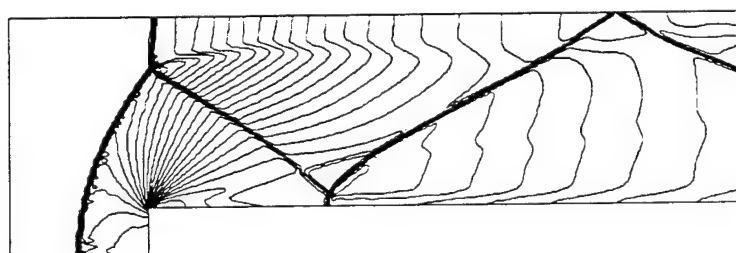
47a: Structured Meshes (16140 Cells)
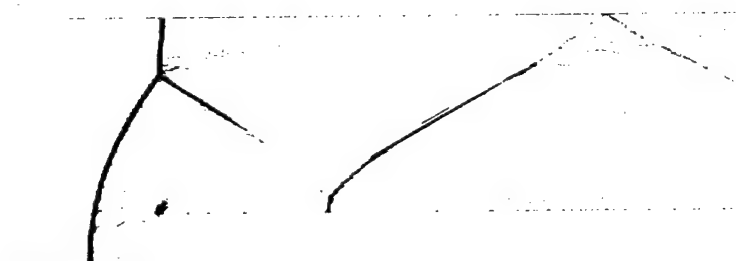
47b: Unstructured Meshes (18110 Nodes)
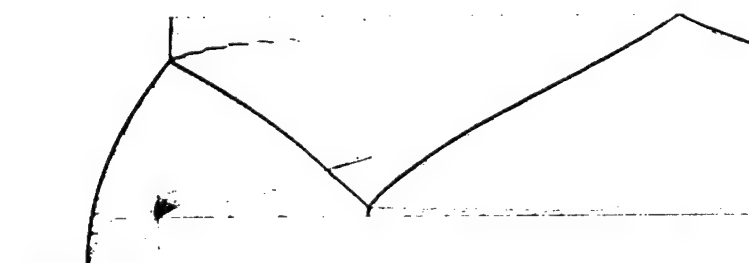
Figure 47: Density Distribution with LED-BGK Scheme at t = 4.0
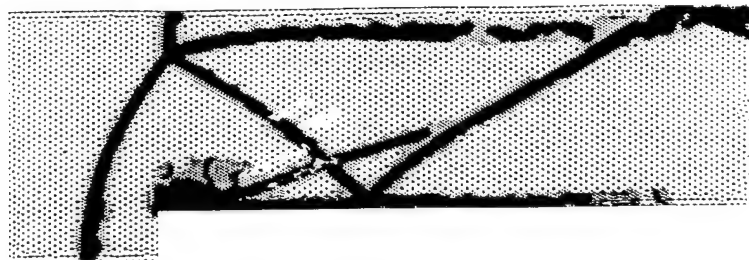
48a: Typical Adapted Mesh Distribution
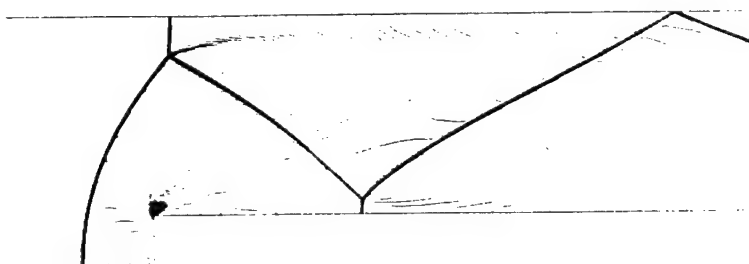
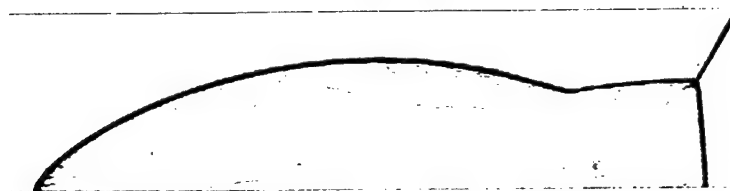48b: Density Contours with LED-Csplit Scheme
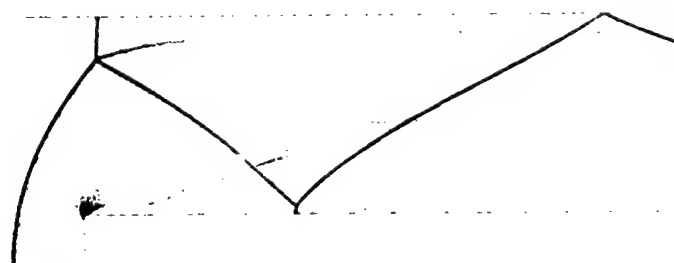
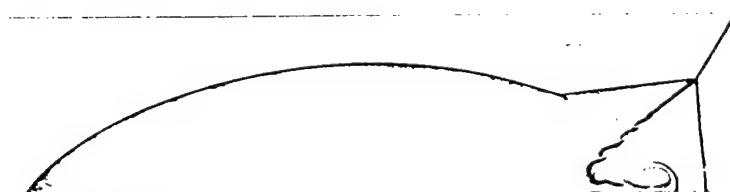48c: Density Contours with LED-CUSP Scheme

48d: Density Contours with LED-BGK Scheme

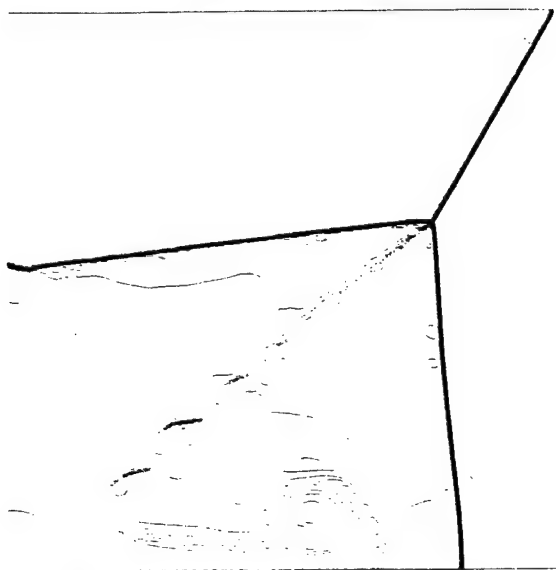Figure 48: *Forward Facing Step. LED Schemes at $t = 3.0$*

49a: Structured Mesh (480×120 Cells)
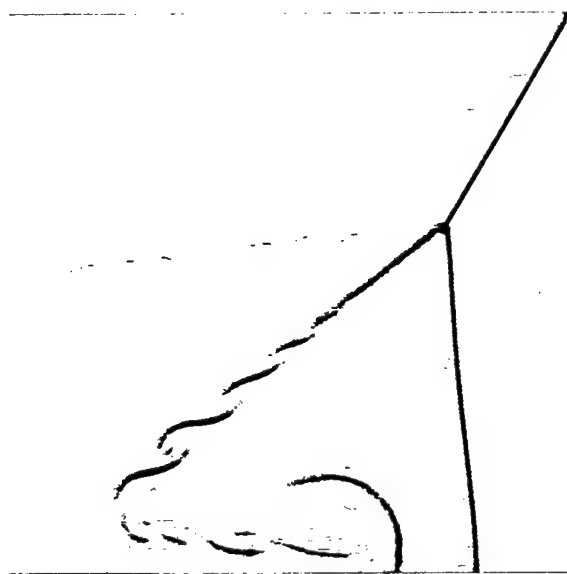
49b: Unstructured Mesh (17000 Nodes)

49c: Unstructured Adapted Mesh (36245 Nodes)

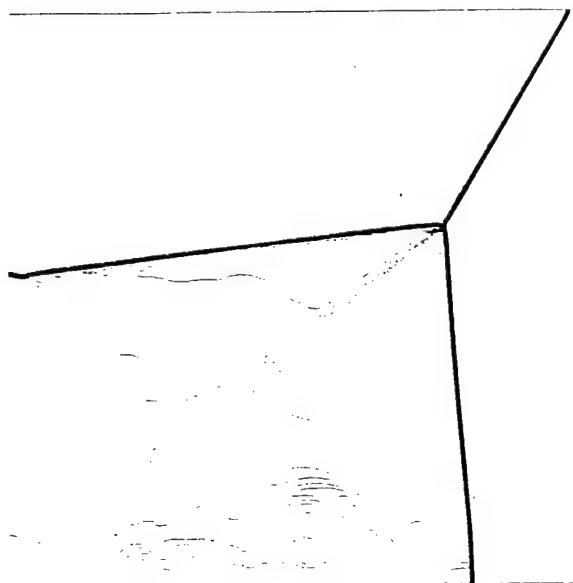Figure 49: *Double Mach Reflection. LED-BGK Scheme*
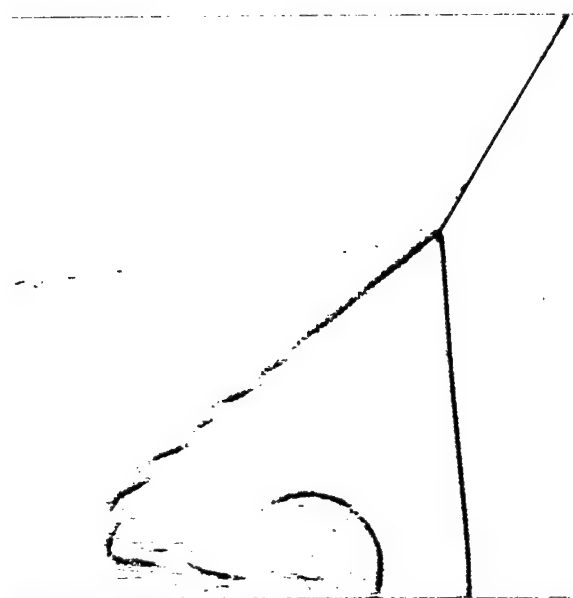
50a: Density Contours

50b: Entropy Contours

Figure 50: *Local View of Double Mach Reflection. LED-Csplit Scheme*

51a: Density Contours

51b: Entropy Contours

Figure 51: *Local View of Double Mach Reflection. LED-CUSP Scheme*

52a: Density Contours
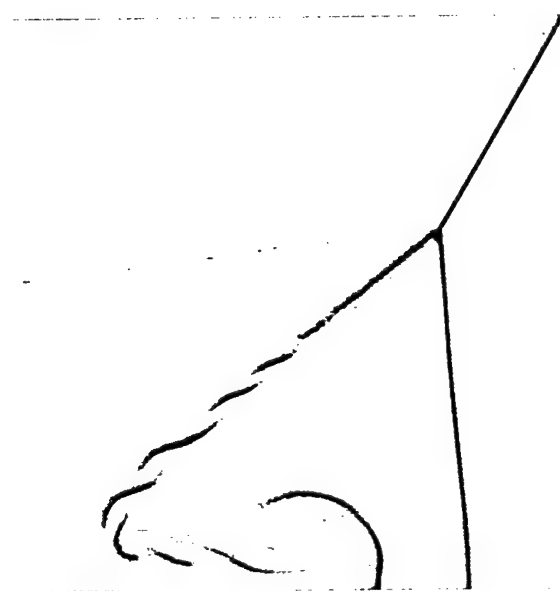
52b: Entropy Contours

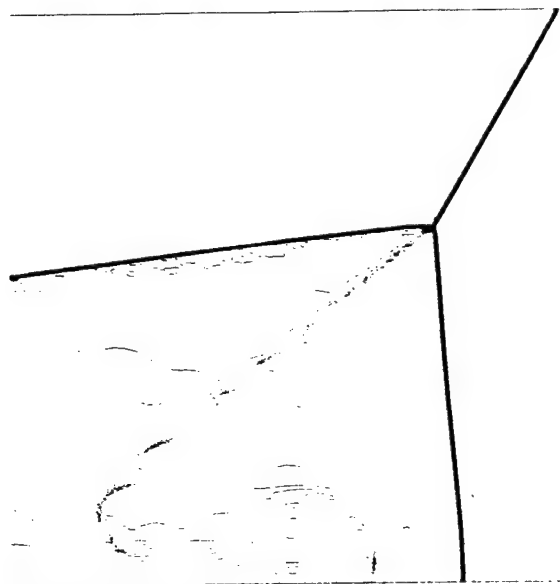Figure 52: *Local View of Double Mach Reflection. LED-BGK Scheme*
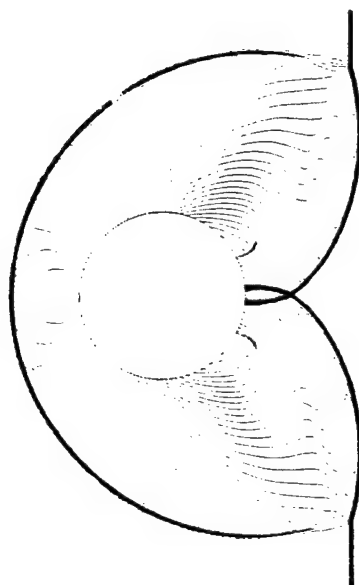
53a: LED-Csplit Scheme
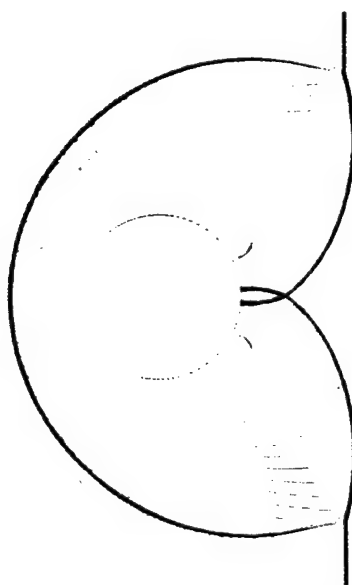
53b: LED-CUSP Scheme
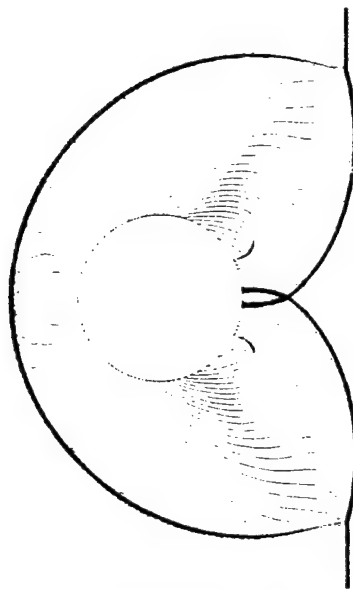
53c: LED-BGK Scheme

Figure 53: Moving Shock over a Cylinder. Density Contours
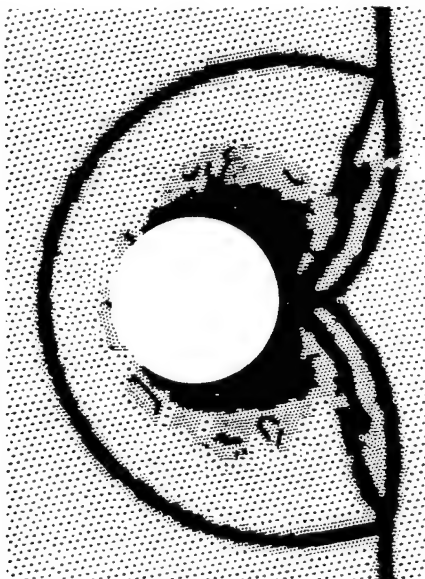
Figure 54: Moving Shock over a Cylinder. Typical Adapted Mesh Distribution

55a: Density Contours with LED-CUSP Scheme
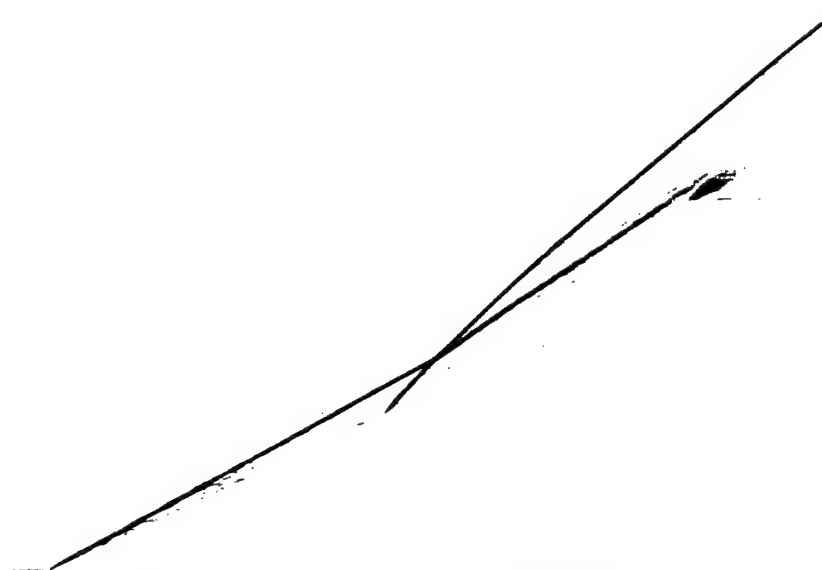
55b: Density Contours with LED-BGK Scheme

Figure 55: Hypersonic Double Cone Flow at t = 0.4

56a: Wide View
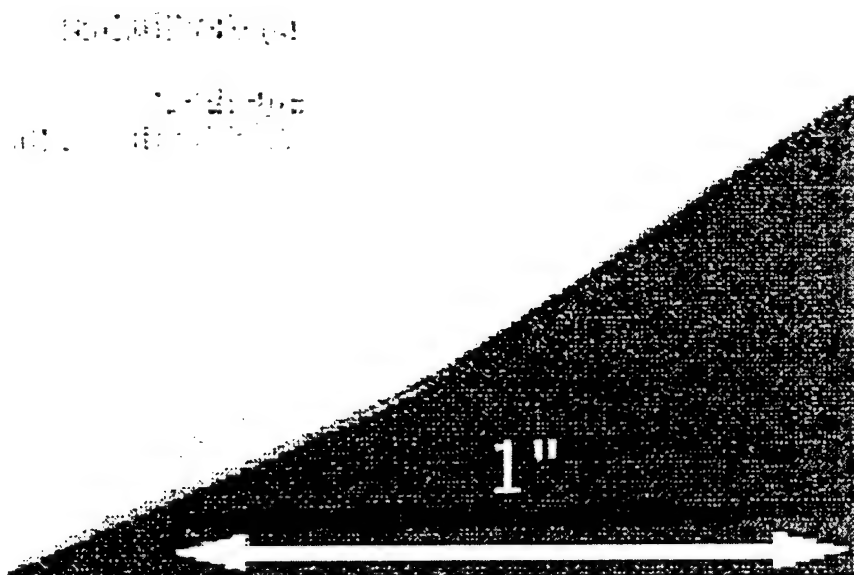
56b: Local View

Figure 56: Schlieren Photographs of Hypersonic Double Cone Flow
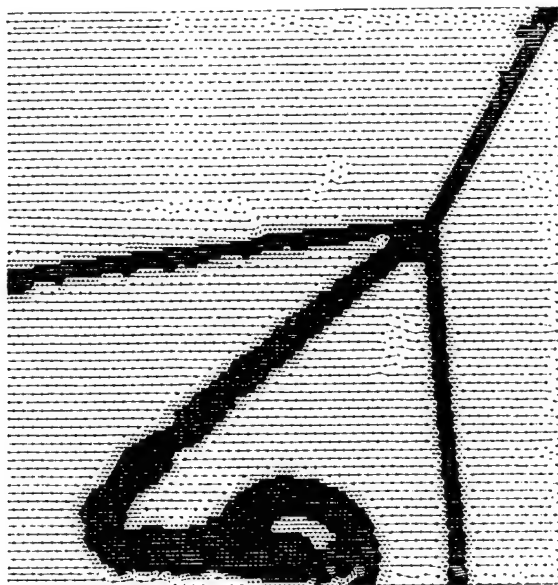
Figure 57: Double Mach Reflection. Typical Adapted Mesh Distribution
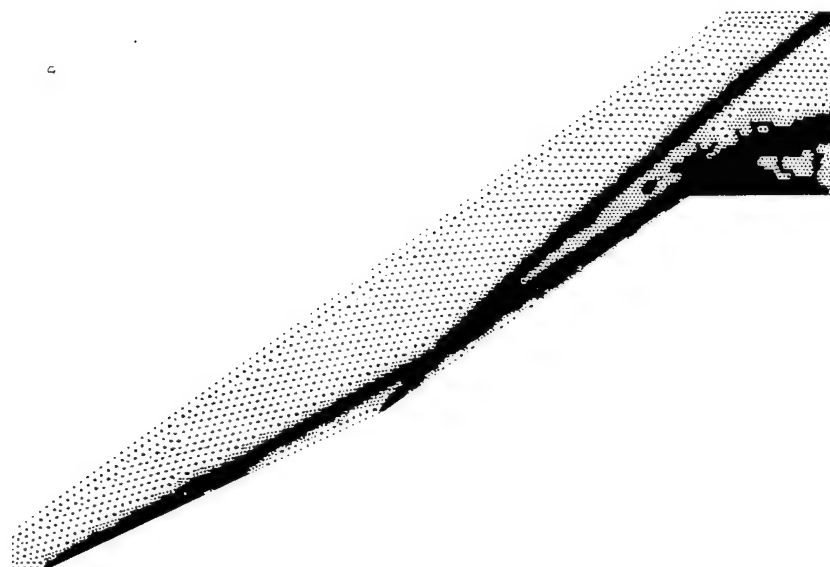
Figure 58: Hypersonic Double Cone Flow. Typical Adapted Mesh Distribution

4   Major Accomplishments

4.1   Simulation of Reactive Flow

A numerical algorithm has been developed. implemented and tested on parallel computing platforms for the solution of the steady-state Euler and Navier-Stokes equations with chemical reactions. Diffusive effects including heat conduction and species diffusion have been included. The algorithm was designed for use with detailed, multispecies chemical models to allow for realistic simulation of reactive flow phenomena.

From the results reported some conclusions may be drawn about the numerical algorithm and its implementation. In general, the algorithm is robust and accurate for both inviscid and viscous high speed reactive flows. Numerical results compare very well with benchmark analytic, asymptotic and experimental problems. Use of the Convective Upwind and Split Pressure (CUSP) scheme for high speed nonreactive and reactive, inviscid and viscous flows yields accurate capture of high gradient regions such as shocks, reaction zones and reaction fronts without oscillation and undue numerical dissipation. Numerous test cases have confirmed the ability of the CUSP scheme to capture highly viscous regions accurately without contaminating the physical solution with artificial viscosity. The wide range of nonreactive and reactive test problems indicates that the CUSP scheme is quite robust and yields very accurate results when compared to existing analytic or experimental test cases.

The point implicit treatment of the chemical source term allows full coupling of the convective, diffusive and reactive terms without the cost of a fully implicit algorithm. Reactive test cases yield very good agreement with experimental and other numerical results, indicating that the point implicit treatment is accurate and quite robust. The convergence rate of reactive simulations using this scheme is quite good due to the high CFL number and correspondingly large time step allowed by the multistage time stepping scheme in combination with the effective preconditioning of the point implicit treatment. In addition, in certain circumstances, the full inversion of the source term Jacobian matrix used to precondition the equation may be replaced by a diagonalized Jacobian matrix, thus reducing computational costs. However, in some simulations, this diagonalization led to a loss of numerical stability and robustness and thus must be investigated further.

The point implicit formulation also leads to a fully explicit scheme which lends itself to relatively straightforward, and more importantly, efficient parallelization due to the small spatial stencil of the scheme. The relatively large amount of work done per cell compared to the number of variables that must be transferred across processor boundaries yields a very efficient parallel algorithm. Numerical results on a distributed memory IBM SP-2 indicate excellent parallel efficiency for both inviscid and viscous reactive flow calculations. This high degree of efficiency allows the algorithm to scale quite well and enables greater resolution to be obtained, when needed, on a larger number of processors in nearly the same amount of time as the original calculation.

Convergence acceleration techniques such as local time stepping and multigrid make the algorithm numerically efficient. Multigrid acceleration, in particular, enables the efficient simulation of flows including diffusive transport of mass, momentum and energy. The use of a properly formulated multigrid scheme yields significant convergence acceleration in both cycle time and wall clock time without loss of accuracy.

The combination of parallel efficiency and scalability, multigrid acceleration and a numerical dissipation scheme able to accurately capture complicated interactions of shocks and reaction zones enables the use of fully coupled, detailed chemistry instead of simplified global reaction models. The simulation of reactive flows with large numbers of species and reactions while including species diffusion effects may be attempted because of the convergence properties and efficiency of the algorithm. Detailed chemical

models including up to nineteen species and 52 reactions have been used to accurately compute reactive hydrogen and methane flows.

In addition. the numerical algorithm was used to investigate weak and strong hydrogen–air reaction regimes in an experimental facility used in the University Research Initiative at Princeton University. Numerical simulations confirmed the finding of one experiment and have been used to predict conditions necessary for achieving strong reaction in that particular experimental facility. Specifically. for the range of static pressures and Mach numbers currently attainable, the length of the test section and ramp must be increased significantly in order to observe strong reaction. Alternatively. the free stream Mach number or pressure must be increased to allow a strong reaction to take place over the current length of the experimental facility.

4.2   BGK-schemes

Within a finite volume framework, an robust and accurate LED-BGK solver has been developed on unstructured adaptive mesh. In the initial reconstruction step, the LED interpolation has been employed to obtain left and right values across the cell interface. In the gas evolution step, the integral solution of the collisional BGK model is used to compute the numerical fluxes. It has been observed that the BGK model provides a good alternative to Riemann solvers for the gas evolution step. Numerical results indicate that the LED-BGK solver captures both physical discontinuities and expansion regions very well without spurious oscillations. Numerical comparison with the Roe-averaged characteristic splitting and Jameson's CUSP splitting also confirms the accuracy and robustness of the current BGK solver. The h-refinement mesh adaptation method greatly improves the resolution of physical discontinuities and shows the details of local flow patterns. This validates the capability of the current numerical approach to provide a highly accurate solution on complex geometry.

5   Future Work

There are several major areas where further research must be done in the simulation of high speed reactive flows. First, and foremost. is the acquisition of accurate experimental and reaction rate data. The single largest uncertainty in the calculations presented in this work is due to the uncertainty of the reaction mechanism. In addition, the validation of the algorithm for viscous reactive flows is hampered by the dearth of experimental data for such flows. Accurate measurements of shock and reaction front location. temperature and species concentrations (perhaps by nonintrusive optically based diagnostics) would be very useful in determining the range of applicability of the current algorithm.

Vibrational and electronic excitation and relaxation could be included in the current package in a relatively straightforward manner. Both of these phenomena contain convective and "reactive" portions and thus would be natural additions to the current governing equations. The point implicit treatment could be applied to the source terms of these equations as it was to those in the species continuity equations. This would allow the simulation of hypersonic and high enthalpy flows where the inclusion of vibrational and electronic energies may be necessary.

Further investigation into multigrid acceleration is also warranted. When using multigrid acceleration, the robustness of the algorithm is not as high for reactive flows as for nonreactive flows. It may be possible to alter the way in which the chemical source term is treated on the coarser levels in order to increase the robustness. One example would be to compute the chemical source terms on the coarser levels as sums of the source terms on the finer level, instead of evaluating them as functions of the collected variables on the coarse grid. Another possibility would be to diagonalize the source term Jacobian matrix on the coarser levels, leading to a reduction in computational costs. While diagonalization of the source term Jacobian matrix was investigated, additional work needs to be done in order

to fully understand the compromise between computational savings and loss of stability.

The addition of a turbulence model to the current algorithm would be quite useful. This would enable more appropriate simulation of high speed reactive flows. many of which are turbulent. However, the effect of turbulence on the transport of mass. momentum and energy and on chemical reactions is still not well understood. Thus, while a turbulence model would increase the number of flows that could be simulated. it would dramatically increase the amount of validation that would have to be done in order to have confidence in the results of simulations.

Another useful addition to the algorithm would be adaptive gridding and the use of unstructured grids. Adaptive grids would enable the accuracy of the scheme to be increased by adding cells in regions of high gradients to compensate for the lower level of accuracy of the scheme in that area and to better resolve phenomena in those regions. Conversely, in regions of very smooth flow where high spatial accuracy can be achieved with a relatively coarse mesh, cells could be removed in order to reduce the computational time that the algorithm uses. The implementation of a parallel. multigrid adaptive unstructured algorithm would be very challenging. but could yield exceptionally high accuracy at very reasonable computational costs.

Extension of the present algorithm to unsteady flows would enable the simulation of many problems of interest to scientists and engineers. Such problems include unsteady projectile combustion. unsteady combustion in gas turbine combustors and reactive flows in domains with moving boundaries such as internal combustion engines. Obviously. some of these simulations would need both more detailed chemical models for hydrocarbon combustion and also improved turbulence models for turbulent flows. Because the point implicit technique would only yield first order accuracy in time. another method of time advancement would have to be investigated. However, time accurate simulation of reactive flows might be possible with a fully implicit method in which an inner pseudo-time iteration is used to advance the solution during each time step. These time accurate simulations could be combined with the adaptive gridding techniques mentioned above to closely follow regions of high gradients in order to improve the spatial accuracy of the simulations.

The use of a technique such as computational singular perturbation could decrease the computation time of a simulation without compromising the accuracy. In this technique. the algorithm automatically generates reduced mechanisms at every point in the flow field such that the accuracy of the reaction mechanism is not lost. At any particular point in the domain. some chemical reactions may be negligible and thus contribute to unnecessary computational work. Integrating the present algorithm with such an automatic reduced mechanism generator could lead to a significant reduction in computing time.

An extension of the BGK-LED scheme for three-dimensional flow would also be of importance.

References

[1] T. R. A. Bussing and E. M. Murman. Numerical investigation of two-dimensional H_2-air flame-holding over ramps and rearward-facing steps. *Journal of Propulsion*, 3(5):448–454. September–October 1987.

[2] T. R. A. Bussing and E. M. Murman. Finite–volume method for the calculation of compressible chemically reacting flows. *AIAA Journal.* 26(9):1070–1078, September 1988.

[3] C. W. Gear. *Numerical Initial Value Problems in Ordinary Differential Equations.* Prentice-Hall, Inc.. 1971.

[4] A. Jameson. Analysis and design of numerical schemes for gas dynamics 1. artificial diffusion, upwind biasing. limiters and their effect on multigrid convergence. *Int. J. of Comp. Fluid Dyn.*, 4:171–218. 1995.

[5] A. Jameson. Analysis and design of numerical schemes for gas dynamics 2. artificial diffusion and discrete shock structure. *Int. J. of Comp. Fluid Dyn.*. 5:1–38. 1995.

[6] Y. Ju. Lower–upper scheme for chemically reacting flow with finite rate chemistry. *AIAA Journal*. 33(8):1418–14256, August 1995.

[7] H. F. Lehr. Experiments on shock–induced combustion. *Astronautica Acta*. 17:589–596. 1972.

[8] L. Martinelli. *Calculation of Viscous Flows with a Multigrid Method*. PhD thesis. Princeton University, Department of Mechanical & Aerospace Engineering, October 1987.

[9] A. Matsuo and T. Fujiwara. Numerical investigation of oscillatory instability in shock–induced combustion around a blunt body. *AIAA Journal*, 31(10):1835–1841, October 1993.

[10] A. Matuso, K. Fujii, and T. Fujiwara. Flow features of shock–induced combustion around projectile traveling at hypervelocities. *AIAA Journal*, 33(6):1056–1063, June 1995.

[11] G. Palmer and E. Venkatapathy. Comparison of nonequilibrium solution algorithms applied to chemically stiff hypersonic flows. *AIAA Journal*, 33(7):1211–1219, July 1995.

[12] J. S. Shuen and S. Yoon. Numerical study of chemically reacting flows using a lower–upper symmetric successive overrelaxation scheme. *AIAA Journal*, 27(12):1752–1760. December 1989.

[13] S. Tatsumi, L. Martinelli, and A. Jameson. Design, implementation, and validation of flux limited schemes for the solution of the compressible Navier-Stokes equations. *AIAA paper 94-0647*. AIAA 32nd Aerospace Sciences Meeting. Reno. NV, January 1994.

[14] S. Tatsumi. L. Martinelli, and A. Jameson. A new high resolution scheme for compressible viscous flow with shocks. *AIAA paper 95-0466*, AIAA 33rd Aerospace Sciences Meeting and Exhibit. Reno. NV. January 9-12 1995.

[15] G. J. Wilson and M. A. Sussman. Computation of unsteady shock-induced combustion using logarithmic species conservation equations. *AIAA Journal*. 31(2):294–301. February 1993.

[16] H. C. Yee and J. L. Shinn. Semi–implicit and fully implicit shock–capturing methods for nonequilibrium flows. *AIAA Journal*, 27(3):299–307. March 1989.

[17] S. Yungster. Numerical study of shock-wave/boundary-layer interactions in premixed combustible gases. *AIAA Journal*. 30(10):2379-2387. 1992.

[18] S. Yungster and A. P. Bruckner. Computational studies of a superdetonative ram accelerator mode. *Journal of Propulsion and Power*. 8(2):457–463, March–April 1992.

[19] S. Yungster, S. Eberhardt, and A. P. Bruckner. Numerical simulation of hypervelocity projectiles in detonable gases. *AIAA Journal*. 29(2):187-199, February 1991.

[20] S. Yungster and M. J. Rabinowitz. Computation of shock–induced combustion using a detailed methane–air mechanism. *Journal of Propulsion and Power*, 10(5):609–617, 1994.

[21] G. J. Wilson and R. W. MacCormack. Modeling supersonic combustion using a fully implicit numerical method. *AIAA Journal*. 30(4):1008–1015, April 1992.

[22] J. S. Evans and C. J. Schexnayder. Influence of chemical kinetics and unmixedness on burning in supersonic hydrogen flames. *AIAA Journal*, 18(2):180–193, February 1980.

[23] T. Chitsomboon. A. Kumar. and S. N. Tiwari. Numerical study of finite–rate supersonic combustion using parabolized equations. *AIAA paper 87-0088*. AIAA 25th Aerospace Sciences Meeting and Exhibit. Reno, NV, January 1987.

[24] J. Fielding. An experimental study of supersonic laminar reacting boundary layers. Master's thesis. Princeton University. Department of Mechanical and Aerospace Engineering. January 1997.

[25] P. Arminjon and A. Dervieux. INRIA Report 1111. 1989 (unpublished).

[26] T.J. Baker. "Triangulations, Mesh Generation and Point Placement Strategies." in *Proceedings Frontiers of Computational Fluid Dynamics.* edited by Caughey (1994), p. 101.

[27] T.J. Baker. *Finite Elements in Analysis and Design* (1997), to appear.

[28] P.P. Baum and R. Löhner, in *AIAA 22nd Fluid Dynamics Conference.* 1991. 91-1666 (unpublished).

[29] M.J. Berger and A. Jameson, *AIAA J.* **82**, 561 (1985).

[30] M.J. Berger and P. Colella, *J. Comp. Phys.* **82**, 64 (1989).

[31] M. Delanyne and J.A. Essers, in *12th AIAA CFD Conference*, 1995, CP-95-1710 (unpublished).

[32] S. M. Deshpande, NASA Langley Tech. Paper No. 2613, (1986).

[33] B. Einefldt. C.D. Munz, P.L. Roe and B. Sjögreen, *J. Comp. Phys.* **92**. 273 (1991).

[34] S.K. Godunov. *Math. Sbornik* **47**. 271 (1959).

[35] A. Harten. *J. Comp. Phys.* **49**, 357 (1983).

[36] A. Harten. B. Enquist, S. Osher and S. Chakravarthy. *J. Comp. Phys.* **171**. 231 (1987).

[37] A. Harten. P.D. Lax and B. Van Leer, *SIAM Rev.* **25**, 35 (1983).

[38] A. Jameson. T.J. Baker and N.P. Weatherhill, AIAA paper 85-0121, 1985 (unpublished).

[39] A. Jameson. The Present Status, Challenges. and Future Developments in Computational Fluid Dynamics. in *AGARD 77th Fluid Dynamics Panel Symposium,* (1995).

[40] A. Jameson. *Int. J. Num. Met. Flu.* **20**. 743 (1996).

[41] C. Johnson and P. Hansboro, *Comp. Meth. Appl. Mech. and Eng.* **101**, 143 (1992).

[42] C.A. Kim and A. Jameson, in *12th AIAA CFD Conference*, 1995, CP-95-1738 (unpublished).

[43] C.A. Kim, K. Xu, L. Martinelli and A. Jameson, *Int. J. Num. Meth. Flu.* (1997), in press.

[44] C.A. Kim. A. Jameson, L. Martinelli and K. Xu, AIAA paper 97-0328, 1997 (unpublished).

[45] C.A. Kim. Ph.D Thesis, Princeton University, Princeton, 1997, (unpublished).

[46] M.N. Kogan. *Rarefied Gas Dynamics* (Plenum Press, New York).

[47] R. Löhner, *Comp. Meth. App. Mech. and Eng.* **61**, 323 (1987).

[48] R. Löhner. K. Morgan, J. Peraire and M. Vahdati, *Int. J. Num. Met. Flu.* **7**, 1093 (1987).

[49] M.N. Macrossan and R.I. Oliver. *Int. J. Num. Met. Flu.* **17**, 177 (1993).

[50] T. Magruder and A.J. Smits. Private Communication. (1997).

[51] J.C. Mandal and S.M. Deshpande. *Computers and Fluids* **23**, 447 (1994).

[52] T.J. Mitty, T.J. Baker and A. Jameson. *Computers and Fluids* **22**, 271 (1993).

[53] J.M. Moschetta and D.I. Pullin. *J. Comp. Phys.* **133**, 193 (1997).

[54] B. Perthame. *SIAM J. Num. Anal.* **29**, (1992).

[55] D.I. Pullin. *J. Comp. Phys.* **34**, 231 (1980).

[56] J. Quirk. *Int. J. Num. Met. Flu.* **18**, 555 (1994).

[57] R.D. Rausch. J.T. Batina and H.T.Y. Yang, in *31st Aerospace Sciences Meeting and Exhibit*, 1993. 93-0670 (unpublished).

[58] S. Rebay. *J. Comp. Phys.* **106**, 124 (1993).

[59] P.L. Roe. *J. Comp. Phys.* **43**, 357 (1981).

[60] C.W. Shu and S. Osher, *J. Comp. Phys.* **82**, 32 (1989).

[61] S. Tatsumi, L. Martinelli and A. Jameson, *AIAA J.* **33**, 252 (1995).

[62] N.P. Weatherhill, O. Hassan, M.J. Marchant and D.L. Marcum, in *11th AIAA CFD Conference*, 1993, CP-93-3390 (unpublished).

[63] P. Woodward and P. Colella, *J. Comp. Phys.* **54**, 115 (1984).

[64] K. Xu and K.H. Predergast, *J. Comp. Phys.* **109**, 53 (1993).

[65] K. Xu and K.H. Predergast, *J. Comp. Phys.* **114**, 9 (1994).

[66] K. Xu, L. Martinelli and A. Jameson, *J. Comp. Phys.* **120**, 48 (1995).

[67] K. Xu, C.A. Kim, L. Matinelli and A. Jameson, *Int. J. Comp. Flu. Dyna.* **7**, 213 (1996).

1. Gas-Kinetic Finite Volume Methods, (with K. Xu and L. Martinelli) Proceedings of 14th International Conference on Numerical Methods in Fluid Dynamics, Bangalore, July 1994

2. A New High Resolution Scheme for Compressible Viscous Flows with Shocks (with S. Tatsumi and L. Martinelli) AIAA Paper 95-0466, AIAA 33rd Aerospace Sciences Meeting and Exhibit, Reno, January 1995

3. Euler Multigrid Calculations Using a Gas-Kinetic Scheme (with K. Xu and L. Martinelli) AIAA Paper 95-0206, AIAA 33rd Aerospace Sciences Meeting and Exhibit, Reno, January 1995

4. Positive Schemes and Shock Modelling for Compressible Flows, Proceedings of 8th Finite Elements in Fluids Conference, Barcelona, September 1993, International Journal for Numerical Methods in Fluids, Vol. 20, 1995, pp. 743-776

5. Flux Limited Dissipation Schemes for High Speed Unsteady Flows (with C.A. Kim) AIAA Paper No. 95-1738, AIAA 12th Computational Fluid Dynamics Conference, San Diego, June 1995

6. Gas Kinetic Relaxation (BKG-Type) Schemes for the Compressible Euler Equations (with K. Xu) AIAA Paper No. 95-1736, AIAA 12th Computational Fluid Dynamics Conference, San Diego, June 1995

7. Gas-Kinetic Finite Volume Methods, Flux-Vector Splitting and Artificial Diffusion (with K. Xu, L. Martinelli) Journal of Computational Physics, Vol. 120, August 1995, pp. 48 - 65

8. BGK-Based Schemes for the Simulation of Compressible Flow (with K. Xu, C. Kim, L. Martinelli) International Journal of Computational Fluid Dynamics, Vol. 7, 1996, pp. 213-235.

9. Analysis and Design of Numerical Schemes for Gas Dynamics 1 Artificial Diffusion, Upwind Biasing, Limiters and Their Effect on Accuracy and Multigrid Convergence, RIACS Technical Report 94.15, International Journal of Computational Fluid Dynamics, Vol. 4, 1995, pp. 171-218

10. Analysis and Design of Numerical Schemes for Gas Dynamics 2 Artificial Diffusion and Discrete Shock Structure, RIACS Report No. 94.16, International Journal of Computational Fluid Dynamics, Vol. 5, 1995, pp. 1-38

11. On the Construction of the BGK-Type Schemes for Compressible Flow Simulations (with K. Xu, C. Kim, L. Martinelli) Proceedings of 6th International Symposium on Computational Fluid Dynamics, Lake Tahoe, September 1995

12. On the Construction of the BGK-Type Schemes for Compressible Flow Simulations (with K. Xu, C. Kim, L. Martinelli) AIAA Paper 96-0525, AIAA 34th Aerospace Sciences Meeting and Exhibit, Reno, January 1996

13. Parallel Computation of Supersonic Reactive Flows with Detailed Chemistry (with S. Sheffer, L. Martinelli), AIAA 97-0899, AIAA 35th Aerospace Sciences Meeting and Exhibit, Reno, January 1997

14. An Accurate LED-BGK Solver on Unstructured Adaptive Meshes (with C.A. Kim, K. Xu, L. Martinelli), AIAA 97-0328, AIAA 35th Aerospace Sciences Meeting and Exhibit, Reno, January 1997

15. A Multigrid Method for High Speed Reactive Flows (with S. Sheffer, L. Martinelli) AIAA 97-2106, AIAA 13th Computational Fluid Dynamics Conference, Snowmass, June 1997

16. Simulation of Supersonic Reacting Hydrocarbon Flows with Detailed Chemistry (with S. Sheffer, L. Martinelli), AIAA 97-3240 33rd AIAA/ASME/SAE/ASEE Joint Propulsion Conference and Exhibit, Seattle, July 1997

17. Analysis and Implementation of the Gas-Kinetic BGK Scheme for Computational Gas Dynamics (WITH K. Xu, C. Kim, L. Martinelli) International Journal of Numerical Methods in Fluids, Vol. 25, No. 1, July 1997, pp. 21-49

Task 4: Control of Combustion Systems

Modelling versus Control of Combustion System

Simulation of complex engineering systems requires reliable and accurate mathematical models. In reactive flow problems involving complex chemical kinetics, the quality of the models is usually not very good. It is not unusual to u se rate coefficients which are not accurately known. The details of turbulent mixing processes in the flow are not fully understood. The coupling of chemical reactions and turbulence compounds the difficulties.

Consider the following example: if the pressure in a scramjet combustor is found to oscillate when the fuel injector rate is constant, can the fuel injection rate be controlled such that the oscillation is suppressed? The usual approach would be: build an accurate and reliable reactive gasdynamic model and try out various time-dependent fuel injection profiles and see what happens to the pressure oscillations in the simulations.

In the attached paper Lam has explored the provocative idea: is it possible to exert control of the performance of a complex, nonlinear system *without* the need for a reliable and accurate mathematical model? The answer he has found is a qualified **yes** for finite dimensional problems. Two papers [1,2] were written and were presented in international conferences. Another paper [3] is in progress. The extension to infinite dimensional problems remains to be explored.

References

[1]   S.H. Lam, "Quasi-Steady Approximation and Adaptive Nonlinear Controls," presented in the "Physical Chemical Modelling in CFD" session, 15th IMACS World Congress on Scientific Computations, Modelling and Applied Mathematics, Berlin, August, 1997.

[2]   S.H. Lam, "A Robust Universal Controller," presented at the ASME IMECE at Dallas, Texas, November, 1997.

[3]   S.H. Lam, "Universal Controller for Reasonable Non-Linear Systems", MAE Report 2089, Department of Mechanical and Aerospace Engineering, Princeton University, 1997.

A Robust Universal Controller[1]

S. H. Lam

Princeton University
Department of Mechanical and Aerospace Engineering
Princeton, NJ 08544
lam@princeton.edu

Abstract

The present paper advocates the use of ODE-based (instead of algebra-based) constraints on the output variables of a controlled system, and the use of dynamic control laws (instead of static control laws)—when finite but small errors in honoring the constraints are considered acceptable. It is assumed that the sensor signals are reliable and have good signal-to-noise ratios, that the controller has ample computational power, and that the hardware/software "sampling time" t_s is much smaller than the system characteristic time t_g. A universal *dynamic* control law is proposed which does not require detailed knowledge of the system itself—and is therefore completely robust with respect to uncertainties of the system—provided the control problem to be solved is reasonable. The meaning of the equivocal word "reasonable" will be explained.

1 Introduction

The approach advocated by this paper is based on the concatenation of two new ideas:

- Instead of imposing *algebra-based* constraints on the sensor signals, a set of *ODE-based* constraints are specified.
- Instead of looking for *static control laws*, the new approach looks for *dynamic control laws* which *approximately* honor the ODE-based constraints.

With this new approach, the only information about a dynamic system needed by the controller is some "surrogate" of the *extended pulse-response matrix* $B_i^m(t)$ (defined in §2.3 later by Eq. (7c)) which is closely related—but is not identical—to the so-called "decoupling matrix" (Isidori, 1995). Most importantly,

this $B_i^m(t)$ matrix can be determined on-the-fly—in principle—directly by the controller itself (see §2.3). Unlike most current adaptive control theories (Ioannou and Sun, 1996; Marino and Tomei, 1995; Krstić *et. al.*, 1995; Kokotović *et. al.*, 1991; Kokotović *et. al.*, 1986; Ioannou and Kokotović, 1983), no detailed knowledge of the system is needed—not even a parametrized form. The present theory exploits $t_s/t_g << 1$, the virtually unlimited computing power available to the controller, and the mathematical insights provided by the so-called *quasi-steady approximation* on stable "stiff" ODE's (O'Malley, 1991; Lam, 1993; Lam and Goussis, 1994). The proposed *universal dynamic control law* is in the form of a stable stiff ODE for the control inputs, and its numerical solution (using Euler's method) automatically generates an *approximation* to the exact static control law—using only the current and past sensor signals, the past control inputs, and a "surrogate" of the real $B_i^m(t)$. The theory of the "regular" case—when the true $B_{i'}^i$ is non-singular and not nearly singular—is presented, and a simple example is provided in §3.1.1.. The generalization to the "irregular" case—when $B_{i'}^i$ is singular or nearly singular—is non-trivial. Only a brief summary of the major results of the irregular case is presented here: the details are presented in separate papers (Lam, 1997a,b).

2 Formulation

A system is to be controlled by a black box with I actuator control inputs (to the system) and I primary sensor outputs (from the system) which are assumed to be reliable and have good signal-to-noise ratios. The job of the black box is to compute and issue the appropriate control input signals to the system so that the resulting sensor signals outputted from the system indeed honor the user-specified constraints satisfactorily—*i.e.* the measured constraint errors are kept below some user-specified, finite *accuracy thresh-*

old. We assume that the black box has no detailed knowledge of the system except for the following:

1. The maximum allowable amplitudes of the actuator control inputs are known.

2. The characteristic timescale of the system is known to be of the order of t_g seconds. A pragmatic definition of t_g is the following: if any of the control inputs were suddenly set to a "wrong" (but allowable) value, the measured constraint errors would evolve continuously and become significant in no less than t_g seconds. In other words, t_g is the minimum "grace period" allowed by the problem. Hence, t_g can in principle be directly measured by the black box itself.

3. The *sampling period* t_s of the system, defined as the time required by the black box hardware/software to compute and update the control inputs based on the current and past sensor outputs and control inputs, is much, much smaller than t_g.

The black box has full detailed knowledge of the desired ODE-based constraints and the acceptable threshold of constraint errors. It is allowed to use only the present and past sensor signals (output feedback) in computing the control inputs to the system. Obviously, it must also have the ability to identify "unreasonable" tasks which cannot be performed by the system and so inform the user.

In the present paper, a function of time is said to be *smooth* if it is differentiable and its characteristic timescale is $O(t_g)$.

2.1 A Dynamic Model of the System

Consider the following nonlinear dynamical system for a N-dimensional column vector $\mathbf{x}(t)$:

$$\frac{d\mathbf{x}}{dt} = \mathbf{f} + \sum_{i=1}^{I} \mathbf{b}_i u^i, \qquad (1)$$

where $\mathbf{f}(\mathbf{x},t)$ and the $\mathbf{b}_i(\mathbf{x},t)$'s are differentiable and bounded (column) vector functions of $\mathbf{x}$ and t and $I \leq N$. The first term on the right hand side represents the resultant *applied force* acting on the system, while the second term represents the resultant *control force* acting on the system, expressed as the sum of I linearly independent *actuator forces*. We attribute no special significance to the point $\mathbf{x} = 0$, make no assumption on the value of $\mathbf{f}(0,t)$ or the functional form of $\mathbf{f}(\mathbf{x},t)$. The column vector $\mathbf{b}_i(\mathbf{x},t)$ and the scalars u^i's

represent the direction and the amplitude—the latter is called *control input* here—of the i-th actuator force, respectively. We assume that the $u^i(t)$'s have been non-dimensionalized by their (known) maximum allowable values so that $u^i = O(1)$ is required. The characteristic timescale t_g of the problem (as described previously) is, loosely speaking, determined by the order of magnitude of the $\mathbf{b}_i$'s. No loss of generality was incurred by assuming that the right hand side of Eq. (1) is linear with respect to the u^i's and contains none of their time derivatives. If the right hand side of Eq. (1) is a general function $\mathbf{f}(\mathbf{x},t;u^i,\dot{u}^i,\ddot{u}^i,\ldots)$, it can always be transformed into the the form of the current Eq. (1) by introducing new state variables and new control inputs (Lane and Stengel, 1988).

There are I sensor signals. The i-th sensor signal is denoted by y^i which is a measurement of the current state of the system:

$$y^i = \psi^i(\mathbf{x},t), \quad i = 1, \ldots, I, \qquad (2)$$

where the $\psi^i(\mathbf{x},t)$'s are I linearly independent, smooth and differentiable functions of $\mathbf{x}$ and t. We assume the y^i's have been appropriately non-dimensionalized, and call them the *primary outputs* of the system. The primary ψ^i's are strictly forbidden to depend on the u^i's. Under certain well-defined conditions, the problem may spawn additional $J \geq 0$ *derived outputs* y^{I+j}'s (Lam, 1997a,b). By including the derived outputs, the total number of outputs becomes $M = I + J \leq N$ (M can be interpreted as the sum of "relative degrees" of the primary outputs). Together the M outputs can be succinctly represented by:

$$y^m = \psi^m(\mathbf{x},t;\ldots), \quad m = 1, \ldots, M. \qquad (3)$$

We assume that $\psi^m(\mathbf{x},t) = 0$ is an non-empty region in $\mathbf{x}$ space. Unlike the primary ψ^i's which have no dependence at all on the u^i's, the derived ψ^{I+j}'s may have a "weak" dependence.

The mathematical problem is to find control algorithms to compute the $u^i(t)$'s—without using detailed knowledge of the system—such that not only the resulting $y^m(t)$'s satisfactorily honor the user-specified constraint equations, but also the $u^i(t)$'s are $O(1)$. In the present paper, we shall confine our attention mostly to the regular case when $B^i_{i'}$ is non-singular (and therefore $J = 0$ and $M = I$); only a brief summary of results of the irregular case is included.

2.2 The Constraint Equations

We divide the N-dimensional $\mathbf{x}$ space into two complementary subspaces: a M-dimensional *output sub-*

space $\{y^1, \ldots, y^M\}$ (which includes both primary and derived output variables), and its complementary K-dimensional *residual subspace*, $\{y^{M+1}, \ldots, y^N\}$ where $K = N - M \geq 0$. The output subspace is defined by Eq. (3). The residual subspace is defined by

$$y^{M+k} = \psi^{M+k}(\mathbf{x}, t), \quad k = 1, \ldots, K, \qquad (4)$$

where the $\psi^{M+k}(\mathbf{x}, t)$'s are any differentiable functions subject to the requirement that the transformation Jacobian between $\mathbf{x}$ and $\mathbf{y}$ is non-singular. In the dynamics community, the residual variables y^{M+k}'s are called *generalized coordinates*.

Conventionally, *algebra-based constraints* are imposed on the output variables:

$$y^m(t) = O(\epsilon), \qquad (5a)$$

where ϵ is a user-specified dimensionless accuracy threshold. Such problems are called *tracking* or *regulation* problems. In the present paper, we shall impose, instead of Eq. (5a), the following *ODE-based constraints*:

$$\frac{dy^m}{dt} + \phi^m(\mathbf{y}, t; \varpi^{m'}) = O(\epsilon/t_g), \qquad (5b)$$

where the $\phi^m(\mathbf{y}, t; \varpi^{m'})$'s are user-specified functions (and the $\varpi^{m'}$'s are *residual controls* to be exploited later). It is easy to be convinced that Eq. (5b) can include Eq. (5a) as a special case.

When $N > M$, the stability of the residual variables is sometimes also of interest. It is possible to exert some influence on the residual variables of the system *provided* some additional information is available to the controller. The *residual control problem* will be briefly discussed in §3.2.2.

2.2.1 A Special Choice of $\phi^m(\mathbf{y}, t; \varpi^{m'})$: In order for the universal controller to be able to compute $\mathbf{u}(t)$ from Eq. (9), the function $\phi^m(\mathbf{y}, t; \varpi^{m'})$'s should depend only on the y^m's (output feedback). The following special choice is of particular interest:

$$\phi^m(\mathbf{y}, t; \varpi^{m'}) = \frac{1}{\tau} \sum_{m'=1}^{M} \Omega_{m'}^m \left(y^{m'} - \varpi^{m'} \right) \qquad (6)$$

where $\tau > 0$ is a user-chosen characteristic controller timescale (the "settling time"), $\Omega_{m'}^m$ is a $M \times M$ dimensionless positive-resolute matrix (see §3.1 later), and the ϖ^m's are residual controls which are not allowed to depend on the y^m's but may depend smoothly on t (it will later be allowed to depend on the y^{M+k}'s in dealing with the residual control problem). When this special choice Eq. (6) is used, it is easy to show (using the quasi-steady approximation) that $y^m \approx \varpi^m$ is a good approximate solution of Eq. (5b) when $\tau \ll t_g$.

2.3 Dynamics of Output and Residual Variables

Differentiating Eq. (3) with respect to time and using Eq. (1), we obtain the ODE's for the output variables:

$$\frac{dy^m}{dt} = g^m + \sum_{i=1}^{I} B_i^m u^i, \qquad (7a)$$

where

$$g^m(\mathbf{x}, t) = \frac{\partial \psi^m}{\partial t} + \mathbf{c}^m \cdot \mathbf{f}, \qquad (7b)$$

$$B_i^m(\mathbf{x}, t) \equiv \mathbf{c}^m \cdot \mathbf{b}_i, \qquad (7c)$$

$$\mathbf{c}^m(\mathbf{x}, t) \equiv \frac{\partial \psi^m}{\partial \mathbf{x}}. \qquad (7d)$$

The M row vectors $\mathbf{c}^m$'s are assumed linearly independent. The order of magnitude of B_i^m is $O(1/t_g)$ (based the pragmatic definition of t_g given previously). If B_i^i is non-singular and *not* nearly singular, the problem is *regular* ($M = I$), otherwise, it is *irregular* ($M > I$). For regular problems, the g^i's have no dependence at all on the u^i's. We shall see later in §4 that for irregular problems the same cannot be said for the derived g^m's.

Geometrically, the row vector $\mathbf{c}^m$ is normal to the $\psi^m = 0$ surface. The column vector $\mathbf{b}_i$ represents the direction of the i-th actuator force vector. The $M \times I$ rectangular matrix $B_i^m(\mathbf{x}, t)$, defined as the dot product of $\mathbf{c}^m(\mathbf{x}, t)$ with $\mathbf{b}_i(\mathbf{x}, t)$, plays a most important role in the present theory. It is *not* the same as the $I \times I$ square *decoupling matrix* in standard nonlinear control textbooks (Isidori, 1995; Marino, 1995)—even though they are closely related. Its matrix elements are called *first Markov parameters* in linear system textbooks (Rugh, 1996; Brogan, 1985; Kailath, 1980; Chen, 1970). To avoid confusion, we shall call it the *pulse-response matrix* of the system since in principle it can be directly determined on the-fly by the controller by pulsing the u^i's and measuring the immediate response of the y^m's.

The ODE's for the remaining K residual variables y^{M+k}'s (*i.e.* generalized coordinates) are simply given by (7a,b,c,d) with the superscript index m replaced by $M + k$.

3 The Regular Case

We confine our attention to regular problems for which no additional derived outputs are needed ($M = I$). The completely straightforward treatment below serves as a guide for the more involved treatment of singular and nearly singular problems—which must deal with the complications of derived outputs.

Since $[B_{i'}^i]^{-1}$ exists, we can analytically eliminate dy^i/dt between Eq. (7a) and Eq. (5b) and solve for the u^i's (with ϵ set to zero). The resulting *exact* static control law, denoted by u_∞^i, is:

$$u_\infty^i(\mathbf{x}, t) \equiv u_o^i(\mathbf{x}, t) - \sum_{i'=1}^{I} [B_i^{i'}]^{-1} \phi^{i'}(\mathbf{y}, t; \varpi^i). \quad (8a)$$

where $u_o^i(\mathbf{x}, t)$ is:

$$u_o^i(\mathbf{x}, t) \equiv - \sum_{i'=1}^{I} [B_i^{i'}]^{-1} g^{i'}, \quad (8b)$$

Note that u_o^i has no dependence on the u^i's because the primary $g^i(\mathbf{x}, t)$'s are strictly forbidden to have any dependence at all on the u^i's.

This exact static control law u_∞^i cannot function as an universal controller because its evaluation requires detailed knowledge of the system (and full state feedback).

3.1 Regular Universal Dynamic Control Law

We now assume that, in addition to good quality $y^i(t)$'s and $\dot{y}^i(t)$'s, a certain non-singular "surrogate matrix" $\bar{B}_{i'}^i(t)$ is also somehow made available to the controller. The proposed *regular universal dynamic control law* is:

$$\frac{du^i}{dt} = -\frac{1}{\Delta t} \sum_{i'=1}^{I} [\bar{B}_i^{i'}]^{-1} \left(\dot{y}^{i'} + \phi^{i'}(\mathbf{y}, t, \varpi^{i'}) \right), \quad (9)$$

where Δt is a user-chosen "small" positive timescale such that $\Delta t/t_g = O(\epsilon)$. What properties must $\bar{B}_i^{i'}$ have in order to ensure that Eq. (9) is asymptotically stable? Using Eq. (7a) to eliminate $\dot{y}^i$ from Eq. (9), factoring out $B_{i'}^i$ and using Eq. (8b), we obtain:

$$\frac{du^i}{dt} = -\frac{1}{\Delta t} \sum_{i'=1}^{I} \bar{W}_{i'}^i \left(u^{i'} - u_\infty^{i'} \right), \quad (10a)$$

where u_∞^i was given previously by Eq. (8a) and

$$\bar{W}_{i'}^i \equiv \sum_{i''=1}^{I} [\bar{B}_i^{i''}]^{-1} B_{i'}^{i''}. \quad (10b)$$

We are reminded that u_∞^i is known to have no dependence at all either on the u^i's or their higher time derivatives. Hence Eq. (10a), and therefore Eq. (9), is simply a system of first order ODE's for the u^i's when the problem is regular.

We shall call a matrix a *resolute* matrix if all the real part of its eigenvalues are of the same sign *and* are all $O(1)$. A resolute matrix is said to be *positive-resolute* if the real part of all its eigenvalues are positive. By inspection of Eq. (10a), we require $\bar{W}_{i'}^i$ to be positive-resolute to ensure the asymptotic stability of Eq. (10a) and therefore Eq. (9), and to allow Δt to be interpreted as the characteristic time needed by the dynamic control law to allow u^i to converge to an approximation of u_∞^i, regardless of its initial condition. Whenever $u^i(t)$ computed from Eq. (9) is found to be bounded and smooth using $\Delta t/t_g = O(\epsilon) << 1$, we can conclude—using insights from the methodology of quasi-steady approximation—that the $u^i(t)$'s obtained are good approximations to the $u_\infty^i(\mathbf{x}(t), t)$'s. Formally, we have $u^i = u_\infty^i + O(\Delta t/t_g)$ for $t >> \Delta t$. For best performance, the smallest allowable value should be used for Δt (*e.g.* $\Delta t = t_s$).

While the most simple-minded choice for $\bar{B}_{i'}^i$ for a regular problem is obviously $B_{i'}^i$ (so that $\bar{W}_{i'}^i$ is the identity matrix), we see that any non-ideal surrogate $\bar{B}_{i'}^i$ can be used so long as the resulting $\bar{W}_{i'}^i$ is positive-resolute. The details of a positive-resolute $\bar{W}_{i'}^i$ impact the u^i's only in a brief $O(\Delta t)$ transient period. In other words, the condition on $\bar{B}_{i'}^i$ is quite weak for regular problems.

3.1.1 A Simple Example: In this subsection only, superscript of column vectors will appear as a subscript to avoid confusion with exponents. Consider a problem with $I = 2$ and its impulse-response matrix $B_{i'}^i(t)$ is assumed known (it is non-singular and its smallest singular value is $O(1/t_g)$), and the measured $y_i(t)$'s *and* $\dot{y}_i(t)$'s are assumed reliable and have good signal-to-noise ratios. We do not know N (except that $N \geq 2$), $\mathbf{f}(\mathbf{x}, t)$, $\mathbf{b}_i(\mathbf{x}, t)$, $\psi_i(\mathbf{x}, t)$ or $\mathbf{c}_i(\mathbf{x}, t)$. It is desired for the y_i's to emulate a Van der Pols oscillator:

$$\phi_1 = -y_1, \quad (11a)$$
$$\phi_2 = -\mu(1 - y_1^2)y_2 + \kappa^2 y_1, \quad (11b)$$

where μ and κ are user-chosen positive constants with $\kappa t_g = O(1)$.

Using $\bar{B}_{i'}^i \approx B_{i'}^i(t)$ and choosing Δt such that $\kappa \Delta t = O(\epsilon) << 1$, one can easily verify—using either asymptotic analysis or direct numerical simulations on desktop computers—that the universal dynamic control law Eq. (9) will indeed honor the ODE-based constraints Eq. (5b) with accuracy $O(\epsilon)$ for any reasonable $\mathbf{f}(\mathbf{x}, t)$ (after a brief $O(\Delta t)$ transient). If the resulting $u_i(t)$'s—which depend on $\mathbf{f}(\mathbf{x}, t)$—are $O(1)$, then all is well.

If instead it is desired for the y_i's to remain $O(\epsilon)$ (*i.e.* a regulation problem), the universal controller can use

the special ϕ_i given by Eq. (6) with $\varpi_i = 0$. One can also easily verify that the desired algebra-based constraints are honored (after a brief $O(\tau)$ transient).

3.2 Dynamics of Residual Variables

If $K = N - M > 0$, what happens to the K residual variables y^{M+k}'s? Since the universal controller is unaware of even their existence, this question is meaningful only if some supplementary information such as additional sensor measurements and/or indeed a detailed mathematical model are made available to the controller. If no such information are provided, the universal controller is incapable of accepting any responsibility for influencing the unobserved y^{M+k}'s. To continue the discussion, we assume that all needed supplementary information are indeed available.

3.2.1 Zero Dynamics:
When algebra-based constraints $y^m = O(\epsilon)$ are imposed, the dynamics problem of the residual variables y^{M+k}'s obtained by honoring the algebra-based constraints precisely (*i.e.* $\epsilon = 0$) is classically called the *zero dynamics problem*. We shall generalize the definition of zero dynamics by allowing the y^m's to honor *either* the algebra-based constraints *or* the ODE-based constraints precisely.

If the zero dynamics solutions are deemed acceptable with all residual controls set to zero, then all is well. Generally speaking, the usefulness of the proposed universal controller is limited to such problems. Classically, linear problems with stable zero dynamics are called minimum-phase problems. Otherwise, they are called non-minimum phase problems. Note that whether the problem is linear or nonlinear plays no role in the present theory.

3.2.2 The Residual Control Problems:
Non-zero residual controls ϖ^i's may be used to exert some influence on the residual variables.

If Eq. (6) is adopted, then the following simple-minded strategy is theoretically available: substitute u_∞^i as given by Eq. (8a) for u^i in Eq. (1) to obtain a new control problem. The residual controls ϖ^i's now play the role originally played by the u^i's—except that they are not allowed to depended on the primary output variables y^i's. Up to I offending residual variables may be influenced in some way by the I available residual controls—provided the new residual control problem poses a reasonable problem. An example is worked out in Lam (1997b) to show what can be done.

4 The Irregular Case

When $B_{i'}^i$ is singular or nearly singular, the problem is said to be *irregular*. Irregular problems are quite commonplace in practical systems (Godbole and Sastry, 1995). Hence, the generalization of the present approach is of fundamental interest. Since space limitation here does not allow a full presentation, we shall limit ourselves to a brief summary of the major results presented in Lam (1997b).

For irregular problems, we must search for J additional *derived outputs* y^{I+j}'s such that the traditional rank of the $M \times I$ *extended impulse-response* matrix B_i^m is I. If a full-rank B_i^m can be found, the irregular problem is said to be been *regularizable*; otherwise, the control problem as posed is said to be unreasonable.

An outline of the searching procedure is given below. The singular value decomposition of a full-rank B_i^m is represented by (Golub, 1989):

$$B_i^m = \sum_{i'=1}^{I} [U_m^{i'}]^T \omega(i') V_i^{i'}, \qquad (12)$$

where $U_{m'}^m$ and $V_{i'}^i$ are $M \times M$ and $I \times I$ dimensionless orthogonal matrices and the $\omega(i)$'s are the singular values (always positive by convention) which satisfy the following inequality:

$$\omega(i) > |\omega_*| \qquad (13)$$

where ω_* is a user-chosen signed (small) parameter with the dimension of frequency. The bottom $J = M - I$ rows of $U_{m'}^m$, which do not appear in Eq. (12), are called *left null-vectors* of B_i^m (for obvious reasons). Any row vector $\tilde{U}_m^{(.)}$ which satisfies

$$\sum_{m=1}^{M} \tilde{U}_m^{(.)} B_i^m = O(\omega_*) \qquad (14)$$

is called a left *epsilon-vector* of B_i^m—it can be approximately represented by linear combinations of the J left null-vectors. A bootstrapping procedure is used to recursively find J linearly independent left epsilon-vectors of B_i^m which, in addition to satisfying Eq. (14), also satisfy:

$$\tilde{U}_m^{I+j} = 0, \quad m \geq I+j, \quad j = 1, \ldots, J, \qquad (15)$$

one after the other. A special generalization of Eq. (6) for $\phi^m(y, t; \varpi^{m'})$ is adopted in which all elements of $\Omega_{m'}^m$ are user-chosen except $\Omega_{I+j}^m = [\tilde{U}_m^{I+j}]^T$ for $m \geq I+j$. In addition, the M residual controls ϖ^m's are required to satisfy:

$$\sum_{m,m'=1}^{M} \tilde{U}_m^{I+j} \Omega_{m'}^m \varpi^{m'} = 0. \qquad (16)$$

Hence, only I degrees of freedom are available to the M residual controls.

The J *derived output variables* y^{I+j}'s are defined by:

$$\sum_{m=1}^{M} \bar{U}_m^{I+j} (\dot{y}^m + \phi^m) = O(\omega_*), \qquad j = 1, \ldots, J. \quad (17)$$

The special of $\bar{U}_m^{I+j}$, $\Omega_{m'}^m$, and ϖ^m mentioned above allowed y^{I+j} to be recursively solved for in terms of the y^m's and the $\dot{y}^m$'s where $m < I + j$. Assuming a full-rank B_i^m is found, the *universal dynamic control law* is:

$$\frac{du^i}{dt} = -\frac{1}{\Delta t} \sum_{m=1}^{M} [B_i^m]_*^+ (\dot{y}^m + \phi^m) \quad (18)$$

where $[B_i^m]_*^+$, called the *epsilon-inverse* of B_i^m, is given by (Golub, 1989):

$$[B_i^m]_*^+ \equiv \sum_{i'=1}^{I} [V_i^{i'}]^T \frac{1}{\omega(i')} U_m^{i'}. \quad (19)$$

Operationally, the universal controller is responsible for the numerical integration of Eq. (18) (using Euler's method), while Nature is responsible for the analog integration of the systems of ODE's for the M output variables Eq. (7a) and the K residual variables. We can analytically eliminate $\dot{y}^m$ from Eq. (18) using Eq. (7a) to obtain:

$$\frac{du^i}{dt} = -\frac{1}{\Delta t} (u^i - u_\infty^i) \quad (20)$$

where u_∞^i is now given by an expression similar to Eq. (8a) and Eq. (8b) except that the inverse of B_i^i is replaced by the epsilon-inverse of B_i^m. Most importantly, whenever $\omega_* \neq 0$ the irregular u_∞^i is now "weakly" dependent on the u^i's (and perhaps even their higher time derivatives) because the derived $\psi^{I+j}(\mathbf{x}, t; \ldots)$'s obtained by Eq. (17) are weakly dependent on them. These theoretically negligible "higher order" terms in u_∞^i have subtle and profound consequences on the stability of Eq. (18) or Eq. (20). The universal controller is not a theoretician, and it is incapable of "neglecting" theoretically negligible terms—it must use Eq. (18) as it is displayed above. We denote the order of the highest time derivative of u^i appearing in u_∞^i by q. Hence, whenever $\omega_* \neq 0$ Eq. (18) or Eq. (20) is *not* a a system of first order ODE's, but rather a system of q-th order ODE's for the u^i's. The following recommendations are arrived at after careful scrutiny and analysis. To be assured of stability, Euler's method for numerical integration must be used (to render the small, higher order time derivative terms impotent), *and* Δt must respect as a lower bound τ_* defined by:

$$\tau_* \equiv |\epsilon_*|^{1/q} t_g, \quad \epsilon_* \equiv \omega_* t_g. \quad (21)$$

Because Δt now has a lower bound, the minimum constraint error for irregular problems is $O(|\epsilon_*|^{1/q})$.

5 Reasonable Problems

We are now ready to define what is a reasonable problem. A problem is said to be reasonable if

- its impulse-response matrix B_i^m ($M \geq I$) is nonsingular.
- the $u^i(t)$'s computed by the universal dynamic control laws are $O(1)$ and are smooth.

We take it for granted that the I sensor signals (and their time derivatives) have good signal-to-noise ratios, a good estimate of t_g is known, t_s/t_g is sufficiently small, and a good surrogate to the regularized $B_i^m(t)$ is somehow provided (directly measured or otherwise provided). The control of the residual variables is left to the residual controls when additional information is provided. The design of an universal controller which honors Eq. (6) then simply involves the selection of τ and the user-specifiable elements of the positive-resolute $\Omega_{m'}^m$, matrix. The smallest possible Δt should be used to get the best performance.

The universal controller relies completely on the sensor signals to go about the task of controlling the system. All sensor measurements, including measurement noises, are being interpreted by the universal controller as externally applied forces acting on the system. It blindly strives to make the measured $y^m(t)$'s honor the ODE-based constraints within the user-specified constraint error threshold. Hence, the measured $y^m(t)$'s must be reliable and have very good signal-to-noise ratio in order for the universal controller to be usable.

Theoretically, u_∞^i as given by Eq. (8a) can be rewritten for any general ϕ^i as:

$$u_\infty^i = -\sum_{m=1}^{M} [B_i^m]_*^+ (\phi^m + g^m). \quad (22)$$

Since $u^i \approx u_\infty^i$, Eq. (22) can be used to estimate the magnitude of the u^i's. Since $[B_i^m]_*^+ = O(t_g)$ (by definition of t_g), we require $\phi^m + g^m = O(1/t_g)$ for reasonable problems.

6 Concluding Remarks

The strength of the present approach is that no detailed knowledge of the system is needed. Whether the problem is linear or nonlinear is irrelevant, so long as it

is reasonable in accordance with §5. The Achilles' heel is that it requires not only reliable sensor signals of the output variables, but also their time derivatives. This is the price paid for robustness with respect to the system. Obviously, no one should expect any controller, which is not only uninformed about the system to be controlled but is also provided with unreliable sensor signals, to be able to perform its assigned control task successfully. The universal controller simply expects all sensor signals to be reliable and to have "sufficiently good" signal-to-noise ratios. Ideally, the highest time derivatives of the primary output variables should be reliably measured by the sensors, and their lower time derivatives and the primary output variables themselves should be obtained by numerical integration. Obviously, if enough detailed knowledge about the system is provided, the universal controller can certainly take advantage of the additional information to construct observers and use them to reduce its present total reliance on the sensor signals.

The controller can exert an influence on the unobserved residual variables y^{M+k}'s of the system by the use of the I degrees of freedom available in the residual controls—provided some additional information and knowledge are provided to the controller.

The universal dynamic control laws presented above are in the form of ODE's for the u^i's. For irregular problems with $\epsilon_\bullet \neq 0$, it is theoretically imperative that Euler's method be used when $q \geq 2$. The achievable accuracy of the universal controller degrades as q increases (because the lower bound for Δt increases). A discussion of this point is given in Lam (1997b).

It is possible for a system to be non-regularizable at certain isolated special system configurations, but can be literally "shaken" off such "top-dead-center" configurations by random pulsing of the actuators. It is also possible for a generally reasonable problem to tolerate brief unreasonable periods (e.g. its zero dynamics problem becomes temporarily non-minimum phase). In numerical simulations, the universal controller is quite capable of recovering from such episodes.

References

[1]   Brogan, W. L., 1985. *Modern Control Theory*, Prentice Hall, Inc.

[2]   Chen, C. T., 1970. *Introduction to Linear System Theory*, Holt, Reinhart and Winston, Inc.

[3]   Godbole, D. N. and Sastry, S. S., 1995. "Approximate Decoupling and Asymptotic Tracking for MIMO Systems," IEEE Transactions on Automatic Control, Vol. 40, **3**, pp. 441-450.

[4]   Golub, G. H. and Van Loan C. F., 1989. *Matrix Computations*, Second Edition, The Johns Hopkins University Press.

[5]   Ioannou, P. A. and Kokotović, P. V., 1983. *Adaptive Systems with Reduced Models*, Lecture Notes in Control and Information Sciences, #47, Springer-Verlag.

[6]   Ioannou, P. A. and Sun, J., 1996. *Robust Adaptive Control*, Prentice Hall.

[7]   Isidori, Alberto, 1995. *Nonlinear Control Systems*, 3rd Edition, Springer-Verlag.

[8]   Kailath, T., 1980. *Linear Systems*, Prentice Hall.

[9]   Kokotović, P. V., Kanellakopoulos, I. and Morse, A. S., 1991. "Adaptive Feedback Linearization of Nonlinear Systems," pp. 347-434, and Praly, L., Bastin, G., Pomet, J. B. and Jiang, Z. P., "Adaptive Stabilization of Nonlinear Systems," pp. 311-346, Kokotović, P. V. (Ed.), in *Foundations of Adaptive Control*, Lecture Notes in Control and Informational Sciences, **160**, Thoma, M. and Wyner, A., Editors, Springer-Verlag.

[10]   Kokotović, P., Khalil, H. K. and O'Reilly, J., 1986. *Singular Perturbation Methods in Control: Analysis and Design*, Academic Press.

[11]   Krstić, M., Kanellakopoulos, I. and Kokotović, P., 1995. *Nonlinear and Adaptive Control Design*, John Wiley and Sons, Inc.

[12]   Lam, S. H., 1993. "Using CSP to Understand Complex Chemical Kinetics," *Combustion Science and Technology*, **89**, 5-6, pp. 375-404.

[13]   Lam, S. H. and Goussis, D. A., 1994. "The CSP Method for Simplifying Kinetics," *International Journal of Chemical Kinetics*, **26**, pp. 461-486.

[14]   Lam, S. H., 1997a. "Quasi-steady approximation and adaptive nonlinear control," presented in the *15th IMACS World Congress on Scientific Computation, Modeling and Applied Mathematics*, Berlin.

[15]   Lam, S. H., 1997b. "Universal Controller for Reasonable Nonlinear Systems," MAE Report 2089, Department of Mechanical and Aerospace Engineering, Princeton University.

[16]   Lane, S. H. and Stengel, R. F., 1988. "Flight Control Design Using Nonlinear Inverse Dynamics," *Automatica*, Vol. 24, **4**, pp. 471-483.

[17]   Marino, R. and Tomei, P., 1995. *Nonlinear Control Design, Geometric, Adaptive and Robust*, Prentice Hall.

[18]   O'Malley, R. E. Jr., 1991. *Singular perturbation methods for ordinary differential equations*, Applied Mathematical Sciences **89**, Springer-Verlag.

[19]   Rugh, W. J., 1996. *Linear System Theory*, 2nd Edition, Prentice Hall.

Quasi-Steady Approximation and Adaptive Nonlinear Controls[*]

S. H. Lam

Department of Mechanical and Aerospace Engineering
Princeton University, Princeton, NJ 08544 U.S.A.

Keywords: Quasi-steady approximation, Adaptive, Robust, Nonlinear, Control.

ABSTRACT

Accurate and realistic mathematical modeling is always essential for conventional computer simulations such as CFD calculations of reacting flow systems. However, if the goal is not merely to make passive "what if" predictions but rather to use the available "actuators" in the system to exert active control over the dynamical behaviors of certain measured output variables, then the problem becomes a control problem. The present paper shows that (for finite dimensional dynamical systems only) it it possible to find "control laws" to accomplish the desired control objectives without having detailed knowledge of the mathematical model— provided reliable and accurate sensor measurements of the output variables are available.

1. INTRODUCTION

Consider the following general dynamical model of an engineering system [1, 2, 3, 4]:

$$\frac{d\mathbf{x}}{dt} = \mathbf{f} + \sum_{i=1}^{I} \mathbf{b}_i u^i. \tag{1}$$

where x is a N-dimensional column vector representing the state of the system. On the right hand side, the first term $\mathbf{f}(\mathbf{x}, t)$ represents the intrinsic (*i.e.* open-loop) dynamics of the system, and the second term represents the resultant effects of I actuators which may be present in the system. Usually, I sensors measurements are assumed available. In the community of computer simulations (such as CFD), the control term is nearly always absent. The goal of computations is usually a passive one: to obtain $\mathbf{x}(t)$ based on the best open-loop model $\mathbf{f}(\mathbf{x}, t)$ available for the system. In the control community, on the other hand, the control term is of prime importance. The goal is now an active one: to find "control laws" for the I actuator control signals u^i's such that the resulting sensor measurements will honor certain user-specified constraints. Consider the following scenario: the pressure of a combustion chamber is found to have undesirable oscillations when its fuel injection rate is held constant. Control engineers would look for a fuel injection control law using pressure feedback which could suppress the oscillations, while CFD'ers would most probably perform a number of computer simulations using different fuel injection time profiles to gain "understandings." A widely accepted conventional wisdom is that detailed and accurate knowledge of the open-loop term, $\mathbf{f}(\mathbf{x}, t)$, is important in either efforts. In the present paper, we shall show that it is possible to solve the control problem *without* detailed knowledge of $\mathbf{f}(x, t)$, provided the actuators and the sensors are intelligently chosen, and that the sensor measurements are reliable and have sufficiently good signal-to-noise ratios. The methodology used to achieve this feat is "quasi-steady approximation" [5, 6, 7] a concept familiar in reduced chemistry modeling of complex reaction systems.

2. A ROBUST ADDAPTIVE CONTROLLER

We assume the system is to be controlled by a (microprocessor-based) controller which is responsible for computing and issuing the I actuator control signals $u^i(t)$'s to the system using information provided by the I sensor measurements. Each sensor signal y^i is a measurement of the state of the system:

$$y^i = \Psi^i(\mathbf{x}, t), \qquad i = 1, \ldots, I, \tag{2}$$

where the $\Psi^i(\mathbf{x}, t)$'s are assumed differentiable with respect to its arguments. If $K = N - I > 0$, we can formally introduce y^{I+k} by

$$y^{I+k} = \Psi^{I+k}(\mathbf{x}, t), \quad k = 1, \ldots, K, \tag{3}$$

so that $\mathbf{y} = \{y^1, \ldots, y^N\}$ is an alternative state vector of the system under consideration (the Jacobian of the coordinate transformation is assumed nonsingular). We call the first I elements of $\mathbf{y}$ the *output variables*, and the remaining K elements the *residual variables*.

Dynamics of the Output Variables

Differentiating y^i with respect to t, we obtain

$$\frac{dy^i}{dt} = g^i + \sum_{i'=1}^{I} B_{i'}^i u^{i'}. \tag{4}$$

where

$$g^i(\mathbf{x}, t) \;\equiv\; \frac{\partial \Psi^i}{\partial t} + \mathbf{c}^i \cdot \mathbf{f}, \tag{5}$$

$$\mathbf{c}^i(\mathbf{x}, t) \;\equiv\; \frac{\partial \Psi^i}{\partial \mathbf{x}}, \tag{6}$$

$$B_{i'}^i \;\equiv\; \mathbf{c}^i \cdot \mathbf{b}_{i'}. \tag{7}$$

Since the Ψ^i's are known to be independent of the u^i's, the g^i's are known to be independent of time derivatives of the u^i's.

In the following developments, we shall assume that $B_{i'}^i(t)$ is known since, according to (4), it can in principle be directly measured on-the-fly by the controller by pulsing the u^i's.

ODE-Based Constraints

In a control problem, the behaviors of the measured $y^i(t)$'s are of special interest to the control engineers. For example, it may be desirable (for tracking or regulation problems) to keep the y^i's below some user-specified accuracy threshold δ. Instead of such *algebraic constraints*, we propose to impose the following ODE-based constraints:

$$\Phi^i(\dot{y}^i, \phi^i, t) \equiv \frac{dy^i}{dt} + \phi^i(\mathbf{y}, t) = O(\delta), \tag{8}$$

where the $\phi(\mathbf{y}, t)$'s are $O(1)$ functions of the arguments and can be freely chosen by the users. For example, a possible choice is:

$$\phi^i(\mathbf{y}, t) = \frac{1}{\tau} \sum_{i'=1}^{I} \Lambda_{i'}^i \left(y^{i'} - \varpi^{i'} \right) \tag{9}$$

where $\tau > 0$ is a time constant, $\Lambda_{i'}^i$ is a real matrix and the *residual controls* $\varpi^i(t)$'s are allowed to depend on t and perhaps the residual variables y^{I+k}'s. For example, if we choose $\Lambda_{i'}^i$ to be positive-definite and the ϖ^i's to be zeros, then this special ODE-constraint guarantees that the y^i's are $O(\delta)$ for $t \gg \tau$.

Exact Static Control Law $u^i_\infty(\mathbf{x}, t)$

The control law $u^i = u^i_\infty(\mathbf{x}, t)$ required to precisely honor the ODE-based constraint (8) with $\delta = 0$ can readily be found as follows. Eliminating dy^i/dt between (4) and (8) with $\delta = 0$, we obtain:

$$\sum_{i'=1}^{I} B^i_{i'} u^{i'}_\infty = -(\phi^i + g^i).$$ (10)

Assuming $B^i_{i'}$ to be nonsingular, we can solve for u^i_∞ directly to obtain:

$$u^i_\infty(\mathbf{x}, t) = - \sum_{i'=1}^{I} [B^{i'}_i]^{-1}(\phi^i + g^i).$$ (11)

The use of this static control law $u^i = u^i_\infty(\mathbf{x}, t)$ as given by (11) requires detailed knowledge of the system model (specifically, the g^i's), and full state feedback, *i.e.* $\mathbf{x}(t)$ itself.

The Proposed Dynamic Universal Controller When $B^i_{i'}$ is Nonsingular

The present paper proposes the following dynamic universal control law:

$$\frac{du^i}{dt} = -\frac{1}{\Delta t} \sum_{i'=1}^{I} W^i_{i'}(u^{i'} - u^{i'}_\infty).$$ (12)

where $W^i_{i'}$ is a positive-definite real matrix, and Δt is a small time constant—both are to be user-chosen. Note that $u^i_\infty(\mathbf{x}, t)$ as given by (11) has no dependence on the u^i's or their time derivatives. In the $\Delta t << 1$ limit, the quasi-steady approximation can be applied, yielding for $t >> \Delta t$:

$$u^i = u^i_\infty(\mathbf{x}, t) + O(\Delta t).$$ (13)

Hence, if we choose $\Delta t = O(\delta)$, numerical integration of (12) will recover approximately the static control law. At this point, the use of (12) offers no advantage at all over using $u^i = u^i_\infty(\mathbf{x}, t)$ directly—other than the introduction of constraint errors.

However, (12) does offer an outstanding advantage which only becomes obvious when it is rewritten in an alternative form. By definition of the matrix inverse, we have

$$\sum_{i''=1}^{I} [B^{i''}_i]^{-1} B^{i''}_{i'} = \delta^i_{i'}$$ (14)

where $\delta^i_{i'}$ is the identify matrix. We now rewrite $W^i_{i'}$ as follows:

$$W^i_{i'} = \sum_{i''=1}^{I} W^i_{i''} \delta^{i''}_{i'}.$$ (15)

Using (15) in (12) and with the help of (14), (10) and (4), we obtain,

$$\frac{du^i}{dt} = -\frac{1}{\Delta t} \sum_{i'=1}^{I} Z^i_{i'} \left(\frac{dy^{i'}}{dt} + \phi^{i'} \right),$$ (16)

where $Z^i_{i'}$ is a nonsingular matrix:

$$Z^i_{i'} \equiv \sum_{i''=1}^{I} W^i_{i''} [B^{i'}_{I''}]^{-1}.$$ (17)

Since (16) is mathematically identical to (12) which is known to be stable in the small Δt limit, so is (16). Unlike (12), however, (16) does *not* require knowledge of $u^i_\infty(\mathbf{x}, t)$. Instead, (16) requires $B^i_{i'}(t)$, the $\dot{y}^i(t)$'s and whatever $y^n(i)$'s are needed for the evaluation of the user-chosen $\phi^i(\mathbf{y}, t)$'s, in addition to specific (but rather flexible) choices for $W^i_{i'}$ and Δt. For example, the choices $W^i_{i'} = \delta^i_{i'}$ and $\Delta t = \delta$ would do very well indeed. Certainly, the (microprocessor-based) controller is capable of numerically integrating this ODE, leaving the "real" dynamical equations of the system (1) to be integrated by the Laws of Nature. It is readily verified that together they will honor the ODE-based constraints—no explicit knowledge of $\mathbf{f}(\mathbf{x}, t)$ is needed.

3. WHEN $B^i_{i'}$ IS SINGULAR OR NEARLY SINGULAR

Many engineering systems have singular or nearly-singular $B^i_{i'}$'s. Generalizations to include such problems involves the extensive use of the concepts and tools of singular value decomposition. The singular value decomposition [8] of $B^i_{i'}$ is written as follows:

$$B^i_{i'} = \sum_{i'''=1}^{I} [U^{i'''}_i]^T \omega(i''') V^{i'''}_{i'} \tag{18}$$

where $U^{i'''}_i$ and $V^{i'''}_{i'}$ are unitary matrices and $\omega(i''') \geq 0$ are the singular values ordered in descending magnitudes. The number of non-zero singular values is by definition the traditional rank of $B^i_{i'}$. Consider now the case when $J > 0$ of the smallest singular values of $B^i_{i'}$ are $O(\epsilon)$ where ϵ is either precisely zero or is a "sufficiently small" number. The *epsilon-rank* of $B^i_{i'}$ is defined as the number of above threshold singular values. *i.e.* $I - J$. Because $U^i_{i'}$ is a unitary matrix, we have:

$$\sum_{i=1}^{I} U^{I+1-j}_i B^i_{i'} = \omega(I+1-j) V^{I+1-j}_{i'} = O(\epsilon), \qquad j = 1, \ldots, J. \tag{19}$$

The U^{I+1-j}_i's, which are the bottom J rows of $U^i_{i'}$ and play a major of role in the subsequent development, are called the *left epsilon-vectors* of $B^i_{i'}$.

In order for the control problem to have a solution, J additional *derived output variables* y^{I+j}'s must be found, and the resulting extended $M \times I$ rectangular matrix B^m_i (where $M = I + J$) must have full epsilon-rank. For the sake of simplicity, we limit our theoretical developments to the following special ODE-based constraints for the M output variables:

$$\Phi^m = \frac{dy^m}{dt} + \frac{1}{\tau} \sum_{m'=1}^{M} \Omega^m_{m'} (y^{m'} - \varpi^{m'}) = O(\delta), \qquad m = 1, \ldots, M. \tag{20}$$

where τ, $\Omega^m_{m'}$ and the ϖ^m are parameters analogously defined as previously in (9). Unlike the previous case, however, there are certain restrictions on $\Omega^m_{m'}$ and the ϖ^m's as we shall see presently.

Only the theoretical results for the case $J = 1$ (and thus $M = I + 1$) are presented here. For details of the derivations, see [5]. The sole newly promoted y^M is:

$$y^M = \Psi^M(\mathbf{x}, t; \epsilon) \equiv \sum_{i=1}^{I} U^I_i \left(\frac{dy^i}{dt} + \frac{1}{\tau} \sum_{i'=1}^{M} \Omega^i_{i'} y^{i'} \right) \tag{21}$$

which can be rewritten in the following more elegant form:

$$\sum_{i=1}^{I} U^I_i \Phi^i = 0, \tag{22}$$

provided

$$\Omega_M^i = -\tau [U_i^I]^T, \qquad i = 1, \ldots I, \tag{23}$$

and that the ϖ^i's satisfy

$$\sum_{i,i'=1}^{I} U_i^I \Omega_{ii'}^i \varpi^{i'} = 0. \tag{24}$$

Except for (23), all remaining elements of $\Omega_{ii'}^i$ are completely free to be chosen. Note that $y^M(t)$ is expressed completely in terms of the I primary sensor signals y^i's. Note that whenever $\epsilon \neq 0$, $\Psi^M(\mathbf{x}, t; \epsilon)$ has an $O(\epsilon)$ dependence on the u^i's.

Differentiating (21) with respect to time, the ODE for y^M can be derived with the help of (1). We assume that the resulting $M \times I$ real matrix $B_i^m(t)$ has full epsilon rank and is known to the controller. Its singular value decomposition can be computed. The epsilon-inverse of B_i^m is denoted by $[B_i^m]^+$ and is given by:

$$[B_i^m]^+ \equiv \sum_{i'=1}^{I} [\check{V}_i^{i'}]^T \frac{1}{\check{\omega}(i')} \check{U}_m^{i'}. \tag{25}$$

where $\check{U}_m^i$, $\check{V}_{i'}^i$ and $\check{\omega}(i) > \epsilon$ are the corresponding unitary matrices and singular values of B_i^m. If we pad the row vector U_i^I (the left epsilon-vector of $B_{i'}^i$) with a trailing zero, the resulting row vector (to be denoted by $\check{U}_m^M$) is automatically qualified to be a left epsilon-vector of B_i^m, and is expected to be a good approximation to the true left null-vector of B_i^m, $\check{U}_m^M$, since $\epsilon << 1$.

The proposed universal dynamic control law is:

$$\frac{du^i}{dt} = -\frac{1}{\Delta t} \sum_{m=1}^{M} \check{Z}_m^i \left(\frac{dy^m}{dt} + \frac{1}{\tau} \sum_{m'=1}^{M} \Omega_{mm'}^m (y^{m'} - \varpi^{m'}) \right) \tag{26}$$

where

$$\check{Z}_m^i \equiv \sum_{i'=1}^{I} W_{i'}^i [B_{i'}^m]^+ \tag{27}$$

and $\Delta t > 0$ and $W_{i'}^i$ have the same physical meanings as before.

If the original $B_{i'}^i$ is strictly singular (*i.e.* $\epsilon = 0$), it is straightforward to show that in the limit of $\Delta t \to 0$ the quasi-approximation can be applied to (26), and the dynamics of the resulting output variables will indeed honor the ODE-based constraints for $t >> \Delta t$. However, if the original $B_{i'}^i$ is nearly-singular (*i.e.* $\epsilon \neq 0$), then depending on the sign of ϵ, a lower limit may need to be imposed on the value of Δt. This is because when dy^M/dt on the right hand side of (26) is eliminated by using its own dynamical equation, the g^M term contains an $O(\epsilon)$ contribution involving du^i/dt. Stability consideration of (26) then requires that $\Delta t >> |\epsilon|$ whenever the sign of ϵ is uncertain. Pragmatically speaking, the controller is most likely to use Euler's method to numerically integrate (26). Consequently, a lower bound for the accuracy threshold for ODE-constraints must always be respected whenever ϵ is not precisely zero—when the original $B_{i'}^i$ is nearly-singular.

5. DISCUSSIONS

The present theory requires that reliable sensor signals with sufficiently good signal-to-noise ratios are available. It strongly prefers to directly measure the time derivatives of the output variables instead of getting them by numerical differentiation. In addition, the impulse-response matrix $B_i^m(t)$ is assumed available. If the choice and design of the actuators are at the disposal of the control engineers, a time-invariant and nonsingular $B_{i'}^i$ would be preferred. The option of direct measurements of $B_i^m(t)$ on-the-fly by pulsing the u^i's is assumed available.

4. AN EXAMPLE

Consider the $N = 3$, $I = 1$ case with

$$\mathbf{f} = \begin{vmatrix} f_1(x_1, x_2, x_3, t) \\ f_2(x_1, x_2, x_3, t) \\ f_3(x_1, x_2, x_3, t) \end{vmatrix}, \qquad \mathbf{b}_1 = \begin{vmatrix} \epsilon \\ 1 \\ 0 \end{vmatrix}, \qquad y_1 = x_1. \tag{28}$$

All superscripts have been moved to become subscripts to avoid confusion with exponents. We assume that $\partial f_1 / \partial x_2$ is of $O(1)$ and is never zero, while ϵ is a small parameter of uncertain sign. We have $B_{1,1} = \epsilon$ and the problem is either singular or nearly-singular. For the ODE-based constraints, we choose, in accordance to (23),

$$\Omega_{m,m'} = \tau \begin{vmatrix} 1/\tau_1 & -1/\tau \\ 0 & 1/\tau_2 \end{vmatrix} \tag{29}$$

where τ_1 and τ_2 are positive free parameters. We require $\varpi_1 = 0$ in accordance to (24). The new derived output variable is simply $y_2 = dy_1/dt + y_1/\tau_1$. The dynamical equation for y_2 can readily be derived and expressed in the form of (4). We have $g_2 = \partial f_1/\partial t + f_1 \partial f_1/\partial x_1 + f_2 \partial f_1/\partial x_2 + f_3 \partial f_1/\partial x_3 + \epsilon du_1/dt$, and the new entry to the impulse-response matrix is $B_{2,1}(t) = \partial f_1/\partial x_2 + \epsilon(\partial f_1/\partial x_1 + 1/\tau_1)$. The universal dynamic control law is:

$$\frac{du_1}{dt} = -\frac{1}{\Delta t} \left(\frac{B_{2,1}}{\epsilon^2 + B_{2,1}^2} \right) \left(\frac{dy_2}{dt} + \frac{1}{\tau_2}(y_2 - \varpi_2) \right). \tag{30}$$

where $\varpi_2(x_3, t)$ is available to exert some influence on $x_3(t)$.

If $\epsilon = 0$ precisely, (30) can accept asymptotically small values for Δt and remain stable. However, if $\epsilon \neq 0$, then the $\epsilon du_1/dt$ term implicit in dy_2/dt through g_2 can compete with the du_1/dt term on the left hand side. If ϵ is negative, a lower bound $\Delta t > |\epsilon|$ must be imposed. The readers can easily verify using desktop computers that (30) indeed solves the control problem provided $B_{2,1}(t)$ is $O(1)$ and is provided to the controller, and that the lower bound $\Delta t > |\epsilon|$ is respected.

References

[1] Ioannou, P. A. and Sun, J., *Robust Adaptive Control*, Prentice Hall, 1996.

[2] Marino, R. and Tomei, P., *Nonlinear Control Design, Geometric, Adaptive and Robust*, Prentice Hall, 1995.

[3] Isidori, Alberto, *Nonlinear Control Systems*, 3rd Edition, Springer-Verlag, 1995.

[4] Krstić, M., Kanellakopoulos, I. and Kokotović, P., *Nonlinear and Adaptive Control Design*, John Wiley and Sons, Inc. 1995.

[5] S. H. Lam, "Universal Controller for Reasonable Non-Linear Systems," MAE Report 2089, Department of Mechanical and Aerospace Engineering, Princeton University, April, 1997.

[6] S. H. Lam, "Using CSP to Understand Complex Chemical Kinetics," *Combustion Science and Technology*, **89**, 5-6, pp. 375-404, 1993.

[7] S. H. Lam and D. A. Goussis, "The CSP Method for Simplifying Kinetics," *International Journal of Chemical Kinetics*, **26**, pp. 461-486, 1994.

[8] Golub, G. H. and Van Loan C. F., *Matrix Computations*, Second Edition, The Johns Hopkins University Press, 1989.

APPENDIX A

An Experimental Study of Supersonic
Laminar Reacting Boundary Layers

Joseph Fielding
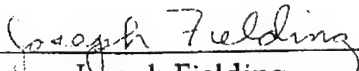
A DISSERTATION
PRESENTED TO THE FACULTY
OF PRINCETON UNIVERSITY
IN CANDIDACY FOR THE DEGREE
OF MASTER OF SCIENCE IN ENGINEERING

RECOMMENDED FOR ACCEPTANCE
BY THE DEPARTMENT OF
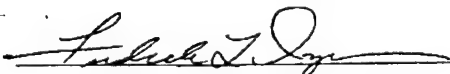MECHANICAL AND AEROSPACE ENGINEERING

JANUARY 1997

An Experimental Study of Supersonic Laminar Reacting Boundary Layers

Prepared by:

Joseph Fielding

Joseph Fielding

Approved by:

Professor Frederick L. Dryer
Thesis Advisor

Professor Alexander J. Smits
Thesis Reader

Abstract

A pilot-scale supersonic combustion tunnel was designed and constructed to operate with initial stagnation temperatures up to 840 K and static pressure/stagnation temperatures of 0.01-0.07 atm/300-840 K in the test section. Vitiation of the nitrogen/oxygen gas supply by burning hydrogen in the upstream settling chamber extended the effective stagnation temperatures to 1100 K. The facility was instrumented with a schlieren/shadowgraph system and ultraviolet-intensified imaging of chemiluminescence from excited hydroxyl radicals (OH^*) to study the initiation and combustion properties of nitrogen-diluted hydrogen/oxygen mixtures at Mach 3.0 over flat plate and wedge-type center bodies. Reaction initiation by thermal recovery from viscous heating in laminar boundary layers on non-catalytic and catalytic surfaces as well as through seeding of the flow with radicals was investigated.

Flat plate experiments at stagnation temperatures of 920 K and a static pressure of 0.6 atmospheres show no conclusive evidence to support the effectiveness of platinum catalytic action at the surface for enhancing reaction initiation. Reaction initiation was achieved by seeding the flow with radicals produced by hydrogen/oxygen reaction chemistry in the subsonic nozzle inlet, followed by subsequent reaction quenching in the nozzle throat. Employing a wedge geometry and increased stagnation temperatures (to 1070 K), chemiluminescence was observed downstream of the oblique shocks generated by the wedge leading edge.

Qualitative zero and one-dimensional kinetic modeling of the hydrogen-oxygen reaction under the conditions of these experiments showed that the majority of the chemical energy potential present in the initial reactants resides in the flow as dissociated species rather than as sensible enthalpy changes once the reaction process is initiated. Results suggested that reaction heat release and

the attendant density changes on mixing are strongly coupled with the reaction conditions.

Operating regimes within the pressure-temperature plane were examined using a Damköhler number analysis, with convective characteristic times defined using the supersonic free stream velocity, and chemical times characterized by the maximum rate of reactant consumption. The analysis points toward two regimes separated by a critical pressure. Below this pressure, chemical times are dominated by branching rates, and reactants are consumed with little exoergic coupling from slow recombination of intermediate radical species. Essentially, chemical enthalpy resides in heat of formation terms associated with high radical concentrations. Above some critical pressure, reactant conversion produces much lower radical product concentrations, and the chemical energy conversion appears primarily as sensible enthalpy. The locally coupled temperature increase leads to thermally accelerated kinetics and much shorter chemical times.

Acknowledgments

Finally, I extend my love and deepest gratitude to Melissa Pecullan for making my time here at Princeton very special. It is through her compassion, companionship, and proofreading that this thesis was possible.

Table of Contents

List of Tables

List of Figures

x

Chapter 1. Introduction

1.1 Motivation for Research

Supersonic combustion has received considerable attention in recent years for application to air-breathing propulsions systems at hypersonic flight speeds. The United States' National Aerospace Plane (NASP) and High Speed Civil Transport (HSCT) as well as similar projects in Europe and Japan have stimulated renewed interest in hypersonic aerodynamics and propulsion. These second-generation space transportation systems propose staged propulsion for the wide range of flight speeds that will be encountered in earth-to-orbit operation.(Billig, 1991) Increased intake air recovery temperatures associated with flight in the hypersonic range (beyond Mach 6) point to utilizing thermal self-ignition of fuels in supersonic ramjet combustors. Improved understanding of chemical kinetics, heat transfer, and mixing processes in high speed flows is critical to successful implementation and optimization of the engine design.

The increased ability to predict and model complex fluid dynamics of chemically reactive flows using numerical techniques is essential to the design process. In the case of hypersonic flight technology, it is often either impractical or impossible to reproduce the anticipated flight conditions experimentally due to the limitations of existing facilities. Beyond Mach 8, restrictions of air supply and generation of extreme temperatures limit the reproduction of flight conditions to short-duration pulse facilities.(Dunn et al., 1991)

For this reason, the use of computers is vital for prediction of the engine flow field characteristics and handling complicated geometries of airframe designs. Computational fluid dynamics (CFD) has seen major breakthroughs thanks to ever-increasing computing power, speed, storage, and improved

1

algorithms; but there is an imperative for benchmark experiments investigating various aspects of these high speed flows to provide a primary database with which to test and validate the numerical modeling efforts over a wide range of parameters.

Simplified conditions are required in these experiments to decrease the associated modeling complexity of the system. Laminar flow is attractive from a numerical modeling standpoint because the coupling of turbulence and chemistry complicates the validation process. A two-dimensional, reacting, supersonic laminar flow is a system which can be realistically studied in an experimental setting.

This thesis recounts the design and implementation of a pilot-scale, two-dimensional, laminar, high enthalpy, supersonic wind tunnel for combustion studies of high speed reacting flows. The Mach 3 facility (2.54 cm x 2.54 cm test-section) was designed and constructed, and initial combustion experiments were performed using nitrogen diluted hydrogen-oxygen mixtures. This work was directed toward developing and analyzing methods for achieving localized, controlled ignition and heat release within a supersonic reacting flow. Specifically, the issue of igniting hydrogen-oxygen-nitrogen mixtures in a supersonic laminar boundary layer was addressed. Reaction initiation from viscous heating on non-catalytic and catalytic surfaces as well as through seeding of the flow with radicals was investigated.

Hydrogen was chosen for these studies because it is frequently considered the fuel of choice for supersonic combustion applications.(Billig, 1991) Furthermore, the $H_2 - O_2$ chemistry was studied in a variety of experimental systems over a wide range of conditions, and research on this kinetic system here at Princeton has been extensive.(Yetter, et al., 1991; Kim, 1994; Mueller, 1996) Here, we have also speculated that the unique explosion limit behavior of the hydrogen-oxygen system provides an innovative means of potentially igniting reactive pre-mixed $H_2 - O_2 - N_2$ mixtures in a supersonic stream; this speculation is discussed in greater detail at the end of this chapter.

2

Much of the work supports that under some range of operating parameters, the speculation can be experimentally established.

In addition to providing useful information for CFD code testing and validation, this work also provided data to assist in operational design for a larger Mach 3 combustion tunnel under construction within the Gas Dynamics Laboratory at the Princeton James Forrestal Campus. Experiments of this type in the Forrestal facility will require larger expenditures of resources for a single run. The cross-sectional area of the test section will be increased, necessitating higher mass flow rates. As a consequence, power requirements for heating of the various streams will also increase proportionally. Another significant factor is the time required to modify the physical configuration of the tunnel system.

The large-scale experiments involved prohibit changes to models inserted inside the test section and placement of probes, fuel injectors, and gas supply plumbing. Such modifications to the pilot-scale facility described in this report require significantly less investment of time and labor, making it the ideal test facility in which to investigate parametric issues.

1.2 Applications: Air-Breathing Propulsion

Interest in air-breathing propulsion for utilization in space plane and hypersonic transport systems has caused researchers and combustion engineers both in the U.S. and abroad to critically evaluate the current state of ramjet and scramjet technologies. Engines will have to operate over a wide range of inlet air temperatures and pressures depending on the altitude and flight Mach number. Also, airframe geometries and engine placement will have significant impact on the velocity distribution at the engine inlet. Understanding the characteristics of fuel-related processes such as injection, mixing, ignition, and combustion is critical for successful implementation of air-breathing technology at hypersonic flight speeds.

The variation of pressure and temperature with geometric altitude for the U.S. Standard Atmosphere is shown in Figure 1.1. Consider a hypothetical aircraft operating at an altitude of 25 km at supersonic flight Mach numbers. From the figure, the inlet condition of the air would be $T = 217$ K and $P = 2.5$ kPa (0.025 atm). These values represent the static flow conditions at the operating Mach number of the vehicle. Assuming that the fluid behaves as an ideal gas (a poor assumption when dissociation temperatures are reached), the corresponding stagnation conditions are plotted in Figure 1.2 for a range of flight Mach numbers. The significance of this exercise becomes apparent when it is noted that beyond $M_\infty = 4$, temperatures are high enough in the engine for potential thermal self-ignition of fuel-air mixtures. Studies of supersonic combustion have not previously attempted to investigate these more realistic static pressures which will be encountered, further emphasizing the need for research such as described in this thesis.

Environmental issues pose additional incentives for greater understanding of the aerothermochemistry underlying high speed propulsion concepts. HSCT fleets will operate in the upper portion of the stratosphere (~20 km), closer to the ozone layer than subsonic commercial aircraft; and they will burn more fuel per seat-mile.(Aeronautics and Space Engineering Board, 1992) Nitric oxide (NO_x) emissions at this altitude should have greater impact on ozone depletion than lower flying craft, so stricter emissions standards have been set for allowable engine exhaust levels. Minimization of noise pollution at all altitudes, and imperceptible sonic boom effects over land are also key issues.

Ramjet / Scramjet Operation

A typical ramjet generates thrust by injecting fuel into a combustion zone where the incoming air has been compressed through a supersonic diffuser. Flame stabilization is usually supplied by means of a mechanical flameholder,

4

and the hot, high-pressure product gases are expanded through the exhaust nozzle. The ideal operating cycle is shown on the p-v diagram in Figure 1.3.

Flame-holding utilizing bluff-body stabilization requires establishing a local subsonic region in the recirculation zone behind the flameholder. In this zone, intense mixing with continual addition of fresh unburned fuel and oxidizer from upstream maintains the reaction. Hot combustion products leaving the recirculation zone promote ignition of the main flow.(Cheng et al., 1959)

Zukowski and Marble (1956) proposed that for subsonic flame stabilization using bluff-bodies, the stabilization criteria should be described by a form of Damköhler's first number:

$$Da = \frac{U \dfrac{k}{\rho \, c_p}}{L \, S_L{}^2}$$

where U is the velocity of the flow past the recirculation zone, L is the length of the zone, S_L is the laminar flame speed of the fuel, and $k/\rho \, c_p$ is the thermal diffusivity. Flame stabilization using recirculation zones was studied by Williams et al. (1947) for high-speed subsonic gas streams and by Nicholson and Field (1949) for subsonic and supersonic flame-holders. Winterfeld (1991) performed stabilization experiments of hydrogen-air flames in supersonic free jets up to Mach 2.1 using a variety of cylindrical flame-holder sizes to validate the above criterion and apply it to flame-holder design. These studies showed that proper sizing of the flame-holder combined with appropriate hydrogen-air equivalence ratios promote flame stabilization in the wake.

Enlarging recirculation zones in ramjet combustors becomes impractical because of the large loss of total pressure which results.(Niioka, et al., 1995) Ramjets have several additional disadvantages:

- Slowing the incoming air from supersonic to subsonic speeds for combustion is never isentropic as shown in Figure 1.3. Typically, a finite

5

number of oblique shocks are generated at the engine inlet, and this also entails a pressure loss and consequent decrease in engine efficiency.

- In order to obtain compression in the combustor, the ramjet must already be in motion; therefore, a separate propulsion system is necessary for starting the vehicle from $M_\infty = 0$.

- The thrust specific fuel consumption (TSFC) of ramjets is very high at subsonic speeds, compared with conventional turbojets which are more fuel-efficient up to flight Mach numbers around 3.(Anderson, 1989)

At higher Mach numbers, however, extreme temperatures at the turbine blades in a turbojet create severe material limitations, a problem from which the ramjet does not suffer since there is no turbine. For Mach numbers in the hypersonic regime (generally considered to start around $M_\infty = 6$), the ramjet begins to encounter the same temperature-related material difficulties associated with turbojet operation at supersonic speeds.

The supersonic combustion ramjet (scramjet) handles this problem by decelerating the flow in the diffuser only enough to achieve pressure conditions favorable for combustion. In this situation, flow inside the combustor remains supersonic, fuel is added and combustion occurs. Because the kinetic energy of the flow represents a significant amount of its overall energy, the combustion process may be altered.(Law, 1992) Scramjet engine efficiencies become competitive with those of ramjets above Mach numbers of about 6. (Swithenbank, 1992) The present work contributes new insights on these alterations and constraints on appropriate combustion pressure.

1.3 Supersonic Combustion

Supersonic combustion implies a chemically reacting flow moving at velocities higher than the speed of sound determined by the local thermodynamic conditions. The critical factors addressed in the research of supersonic combustion phenomena typically focus on the techniques used for

6

achieving effective fuel-air mixing, ignition of the mixture, subsequent flame stabilization, as well as selection of the correct fuels. A broad review of research in supersonic combustion by Billig (1993) remarks that the technical areas noted above need to be further addressed for optimal scramjet design.

Early work on supersonic wake combustion was performed by Baker et al., and Scanland and Hebrank (Strahle, 1968), but no measurements were made to determine whether regions of the flame zone were supersonic.(Billig, 1993) The first measurements of this kind were performed by Dorsch et al., using aluminum borohydride, a pyrophoric fuel, injected into an airstream over a flat plate in a Mach 2.46 tunnel.(Fletcher, 1967) Mach numbers calculated from experimental static and pitot pressures indicated that the flow at the interface of the hot gas and the cold free stream was in the sonic and lower supersonic regime, although most of the flame zone was subsonic.

Slutsky et al. (1965) incorporated a pilot flame as an ignition source in a premixed turbulent hydrogen-air supersonic free jet. They studied the effects of thermally controlled combustion in a reactive stream far below autoignition limits. Pilot flames were shown to eliminate the need for flame-holders in the stream, although an additional supply of oxygen was required to maintain the pilot. Ignition of turbulent hydrogen-air mixtures was achieved at Mach 1.47 using this technique.

At higher Mach numbers, air recovery temperatures are sufficient to promote self-ignition of certain fuels. Ignition of fuel-air mixtures through viscous dissipation heating in supersonic boundary layers has potential for use in stabilizing flames in high-speed streams, without the need for large flame-holding geometries. The boundary layer ignition issue has been addressed both asymptotically and numerically for supersonic boundary layers by Im et al. (1993). In that work, explicit expressions are derived for minimum ignition distance along isothermal and adiabatic walls, with ignition defined as the location of thermal runaway in the temperature profile. These studies establish

theoretical viability of the boundary layer ignition concept, but lack empirical data with which to compare their results.

Experimental work in this area is noticeably absent, due to the complex and often dangerous conditions under which a facility must operate to achieve reaction. Much of the numerical modeling work poses and solves problems which are unrealistic for reproduction in an experimental environment. For example, Figueira da Silva et al. (1993) present a boundary layer ignition solution for a premixed stoichiometric H_2-air stream with $M = 4$, $P_\infty = 1$ atm, and $T_\infty = 400$ K. At these conditions, the required pre-mixed stagnation conditions would be $P_0 = 152$ atmospheres and $T_0 = 1680$ K. Experimental reproduction of these conditions for model validation purposes would be extremely difficult.

This experimental effort focused on a technique which would avoid the need for unrealistic settling chamber conditions which preclude premixing fuel-oxidizer mixtures. The concept is based upon the structure of the hydrogen-oxygen explosion limits which are described below.

1.4 Hydrogen - Oxygen Explosion Limits

Explosion limits of combustible mixtures are essentially mappings of the pressure and temperature conditions that separate regions of slow and explosively fast reaction for a particular equivalence ratio. For the H_2 - O_2 system, three different explosion limits were identified between 600 K and 800 K in static reactor work by Lewis and von Elbe (1987). These "classical" explosion limits are shown in Figure 1.4 for a stoichiometric H_2 - O_2 mixture.

The first limit is observed at pressures on the order of a few torr, and is a result of radical deactivation due to collision with the walls of the vessel. At these low pressures, diffusive transport of radicals to walls can dominate over the gas phase collisional rate, effectively terminating the reaction. As expected, the first limit is a sensitive function of the vessel's surface area to volume ratio, as well as the nature of the surface itself.

8

When the pressure is increased above the first explosion limit, gas phase production of radicals exceeds their rate of destruction at the wall, and the system becomes explosively fast. Within this region, the following reactions characterize the system:

$$H + O_2 = OH + O \qquad\qquad (1)$$
$$O + H_2 = H + OH \qquad\qquad (2)$$
$$OH + H_2 = H + H_2O \qquad\qquad (3)$$

The reaction numbers correspond to the mechanism given in Table 1.1 which has been adapted from the $CO-H_2-O_2$ mechanism used by Kim (1994). Reactions 1 and 2 are chain branching involving radical attack on the reactants. The OH generated is able to react with H_2 forming water and another hydrogen atom through the propagating reaction 3. This sequence of reactions is overall chain branched and self-sustaining.

The classical explanation of the second explosion limit is described as a competition between reaction 1 and the third-order reaction

$$H + O_2 + M = HO_2 + M \qquad\qquad (9)$$

Reaction 9 produces the relatively unreactive hydroperoxy radical HO_2, and the reaction may be considered chain terminating if HO_2 is able to diffuse to the walls, thus removing H radicals from the system. Because reaction 9 is termolecular, it is pressure sensitive, and at higher pressures it becomes increasingly competitive with reaction 1 giving rise to the second explosion limit. This limit is largely independent of the vessel geometry, and is described by an expression derived from steady-state, $[M] = 2\, k_1/k_9$, where $[M]$ is the concentration of all possible collisional partners in reaction 9 modified by their third-body or chaperone efficiencies. (Lewis and von Elbe, 1987)

As pressure is further increased in the system, HO_2 concentrations can increase via reaction 9 and enhance production of hydrogen peroxide H_2O_2 through

$$H_2 + HO_2 = H_2O_2 + H \qquad\qquad (17R)$$
$$HO_2 + HO_2 = H_2O_2 + O_2 \qquad\qquad (14).$$

9

This in turn can increase the decomposition of H_2O_2 by the reaction

$$H_2O_2 + M = 2\,OH + M \tag{15}$$

and reaction 9 then becomes chain propagating rather than terminating. While this is used as a partial explanation of the third explosion limit, isothermal calculations by Maas and Warnatz (1988) showed no sudden change in the overall reaction rate at the third limit. In this region, self-heating effects must be taken into account as reported by Kordylewski and Scott (1984), and the reaction is considered to be combined thermal/chain explosive.

There is an additional boundary in the hydrogen-oxygen system, examined in numerical studies by Yetter et al. (1991), which delineates a transition in the chemical kinetic behavior. This boundary, referred to as the extended second limit shown in Figure 1.4, separates the regions where the system is chain explosive (below), and where it is thermal/chain explosive (above). Between the third and extended second limits, the overall reaction is nearly straight chain. Branching occurs almost entirely through the sequence

$$HO_2 + H_2 \rightarrow H_2O_2 + H \rightarrow OH + OH + H$$
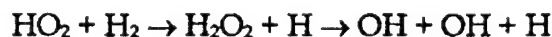
which is slow relative to other chain propagating steps. Furthermore, in comparison to a chemically branched case, production of critical intermediate concentrations of species (eg. H_2O_2) introduces an induction time character that is much longer than that associated with producing a critical radical concentration of H atoms.

1.5   Principle of Operation for a Laminar Supersonic Combustion Facility

The hydrogen-oxygen explosion limits are quite unique and present an interesting opportunity for testing in a supersonic combustion tunnel. In Figure 1.5, a point between the second and third limits in the non-explosive regime is used to represent initial conditions in the settling chamber of a supersonic wind tunnel. Isentropic expansion to Mach 3 and subsequent recovery in a boundary layer at near-constant pressure assuming an adiabatic wall thermal recovery

factor of about 0.85 (Schlichting, 1960) puts the system inside the second explosion limit. Transferring this concept to an *h-s* coordinate (frequently called a Mollier diagram) and using the classical explosion limits as stagnation conditions, a line can be drawn showing the static conditions at Mach 3, as shown in Figure 1.6.

Maintaining laminar flow conditions is desirable for several reasons. Numerical modeling for laminar flows is less computationally intensive because it eliminates the fluctuation of velocities, concentrations, and other variables. Turbulent transport and its interaction with a chemically reacting system often makes modeling problems intractable. At subsonic speeds, transition occurs along a flat plate at a distance x from the leading edge, determined by $Re_{x,crit} \approx 3.5 \times 10^5$ to 10^6.(Schlichting, 1960) This may be used as a guideline for supersonic speeds at moderate Mach number ($M \leq 3$). Experimentally, a low Reynolds number will increase the critical distance at which a boundary layer will transition from laminar to turbulent conditions.

This approach requires test section static pressures which are very low (0.01-0.07 atm), a concept which focused the present work on these conditions. The effects of pressure on kinetics in high speed reacting streams is discussed by Yetter et al. (1992). Most combustion studies in supersonic wind tunnels to date have employed static pressures on the order of one atmosphere. This research effort was directed towards the construction of a wind tunnel facility to exploit the operating principle detailed in the figure. Experiments used temperature recovery through viscous heating in the boundary layer formed over a test model to move hydrogen-oxygen-nitrogen mixtures into the explosive region. The proposed operating conditions are similar to those which would be experienced in a supersonic combustion based air-breathing engine, further emphasizing the critical nature of this research.

11

1.6 Organization of Thesis

Chapter 2 presents a description of the pilot-scale Supersonic Combustion Facility. Considerable effort was made to provide a complete profile of the experimental apparatus and diagnostic tools used throughout this research effort. Results and observations are presented in Chapter 3 for investigation of the ignition and combustion characteristics of nitrogen diluted hydrogen-oxygen mixtures using various configurations and a range of conditions. Chapter 4 details the analysis of these experiments, numerical modeling performed to supplement the effort, including zero and quasi one-dimensional reacting flow calculations. Chapter 5 presents a summary and conclusions drawn from this research.

Table 1.1: H_2–O_2 Reaction Mechanism (Kim, 1994)

Units are cm^3 - mole - sec - kcal - K

$k = A\ T^n\ exp(-E_a/RT)$

	H_2 - O_2 Chain reactions	ΔH^0_{298}	$\log(A_f)$	n_f	$E_{a,f}$	Temp Range (K)
1.	$H + O_2 = O + OH$	16.77	14.28	0.00	16.44	962 - 2577
2.	$O + H_2 = H + OH$	1.85	4.71	2.67	6.29	297 - 2495
3.	$H_2 + OH = H_2O + O$	-15.01	8.33	1.51	3.43	250 - 2581
4.	$O + H_2O = OH + OH$	16.88	6.47	2.02	13.4	800 - 2000
	H_2 - O_2 Dissociation/Recombination reactions					
5.	$H_2 + M = H + H + M$	104.2	19.66	-1.40	104.38	600 - 2000
6.	$O + O + M = O_2 + M$	-119.1	15.79	-0.50	0.00	2000 - 10000
7.	$O + H + M = OH + M$	-102.3	18.67	-1.0	0.00	
8.	$H + OH + M = H_2O + M$	-119.2	22.35	-2.00	0.00	1000 - 3000
	Formation and Consumption of HO_2					
9.	$H + O_2 + M = HO_2 + M$	-49.1	$k_0 = 6.70 \times 10^{19}\ T^{-1.42}$			200 - 2000
			$k_\infty = 4.517 \times 10^{13}$			
10.	$HO_2 + H = H_2 + O_2$	-55.1	13.82	0.00	2.13	298 - 773
11.	$HO_2 + H = OH + OH$	-36.47	14.23	0.0	0.87	298 - 773
12.	$HO_2 + O = OH + O_2$	-52.23	13.24	0.00	-0.40	200 - 400
13.	$HO_2 + OH = H_2O + O_2$	-70.11	16.28	-1.00	0.00	250 - 1050
	Formation and Consumption of H_2O_2					
14.	$HO_2 + HO_2 = H_2O_2 + O_2$	-38.53	$k = 4.2 \times 10^{14}\ exp(-11.98/RT)$			300 - 1100
			$+ 1.3 \times 10^{11}\ exp(1.629/RT)$			
15.	$H_2O_2 + M = OH + OH + M$	-51.14	$k_0 = 1.2 \times 10^{17}\ exp(-45.5/RT)$			200 - 1500
			$k_\infty = 2.95 \times 10^{14}\ exp(-48.4/RT)$			
16.	$H_2O_2 + H = H_2O + OH$	-68.05	13.00	0.0	3.59	283 - 800
17.	$H_2O_2 + H = H_2 + HO_2$	-16.57	13.68	0.00	7.95	283 - 800
18.	$H_2O_2 + O = OH + HO_2$	-14.7	6.98	2.00	3.97	283 - 800
19.	$H_2O_2 + OH = H_2O + HO_2$	-31.58	$k = 1 \times 10^{12}$			283 - 1250
			$+ 5.8 \times 10^{14}\ exp(-9.56/RT)$			

Chaperone efficiencies:

$\varepsilon_{N_2} = 1$, $\varepsilon_{H_2} = 2.5$, $\varepsilon_{H_2O} = 12$
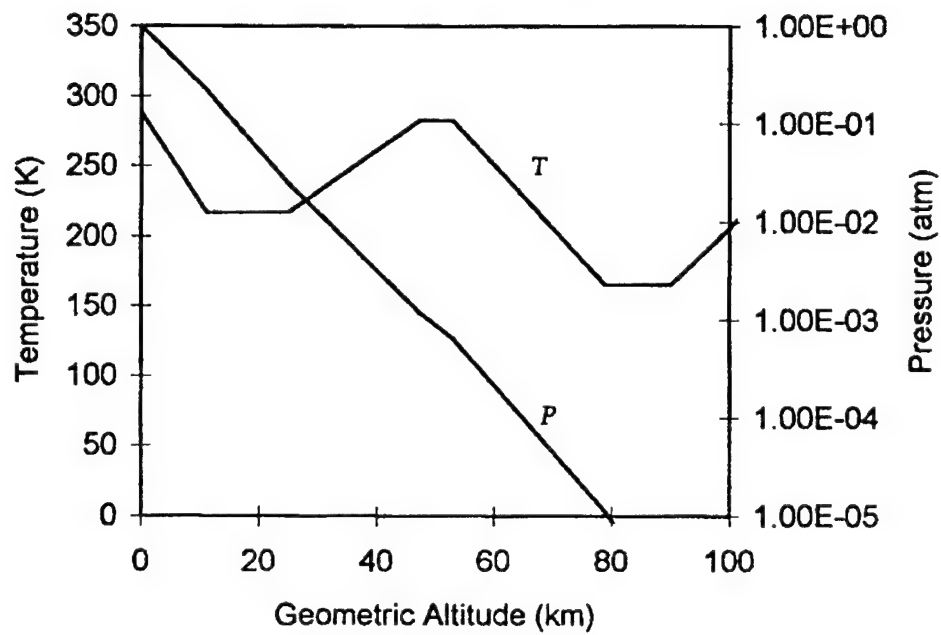
Figure 1.1: Pressure and temperature of the U.S. Standard Atmosphere (ARDC 1959) according to geometric altitude.
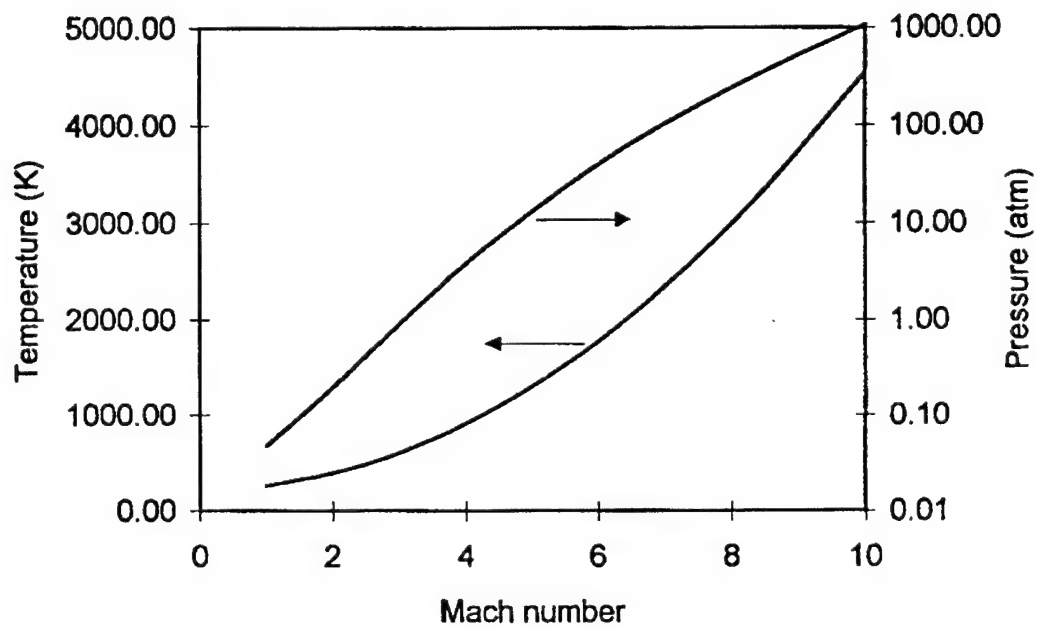
Figure 1.2: Stagnation pressure and conditions for varying flight Mach number at a cruise altitude of 25 km.
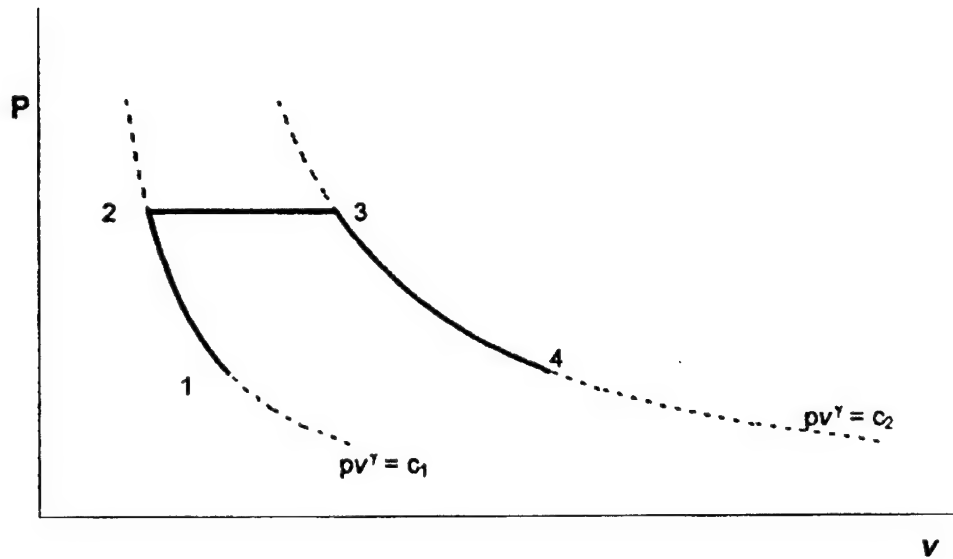
Figure 1.3: Ideal operating cycle for a ramjet on a pressure-specific volume diagram. The points represent: 1) Inlet air, 2) Combustor inlet, 3) Combustor exit, 4) Exhaust exit. Processes 1-2 and 3-4 lie along different isentropes, and 2-3 is a constant-pressure expansion.
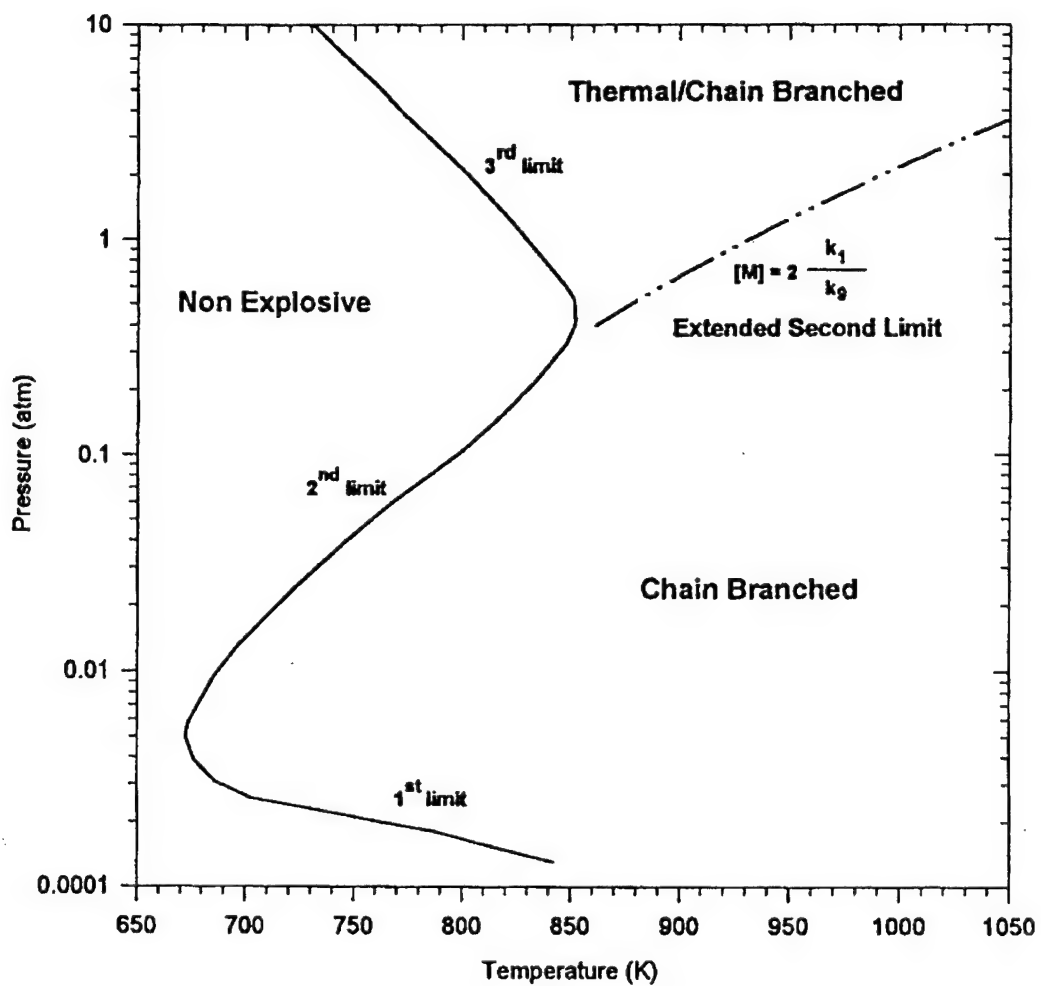
Figure 1.4: Classical explosion limits for the stoichiometric hydrogen-oxygen system. The extended second limit which delineates a transition between chain branched and mixed thermal/chain branched chemistry is also shown.
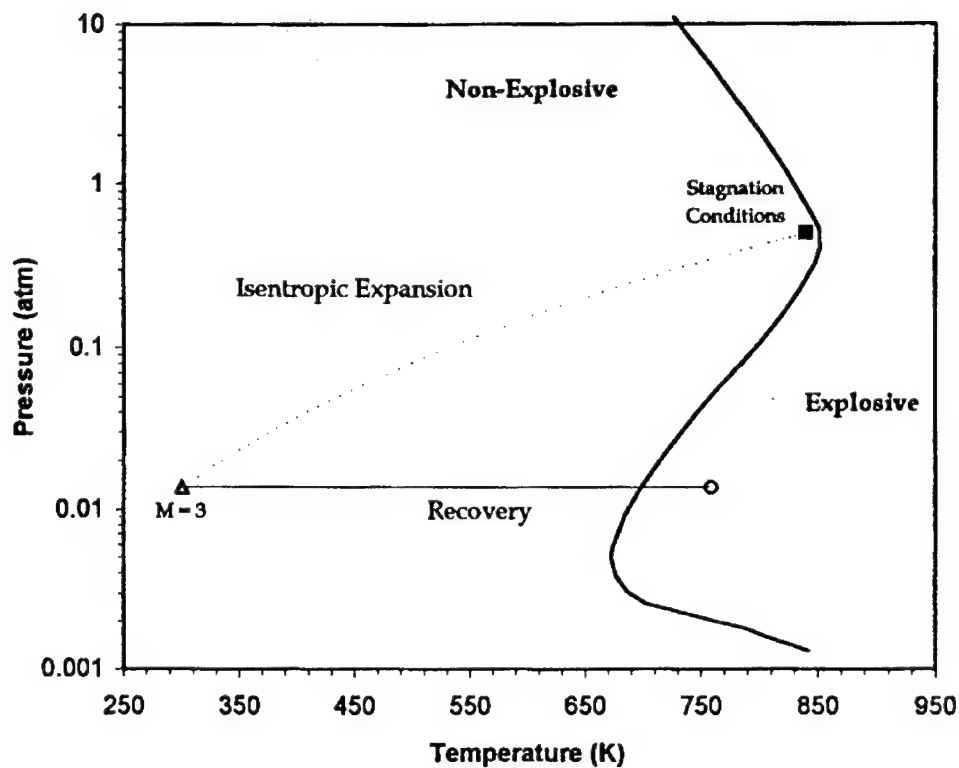
Figure 1.5: Operating concept for the Supersonic Combustion Facility superimposed over the classical explosion limits for the hydrogen-oxygen system. Starting from arbitrary stagnation conditions ($P_0 = 0.5$ atm, $T_0 = 840$ K) in a non-explosive regime, isentropic expansion to Mach 3 and subsequent recovery in a boundary layer (assuming a reasonable recovery factor, $f \approx 0.85$) puts the system inside the explosive regime.

18
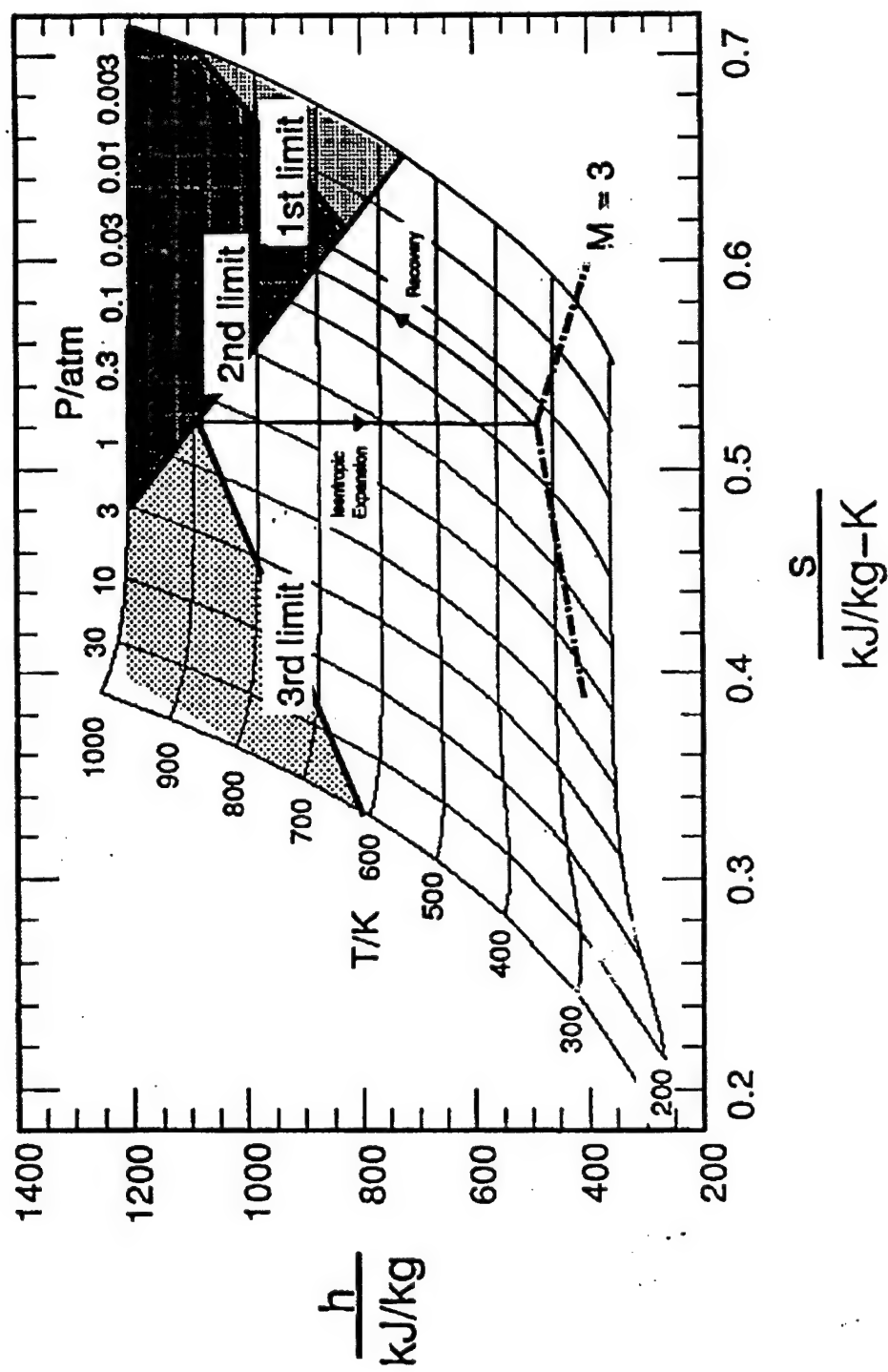
Figure 1.6: Mollier diagram (enthalpy-entropy) of the operating concept for the Supersonic Combustion Facility. The hydrogen-oxygen explosion limits are sketched, along with a line showing static conditions at Mach 3 using these limits as stagnation conditions (courtesy Yetter).

Chapter 2.   Experimental Technique

Introduction

Implementation of supersonic flow requires consideration of a number of factors contributing to the design of the wind tunnel. The task is complicated when additional constraints required for a reacting flow are taken into account. By operating a combustion tunnel with heated flow at subatmospheric static pressures, it is possible to move a hydrogen-oxygen mixture from a non-explosive state in the free-stream to an explosive state in the supersonic boundary layer. This principle became the driving force behind the design and implementation of the pilot supersonic combustion facility described in this section.

2.1 Pilot Supersonic Combustion Facility Configuration

Figure 2.1 shows the arrangement of the pilot Supersonic Combustion Facility (SCF). All surfaces in contact with the hot, flowing gases are 304 stainless steel, except the test section side walls, which are quartz, and Viton O-rings used in the nozzle/test section. Standard 3" schedule 40 piping (7.62 cm inner diameter, 0.635 cm wall thickness) encloses the packed bed, settling chamber, and diffuser liner. The flanges used on these parts and on the nozzle/test section are 304 stainless steel (150 lb. rating) and flange interfaces are sealed with spiral wound carbon fiber gaskets. A hot wall pressure shell design was possible because the primary operating conditions only expose the vessel to pressures that are subatmospheric to slightly above atmospheric. ANSI 304 stainless steel is chosen for its corrosion resistance and ability to withstand high temperature.

Packed Bed Storage Heater

A storage heater utilizing a pebble bed is the primary method for increasing the enthalpy of the tunnel gas flow. Two Lindberg Moldatherm II cylindrical electrical resistance heating modules surround a 7.62 cm inner diameter pipe enclosing the packed bed. Each module is rated for 3600 W at full load, and the two units are controlled by a single Omega series CN76000 microprocessor-based temperature controller. The bed consists of stainless steel spheres 0.635 cm in diameter, with a total mass of 13.61 kilograms and a depth of 76.2 cm. One 0.635 cm thick perforated plate supports the spheres inside the base of the heater pipe, and a similar grating is located at the top. The upper grating eliminates the possibility of lifting the spheres downstream as a result of fluidizing the bed from excessive pressure drop.

In operation, the heaters are set to maintain the outer wall of the vessel at a constant temperature, monitored by a type K thermocouple (nickel/nickel-chromium; Omega) mounted to the surface. The pipe is "soaked" over a period of several hours, transferring thermal energy into the packed bed before an experimental run. Safety considerations and risk of thermal creep require that the wall temperature of the heater vessel not exceed 800 °C (1073 K).

The flow exiting the heater enters the settling chamber through a 90 degree elbow. Heat losses through the system are alleviated with the addition of a flexible tape heater (Omega model SST051-080, 620 watts) around the elbow and by insulating piping components with a combination of 2" thick pipe insulation and ceramic blanket (Cotronics Corp.).

Run times are determined by the duration over which the gas exiting the packed bed maintains a nearly constant temperature, which is affected by the desired stagnation pressure in the settling chamber. Initially, a transient effect is observed (Figure 2.2), which corresponds to tunnel components reaching a steady-state temperature. Successful operation with runs as long as seven minutes or more have been achieved with flow rates around 15 g/s.

21

Combustion Heating

The packed bed storage heater provides settling chamber temperatures up to 840 K at the maximum allowable wall temperature. For extended operation at higher stagnation temperatures, it is possible to burn quantities of hydrogen with added oxygen to further increase the enthalpy of the stream, essentially forming a "vitiated" air. Hydrogen is injected at the upstream end of the settling chamber and reacts with some of the oxygen, forming water and other equilibrium products.

The advantage of utilizing this two-stage heating process derives from exposing fewer tunnel components to high test temperatures, and the ability to do so for a fraction of the total experiment run time. Thus, the danger of compromising structural integrity as a result of thermal effects is minimized. Increased total run times up to 12 minutes are possible simply by monitoring and adjusting the amount of fuel consumed upstream to heat the flow.

Settling Chamber

The settling chamber consists of a stainless steel pipe of 61 cm length and 7.62 cm I.D. Access ports for measurement of stagnation temperature and pressure are located 15.24 cm upstream of the start of the two-dimensional nozzle inlet; and additional ports are located on each flange. The upstream flange port is the location of primary fuel injection for reactive heating of the main flow. Because the tunnel is designed for combustion experiments, there is safety concern over the possibility of overpressurizing piping components upstream of the throat. This could occur if a test section model malfunctioned and created a physical blockage, or a drop in ejector motive supply pressure caused the tunnel to "unstart" during a reacting flow experiment and flashback or detonation ensued.

To protect the apparatus and laboratory personnel, a 2.54 cm diameter reverse-acting burst disk assembly (FDI Frangible Disks) rated for 50 psig at

900 °F is located in the settling chamber section about 15 cm downstream from its entrance. Overpressurization will blow the disk and tunnel gases vent into the exhaust system through a 91 cm stainless steel flexible hose.

Ejector Performance / Selection

To achieve the desired pressure ratio P_0/P_{exit} for tunnel startup, a Fox Valve Development Corporation 4" series 250-AJV-75 Ejector Vacuum Pump reduces the diffuser exit pressure. The motive flow is nitrogen supplied at 230 psig and a flowrate of 2650 pounds per hour (PPH). The ejector is capable of providing rated suction pressures down to 75 torr with a suction flow of 165 PPH (20.8 g/s), although pressures slightly lower than this value have been obtained in trials.

The pressure ratio required to theoretically run a tunnel can be quite different from the actual value needed for successful startup. Figure 2.3 shows the probable maximum ratios needed for starting tunnels of different Mach numbers. Normal shock theory gives the total pressure ratio across a shock (with upstream Mach number M_1) as

$$\frac{P_{t2}}{P_{t1}} = \left[\frac{(\gamma + 1)}{2\,\gamma\,M_1^{\,2} - (\gamma - 1)} \right]^{1/(\gamma-1)} \left[\frac{(\gamma + 1)\,M_1^{\,2}}{(\gamma + 1)\,M_1^{\,2} + 2} \right]^{\gamma/(\gamma-1)} \tag{1}$$

and for a Mach number of 3 and a specific heat ratio of 1.4, this pressure ratio is 0.3283, corresponding to a compression ratio of 3.04 in Figure 2.3 (the tunnel compression ratio is P_{t1}/P_{t2}). The theoretical line is different from the empirically defined line in Figure 2.3 which predicts a pressure ratio nearly twice this value for starting a Mach 3 tunnel.

To account for these factors, a pressure ratio of 7:1 (P_0/P_{exit}) is employed as a baseline at the tunnel mass flow rate conditions of 20 g/s. Unfortunately, the performance of an ejector is non-linear over the range of suction mass flow rates. Indeed, the design of the ejector itself is centered around a single

23

operating point, and subsequent performance at off-design conditions is largely determined by that point, and to a lesser extent by the motive flow conditions.(Fox Valve Corp., 1994) The SCF ejector supplies the largest pressure ratio over the widest range of tunnel mass flow rates possible.

The nitrogen motive flow serves a secondary purpose in terms of diluting the tunnel gases, resulting in reasonable exhaust temperatures and quenching any reactions downstream of the ejector. Operation of the wind tunnel with high concentrations of hydrogen creates conditions in the diffuser that are within flammability limits and potentially within detonation limits for hydrogen-oxygen and hydrogen-air systems. Lean flammability and detonation limits of hydrogen-air systems at one atmosphere are 4% and 18% fuel by volume, respectively.(Glassman, 1987) This is one of the primary reasons a vacuum tank cannot be employed to provide the needed pressure ratio for tunnel startup and operation. While evacuating a large tank eliminates the need for high motive gas flows, run times are shortened (for reasonable sized tanks), and the exhaust gases within the tank pose a hazard in terms of explosion. While the vacuum tank is being filled with high temperature tunnel gases, increasing pressure inside the tank can cause the system to cross the first limit (Figure 1.4) and explode.

If needed, further reduction of the exit pressure would be possible in the future by installing a two-stage ejector system. This would require much higher motive mass flowrates and modification of the exhaust system. Such an alteration would likely be necessary to operate the tunnel with a hypersonic nozzle or increased mass flow rates (higher stagnation/static pressures).

Silencer

To reduce the levels of ambient noise in the laboratory during wind tunnel operation, a Burgess-Manning model BMA-4 silencer is located in-line following the ejector and prior to the exhaust. The mixed ejector motive gas and

tunnel supply gas pass through a tubing arrangement and snubbing chambers designed to attenuate the noise over a wide range of frequencies. Peak dynamic loss is over 30 dB at around 400 Hz falling to approximately 24 dB above 2000 Hz. (BMA, 1994)

Nozzle design

The operation of the wind tunnel centers around the convergent-divergent nozzle which accelerates the flow from subsonic to supersonic velocities. Certain key design parameters determine the size and shape of the nozzle; these are Mach number and cross-sectional area of the test-section. In this experiment, the inlet section also serves as a transition from three-dimensional flow in the circular cross-section settling chamber to two-dimensional flow through the test section. The nozzle operates as a nominal Mach number of M = 3, and the test section has a square 2.54 cm x 2.54 cm cross-section. Since the nozzle is two-dimensional, the width of nozzle and test section remains 2.54 cm for its entire length.

There are three flow regimes inside the nozzle/test section which is integrated into a single unit. Figure 2.4 details the typical flow conditions in the inlet, converging, and diverging regions of the nozzle and test section. Because the settling chamber has a 7.62 cm diameter circular cross-section, it is necessary to provide an inlet portion which establishes the flow as two-dimensional prior to entering the contraction. This rectangular cross-section inlet is 12 cm long and has a height of 7.62 cm and 2.54 cm width.

A nozzle contour provides a smooth and ideally isentropic transition from subsonic speeds ($M_0 \ll 1$) to a supersonic design Mach number (M_{test}). The subsonic portion of the nozzle accelerates the flow to the sonic velocity at the throat. In general, the procedures for generating the curve of the subsonic portion of the nozzle are arbitrary, and empirical evidence suggests employing a

25

long smooth curve approaching zero curvature at the throat. (Beckwith and Moore, 1955) A circular arc of radius 7.62 cm is employed for this purpose.

The diverging portion of the nozzle was generated using the method of characteristics for a minimum length nozzle. The method of characteristics is a numerical technique for solving hyperbolic partial-differential equations using ordinary differential equations relating dependent variables along characteristic lines. For shock-free flow in the test-section, it is essential that the shocks generated by expanding the flow from sonic velocity at the throat to the design Mach number be "canceled" at the contoured nozzle walls.

Figure 2.5 shows the theoretical one-dimensional Mach number, pressure, and temperature ratios for the nozzle design implemented in this experimental effort. The slight inflection in the profiles at the throat is a result of matching a circular arc approach to the minimum length nozzle contour, and has no effect on the nozzle performance or flow quality. This design satisfies the minimum curvature condition while maintaining the shortest length for producing shock-free supersonic flow in the test section.

Test Section

Following the end of the supersonic nozzle is a 2.54 cm square constant-area test section. The nozzle and test section are integrated into a single frame (Figure 2.6) as this was determined to be the optimal configuration for economical fabrication and convenient tunnel access. The parallel walls of the tunnel consist of two polished 6.096 mm ±0.127 mm thick optical grade fused quartz windows 27.84 cm long and 5.00 cm high, providing access for optical diagnostics. Quartz is chosen rather than glass for its ability to pass light in the ultraviolet wavelengths, which is essential for ultraviolet (UV) imaging of spontaneous emission of the electronically excited hydroxyl radical (described in Section 2.3).

The nozzle contour plates and window holders can be removed separately. This design has the advantage of increased accessibility for the

purposes of cleaning and replacing quartz windows or re-configuring the test section. It is possible to remove and change the test section model without opening the flange bolts which hold the frame to the wind tunnel system.

Viton O-rings (3/32" O.D.) are used to seal the individual plates against the frame, and the windows have additional Viton O-rings (1/8" O.D.) to seal the quartz/window holder interface.

Diffuser

A diffuser serves the purpose of decelerating a flow with minimal loss in total pressure. Slowing a flow from supersonic to subsonic velocity through a normal shock at the design Mach number generates losses larger than are necessary. As noted previously, the empirical values for required operating pressure ratios are typically greater than those predicted by one-dimensional gas dynamic theory. This problem can be alleviated in part by the addition of a diffuser, decreasing the required pressure ratio for running the tunnel, and also providing a safety margin while running the tunnel in cases of potential thermal choking and subsequent tunnel unstart.

In principle, a supersonic diffuser works much like the description of the ramjet inlet given in Section 1.2. Oblique shocks generated by models or obstructions in the test section continue to reflect from tunnel surfaces until eventually a normal shock is formed somewhere in the diffuser. Following the normal shock, the flow is subsonic and further increase in the area ratio now decelerates the flow. Thus, the diffuser operates in both supersonic and subsonic flow regimes. The efficiency of the diffuser is determined by the number of oblique shocks the flow passes through before the normal shock forms. In the limiting case of isentropic operation, an infinite number of oblique shocks are required, such that the normal shock forms at a flow Mach number of unity.

Unfortunately, diffuser design is based largely on general rules rather than on strict compliance with theory as in nozzle design. Increasing the area

27

ratio over as long a length as possible is the ideal configuration. If the diffuser is too short, then the flow will separate from the diffuser walls and create further total pressure losses. Pope and Goin (1965) suggest a diffuser with a total angle between walls less than 6.0 degrees.

The diffuser designed for the SCF employs a unique liner and shell approach which made construction simple and extremely cost-effective. Figure 2.7 is a photograph of the liner and shell of the diffuser. The liner is 3.175 mm thick stainless steel fashioned in a conical geometry with a total expansion angle of 5 degrees over a 38.1 cm length. The liner fits into a standard 3" schedule 40 pipe, and a 3.2 mm thick spacer ring prevents vibration of the liner and adds strength radially. Holes drilled in the liner allow pressure equilibration throughout the pipe, and thus the liner never experiences excessive loading due to pressure variation over its internal surface.

Trip Wires/Boundary Layer Growth

While the Mach number should be fixed for a given nozzle contour, a variety of additional factors result in a different operating Mach number. One of these factors is boundary layer growth through the nozzle and into the test section. Thickening boundary layers along the contoured walls and quartz windows will change the effective area ratio at a given location downstream of the throat, reducing the Mach number at that station. Consider Figure 2.9 which shows the Mach number distribution along the vertical axis of the tunnel at a distance of 15.9 cm from the throat. The line represents the theoretical Mach number corrected for boundary layer growth. Experimental points determined from pitot pressure measurements show good agreement and uniformity of the flow. Continued growth and possible laminar-turbulent boundary layer transition presents a problem in terms of increased pressure loss in the tunnel. The addition of trip wires to the nozzle walls can prevent laminar separation of the flow during startup and operation, as well as eliminate shock-induced

boundary layer transition which inevitably results in an increased boundary layer thickness. (Smits, 1995)

The boundary layer thickness is described by the Blasius solution for this problem which gives the result for incompressible laminar boundary layers

$$\delta = \frac{5l}{\sqrt{R_l}}$$ (2),

where R_l is the local Reynolds number $\rho UD/\mu$, and l is the distance from the start of the boundary layer. (Schlichting, 1960) At supersonic speeds, compressibility effects are significant and the boundary layer growth changes with Mach number squared

$$\delta \propto \frac{M_\infty^2}{\sqrt{R_l}}$$ (3)

where M_∞ is the free stream Mach number.(Anderson, 1989) A more appropriate semi-empirical formula is available to approximate δ accounting for non-adiabiticity of the wall:

$$\frac{\delta}{l}\sqrt{R_l} \approx C_w^{1/2}\left[5.0 + \left(0.2 + 0.9\frac{T_w}{T_{aw}}\right)(\gamma - 1)M_\infty^2\right]$$ (4)

where C_w is the Chapman-Rubesin parameter at the wall, defined by $C_w \approx (T_w/T_\infty)^{-1/3}$ for gases. (White, 1991)

For calculating wall boundary layer thickness, the distance l can be measured starting from the throat where δ becomes negligibly thin. (Pope and Goin, 1965) Typical laminar boundary layer thicknesses encountered at the walls of the test section are less than 2 mm. Trip wires of 0.25 mm diameter are cemented to the contoured walls 2.54 cm from the end of the diverging portion of the nozzle to promote transition.

Data Acquisition System

Because run times are short, simultaneously adjusting and manually recording flow parameters is both difficult and further reduces the useful

duration of an experiment. A microcomputer based program created using Visual Basic acquires, displays, and saves important variables during operation of the wind tunnel. The program is responsible for logging selected flow rates, settling chamber temperature and pressure, and local static/pitot pressure taps. These parameters are saved to a tab-delimited text format file which can be opened using any standard database program. The platform selected is an IBM PC with an Analog Devices RTI-815 A/D board installed. This data acquisition board handles 16 analog channels with 0-10 volt input signals at a 31.2 kHz sampling rate and ± 0.02% full-scale accuracy.

Pressure Measurement

Pressures are measured using variable capacitance sensor MKS Baratron Type 122 absolute pressure gauges. A 0-5000 mmHg range transducer supplies readings from the settling chamber, and a 0-1000 mmHg range transducer is used for all test section static and pitot pressure measurements. These transducers have a rated accuracy of 0.5% of reading with a temperature coefficient of 0.04% reading/°C. The output is sent to digital displays and to the A/D board for data logging purposes.

Gas Flow Metering

Flow rates of the fuel and oxidizer are measured using Teledyne-Hastings mass flowmeters. These units have a rated combined accuracy and linearity of ±1%. A wet test meter (Precision Scientific, ±0.5%) provides calibration of the lower flow rates. Determination of the main carrier nitrogen flow rate is made by employing a choked orifice flow calculation through the throat of the nozzle. The uncertainty in this method comes from the error arising in measuring the stagnation parameters. A flow coefficient of unity is employed, which is equivalent to assuming that flow through the converging portion of the nozzle is isentropic. The large ratio of the radius of the circular arc approach to the throat

diameter $R_a/D_{throat} \approx 12.7$, results in a loss coefficient that is negligible, validating the assumption of near-isentropic flow.(Munson et al., 1990)

A slight total temperature drop has been measured between the test section and settling chamber thermocouples. This is attributed to high heat transfer rates through the nozzle and can contribute to the error in the nitrogen flow rate calculation. For typical experimental conditions, this temperature drop (observed to be up to 50 K ; see Figure 2.8) could cause the nitrogen flow rate to be underestimated by approximately 3%. Accounting for the combined accuracies of the stagnation pressure and temperature measurement, the error in calculating the nitrogen flow rate using the method described should be no more than +5%/-2%.

2.2 Experimental Methods

Analyzing the flow conditions in a supersonic wind tunnel requires a combination of specific measurement techniques and understanding of the fluid dynamics in various portions of the facility. Measurement of stagnation and static conditions are outlined.

Settling Chamber Stagnation Conditions/Measurement

Static conditions inside the test section can be calculated by knowing the conditions upstream of the nozzle inside the settling chamber, the test section Mach number, and by employing isentropic flow relationships. Stagnation (also referred to as *total*) pressure and temperature are the parameters of interest, and these are measured in the settling chamber 15.24 cm upstream of the two-dimensional inlet to the nozzle.

Total temperature is measured with a type K exposed junction thermocouple located at the centerline of the flow in the 7.62 cm diameter settling chamber. The thermocouple is constructed of nickel / nickel-chromium wire with a 304 stainless steel sheath. The millivolt level signal is converted to a

31

scaled 0-10 volt output signal by a thermocouple amplifier (Omega CN76000). This signal is passed to an analog to digital converter (Analog Devices RTI-815) which converts the voltage to temperature.

Radial temperature measurements verify that the temperature profile is uniform along the vertical axis of the flow entering the two-dimensional transition to the nozzle and test section. These measurements are shown in Figure 2.8 for two different initial stagnation temperatures.

Uncertainties in the temperature measurement result from catalytic surface reactions, radiative and conductive heat losses, and transient effects. By avoiding the use of thermocouple wire which catalyzes the hydrogen-oxygen system, especially platinum, surface reactions do not pose a problem. Following the approach of Held (1993) for analyzing the temperature probe of the Variable Pressure Flow Reactor (VPFR) which employs similar flow rates and temperatures as in the SCF, temperature fluctuations due to radiation and transient effects are expected to be no greater than 2-3 K for gas temperatures greater than 1000 K. Conduction losses are expected to be negligible since the support wires and most of the sheath are exposed to the full temperature of the flow.

Total pressure measurements are made utilizing a static tap at the wall of the settling chamber, at the same upstream location as the total temperature thermocouple. The velocity of the flow in the settling chamber should be in the low subsonic ($M_{sc} \ll 1$) regime where compressibility effects can be neglected. This allows the use of the standard incompressible Bernoulli equation for analyzing the flow

$$p + \frac{1}{2}\rho V^2 + \gamma z = \text{constant along a streamline} \qquad (3).$$

If we consider a stagnation point 1 where $V_1 = 0$ m/s, and neglect altitude changes, then we can write

$$p_2 - p_1 = \frac{1}{2}\rho V_2^2 \qquad (4)$$

32

which describes the "error" introduced into the stagnation pressure measurement from a flow moving with velocity V_2. Inserting typical operating values for the velocity, pressure, and density in the settling chamber, the total pressure measurement is in error by less than 0.1% (not including transducer uncertainty). These uncertainties are summarized in Table 2.1 below.

Table 2.1: Uncertainty Summary

Measurement	Uncertainty
Temperature	± 3 K
Pressure	± 0.01 atm (± 0.005 atm static)
Flow Rates (H_2, O_2)	$\pm 1\%$
Flow Rate (N_2)	+5% / -2%

Test Section Measurements

Static pressure is measured in the wind tunnel through a static tap located on the top or bottom wall of the test section. A 0.4 mm diameter tap is positioned at the exit of the minimum length nozzle on the upper wall. There are a total of five 3.175 mm access ports along the opposite wall which can also be used to measure pressure.

Total pressure readings are made inside the test section using a pitot probe. In supersonic flow, a normal shock forms upstream of the probe entrance and results in a reading not equal to the freestream pressure, but rather a reduced total pressure, called pitot pressure. The measured values provide a number of alternate ways for computing the Mach number inside of the test section. Utilizing the stagnation pressure measured in the settling chamber p_{t1} and the pitot pressure p_{t2}, Mach number can be found using

$$\frac{p_{t2}}{p_{t1}} = \left[\frac{(\gamma + 1)}{2\,\gamma\,M_1^{\,2} - (\gamma - 1)} \right]^{1/(\gamma-1)} \left[\frac{(\gamma + 1)\,M_1^{\,2}}{(\gamma + 1)\,M_1^{\,2} + 2} \right]^{\gamma/(\gamma-1)}$$

33

and iterative methods or simply by referencing tabulated values. Alternately, using the static test section pressure and the stagnation test section pressure gives the same result.

Gas Supply

The nitrogen, used as a carrier and diluent in the main tunnel flow, is vaporized liquid nitrogen (Liquid Carbonic, Hi-Pure grade, >99.998%). The oxygen is from Airco (>99.993%). Hydrogen is a prepurified grade (>99.99%) from Matheson. The nitrogen and oxygen are mixed several meters upstream before entering the tunnel circuit at the packed bed storage heater. For safety reasons, hydrogen is only injected into the tunnel flow at points downstream of the heater outlet. All reactants are used without further purification.

Hydrogen and oxygen pass through solenoid valves before entering the tunnel circuit. These valves (Snap-Tite Solenoid Valves, 1/4" NPT, full orifice) are normally closed until the solenoid is energized. Fuel/oxidizer flow ceases in the unlikely event of power failure during a run. In addition, the readout connected to the stagnation thermocouple sensor has an alarm option which is programmed prior to the run. If the stagnation temperature exceeds a pre-determined value during an experiment, power to the solenoid valves is shut off, and power can only be restored once the alarm condition has been corrected.

Manual shut-off valves are connected in-line prior to gases entering the wind tunnel as a secondary safety precaution. The redundant safety measures implemented provide a minimum-hazard operating environment for the operator.

2.3 Diagnostics

Schlieren/Shadowgraph System

Flow visualization inside the supersonic test section is achieved through the use of schlieren or shadowgraph techniques. The general principle of this

optical diagnostic depends on the refraction of a beam of light by gradients in the refractive index of the gas through which the beam passes. Changes in refractive index caused by density gradients within the test section bends rays of light passing through the quartz side walls. A knife edge causes these gradients to either add to or subtract from the image at the camera. Thus, density gradients appear as either light or dark regions at the viewing plane. The principles of operation, and practical requirements are described more extensively in the literature. (Meyer-Arendt, 1972; Goldstein, 1983; Kodak, 1977)

There are a wide variety of combinations which can be employed to form a schlieren system. The system chosen for this research is typically referred to as a two-mirror schlieren system because it uses two concave mirrors for collimating and re-focusing the beam of light. There are several advantages to using this system. The ability to place optical components in remote locations is useful since tunnel components occupy a large portion of the available laboratory space. Also, the parallel beam produces an image of superior resolution compared with other schlieren systems. A schematic of a typical two-mirror schlieren system is shown in Figure 2.10. The actual system used to produce the images contained in this document have three additional first surface plane mirrors (not shown in the figure) to direct the parallel beam for more convenient placement of the light source and video camera setup.

A General Radio Strobotac (GR 1538-A) electronic stroboscope followed by an adjustable iris is used to provide a point light source for the system. The first schlieren head consists of an first-surface concave spherical reflector (Edmund Scientific, 6" diameter, 60" focal length, protected aluminized surface), which collimates the expanding beam. The beam of parallel rays is passed through the test section, and sent to a second spherical reflector which refocuses the light onto a knife edge. A new razor blade mounted on a positionable optical support has proven sufficient for this purpose. Following the knife edge are two lenses, one double-convex achromat (50 mm diameter, 96 mm focal length) to adjust for possible chromatic aberration in the beam, and a second

35

optical grade double-convex lens (Edmund Scientific, 50 mm diameter, 150 mm focal length). The position of these lenses relative to the knife edge and the camera determines the size of the image in the field of view, as well as the focus of the image.

The video camera is a General Electric model CID776, and is implemented without the usual compound objective lens because the two bi-convex lenses provide better control over adjusting the image onto the camera array. The camera signal is sent to a video cassette recorder (Panasonic S-VHS) and a television monitor. In this manner, real-time video of the schlieren image can be observed during an experiment and recorded for later analysis.

Ultraviolet-Sensitive Intensified Camera

Spontaneous emission from electronically excited hydroxyl radicals (OH*) within the nozzle and test section was imaged using an ITT Electro-Optical Products UV-sensitive video camera. The OH* radicals which are produced in a reaction zone disappear through the competing reactions:

$$OH^* + M = OH + M \qquad \text{(quenching)}$$
$$OH^* = OH + h\nu \qquad \text{(emission)}$$

The first reaction describes the collisional quenching of the radical by various partners M. Chemiluminescence arises from the second reaction corresponding to the electronic transition $^2\Sigma^+$-$^2\Pi$ which is observed in the ultraviolet OH band at 306.4 nm. A 52 mm glass UV filter assembly (Nikon 1453 NAS) is used to reduce unwanted visible and infrared light while still transmitting much of the light in the ultraviolet spectrum.

Some visible and infrared light does pass through the filter at high camera gain settings. This can have the undesirable effect of saturating the video image when metal and other surfaces are heated. An analytical line filter (Oriel 57030), is used in selected cases to overcome this problem. It has a narrow 10 nm bandwidth with peak transmittance (minimum 15%) centered at 307.1 nm. This

36

filter is used to verify that the luminosity observed in various experiments is due to chemiluminescence arising from the (0,0) transition of the electronically excited hydroxyl radical. The low peak transmittance can cause problems when dealing with low intensity chemiluminescence such as encountered during experiments in the SCF. Increased gain reduces the resolution of the video image; thus, the glass filter assembly was favored in most cases.

2.4 Model Size and Design

Models used in the supersonic test section must meet several criteria for successful implementation. Because the models are subjected to high recovery temperatures, stainless steel is used wherever possible. The size and geometry of the model affects the characteristics of the tunnel in terms of both startup and operation.

There is a maximum size model which can be installed in the test section during startup that will allow the shock system to pass downstream into the diffuser. This maximum is determined from a second throat analysis also used for sizing adjustable diffuser inlets. For a nominal Mach number of 3 in the test section and a specific heat ratio of 1.4, the minimum area ratio for startup of the SCF is $A_2^*/A_T = 0.72$. When the blockage occurring as a result of boundary layer thickening is considered, this ratio further decreases. The maximum theoretical cross-sectional blockage area is $A_B = 1.81$ cm^2. Trials using blockages of 2.42 cm^2 resulted in no startup of the SCF, while blockages of 1.5 cm^2 or less presented few difficulties. These model criteria are summarized in Table 2.2.

All models used in this research employ aerodynamic leading edges to eliminate the possibility of bow shock formation and consequent large pressure losses. The Mach angle for the freestream flow conditions is given by

$$\theta = \sin^{-1} \frac{1}{M} \tag{5}$$

which gives a value of 19.5 degrees using the upper bound for test section Mach number of 3 in the SCF. The maximum turning angle is 34 degrees at M=3

37

before flow behind the oblique shock reaches the sonic velocity. To minimize the pressure loss accompanying passage through the oblique shock, a 4:1 ratio of length to height (14.4°) was employed as a standard design maximum for leading edge angles.

Supports for the model depend on the geometry of the object and its desired location within the test section. For the flat plates described in Chapter 3, streamlined wedge shapes positioned the plates such that the surface was at the centerline of the flow stream. These supports were fastened to the lower wall of the test section with 0-80 stainless steel screws. Disturbances to the flow stream in the form of oblique shocks and the reflected shock train remained below the plate, leaving the boundary layer on the top surface undisturbed. These support systems, taken together with the test geometry, must meet the critical cross-sectional area requirements described above for successful implementation.

Table 2.2: Test Section Model Requirements

Mach Angle (M = 3)	19.5°
A_2^*/A_{throat}	0.72
Maximum Blockage (theory)	1.81 cm^2
Standard Max. Angle	14.4°

2.5 Supersonic Combustion Facility Operation

In practice, a specific sequence of events has been developed into a standard operating procedure for the SCF. The principle is to ensure safe startup of the wind tunnel prior to fuel injection, and to clear all fuel lines (especially when heating the hydrogen) of reactive gases before shutting the system down. These procedures are briefly outlined here to illustrate the execution of an experiment.

Initially, the data acquisition program is activated, diagnostics are running, and power to the main packed bed storage heaters is turned off. The back pressure at the diffuser exit is set to its operating value by opening the motive flow to the ejector system. The flow is controlled by means of a plug valve in line with the nitrogen supply. Once opened, the entire tunnel system (with no flow initially) is evacuated to this pressure.

In order to avoid excessive aerodynamic forces on the models in the test section, startup needs to occur quickly. When the shock system passes through the constant area duct, uneven loading occurs over the surfaces inside depending on the structure of the transient shock train. It is possible to have transonic and supersonic regimes in the test section which may create lift and subsequent large forces, especially over models of significant surface area. This problem is further complicated if a pressure regulator is used to slowly increase the stagnation pressure. This can cause local separation of the flow in the nozzle throat, increasing the uneven loading to greater extent.

A ball valve placed in line following the regulator allows for quick passage of the shock train in the test section and efficient startup. The nitrogen pressure is first set at the regulator and then the ball valve is opened, initiating flow through the SCF tunnel circuit. At this time, the tunnel should be running, which can be confirmed by checking the static pressures inside the test section or by inspection of the schlieren image on the video system (preferable).

Oxygen and hydrogen are injected into the system by opening the manual safety valves, and then energizing the solenoid valves. The pressures used for injection are set prior to the run and adjusted as needed during the experiment. Once the desired temperature has been reached by metering the correct flow rate of fuel upstream, secondary hydrogen is injected by opening the manual safety valve and switching the selector valve from purge nitrogen to hydrogen position. When the fuel is not flowing, there is always a small flow of nitrogen through the fuel lines to remove hydrogen from the lines going to the heater and upstream portion of the settling chamber.

During shutdown of the Supersonic Combustion Facility, the process is reversed. Fuel lines are purged with nitrogen while the tunnel is still running allowing a high level of dilution in the exhaust stream. The main tunnel flow is cut via the ball valve in the same rapid fashion as during startup. Finally, the ejector motive flow is stopped, and the run is complete.

Accessible Conditions

The range of accessible operating conditions for the Supersonic Combustion Facility designed for this research and described in this chapter, is summarized in Table 2.3 below.

Table 2.3: Summary of the Accessible Region for the SCF

Design Mach number:	3	
Settling Chamber		
Stagnation Temperatures:	300 - 1100	K
Stagnation Pressure:	0.46 - 1.5	atm
Test Section		
Static Temperatures:	110 - 400	K
Static Pressures:	0.01 - 0.1	atm
Reynolds number:	20000 - 175000	per inch
Mass flow rates:	10 - 30	gm/sec

2.6 Figures
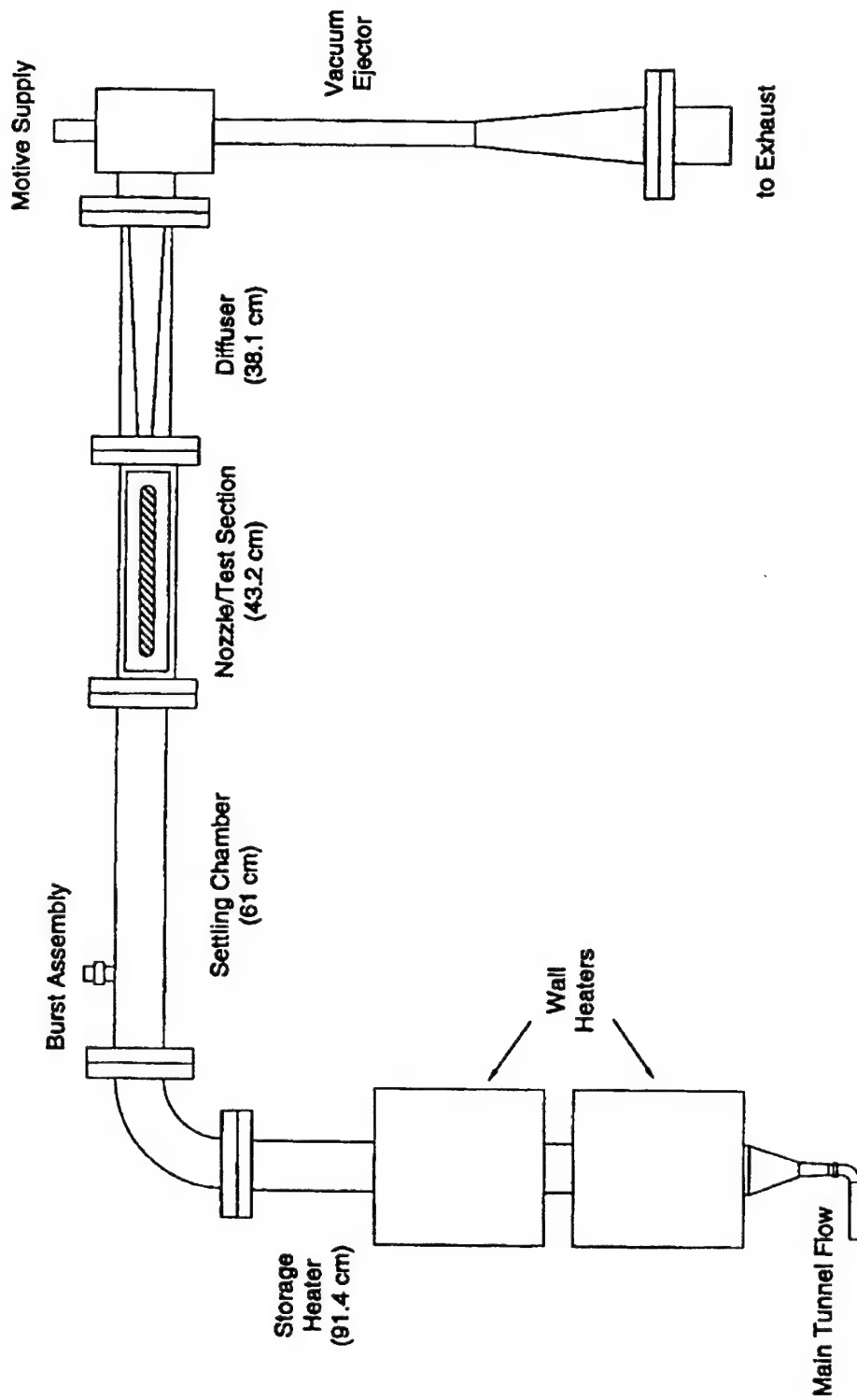
Figure 2.1: Schematic of the supersonic combustion facility (to scale).
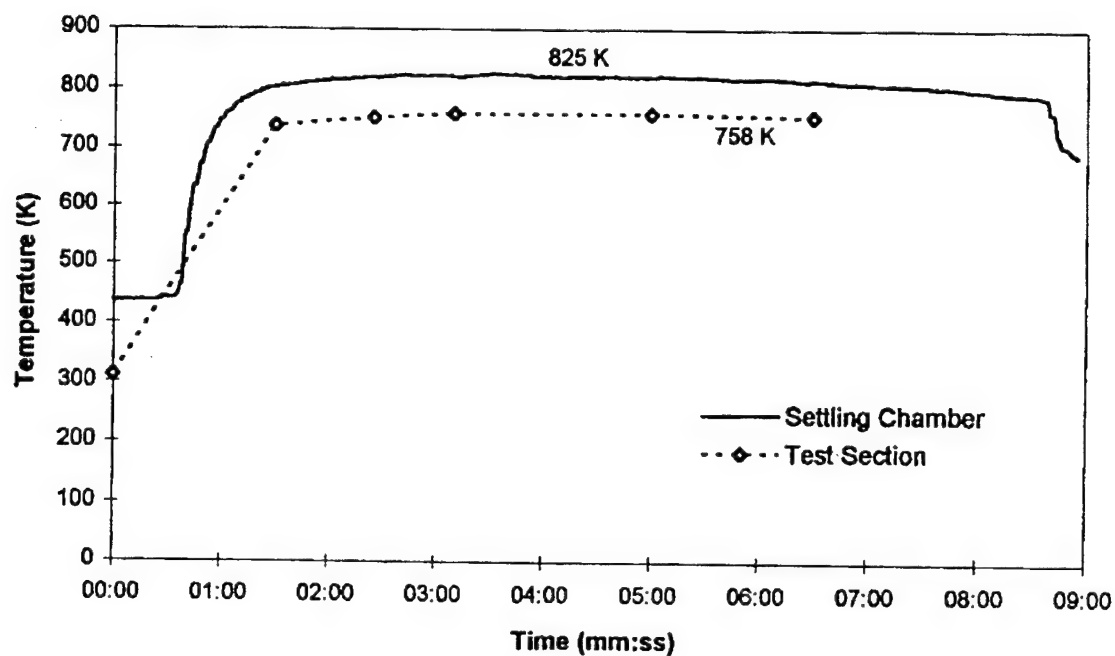
Figure 2.2: Typical temperature profile in the SCF measured at the centerline of the flow in the settling chamber and the test section (behind a flat plate test model).
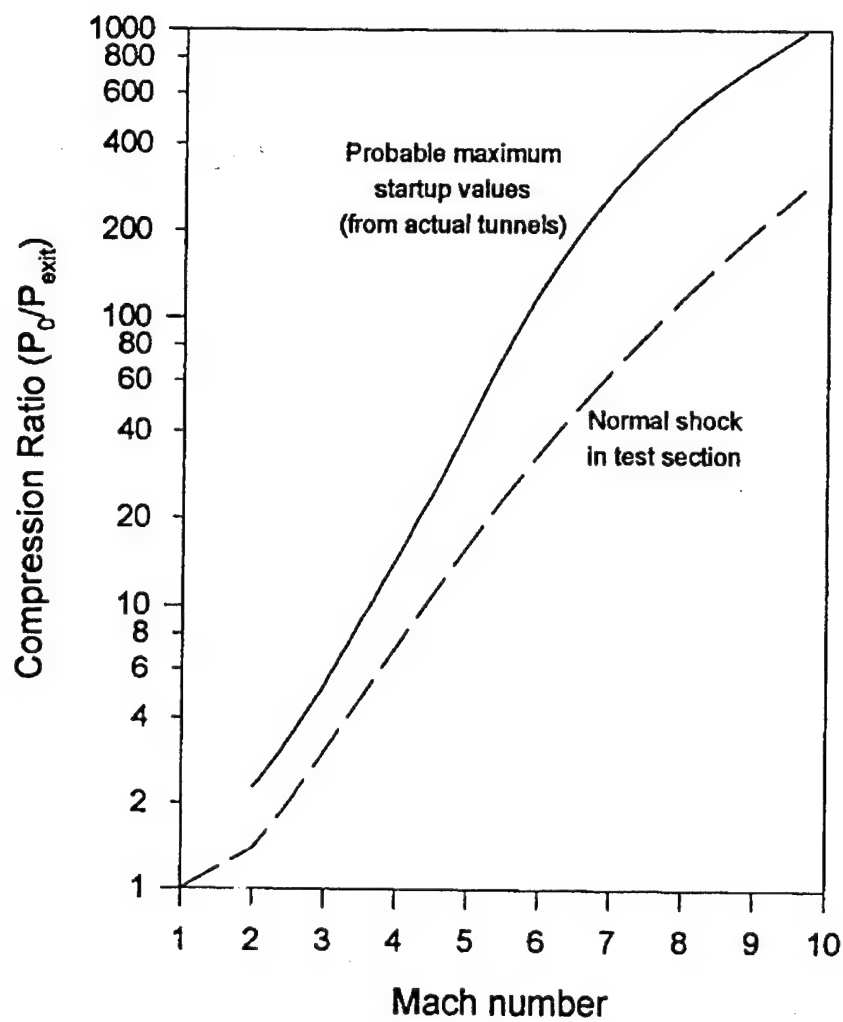
Figure 2.3: Probable maximum pressure ratios for starting tunnels over a range of Mach numbers (adapted from Pope and Goin, 1965). Lines are shown for theoretical and empirical values for the ratio of stagnation pressure and diffuser exit pressure.
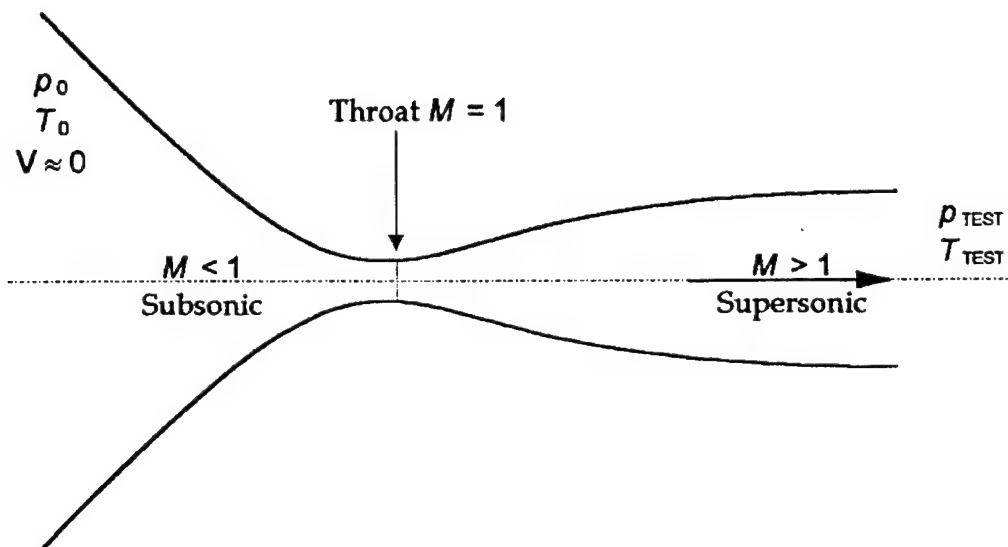
Figure 2.4: Operating flow conditions inside the supersonic nozzle.
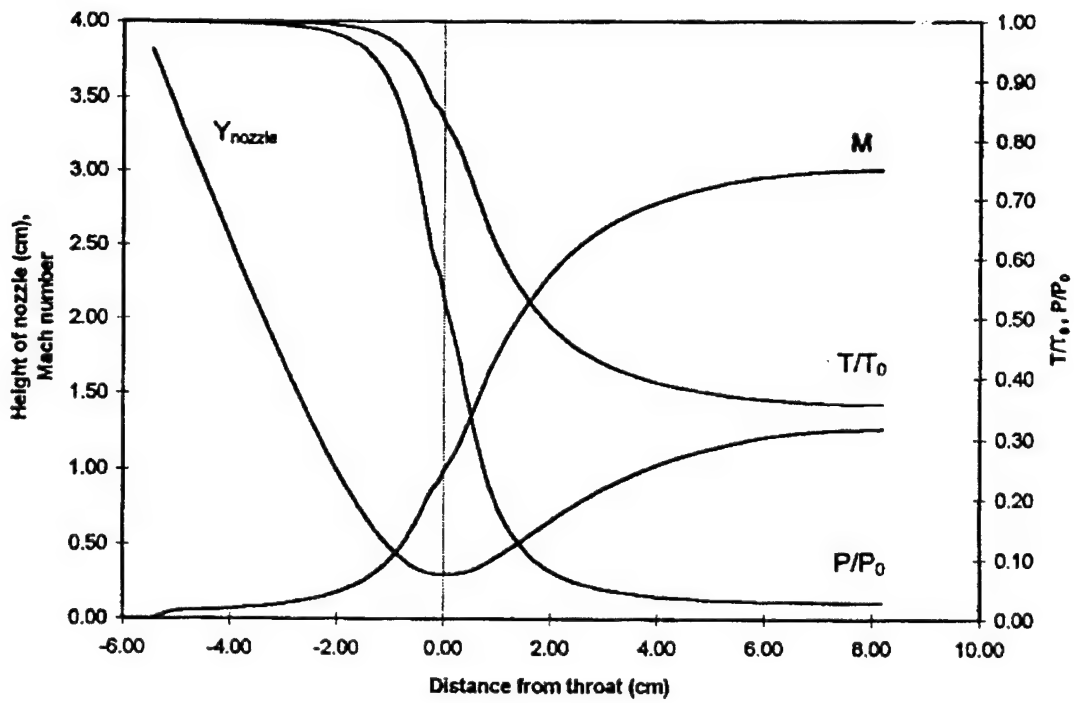
Figure 2.5: Profiles of the calculated Mach number, pressure ratio, and temperature ratio through the contoured nozzle. The dashed line indicates the throat location.

45
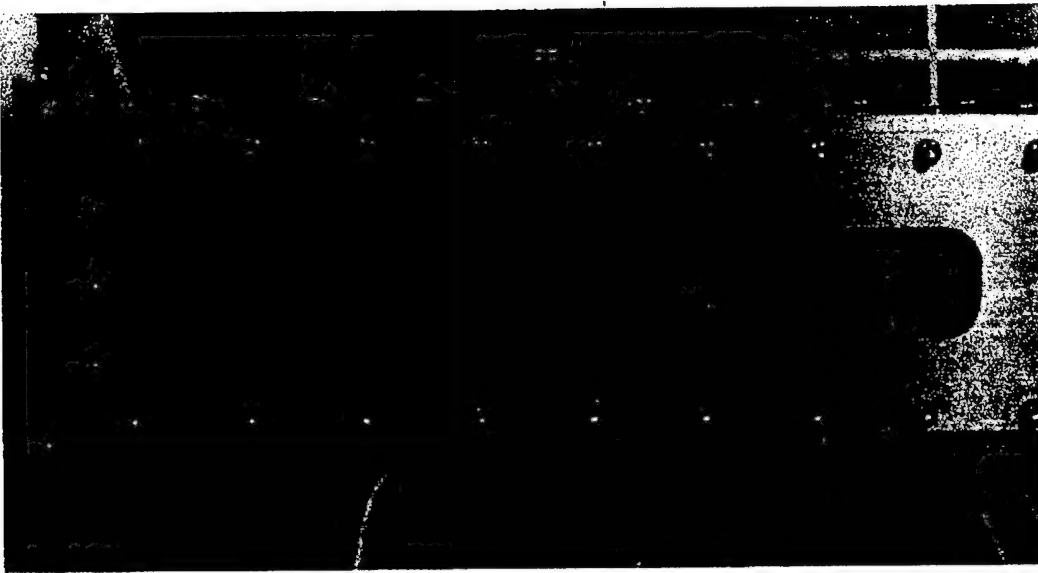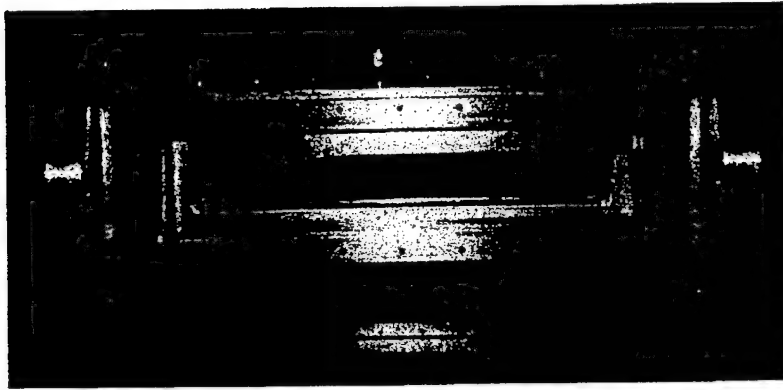
Figure 2.6: Photographs of the test section. (top) With front window holder and bottom contour plate removed. Ruler in photo is 10.2 cm long. (bottom) Showing test model in place with pitot and temperature probes inserted into the test section.
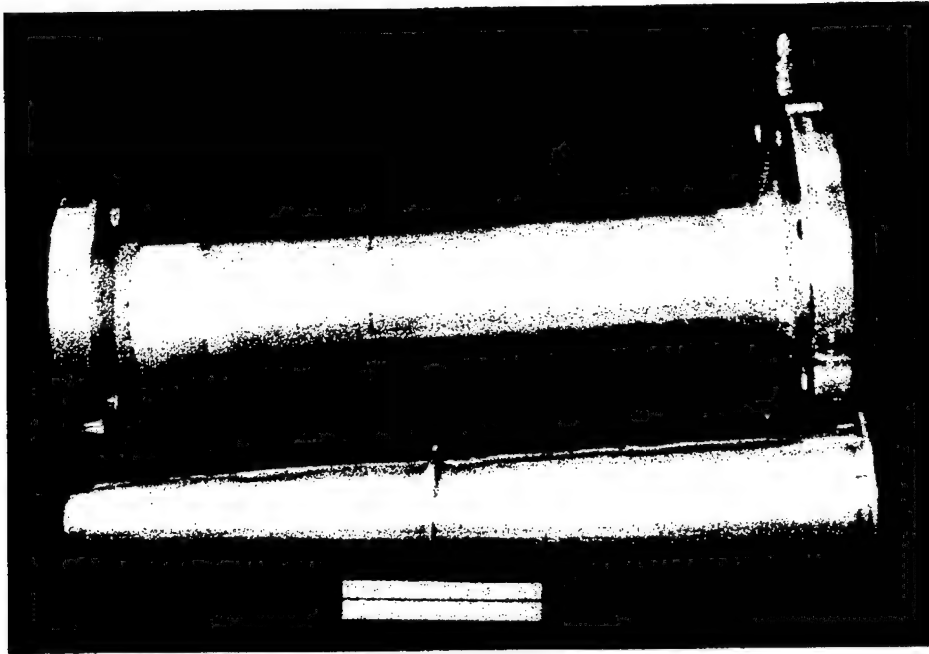
Figure 2.7: Photograph of the supersonic diffuser designed for the Supersonic Combustion Facility showing the outer shell (above) and the diverging liner. (Ruler is 10.2 cm long)
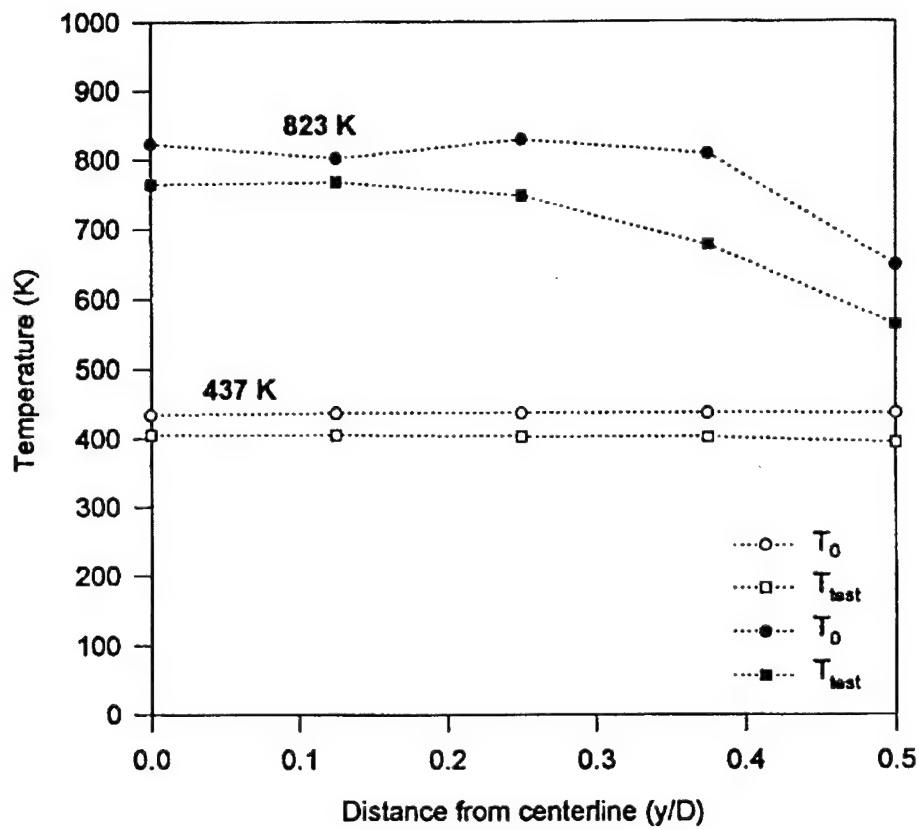
Figure 2.8: Temperature profiles in the settling chamber and test section measured along the vertical axis of the tunnel for two different initial temperatures.
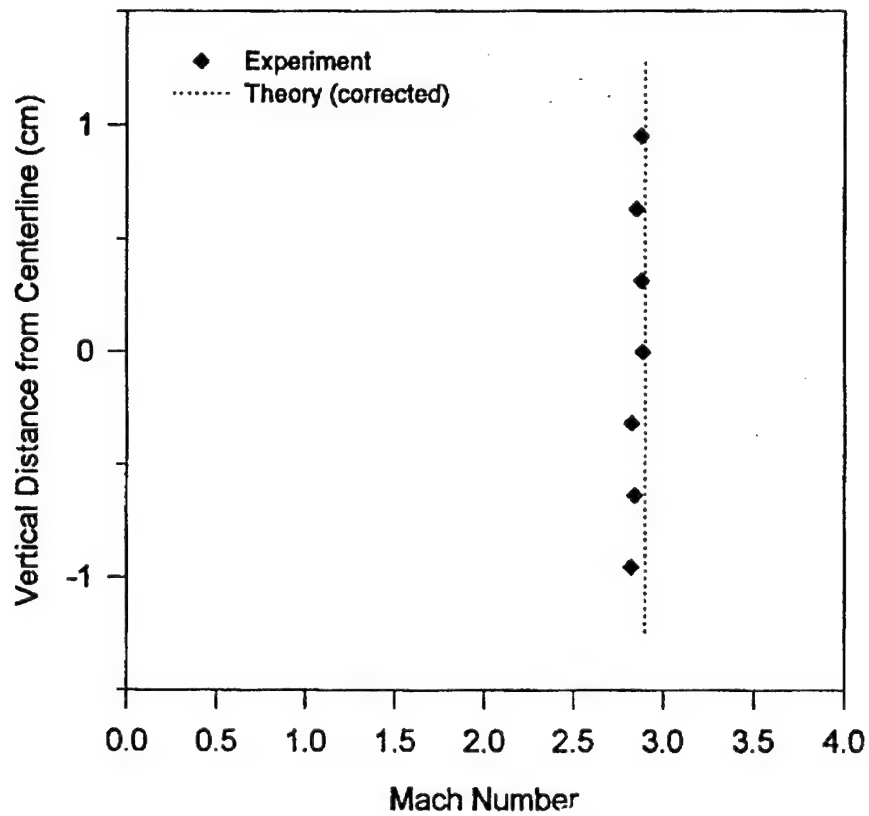
Figure 2.9: Mach number distribution (corrected for boundary layer growth) along the vertical axis of the test section, measured 15.9 cm downstream of the throat.
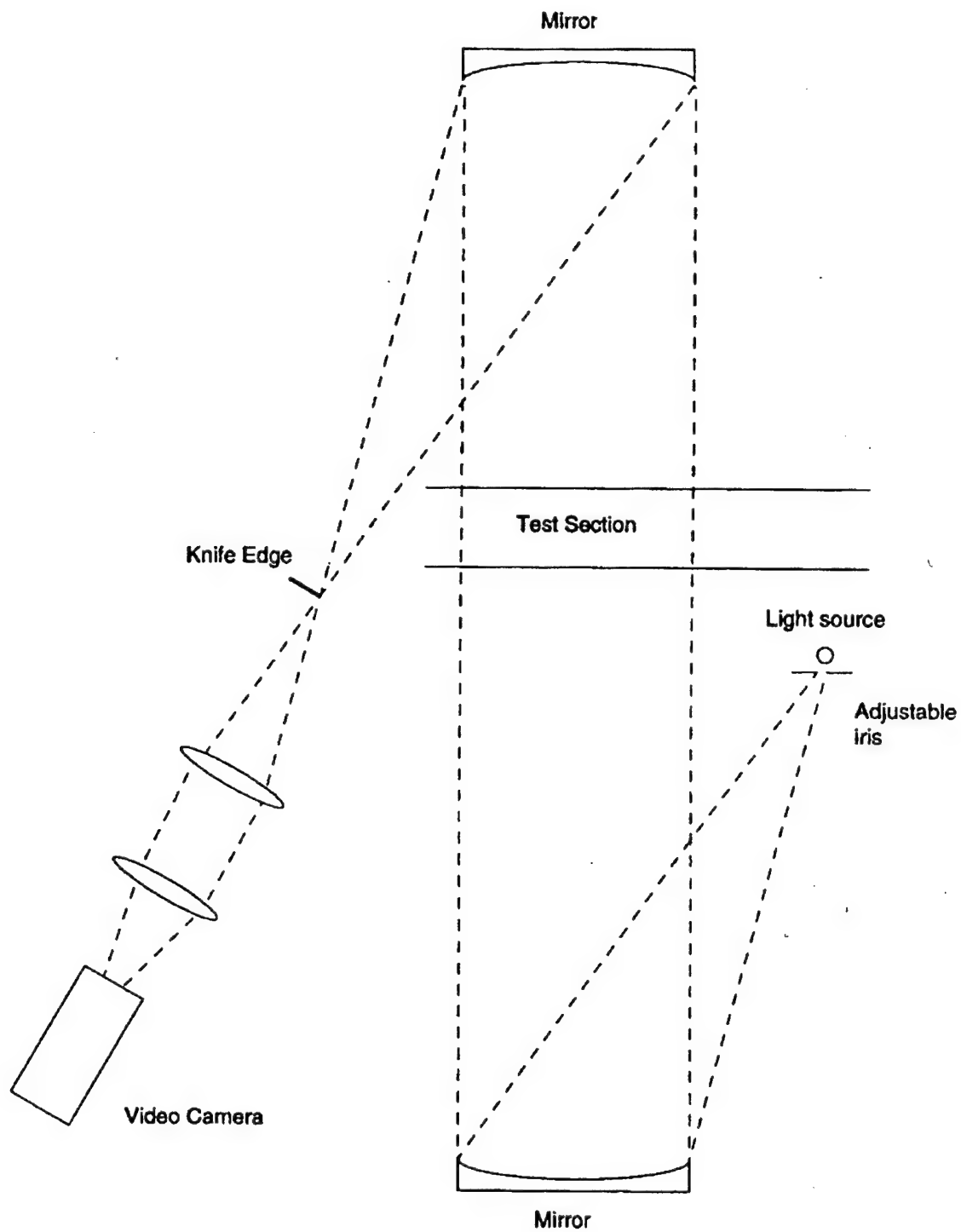
Figure 2.10: A typical two-mirror schlieren system.

Chapter 3. Supersonic Combustion Experiments

Introduction to H_2-O_2-N_2 Experiments

The experiments described in this thesis were designed to investigate chemical reaction of the hydrogen-oxygen system in a laminar boundary layer formed over a test model in supersonic flow. Initially, it was necessary to characterize the system to ensure design conditions were satisfied for the new Supersonic Combustion Facility (SCF). Because combustion experiments at the proposed conditions had never been performed prior to this study, much effort was directed toward the task of identifying optimal parameters for operation of the system. Extreme test conditions required variation of experimental parameters to alter the mixing and fluid dynamics in order to understand the physical processes underlying the observed phenomena.

Part of this process involved examining a number of different test model geometries including:

- Flat plates, with and without catalytic platinum coating
- 12.7 degree (total angle) wedge

In addition to implementing different test section models, varying the location of hydrogen injection provided a range of fuel-oxidizer mixing upstream of the nozzle throat (Figure 3.1). As the injector exit plane is moved closer toward the throat, less time is provided during which the fuel can mix with the nitrogen and oxygen. Turbulent Reynolds numbers inside the settling chamber, combined with longer residence times due to low subsonic convective velocities provides effective mixing for the gas stream prior to entering the two-

dimensional transition. In the most extreme non-mixed case, the injector was positioned 2.54 cm upstream of the throat.

In the remainder of this chapter, the experiments performed in the SCF are described and the corresponding results presented. Many trials were performed for each experimental configuration and chemiluminescence images are meant to be representative of each test sequence as a whole. A summary of experimental conditions is compiled in Table 3.1. The methodology behind various modifications is detailed, although analysis of the observations is reserved for Chapter 4.

<div align="center">Table 3.1: Summary of Experimental Conditions</div>

Test Section Geometry	Injector Position	T_0 (K)	P_0 (atm)	Mole Fraction (%)		Figure	Notes
				$H_{2, inj}$	O_2		
Flate Plate	1	920	0.65	5%	10%	3.4; 3.5	a
Flate Plate	2	930	0.66	3%	10%	3.6; 3.7	b
Flate Plate	2	930	0.66	3%	10%	-	c
Flate Plate	3	950	0.66	<20%	10%	-	d
Wedge	3	1070	0.53	1% - 3%	20%	3.9	e
Wedge	3	1070	0.53	1%	20%	3.10; 3.11	f

[a] Chemiluminescence in boundary layer and wake

[b] Emission outlines shock structure

[c] Counter-flow fuel injection

[d] No chemiluminescence

[e] Transient pre-reaction in throat

[f] Chemiluminescence surrounds wedge

3.1 Laminar Boundary Layer over a Flat Plate in Supersonic Flow

A 0.16 cm thick stainless steel flat plate of length 5.4 cm was inserted at the centerline of the wind tunnel. The top surface of the plate was coated with a thin catalytic film, approximately 0.1 mm thick, applied using a platinum compound based paint which was heated in an oven leaving a pure platinum surface. (Ace Glass Corp., 1995) The flow was turned along the bottom of the plate by a 14° angle, in order that the boundary layer formation along the top of the plate remain undisturbed by the presence of an oblique shock. The tip of the

flat plate was positioned 8.9 cm from the nozzle throat, at the beginning of the constant area test section.

A typical shock formation over a flat plate similar to that used in the reacting flow experiments is shown in Figure 3.2. The flow is non-reacting with a stagnation pressure of 0.6 atm and stagnation temperature of 420 K. Clearly visible are the oblique shock created from turning the flow beneath the plate, and the subsequent expansion fan. The shock structure seen above the plate is the weak shock created from initial formation of the boundary layer along the top surface of the plate. Measurements of the shock angles give a value for the free stream Mach number of 2.8. The computed Mach number (corrected for boundary layer growth) at these conditions is 2.85, in good agreement with the experimental measurement.

The boundary layers are visible over both the plate and at the walls of the test section, and the shear layer formed in the wake of the test geometry is also apparent. Measurement of the boundary layer thickness over the plate gives a value of 0.6 mm, in excellent agreement with a calculated value of 0.56 mm at the end of the flat plate assuming a laminar boundary layer. The flat plate used in the experiments described below differs in that the rear portion of the plate is flat instead of tapered as shown in the schlieren frame. The support for the flat plate models (silhouetted beneath the plate in Figure 3.2) consists of a diamond-shaped wedge to minimize blockage.

Injector Position 1

Fuel hydrogen exited from a tube with a 0.178 cm diameter opening at the center axis of the chamber in the same direction as the heated tunnel nitrogen and oxygen flow. The hydrogen was injected at room temperature (298 K) in a short duration pulse (~ 1 sec) for safety reasons and to eliminate possible transient effects inside the test section due to excessive heating of metal surfaces. The total temperature measured in the test section prior to fuel injection was 810

K (T_0 = 920 K). Combustion heating was used with a hydrogen flow rate of 1% by volume.

During fuel injection at the downstream port, chemiluminescence was observed to fill the entire converging portion of the nozzle (Figure 3.3), clearly indicating that reaction was initiated at a location upstream of the throat. It appears that the system is frozen through the nozzle, and images of the plate (Figure 3.4) revealed that chemiluminescence was visible in the boundary layer on the top and bottom of the plate, as well as in the subsonic wake at the rear of the plate. Figure 3.5 is a grayscale representation of the same image, with flow structures overlaid showing the parameters in each region calculated from known experimental initial conditions (stagnation temperature, pressure, and Mach number).

The qualitative nature of the diagnostic makes it difficult to quantify how much of the fuel was consumed prior to entering the test section, although one-dimensional calculations indicate that reaction was probably completed upstream of the nozzle (modeling is discussed in Chapter 4). Temperatures in the test section, measured slightly downstream of the subsonic wake, exceeded 1100 K during the fuel injection, although the response time of the thermocouple together with the short injection time likely makes this a conservative estimate of the actual temperature rise.

Chemiluminescence did not appear preferentially over the top or bottom surface of the plate, and absolute intensities varied slightly for different trial runs. This would be consistent with incomplete turbulent mixing of the gases within the tunnel. Typical boundary layer thickness over the top of the plate was measured to be 1 mm, comparing very well with 0.9 mm predicted by the Blasius solution. Note that the luminous region within the boundary layer appears to vary in thickness over its length.

When settling chamber total temperatures were lowered such that ignition of the hydrogen did not occur upstream of the throat, no chemiluminescence was observed in the test section. The absence of pre-reaction

inside the settling chamber was identified by a decrease in total temperature during fuel injection rather than a temperature rise, and the lack of chemiluminescence in the contraction of the nozzle.

Allowing the gas mixture to react inside the settling chamber and inlet, and then quench through the nozzle provides a means of eliminating the induction time associated with the boundary layer problem. High radical concentrations frozen in the flow after the expansion would more quickly initiate reaction inside the boundary layer as a result of the recovery temperature at the surface. In subsequent experiments, attempts were not made to suppress reaction upstream of the nozzle during hydrogen injection.

Injector Position 2

The injector position was moved closer to the nozzle throat in an effort to ensure unburned fuel was present inside the test section. A second injector was constructed to compensate for the reduced mixing time and increase fuel distribution along the vertical axis of the tunnel. This design employed five equispaced holes of 0.5 mm diameter, arranged vertically to fill the inlet region with hydrogen. Hydrogen was injected at a temperature of 298 K.

Experimental conditions were kept approximately the same as in the first experiment. For hydrogen injection flow rates up to 3% by volume overall, ignition occurred upstream of the contraction as evidenced by chemiluminescence in the nozzle. In this configuration however, test section chemiluminescence was no longer confined to the boundary layer and the wake region of the flat plate. The emission (Figure 3.6) filled the test section for hydrogen mass flow rates of 3% by volume of the total flow. Beneath the plate, the oblique shock and expansion fan are clearly outlined as a result of the chemiluminescence. The Mach number for this run was calculated to be 2.5 from pitot measurements without fuel injection, although the angles of the shocks highlighted by the chemiluminescence along the top and bottom of the plate are more indicative of a Mach number of about 2.6 as shown in Figure 3.7. The

intensity of the chemiluminescence clearly increases behind the oblique shock, and then decreases in intensity as the pressure drops through the Prandtl-Meyer expansion.

Some luminosity is visible in the boundary layer on the plate surface which increases in intensity at a distance of 1.5 cm from the plate tip. The thickness of the luminous layer is around 0.4 mm (± 0.15 mm) compared with a non-reacting laminar calculated value of 0.9 mm. Chemiluminescence did not always appear in the boundary layer, and in instances where it did occur, it did so at the start of hydrogen injection and then tended to disappear as the tip of the plate began to heat.

As with the previous injector position, unless reaction was initiated upstream of the nozzle, no chemiluminescence was observed in the test section. Test section temperatures in the wake of the flat plate were measured in excess of 1000 K for the maximum injected hydrogen flow fraction.

At the same streamwise position, the five-hole injector was rotated such that the fuel was now directed upstream in a counter-flow configuration with the heated nitrogen and oxygen. For conditions identical to those described in the previous section, observed chemiluminescent patterns were similar with a few exceptions:

- Luminous intensity behind the shocks was slightly decreased.
- Chemiluminescence was observed more consistently (compared with the co-axial fuel injection case) in the boundary layer on both surfaces of the plate. But this emission occurred mostly at the upper leading edge of the plate, and intensity decayed with distance along the plate and eventually vanished.
- No chemiluminescence was visualized in the wake region.

Injector Position 3

Returning to the co-axial open tube injector, the exit plane of the tube was moved inside the converging portion of the nozzle. At this position, the pressure

56

ratio P/P_0 is 0.99 and T/T_0 is 1.00, and the Mach number of the main tunnel flow is about 0.12. For stagnation pressures of 0.65 atmosphere, hydrogen was injected at 298 K with fuel flow rates up to 20% by volume. Stagnation temperatures were as high as 950 K and oxygen concentrations were 10% by volume. At these conditions, no chemiluminescence was observed anywhere in the nozzle or in the tunnel. Test section temperatures measured in the wake of the flat plate showed significant temperature drops during hydrogen injection.

3.2 Wedge Configuration

A 12.7 degree (total angle) wedge geometry was designed such that oblique shocks form over both sides of the wedge, with consequent increase in static pressure and temperature. The rear of the wedge was truncated to create a large recirculation zone in the wake and the model thickness was increased to 3.18 mm. It was anticipated that longer residence times associated with local subsonic velocities in the wake would make conditions more favorable for reaction. Overall length of the model is 2.7 cm.

Schlieren of the wedge in supersonic flow is presented in Figure 3.8. Stagnation conditions are $P_0 = 0.7$ atmosphere and $T_0 = 420$ K. After measuring the angle β of the shock emanating from the tip of the wedge and knowing the flow deflection θ, the Mach number was determined from oblique shock tables ($\theta = 6.34°$, $\beta = 28°$) giving a value of M = 2.6. The structure of the wake is visible including the corner expansion, wake shock, and recompression shock in the downstream region. Slight asymmetry in the flow downstream of the wedge is a result of the model support (swept-back shape silhouetted in the figure) generating oblique shocks from the side and lower wall, and the interaction with the two-dimensional wake.

Effects of Fuel Heating

A fuel line heater was added to the system to bring the hydrogen temperature closer to that of the main tunnel flow. The heater consists of an 800 watt oven (Lindberg) through which passes 15 feet of 1/8" copper tubing formed into a roughly 1" outer diameter coil. With stagnation conditions of $P_0 =$ 0.53 atmosphere and $T_0 = 1070$ K, and oxygen concentrations of 20% by volume, increasing fuel temperature from 298 K to 746 K resulted in observations of faint chemiluminescence in the throat region. This chemiluminescence was unsteady and had an appearance similar to a lifted diffusion flame (Figure 3.9a). As the hydrogen flow rate was decreased from five percent by volume to roughly one percent at the stated conditions, the injection process eventually stabilized into a hydrogen jet diffusion flame (Figure 3.9b).

Increased mass flow rates while the chemiluminescence was unstable resulted in lifted flames and subsequent blow-off of the reaction zone due to high exit velocities. Once the flame was stabilized on the injector tube, it was difficult to obtain any lifting by increasing fuel flow rates up to 7%.

Diffusion Flame over Wedge

With the hydrogen injector burning in an unstable mode through the nozzle as described, some faint chemiluminescence was detected downstream in the test section over the wedge, and this too exhibited unstable behavior. After stabilization at the injector tube was established, chemiluminescence surrounded the wedge in a definite pattern as shown in Figure 3.10. This pattern clearly outlines the fluid mechanical structures such as the oblique shocks emanating from the wedge tip. The luminosity appeared to extend over the length of the nozzle expansion from the injector right up to the wedge location and through the tunnel, and only the intensity varied. Pressure and temperature flow conditions are overlaid on the corresponding grayscale image in Figure 3.11.

Other observations:

- Chemiluminescence continued though the entire length of the test section in a thin region above and below the wedge.
- The boundary layer over the wedge appears to be a region of less intense reaction.
- Luminous intensity in the wake was virtually nonexistent, indicating that no reaction was occurring in the zone.
- Immediately behind the oblique shocks over both sides of the wedge, some sort of shock train is highlighted because of greater luminous intensity. This is more apparent over the upper surface in equivalent grayscale images (Figure 3.11).
- Attempts to ignite the mixture in the wake were carried out unsuccessfully using a 0.25 mm tungsten wire as a thermal source.

The Mach number is 2.1 as measured from the leading luminous oblique shocks. Non-uniformity in composition and temperature resulting from mixing and reaction would result in a flowfield that is highly three dimensional; thus, it is likely that this Mach number is not representative of the entire flow.

Wedge Boundary Layer Observations

Boundary layer thickness was measured from the interface of the regions of high and low luminosity above the wedge surface. These measurements give a thickness of around 0.4 mm (± 0.15 mm), though the validity of this technique may be subject to significant error considering the apparent nonequilibrium nature of the flow. Nonetheless, the theoretical boundary layer thickness for these conditions is 0.5 mm which indicates reasonable agreement.

Over a period of trials employing the wedge model and diffusion flame mode of injection, the metal at the center front edge began to ablate. As the ablation worsened, it created a stagnation point and the luminosity during fuel

injection became very intense at this point. This zone of localized intense reaction did not appear to affect the chemiluminescent pattern, nor did it appear to stimulate reaction in the boundary layer downstream. Eventually, the model had to be removed from the test section.

3.3 Figures
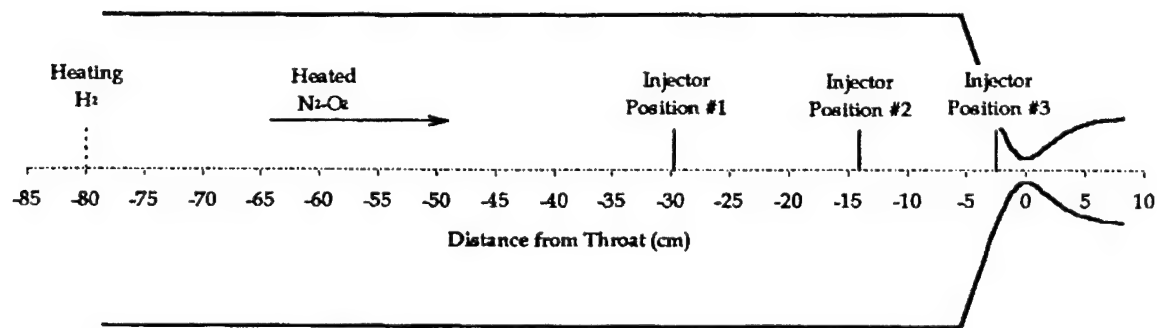
Figure 3.1: Schematic of the injector positions used in this study relative to the throat and nozzle. The start of the settling chamber occurs at $x = -80$ cm, and the test section begins at $x = +9$ cm.
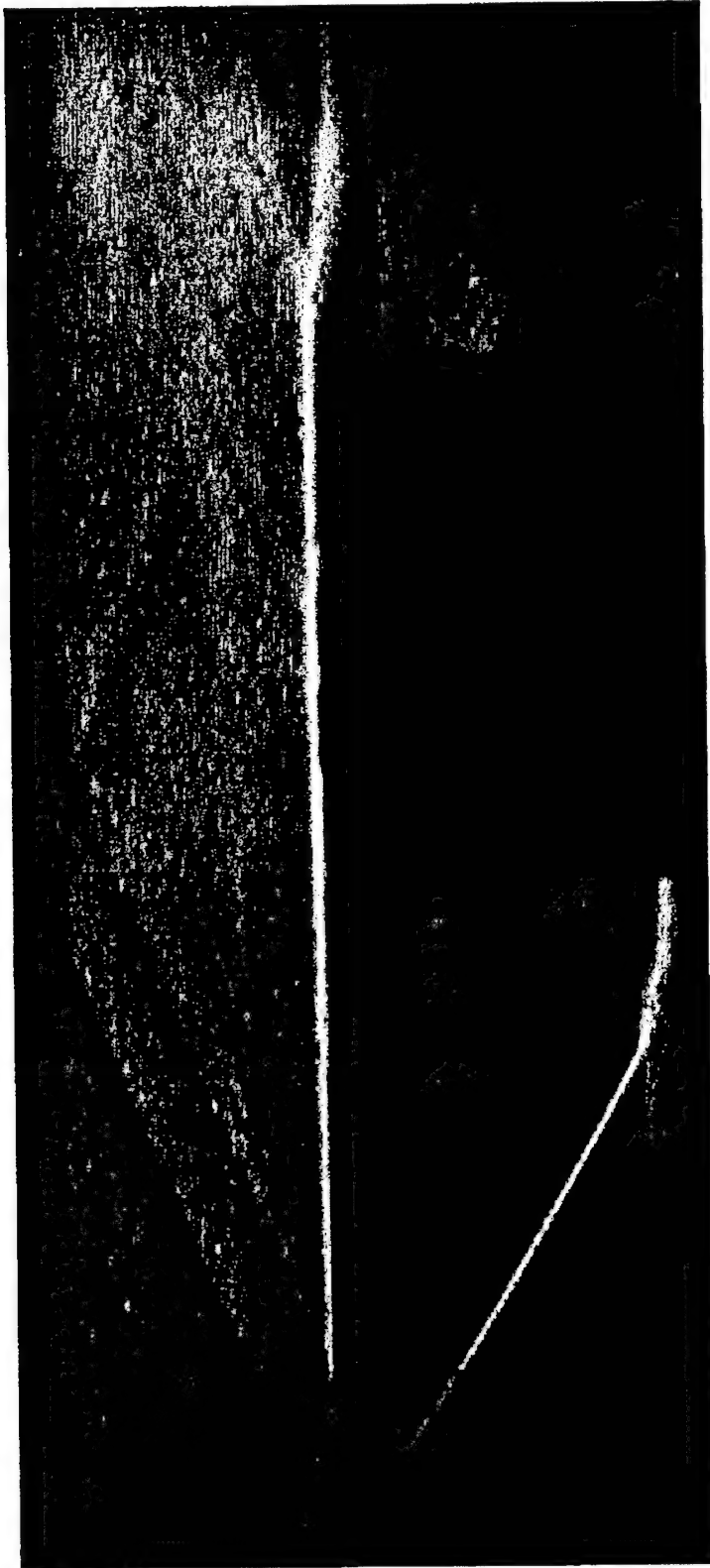
Figure 3.2: Schlieren frame of flow over a flat plate at Mach 2.8 in the Supersonic Combustion Facility.
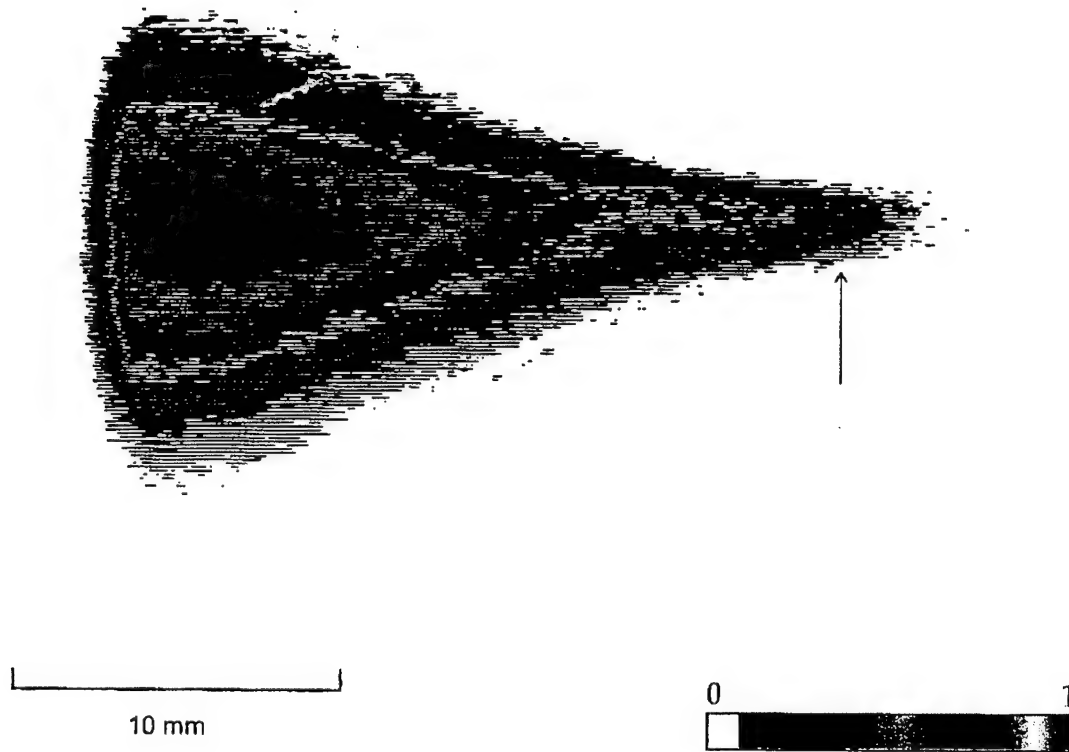
Figure 3.3: Chemiluminescence image showing reaction in the contraction of the nozzle. The arrow indicates the location of the throat. Injector position for this condition is x = -29.8 cm.

10 mm

0   1
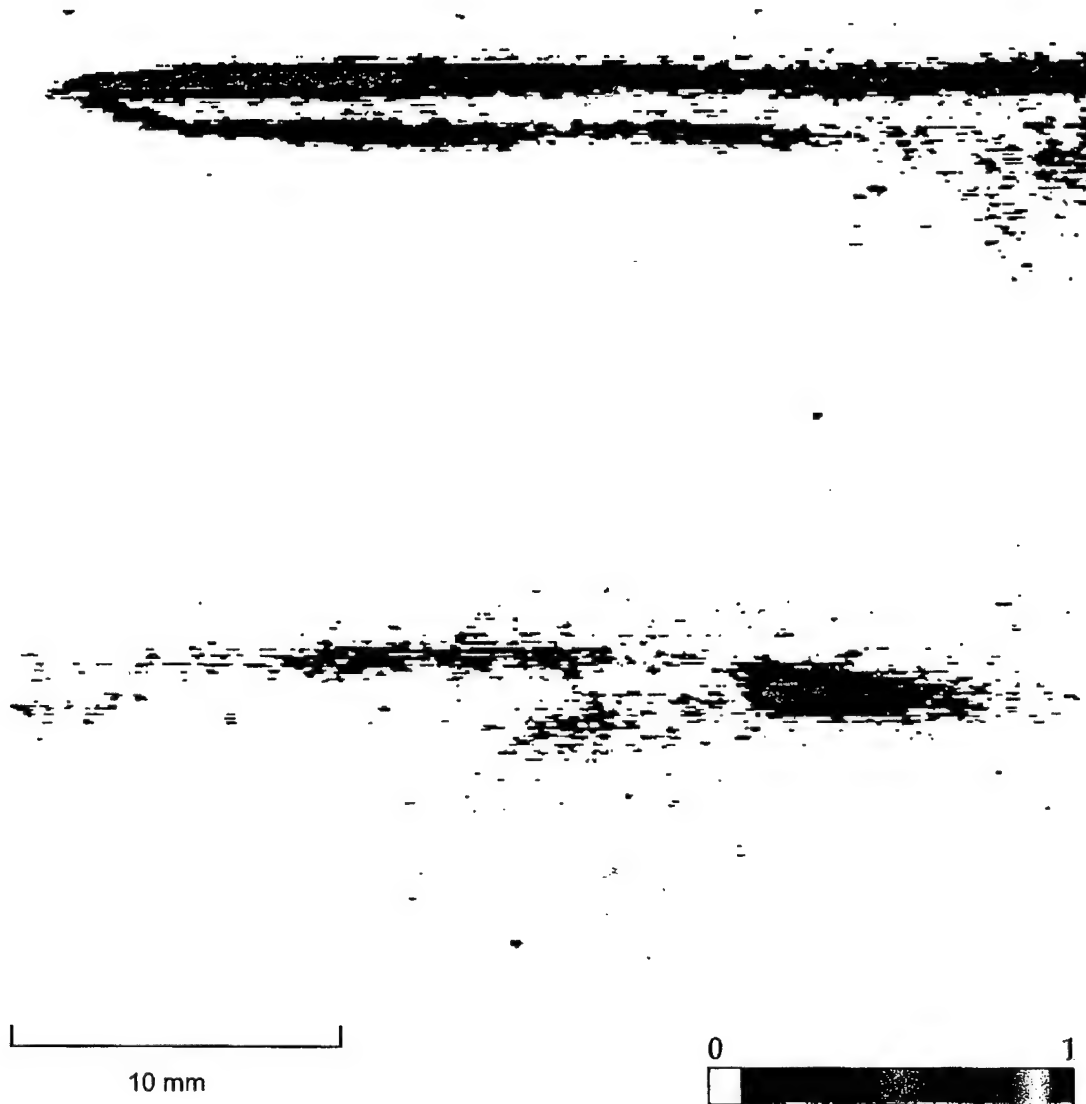
Figure 3.4: (a) Chemiluminescence over the flat plate for the same experimental conditions as in the previous figure. The thickness of the plate (visibly outlined by the emission) is 0.16 cm. (b) Same as above, except showing the rear of the plate and emission in the wake.

M = 2.6
P_0 = 0.66 atm
T_0 = 920 K
P = 0.03 atm
T = 391 K

Mach Line

Boundary Layer

M = 2.55
P = 0.03 atm
T = 400 K

M = 2.0
P = 0.08 atm
T = 512 K

Oblique Shock

Expansion Fan
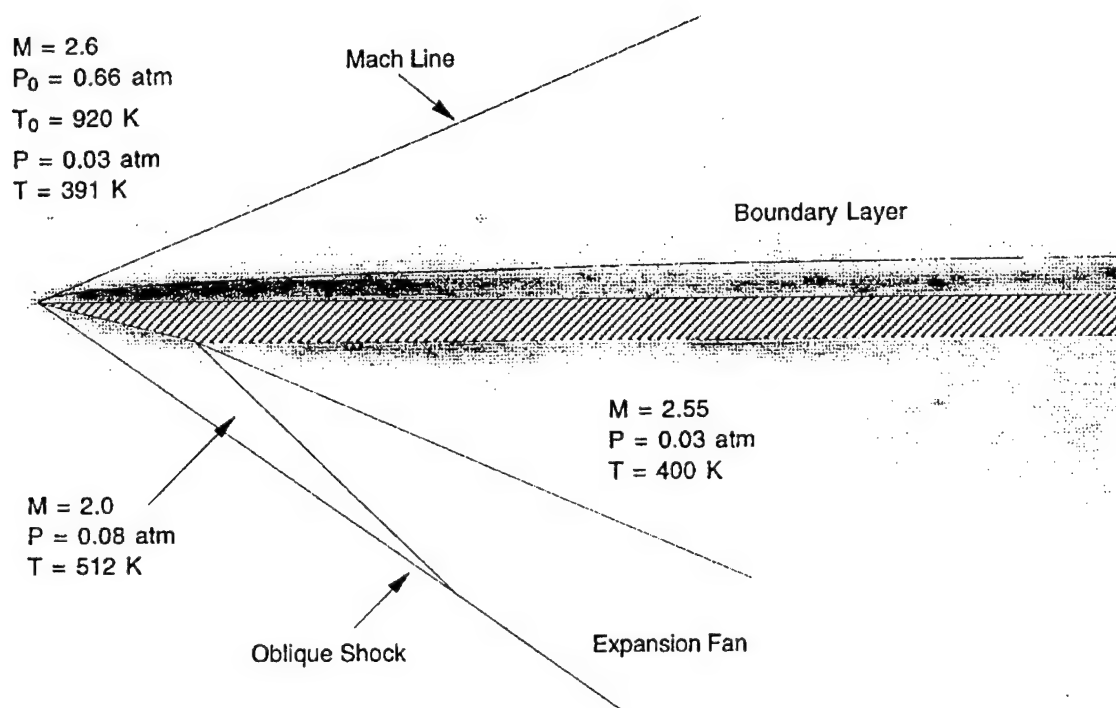
Figure 3.5: Shock structures and pressure-temperature conditions corresponding to Figure 3.4(a).

10 mm

0 ▮▮▮ 1
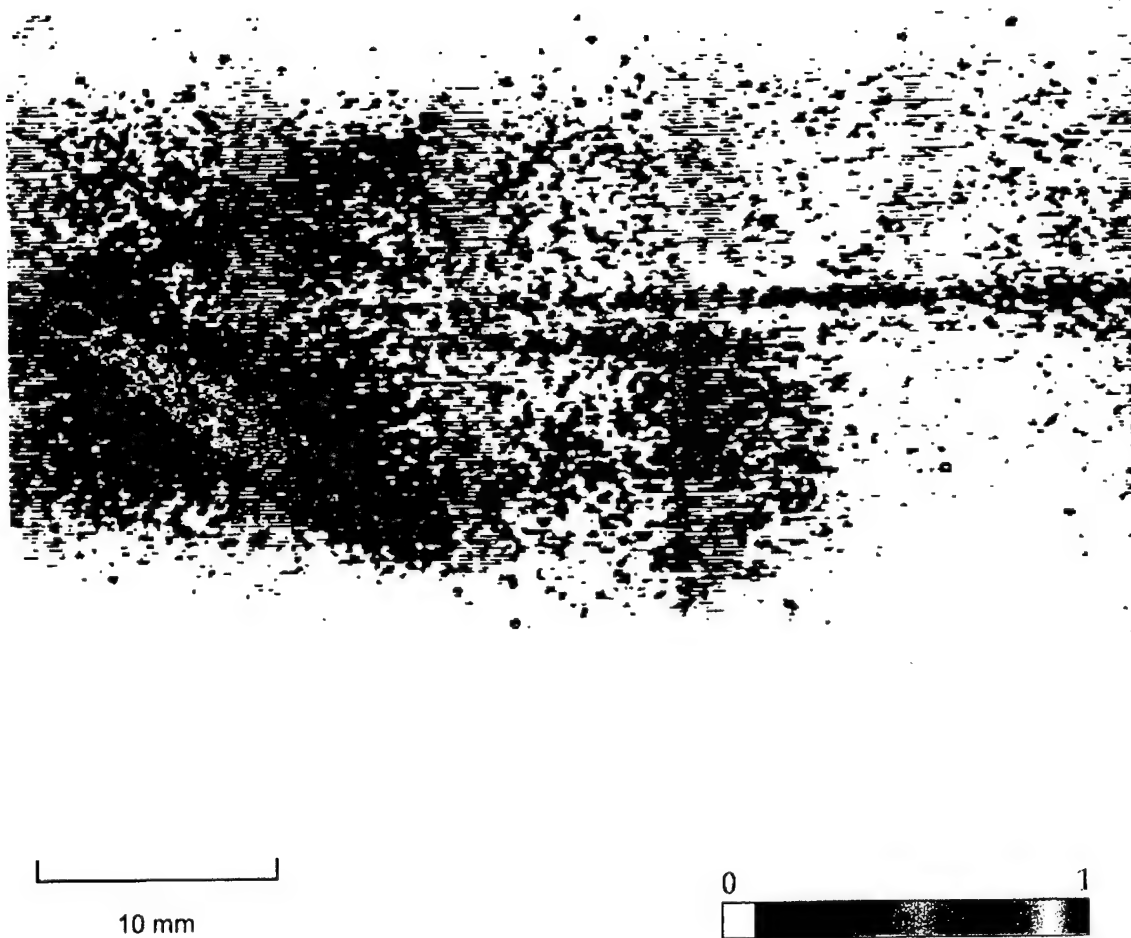
Figure 3.6: Chemiluminescence over the flat plate for injector position 2. Emission is now most intense in the region behind the oblique shock, and the boundary layer emission appears less intense than in the previous figure.

M = 2.5
P_0 = 0.66 atm
T_0 = 930 K
P = 0.04 atm
T = 413 K

Mach Line

Boundary Layer

M = 2.46
P = 0.04 atm
T = 422 K

M = 1.92
P = 0.09 atm
T = 536 K

Oblique Shock

Expansion Fan
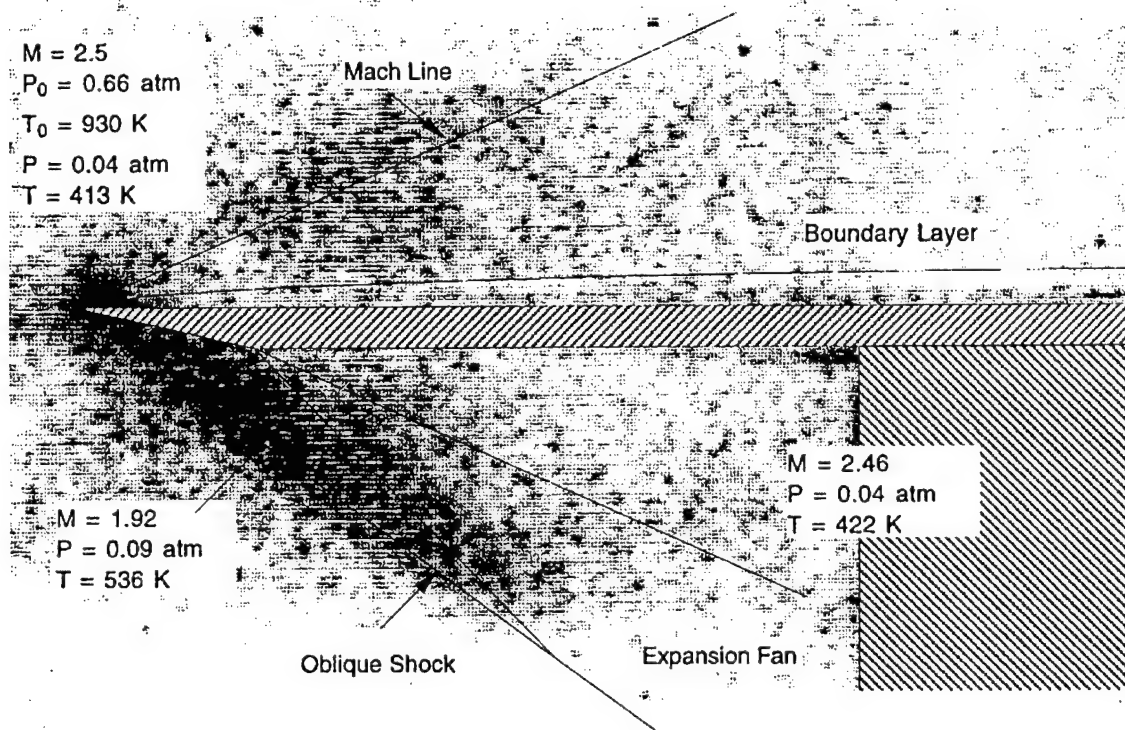
Figure 3.7: Shock structures and pressure-temperature conditions corresponding to Figure 3.6.
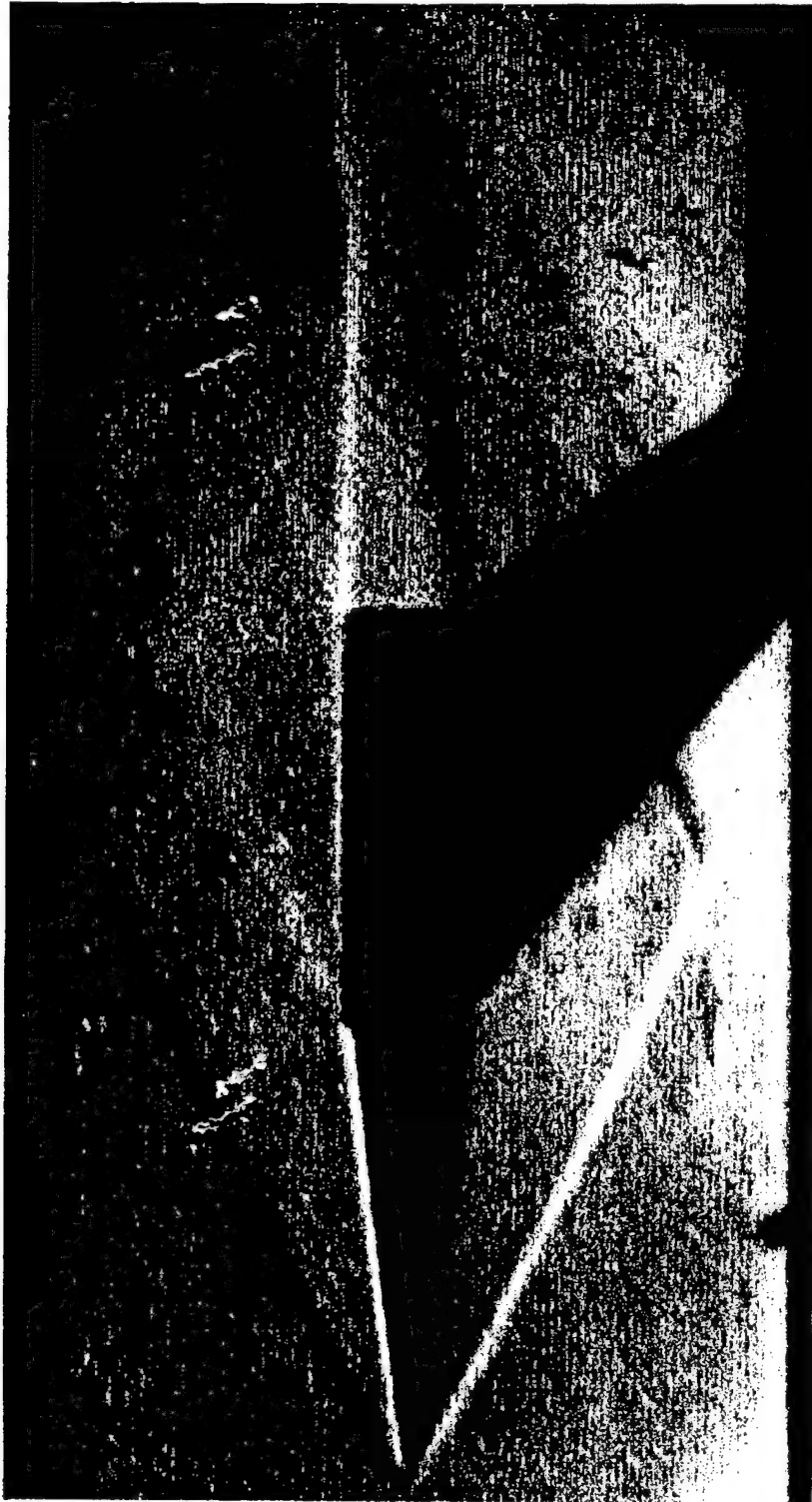
Figure 3.8: Schlieren frame of the wedge test model at Mach 2.6 in the SCF.

10 mm

0   1
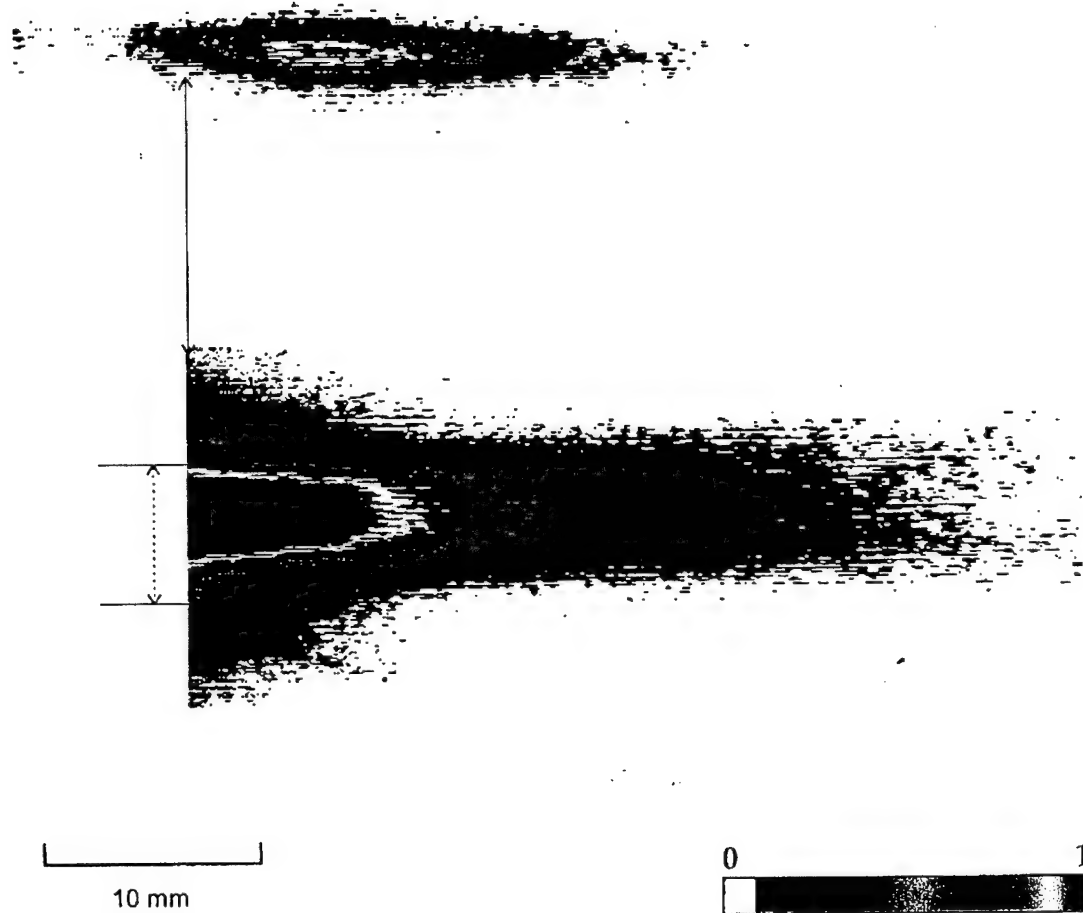
Figure 3.9: (a) Unsteadiness in the pre-reaction following hydrogen injection at $x = -2.54$. (b) Subsequent stabilization of injector in a diffusion flame configuration. The throat height (6 mm) is indicated on the lower image (saturation of the intensified array creates some smearing in the picture outside these lines). The solid arrow indicates the throat position.
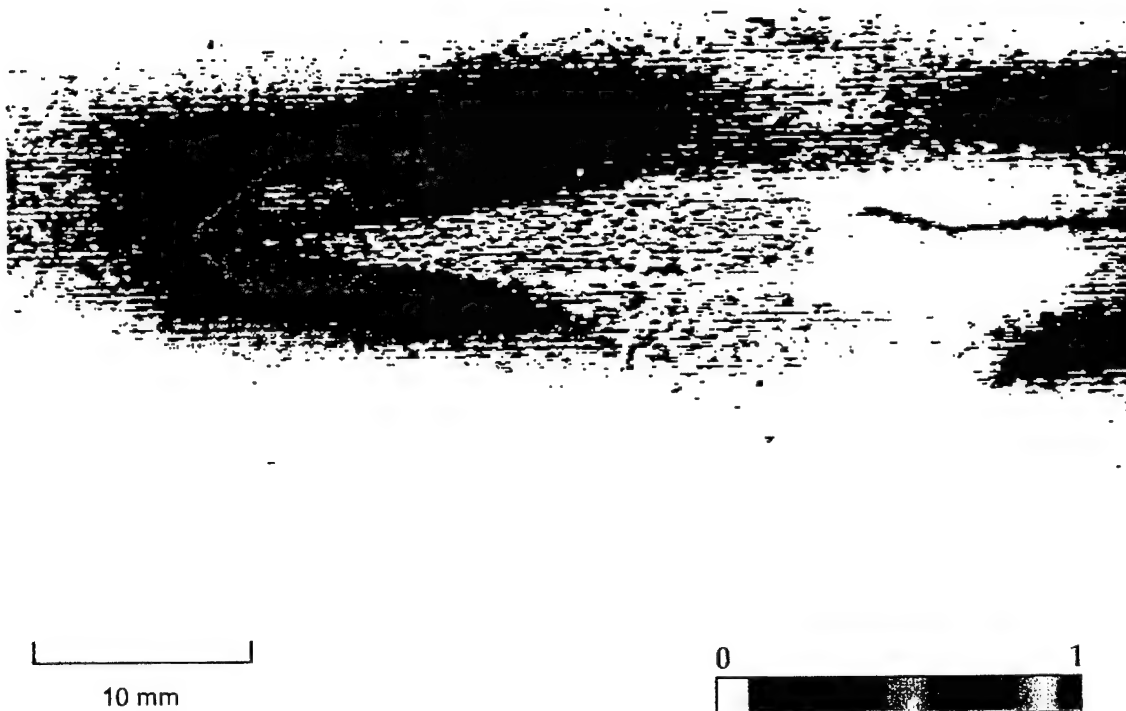
Figure 3.10: Chemiluminescence surrounds the wedge with the injector mode as shown in Figure 3.9b. The most intense region of emission occurs behind the oblique shock near the front of the wedge. Emission continues down the tunnel and the dark regions at the far right are a result of reflected shock interactions. The line (far right, middle) is a tungsten element used in an attempt to stimulate ignition in the wake.

M = 2.1
P_0 = 0.53 atm
T_0 = 1070 K
P = 0.06 atm
T = 569 K

M = 2.1
P = 0.06 atm
T = 570 K

Wake

Oblique Shock

M = 1.87
P = 0.08 atm
T = 630 K

Expansion Fan
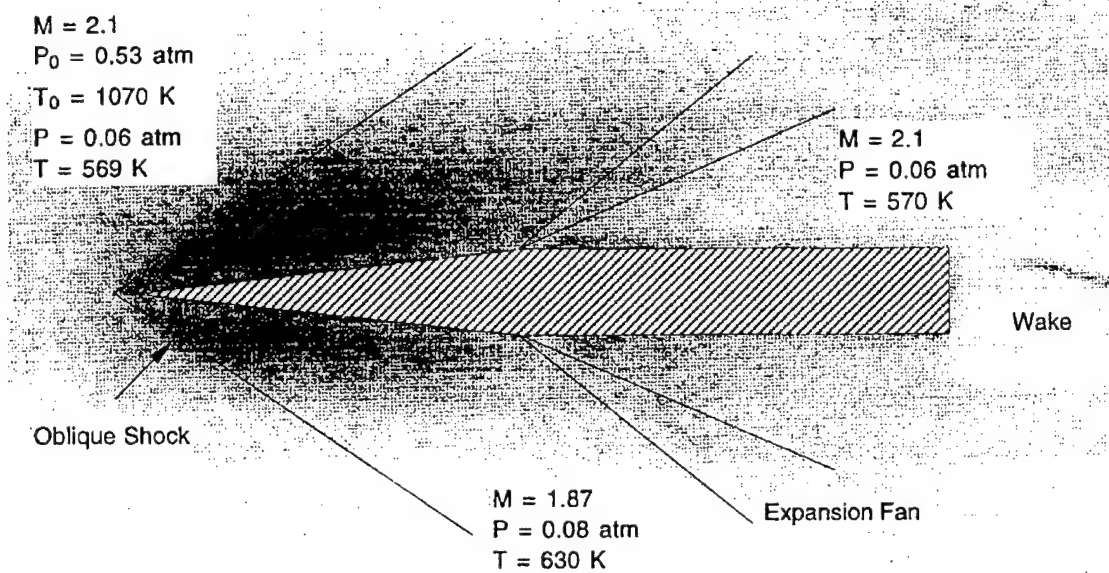
Figure 3.11: Shock structures and pressure-temperature conditions corresponding to Figure 3.10.

Chapter 4. Analysis of Hydrogen-Oxygen-Nitrogen Supersonic Combustion Experiments

Introduction

Experimental results were obtained for a variety of flow conditions, fuel injection locations, and test model geometries. The observed chemiluminescence patterns and their corresponding experimental parameters were described in the previous chapter. In this chapter, qualitative analyses are combined with modeling results to clarify these observations and to better understand the physical processes occurring within the apparatus.

The direction of the experimental program was determined largely by results obtained using ultraviolet imaging techniques for visualization of the excited hydroxyl radical chemiluminescence. The hydroxyl radical has importance for its role in ignition processes and as an indicator of regions of chemical reaction. Thus, before analyzing the results from individual experiments, it is necessary to elucidate the relationship between the hydroxyl radical in its electronically excited form and in the ground state through a discussion of the kinetic pathways which are responsible for OH* formation.

4.1 Chemiluminescence in H_2-O_2 Systems

Reactions leading to the formation of the hydroxyl radical in its electronically excited state (OH*) have been examined for H_2/O_2 systems by Gaydon (1957), Kaskan (1959), Davis, et al. (1973), and Hidaka, et al. (1982). True chemiluminescence in a reacting hydrogen/oxygen system is considered to be the OH* emission resulting from the transition from the first electronic energy level to the ground state ($^2\Sigma^+$-$^2\Pi$), with emission intensities which exceed those

expected from equilibrium considerations. Thermal equilibrium will produce a Maxwell-Boltzmann distribution over the allowable energy states, which for the electronic excitation would give

$$\frac{N^*}{N} = e^{-h\nu/kT} \tag{1}$$

where N^*/N is the fraction of particles in the excited state with excitation energy $h\nu$. In addition to thermal equilibrium, Gaydon (1957) noted that chemical non-equilibrium due to excess radical concentrations would result in abnormally high population of electronically excited states.

Kaskan (1959) found a third order dependence of OH^* on the concentration of the ground state molecule for atmospheric pressure $H_2/O_2/N_2$ flames. This led to the conclusion that the OH^* radiation was non-thermal in nature, since that would require intensity be proportional to the first power of $OH\ ^2\Pi$. Instead, he proposed that the $[OH]^3$ dependence indicated that $OH\ ^2\Sigma^+$ was formed as a result of reactions between species formed in excess of their equilibrium values. Thus, the reactions proposed for OH^* formation involve radical recombination:

$$H + H + OH \rightarrow H_2 + OH^* \tag{2}$$
$$H - OH + OH \rightarrow H_2O + OH^* \tag{3}$$
$$O + H \rightarrow OH^*\ (v' = 2, 3) \tag{4}$$
$$O + H + M \rightarrow OH^*\ (v' = 0) + M \tag{5}$$
$$O + H_2 + OH \rightarrow H_2O + OH^* \tag{6}$$
$$H + O_2 + H_2 \rightarrow H_2O + OH^*. \tag{7}$$
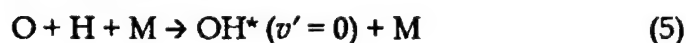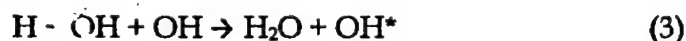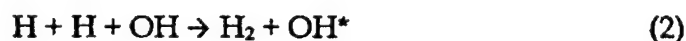
The v' indicates the vibrational energy level likely to be filled as a result of the reaction. Reactions (2), (3), (6), and (7) will generate a distribution of energy levels, with $v' = 0$ most highly populated.

73

Reaction (4) is the inverse pre-dissociation process which in the absence of a third body results in greater energy stored in upper vibrational levels via the route

$$O + H \rightarrow OH\ (^4\Sigma^-) \rightarrow OH\ (^2\Sigma^+)$$
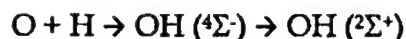
involving a radiationless transition between the two electronic levels for $v' = 2$ or higher (Gaydon and Wolfhard, 1979).

Of these, reaction (3) was identified as contributing most significantly to the intensity of OH* emitted in the 0-0 band for flames (Kaskan, 1959), while reaction (2) did not contribute significantly to emission in any band. Also, since it does not require a third body, the pre-association reaction (4) was concluded to have greater importance in low-pressure systems for emission in the higher bands, eg. the 2-1 and 3-2 transitions. Davis et al. (1973) reported that for lean pre-mixed hydrogen-oxygen flat flames, the contribution to OH* from reactions (5-7) could not be distinguished from contributions by reaction (3), indicating that the entire set of reactions were important in the overall emission.

Shock tube studies of highly dilute H_2-O_2 mixtures were performed by Hidaka et al. (1982) in the range 1200-3200 K at pressures of 50 and 100 torr. Their results showed that reactions (4) and (5) were primarily responsible for OH* emission in their system, with the two-body reaction more important at 50 torr and the termolecular reaction dominating at 100 torr. The proximity of the pressure range examined in this experimental work to that of Hidaka's shock-tube study and the dilute nature of both systems suggests that the mechanism identified for chemiluminescence in that work

$$O + H\ (+ M) \rightarrow OH^*\ (+ M)$$
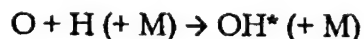
is likely to be the major contributor to OH* emission in the SCF.

Once the excited molecule is formed, de-excitation occurs through one of two possible paths:

$$OH^* \rightarrow OH + h\nu \qquad (8)$$

$$OH^* + M = OH + M. \qquad (9)$$

The first of these reactions describes the radiative de-excitation via spontaneous emission of a photon during the $^2\Sigma^+$-$^2\Pi$ electronic transition while the second corresponds to collisional quenching of the excited radical. The strongest emission in atmospheric flames is observed at a wavelength of 306.4 nm corresponding to the 0-0 band.

4.2 Numerical Modeling Technique

In order to better interpret the experimental results, numerical modeling was performed using the hydrogen-oxygen kinetic mechanism presented in Table 1.1 and several different computational methodologies. This was not intended as an attempt to validate the mechanism under specific experimental conditions, but rather an effort to further clarify the local and global conditions in a non-uniform reacting flow. For simulating the conditions within the variable area nozzle, a quasi one dimensional code was employed (Yetter, 1996). Within the test section and boundary layer, the pressure remains approximately constant, allowing the use of a zero dimensional, constant pressure, adiabatic physical model. These assumptions allow a simplified, first approximation to the reacting boundary layer problem which will inevitably involve transport effects. The impact of this approach will be assessed in individual cases. With both modeling techniques, the systems are assumed to be homogeneous, and heat transfer is neglected.

The one dimensional code models a flowing, non-constant area, chemically reacting system with specified kinetics. User defined inputs include the following parameters:

- The area of the duct as a function of axial position A = A(x)
- Initial pressure, temperature, and velocity of the flow
- Initial species concentrations

The program simultaneously solves the mass, momentum, and energy equations, coupled with the species continuity equations for the reacting system using a standard ordinary differential equation solver. The program employs the CHEMKIN-II chemical kinetics package (Kee, et al., 1989) for handling the reaction mechanism and species information. Discretized spatial stepping is employed using a pre-defined step size, and the procedure halts when tolerance conditions fail at any point. The problem becomes numerically stiff during integration through the throat where M = 1, so calculations are run in two parts for modeling the contraction and expansion portions of the nozzle. Estimates of reaction within the boundary layer can be performed using SENKIN (Lutz, et al., 1987) with the initial conditions determined from the one dimensional calculations.

4.3 Mixing Efficiency

Whether the chemiluminescence observed in the various cases was a result of fuel reacting locally within the test section, recombination of radicals formed upstream of the nozzle throat, or merely thermal effects remained an issue in the early experiments. This motivated re-positioning the injector and examining the effect of mixing on the chemiluminescence intensity and pattern.

Moving the injector closer to the throat has the following effects associated with reducing the residence time of the hydrogen in the subsonic portion of the tunnel upstream of the throat:

1. Less mixing time for the hydrogen in the nitrogen-oxygen flow. This creates regions of high H_2 concentration along the centerline, and in general, greater stratification of the flow.

76

2.   When reaction begins upstream of the throat, less time is available for complete reaction, ensuring unburned H_2 survives into the test section. This reduces the overall amount of radicals in the test section, but may create local "hot spots" of high radical concentration and increased temperature in the flow.

The extent of mixing in the flow was determined through comparisons with experiments involving coaxial jets. An overview of the problem was handled by Beér and Chigier (1974), and Alpinieri (1964) studied turbulent mixing of a hydrogen jet in a co-flowing air stream. In the latter study, the ratio of the outer stream velocity u_e to the jet exit velocity u_j, was varied over a range of values, and measurements were made of the centerline concentration and velocity. The decay characteristics for jets with both density and velocity differences between the inner and outer streams were shown to be a function of the ratio:

$$\frac{\rho_e u_e}{\rho_j u_j}$$

For the experiments described in this thesis, this ratio was computed at individual injector locations (Table 4.1).

The jet exit velocities in most experimental cases considered in the SCF are typically a factor of 10 larger than the external stream velocity. The density difference in this case (hydrogen versus N_2/O_2) is so large that concentration decay along the axis is rapid, and studies show little sensitivity to the velocity ratio. (Alpinieri, 1964) The length of the potential core x_p is given by the empirical relation

$$\frac{x_p}{d_0} = 4 + 12\frac{u_e}{u_j}$$

for $u_e/u_j < 1$, where d_0 is the jet exit diameter (0.178 cm). This gives the potential core length as 5.2 diameters or 0.9 cm, assuming that the inner jet is turbulent.

77

Reynolds numbers for the external stream of heated nitrogen and oxygen exceed 5000 for all conditions examined in the settling chamber, putting this flow in a turbulent regime.(Munson, et al., 1990) The jet Reynolds numbers are in the range 1100 < Re < 3500 for hydrogen injection (refer to Table 4.1 below). Reynolds numbers less than 2000 indicate that the jet is laminar, and the potential core length relationship does not apply. However, turbulence from the external stream will cause the eventual breakup of the jet.

Table 4.1: Fuel jet properties.

	Injector Position (cm)		
	x = -29.8	x = - 14 [a]	x = -2.54
Re_{jet}	3500	2100	1100
u_e/u_j	0.079	0.133	0.102
$u_e\rho_e/u_j\rho_j$	0.35	0.59	1.04

[a] Five-hole distributed injector.

Injector Positions 1 and 2

At injector positions 1 and 2, the decay of hydrogen concentration along the centerline occurred rapidly, due to the high momentum ratio between inner and outer jets. Evidence of this was obtained experimentally during schlieren tests and during chemiluminescence measurements in the subsonic portion of the nozzle. Schlieren video images of the nozzle contraction showed little or no stratification during cold flow studies employing a helium jet in nitrogen at the first two injector stations (T_0 = 423 K, T_{jet} = 300 K, P_0 = 0.66 atm). Chemiluminescence during pre-reaction for these two injector locations was observed to be evenly distributed through the contraction (shown in Figure 3.3). The work performed by Alpinieri (1964) indicates under these conditions that the centerline hydrogen mass concentration approaches complete mixing at distances approximately 5 cm ($x/d_0 \approx 30$) from the point of injection.

This analysis shows that the assumption of a well-mixed system is appropriate in the case of injector position 1 because of the long mixing length and turbulent jet Reynolds number. At injector position 2, jet Reynolds numbers are reduced, but the degree of mixedness is large given the long length available combined with the fact that a five hole injector is employed to increase fuel distribution.

Injector Position 3

For injector position 3, the previous analysis cannot accurately predict the centerline hydrogen concentration due to laminar jet conditions. Schlieren imaging of cold flow trials using a helium jet in nitrogen showed rapid decay of density variations. However, this visualization is dependent upon the relative sensitivity of the system. To obtain an approximate quantitative estimate of centerline hydrogen concentrations, the results of the mixing study were applied, allowing roughly half the distance to the throat for mixing (~1.25 cm). Empirical evidence then indicates that hydrogen concentrations could have approached 40% by volume along the centerline. This has significance in the analysis of the wedge experiment which was shown in Figure 3.10 and in the interpretation of the associated modeling results.

4.4 Flat Plate: Analysis

Chemiluminescence in the boundary layer over the plate was observed in configurations where the hydrogen had the greatest residence time upstream, which corresponds to increased extent of pre-reaction. Note the differences between Figure 3.4 in which the boundary layer and wake regions are visible, and Figure 3.6 showing greater emission in the freestream with little or no intensity in the boundary layer. The experimental differences between these two runs are the location of injection, injector type (centerline tube versus five-hole distributed injector), and fuel amount (5% versus 3% respectively).

Calculations were performed to model these two experimental configurations, using the zero and one-dimensional code described previously and assuming complete mixing of the hydrogen in the flow. The validity of this assumption was assessed in the previous section, and no corrections were made to the resulting profiles. To account for combustion of hydrogen used in heating the main flow, this fuel was assumed to form products in equilibrium concentrations and then mole fractions were adjusted for the additional hydrogen added to the stream.

In the first case, pre-ignition is predicted at the end of the settling chamber. Figure 4.1 shows the temperature, H_2 mole fraction, and radical mole fractions as a function of distance from the throat of the nozzle. Complete burnout of the H_2 occurs before the nozzle location is reached, and residual radical concentrations are frozen at the throat. In the second case, pre-ignition is again predicted, but at a location closer to the throat (Figure 4.2) which is consistent with repositioning the injector downstream. Because the amount of fuel added to the stream is lower in the second case, the predicted temperature rise is smaller, although the final frozen radical concentrations increase slightly.

For the injector position 1, the model suggests that the injected hydrogen is consumed prior to the throat and that chemiluminescence over the flat plate in Figure 3.4 is due to the combination of 1) excess radical concentrations in the flow, and 2) high recovery temperatures in the boundary layer and wake. Considering injector position 2, the situation is slightly altered by the proximity of the hydrogen injection to the nozzle. Radical concentrations frozen in the flow by the expansion process are predicted to be higher than for the first injector location, giving rise to the observed shock-enhanced recombination and resultant chemiluminescence in the free stream shown in Figure 3.6. General agreement between the numerical model prediction and observed experimental temperature rise (Table 4.2) appears to validate these remarks on a qualitative basis.

Table 4.2: Predicted and experimentally observed temperature rise.

Test Geometry	Injector Position	T_0 (K)	$\Delta T_{exp.}$ (K)†	$\Delta T_{calc.}$ (K)	Figure
Flat Plate	1	920	280	370	3.4
Flat Plate	2	930	170	220	3.6
Wedge	3	1070	75	0‡	3.10

† Measured at the centerline of the flow downstream of the test geometry.
‡ No heat release was predicted by the numerical model for this condition.

4.5 Wedge Experiments: Analysis

With hydrogen injected at position 3 the flow is highly non-uniform in hydrogen distribution with large centerline concentrations. The assumption of a homogeneous system in this case is invalid, although some insight may still be gained by examining numerical results. Modeling was performed for this injector station assuming a premixed H_2 mole fraction of 10% as a conservative estimate.

The results of this approximate approach are shown in Figure 4.3. No temperature rise is predicted (Table 4.2), although there is fast growth of radical concentrations. It is clear that the radical concentrations frozen through the expansion of the nozzle are likely to be much higher for this configuration than those previously considered and that the distribution is non-uniform. This statement is in agreement with the chemiluminescence observations made for the wedge test model in Figure 3.10.

Thermal emission was ruled out as the primary source of OH* after further examining the wedge experimental results. Consider Figure 4.4, which shows the calculated relative contributions to intensity from thermal emission and radical recombination as a function of temperature at a pressure of 0.05 atm. The thermal OH* line represents an upper bound for this intensity, calculated using the highest predicted OH concentration from modeling ($X_{OH} \approx 10^{-3}$). The predicted contribution from radical recombination reactions (3)-(7) represents a minimum calculated using the equilibrium radical concentrations ($X_{OH} = 10^{-3}$,

81

$X_O = 10^{-6}$, $X_H = 10^{-7}$), constant with respect to temperature in the figure. It is apparent from the figure that thermal equilibrium cannot possibly account for the intensity of observed emission at the temperatures being considered within the test section ($T_{test} < 600$ K). The points are plotted from a single experimental emission intensity measured with the UV-imaging system using a narrow band analytical line filter. The emission is measured at several points immediately behind the leading edge oblique shock near the wedge tip and averaged. This intensity is plotted twice, at temperatures corresponding to the measured stagnation temperature (1070 K) and the computed static temperature (600 K) assuming a flow Mach number of 2. This illustrates that even within a region of total temperature recovery, chemiluminescence from radical recombination dominates over thermal effects.

Because the actual radical concentrations within the test section are unknown, it is emphasized that the figure cannot provide quantitative information about the contributions of individual reactions to the overall emission intensity. It is interesting to note the importance of the pre-association reaction (3) calculated using the final predicted radical concentrations from Figure 4.3 and shown in Figure 4.4. This is due to the second-order nature of the reaction; it proceeds more quickly than three-body recombination reactions at low pressures, as shown in the shock-tube studies by Hidaka, et al. (1982). The measured point falls below the $O + H \rightarrow OH^*$ line because the narrow band filter does not pass ultraviolet in the 2-1 band (287.5 nm) or the 3-2 band (294.5 nm), although the glass filter used to image Figure 3.10 does pass these wavelengths.

The boundary layer over the wedge and the wake region behind the wedge were noticeably devoid of any apparent chemiluminescence. This may be due in part to a heat loss mechanism or radical destruction at the surface of the model. There is little doubt that radicals were recombining on the wedge surface, as evidenced by the ablation of the wedge tip. Stainless steel (type 304) melts at 1427 °C (1700 K), and this temperature could only have been achieved

either through heat evolved from pre-reaction, or through local radical recombination at the surface of the test model.

4.6 Reactivity: Damköhler Number

Providing a source of radicals frozen in the flow through the nozzle eliminates the induction time issue for ignition of H_2-O_2-N_2 mixtures. The induction time is the time required for growth of the radical pool prior to explosively fast reaction in a combustible mixture. In order to closely examine the reactivity of the system, it is appropriate to use a form of Damköhler's first number which compares the characteristic times for convection and chemistry.

Damköhler number (Da) is the ratio of the characteristic flow time to the chemical time

$$Da = \frac{\tau_f}{\tau_c}$$

For Da > 1, the kinetics are fast compared with convection while Da < 1 indicates that the chemistry is slower than convection. In Chapter 1, Damköhler number was defined approximately with a laminar flame speed S_L appearing in the chemical time. Using the H_2-O_2 kinetic mechanism, and the constant-pressure, adiabatic, zero dimensional modeling approach, the chemical time can be more appropriately defined for systems in terms of a reactivity.

A characteristic time τ_c for the overall reaction can be expressed by examining the ratio

$$\tau_c = \frac{[H_2]_{in}}{\left. \frac{d[H_2]}{dt} \right|_{max}}$$

where $[H_2]_{in}$ is the concentration of hydrogen injected into the system, and $d[H_2]/dt_{max}$ is the maximum rate of change in hydrogen concentration. The concept is illustrated in Figure 4.5 which shows that this value for the characteristic chemical time will be shorter than one which included the

83

induction time as well. This should give an optimistic value (i.e. shorter time) for τ_c in the system and consequently, higher values of the Damköhler number.

Characteristic flow times are usually defined using a characteristic length divided by the velocity of the stream.

$$\tau_f = \frac{L_c}{U_0}$$

In the experimental system, obvious choices for these values would be the length of the constant area test section (15 cm) and the free stream velocity, which for supersonic flow is simply the Mach number M_∞ multiplied by the sound speed

$$U_0 = M_\infty \sqrt{\gamma RT}$$

where γ is the specific heat of the mixture, R the gas constant, and T the local absolute temperature.

The characterization of the reactive nature of a chemical system depends on defining the observation times of interest. Propulsion systems require high extents of reaction within residence times available in the combustor. Similarly, this present problem requires high extents of reaction within the characteristic observation times defined by the test section length scale and the fluid velocity. Thus the term "high" reactivity implies that large extents of reaction will be observed, while "low" reactivity implies that the extent of reaction will be negligibly small. Thus, large Damköhler numbers (Da > 1) are required to obtain the high reactivity condition associated with propulsion and, in this case, substantial reaction in the test section.

Figure 4.6 shows the variation of Damköhler number with temperature for an isobaric adiabatic hydrogen-air system at equivalence ratios of $\phi = 0.25$, 0.50, and 1.00. Pressure is constant at 0.04 atm (~30 torr) and the overall composition is similar to that considered in the experimental work. The overlapping of the $\phi = 0.50$ and $\phi = 1.00$ curves is a consequence of increased values for the gas constant in the expression for sound speed resulting from larger quantities of hydrogen in the flow. This has the effect of increasing

84

characteristic flow velocities for constant Mach number ($M_\infty = 3$ in the figure). The temperatures required for high reactivity are outside of those examined in this research, with Da = 1 for $\phi = 0.25$ occurring above 1800 K.

Convective times within a boundary layer formed in supersonic flow are considerably longer than those of the free stream. Close to the surface, velocities will approach low subsonic values, and the Damköhler number as formulated above will be greater than Figure 4.6 indicates. In the limit, as the wall is approached, the velocity goes to zero and the Damköhler number should be infinite. Figure 4.7 shows the dependence of Da as a function of height in the boundary layer assuming linear profiles for the velocity and temperature through the boundary layer thickness δ (inset). Two different wall temperatures are shown, and the free stream static temperature is 400 K for both cases. About 10% of the boundary layer thickness is in a region of Da > 1 for $T_{wall} = 1000$ K. Increasing the wall temperature to 2000 K increases the region of Da > 1 to 40% of δ. However, the approach outlined in this section does not account for heat loss into the boundary, transport effects, or radical destruction at the surface. These additional factors are nontrivial and require a more rigorous modeling approach.

Such an approach was carried out numerically by Figueira da Silva et al. (1994) for ignition of H_2-air mixtures in supersonic boundary layers. Only atmospheric static pressures were considered for a range of static temperatures and free stream Mach numbers. They studied the factors influencing the induction length over a flat plate, including the wall temperature, equivalence ratio, and Sorêt effect (temperature gradient induced diffusion). Their results showed that increasing the equivalence ratio in the range 0.5 to 2 increases the induction length due to local buildup of unburned hydrogen at the surface caused by the Sorêt effect. This in turn causes a drop in the wall temperature which can be expressed approximately (Schlichting, 1960) as

85

$$T_{wall} \approx T_{\infty}\left(1 + \sqrt{Pr}\frac{\gamma - 1}{2}M_{\infty}^2\right)$$

where Pr is the Prandtl number.

One numerical case examined in the aforementioned study assumed M_{∞} = 2.5, P_{∞} = 1 atm , ϕ = 0.5, with an H_2-air mixture at T_{∞} = 700 K yielding a boundary layer recovery temperature of 1320 K. This gives a value of Da = 8 for the entire 10 cm computational domain. Alternately, following the approach similar to that shown in Figure 4.7, with T_{wall} =1320 K, T_{∞} = 700 K, and linear boundary layer profiles, over 60% of the boundary layer is in a region of Da > 1. Stabilized reaction is predicted in this adiabatic wall case.

Inclusion of the Sorêt effect in their calculation showed that unburned hydrogen diffuses towards the wall when the wall temperature is less than the adiabatic wall temperature. This further decreased the wall temperature because the Prandtl number drops locally and viscous heating becomes less significant. This suggests that incomplete mixing of hydrogen in the main stream might amplify this effect and locally move the boundary layer mixture into a region of Da < 1.

Effect of Pressure on Da

The effect of varying the pressure on Damköhler number is shown in Figure 4.8 for an equivalence ratio of 0.5. As pressure is increased to about 3 atm, less curvature is observed in the profiles as a function of temperature (i.e. Da becomes a linear function of initial temperature). The sudden drop in Da at the low temperature limit of each curve corresponds to the explosion limit temperature.

From this information, contours of Da = 1 can be constructed in the pressure-temperature plane for a Mach 3, ϕ = 0.5, H_2 - air system, with varying characteristic lengths, as represented in Figure 4.9. These characteristic lengths represent the distance over which the fuel would be consumed in the supersonic

86

free stream, provided the reaction proceeded at the fastest rate determined from modeling calculations. Two calculations are represented corresponding to 1) isobaric, adiabatic and 2) isothermal conditions. The isobaric, adiabatic Da=1 contours converge above approximately 0.7 atm indicating that the range of characteristic lengths considered do not strongly influence reactivity. That is, across this boundary, the system rapidly goes from a region of low reactivity to one of high reactivity.

When temperature is held constant, the Da=1 contours are coincident with the extended second limit and above this line, the system has low reactivity. Thus, when the temperature rise from heat release is uncoupled from the reacting system, there is no feedback mechanism by which the maximum rate of H_2 consumption grows exponentially with extent of reaction.

From Figures 4.8 and 4.9, it is apparent that for a given characteristic length, a critical pressure exists above which the mixture is in a region of Da>1 for all temperatures above the explosion temperature. At the conditions of Figure 4.9 for L_c=0.1 m, this critical pressure occurs at 0.5 atm where the isobaric, adiabatic model intersects the second limit.

At pressure is reduced, the isobaric and isothermal lines begin to converge for a given characteristic length. At these conditions, the disappearance of hydrogen does not yield large exothermicity, but large quantities of radicals (with high heats of formation). The overall reaction rate of fuel becomes the limiting reaction time rather than the time required for reaction initiation.

Remarks

The Damköhler number analysis of the supersonic reacting boundary layer clearly indicates that higher operating pressures and temperatures are required in the current experimental approach to stimulate localized reaction and heat release. In the experiments presented, conditions are such that reaction times are not obtained in the length scale of the models unless recovery

temperatures exceed 1800 K (which cannot be achieved within current experimental constraints). The result is a de-coupling of significant chemical heat release from the reaction zone and the absence of a well-defined thermal runaway region inside the boundary layer. Experimental observations made through chemiluminescence measurements are consistent with this analysis.

Figure 4.1: Predicted profiles of temperature, H_2, and radical species as a function of distance from the throat for injector position 1.

Figure 4.2: Predicted profiles of temperature, H_2, and radical species as a function of distance from the throat for injector position 2.
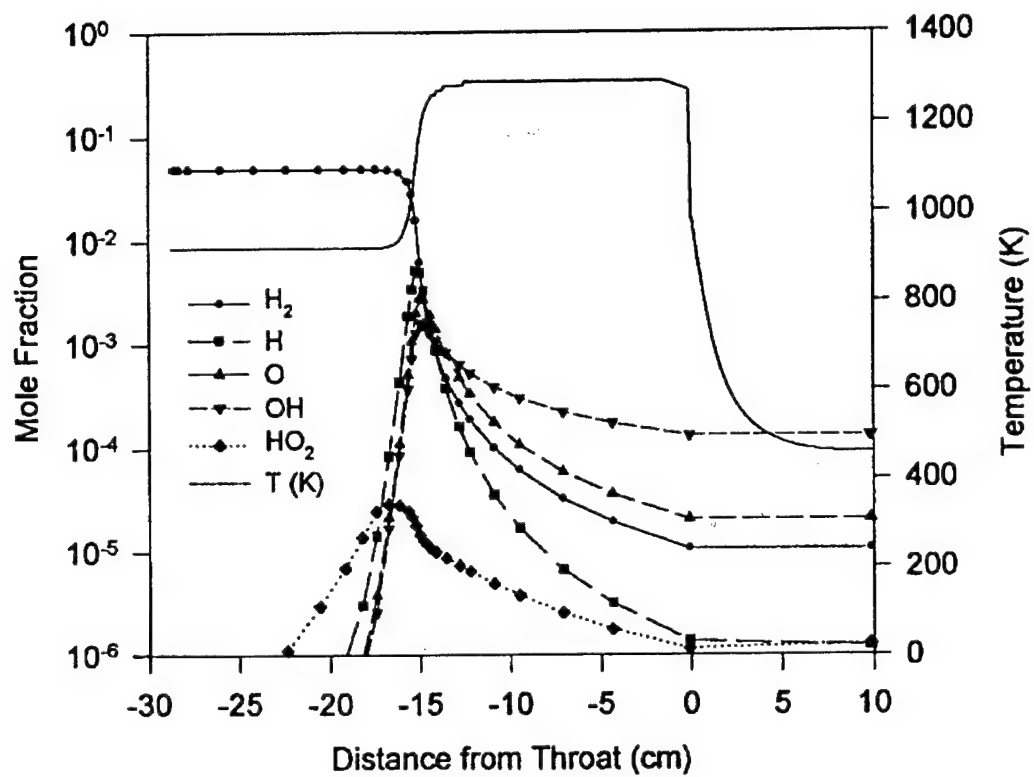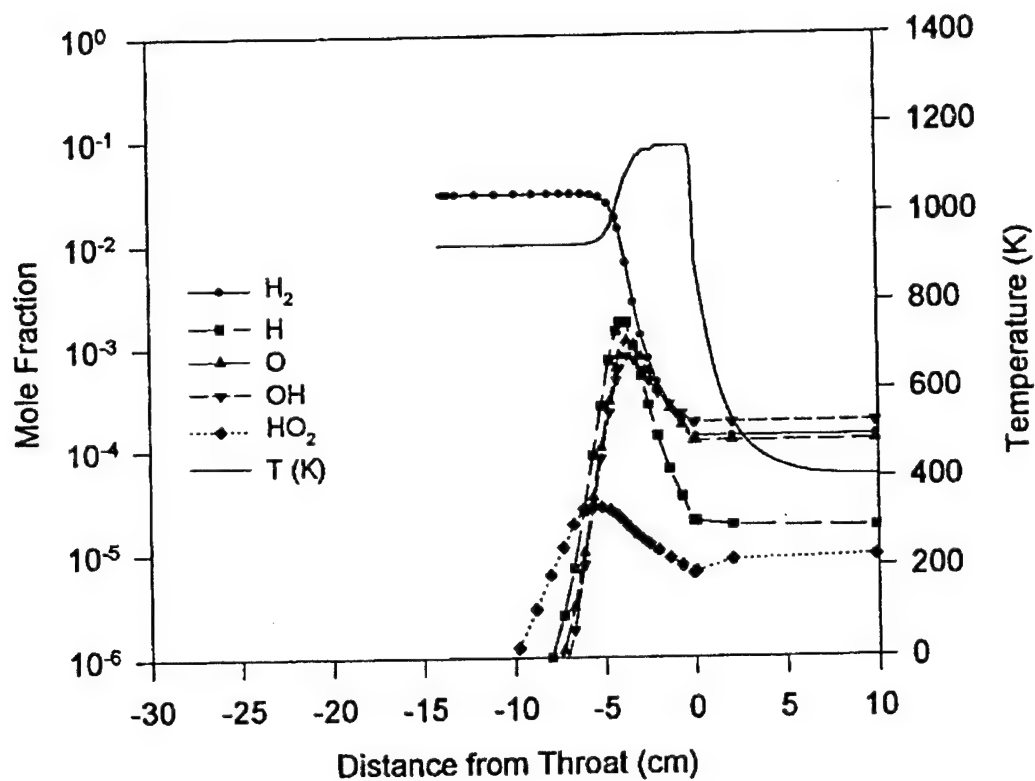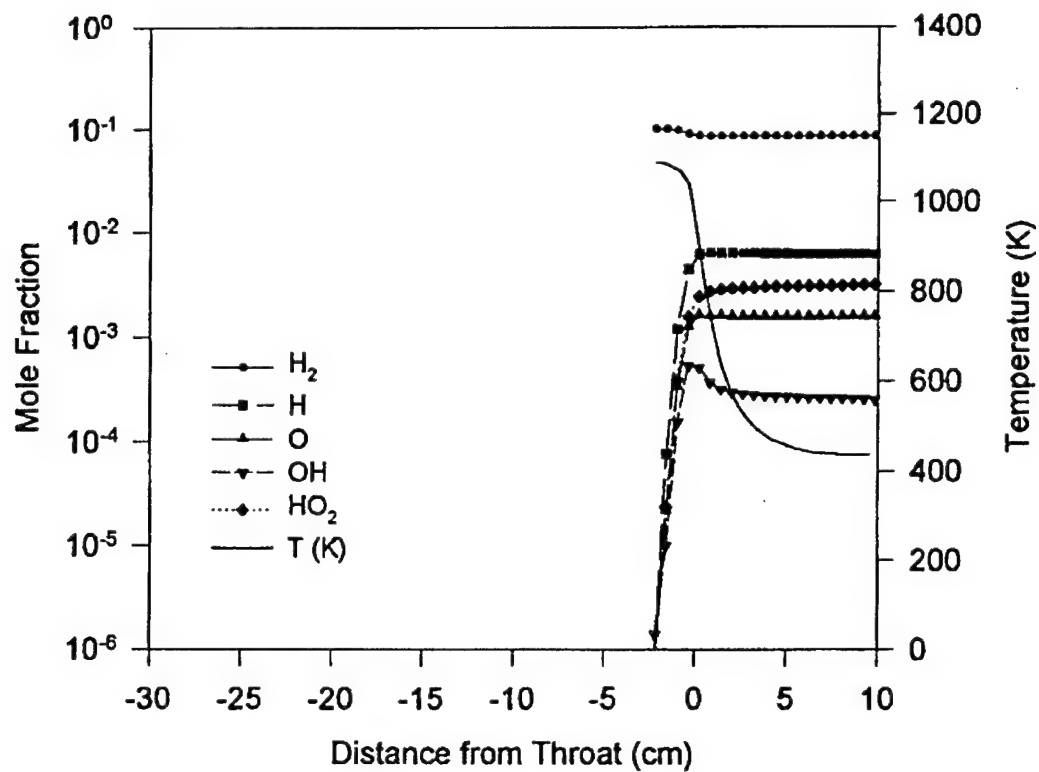
Figure 4.3: Predicted profiles of temperature, H_2, and radical species as a function of distance from the throat for injector position 3.
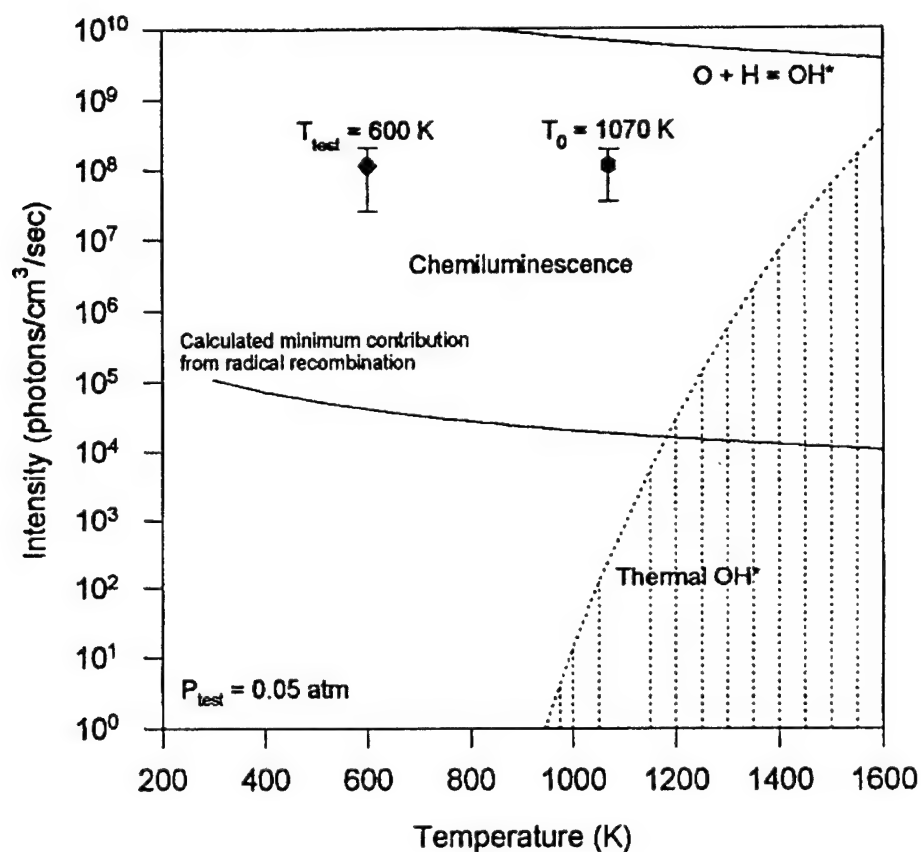
Figure 4.4: Theoretical OH* emission intensity as a function of temperature predicted from various sources. The points are measured from the wedge experiment (injector position 3).
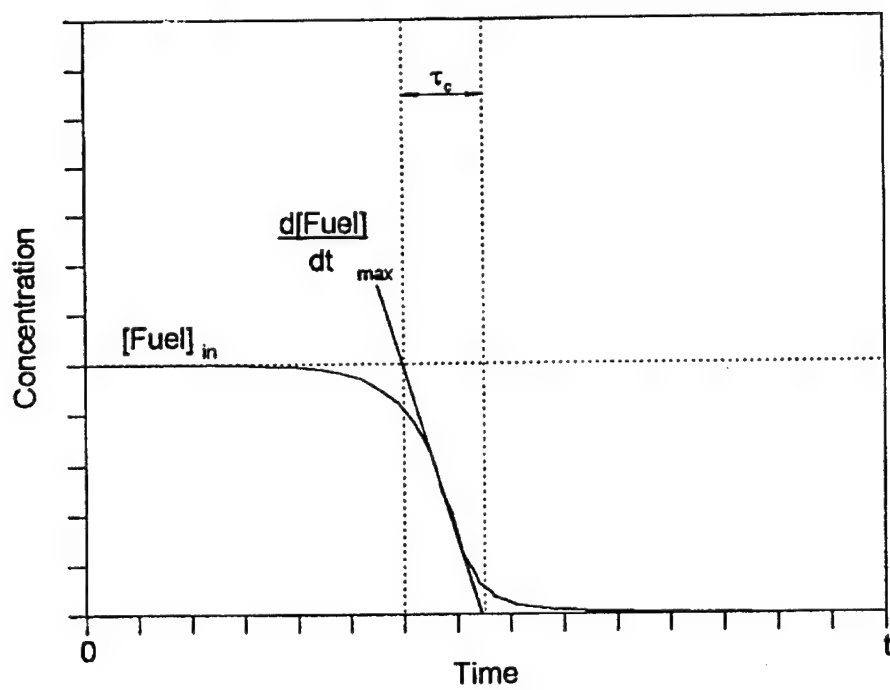
Figure 4.5: Sketch of concentration as a function of time illustrating how the parameters are determined for defining the characteristic chemical time.
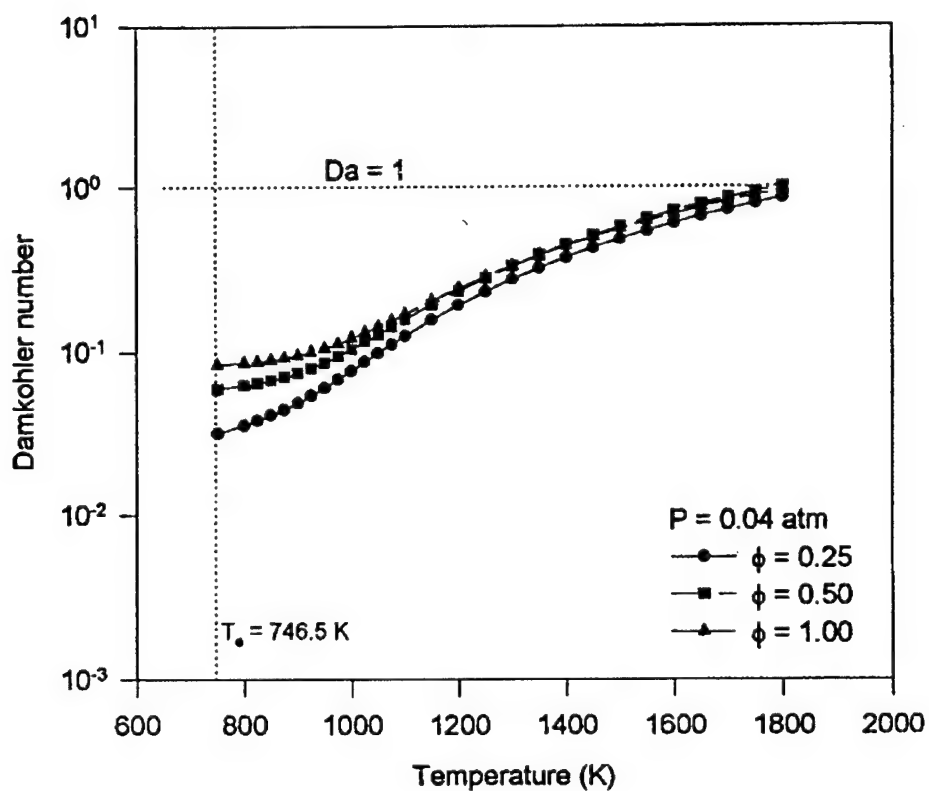
Figure 4.6: Damköhler number versus temperature plot for different H_2- air equivalence ratios at M = 3. Below the explosion limit temperature (T_e), Da becomes zero.

94
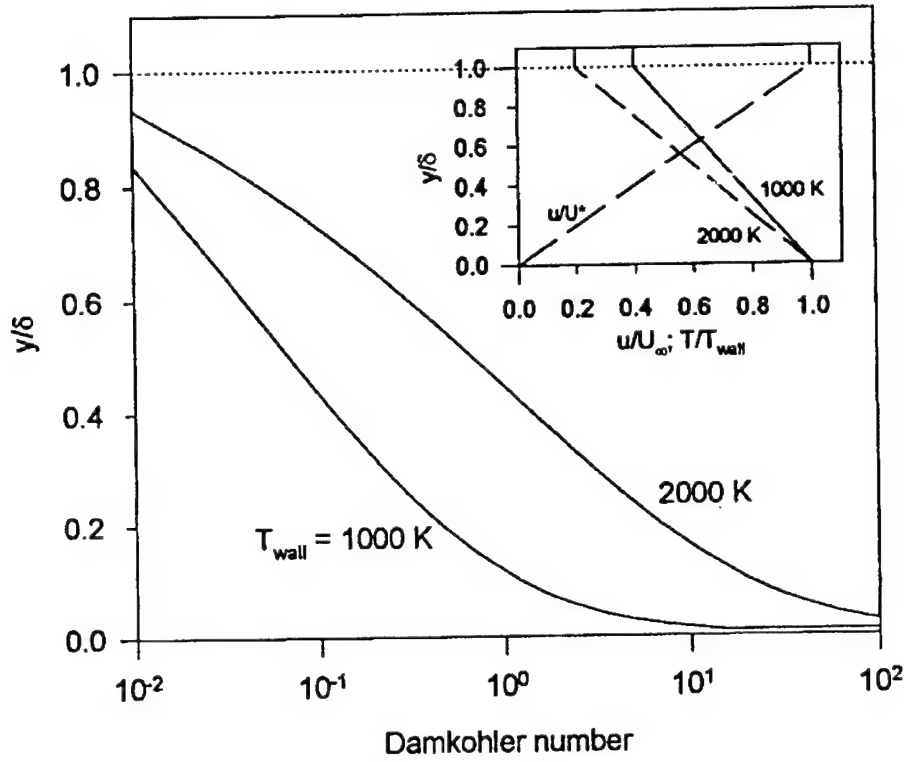
Figure 4.7: Variation of Damköhler number through the boundary layer assuming linear velocity and temperature profiles (inset). Static temperature and pressure are 400 K and 0.04 atm, for both cases shown.
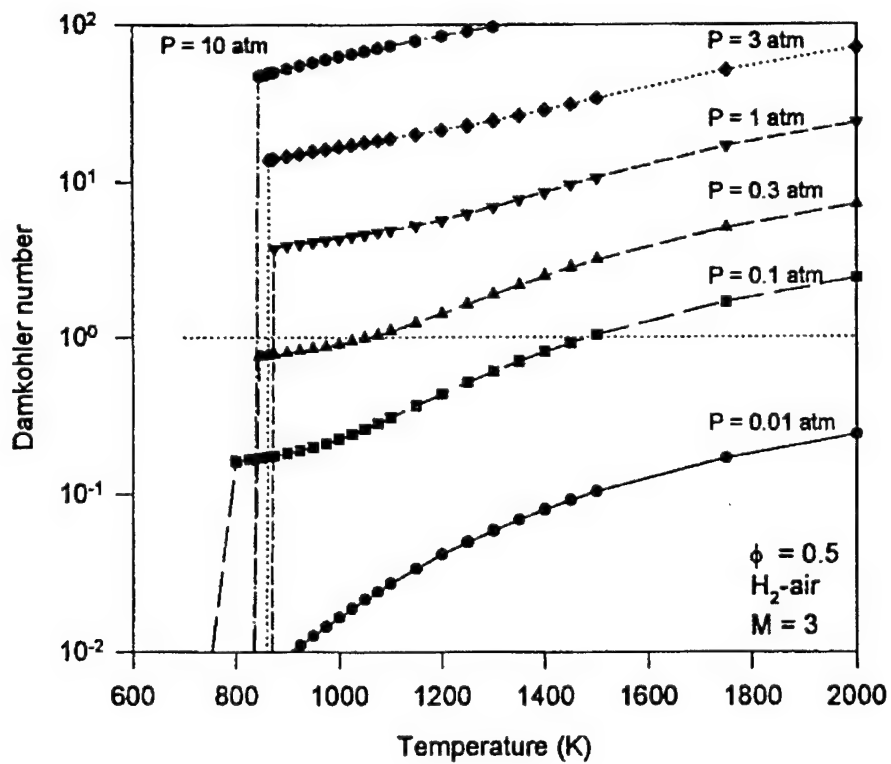
Figure 4.8: Effect of varying pressure on Damköhler number as a function of initial temperature. Conditions correspond to $M_\infty = 3$, $L_c = 0.1$ m, and an equivalence ratio of 0.5.
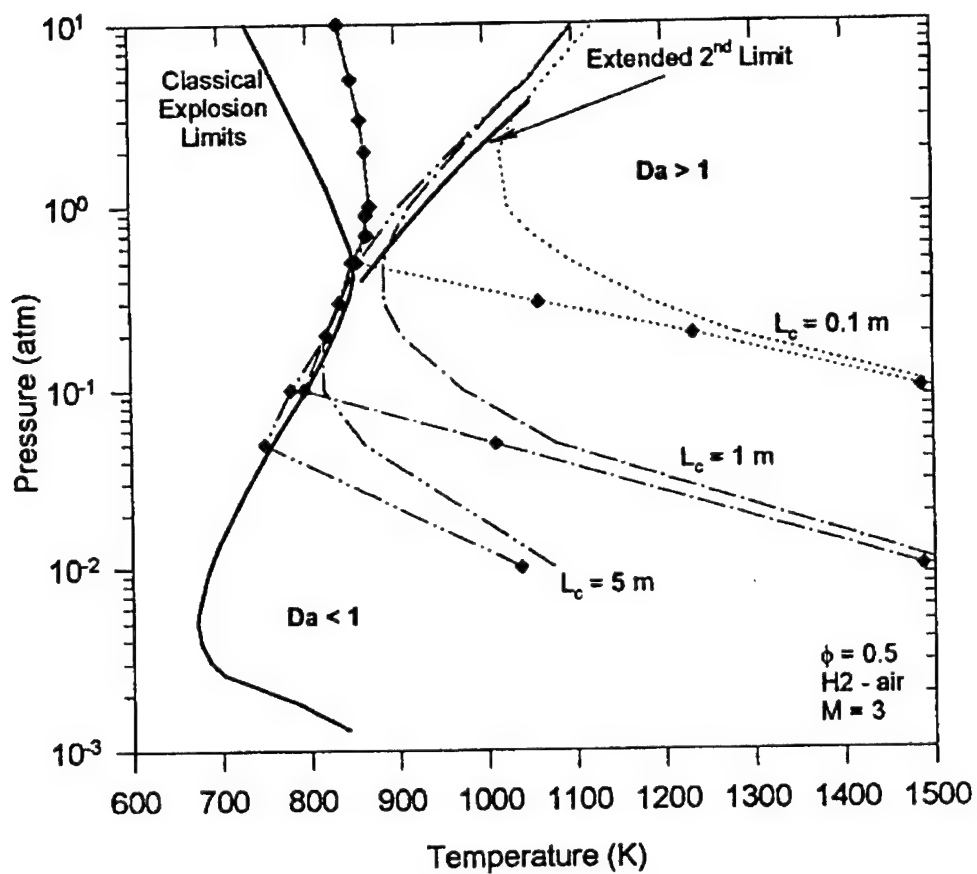
Figure 4.9: Contours of Da=1 in the pressure-temperature plane for different characteristic lengths. Lines with symbols are isobaric, adiabatic calculations and those without symbols are isothermal.

Chapter 5. Conclusions and Future Work

5.1 Summary and Conclusions

The experimental effort described in this thesis involved the design and construction of a supersonic wind tunnel for use in combustion studies of the hydrogen-oxygen system. The design resulted in innovative engineering of the test section to withstand elevated temperatures ($T_0 \approx 1100$ K) and provide accessibility for rapid turnaround times after modifications. The supersonic diffuser was constructed using a unique shell and liner design for simple fabrication and economy. The pilot Supersonic Combustion Facility was operated over a wide range of conditions for validation and combustion experimentation.

An experimental program was carried out to investigate the ignition and combustion of H_2-O_2-N_2 mixtures in the Supersonic Combustion Facility. The approach involved utilizing thermal recovery from viscous heating in a laminar boundary layer to move the gas mixtures from a non-explosive condition in the stagnation chamber to an explosive condition within the boundary layer. Chemiluminescence measurements of excited hydroxyl radicals were used as a diagnostic to visualize regions of reaction in the test section.

Pre-reaction of the combustible mixture upstream of the nozzle provided a source of radicals frozen in the flow through the expansion. Distinct OH* emission patterns were observed over flat plate and wedge geometries for several upstream injector locations. Flat plates with and without catalytic platinum surfaces were examined, although no conclusive evidence was found to indicate that the catalyst enhanced reaction.

Chemiluminescence in the boundary layer and wake (Figure 3.4) was primarily a result of high radical concentrations in the stream, and numerical modeling indicated that burnout of the hydrogen occurred upstream of the throat. Moving the injector position downstream increased emission intensity in zones behind shocks formed from the test model, and boundary layer chemiluminescence decreased (Figure 3.5). A review of the kinetic pathways resulting in OH* formation confirm that this emission is due to termolecular radical recombination processes, specifically

$$O + H (+ M) \rightarrow OH^* (+ M)$$
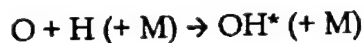
At low pressures, the second-order pre-association form of this reaction becomes dominant.

A third injector position was chosen with the exit plane within the contraction of the nozzle. Pre-reaction was obtained in an unstable mode for settling chamber temperatures near 1000 K and stabilized in a flame configuration at $T_0 \geq 1070$ K with fuel flow rates of about 1% by volume of the total flow and $T_{fuel} \approx 750$ K. Intense OH* emission appears immediately behind the oblique shocks generated at the tip of the model (Figure 3.8). Estimates of the contributions from thermal and non-thermal sources indicates that this emission arises from the recombination processes described in Chapter 4. Examination of the chemiluminescence observed over the wedge shows little reaction occurring within the boundary layer and no reaction evident in the recirculation zone of the wake. The stagnation point at the tip provided an effective region for radical recombination, and local temperatures were sufficiently high to cause ablation of the stainless steel wedge tip.

The reaction analysis performed using the Damköhler number as an indicator of reactivity shows that in the experimental cases, the system is in a regime of low reactivity (Da < 1) for the pressures and temperatures examined. Within the boundary layer, the potential exists for regions where the chemical time is faster than the flow time due to lower convective velocities close to the

wall. At the temperatures considered as part of this study, however, less than 10% of the boundary layer thickness is calculated to be in a regime of $Da > 1$ (Figure 4.7). A two-dimensional numerical study (Figueira da Silva et al., 1994), indicates that unburned hydrogen can diffuse towards the wall as a result of the Sorêt effect when the wall temperature is lower than the adiabatic wall temperature. This decreases the wall temperature further and locally reduces the heat generated through viscous dissipation. Decreasing the degree of fuel mixing potentially inhibits reaction in the boundary layer and wake through local cooling, effectively reducing the Damköhler number in these regions.

The results of this experimental work are very promising because more information has been provided than in previous studies for a supersonic reacting flow system at experimental conditions more realistic for application to high-altitude air-breathing high-speed propulsion systems. It has been shown that the chemical induction time may not the limiting parameter in the design and operation of supersonic combustion ramjets using hydrogen as the primary fuel. At low static pressures encountered in supersonic flow (especially in the upper atmosphere), the overall reaction rate of the hydrogen-oxygen system becomes too slow in comparison with the high convective velocities. This leads to long reaction zones in which the chemical energy is stored in radical species with high heats of formation. The operating principles depicted in Figure 1.6 appear to be achievable in a range of operating parameters where the third limit explosive condition is avoided in the mixing time, and reaction initiation by recovery remains substantially exothermic. Continuing work will look at these conditions using ejector and air supply conditions available in the Gas Dynamics Laboratory at the Forrestal campus. Ongoing effort in this area is needed to expand the database of practical knowledge available for characterizing reacting high-speed flows. In the next section, concepts for extending the current program are detailed.

This research focused on achieving local reaction in a boundary layer in a supersonic stream using several different techniques including increased radical concentrations, catalytic surfaces, and high recovery temperatures. Analysis performed in Section 4.6 indicated that for the severe test section static pressures examined in this study (~0.05 atm), temperatures at the surface need to be above 2000 K for reaction initiation, defined by a unity Damköhler number. Those stagnation temperatures are currently outside the operating range of the experimental facility designed for this research. Additionally, increasing the stagnation chamber temperature beyond theoretical explosion limit temperatures will increase the rate of pre-reaction occurring before the test section is reached.

The insight provided by this analysis suggests several areas for focusing additional effort. The original design concept (Figure 1.6) remains valid, but within the accessible regions of the current facility, intrusive measures such as extreme surface heating are needed in order to stimulate reaction of the hydrogen-oxygen system. Additional concepts for future development are discussed and assessed in terms of their viability.

Increased Stagnation Pressure

A map of stable regions within the pressure-temperature plane is shown in Figure 4.9 along with the classical explosion limits. The curve $L_c = 10$ cm is of interest because it is the length scale currently attainable in the SCF test section. The minimum temperature on the isobaric Da=1 contour occurs at 856 K and 0.5 atm. This is the minimum recovery temperature inside the boundary layer which satisfies Da = 1, and requires a settling chamber temperature of 1060 K (recovery factor = 0.81 for ϕ=0.5). The static pressure can be delivered by increasing P_0 to 18 atmospheres. Upstream injection of the hydrogen is undesirable because of the rapid consumption of fuel which will occur once reaction is initiated at these conditions. Local injection of hydrogen at the plate

surface is a viable alternative. This work can proceed by utilizing the ejector capabilities in the Gas Dynamics Laboratory at the Forrestal Campus.

Heated Surfaces

Additional studies can use intense local heating of a surface to initiate combustion. The surface must span the entire length of the test section to provide maximum residence time, and wall temperatures will likely exceed 2000 K. Few materials are suitable for this type of service, although a tungsten heating element was examined in some experiments. Tungsten has a melting point of 3410°C (3683 K), but becomes very brittle in an oxidizing environment. Ceramic heaters such as zirconium oxide are more likely to survive repeated testing. The difficulty is that such materials have negative resistance gradients with increasing temperature, and require current rather than voltage controlling methodologies to avoid burnout.

Shock Enhancement/Ignition

Shocks formed in supersonic flow present a means of igniting and enhancing combustion of a reactive mixture. Increases in both temperature and pressure behind the shocks create conditions more favorable for fast chemistry. The largest pressure and temperature rise is obtained through a normal shock, but the flow after the shock is always subsonic. Studies of shock-induced ignition of the hydrogen-oxygen system were carried out by Meyer and Oppenheim (1970), using homogeneous mixtures in a tube ignited by a reflected normal shock (shock-tube). Applying information from these studies to flowing systems, however, is complicated by experimental variations and the presence of gradients in the flow.

Measurements of ignition delay utilizing shock-induced combustion were made in a supersonic wind tunnel by Richmond and Shreeve (1967). A normal shock was generated using the intersection of two oblique shocks, and hydrogen

was injected inside the supersonic test section upstream of the shock. Ignition was obtained for stagnation conditions of P_0 = 24 atm and T_0 = 1340 K at a Mach number of about 2. Radical formation at the injector and interaction of the fuel jet and outer flowfield made comparison of their results to shock tube ignition studies difficult.

Oblique shocks may provide a means of creating local zones of higher pressure and temperature, without decelerating the flow to subsonic velocities. This would reduce the recovery temperature requirement in the current configuration of the wind tunnel. For example, if an oblique shock increased the static pressure to 0.2 atm, Figure 4.9 dictates a recovery temperature of 1240 K for L_c = 0.1 m. Steady oblique shock induced combustion of H_2-air was investigated in Mach 3 wind tunnel experiments by Rubins and Rhodes (1963) at conditions of P=0.35 atm, T=1389 K. Their work employed a 28° wedge to produce an oblique shock with hydrogen (T=333-444 K) injected upstream in the supersonic flow.

Shocks would be utilized in conjunction with another technique such as heat addition to stimulate and stabilize the reaction zone. This would provide an excellent method for confirming the Da=1 criteria by allowing a systematic mapping of the stable regions and a direct comparison with the theory of Section 4.6.

Catalysis

Although catalytic enhancement of reaction is not confirmed in this work, catalysis studies of hydrogen in air in a boundary layer over a platinum plate have been examined in detail. (Pfefferle, 1987) These studies show that in some cases, a platinum wall can act as a sink for free radicals except near the leading edge. Further examination of this phenomena is necessary before possible implementation as a source of ignition or reaction enhancement in supersonic

103

streams. It is possible that this technique will be more effective when coupled with a heated surface or some other source of thermal energy.

Alternate Fuels/Additives

Hydrogen was chosen in this study for its high specific energy which makes it a likely candidate for a supersonic combustion fuel. This study indicates, however, that at low pressures encountered in the upper atmosphere, the kinetics of the H_2-O_2 system require significantly high pressures and temperatures to maintain reasonable reaction zone lengths and prevent uncoupling of the location of heat release from the reaction zone. This has great impact on the design of scramjets because it affects the balance that must be established between engine temperatures for maximizing combustion efficiency and meeting material limitations. These pressure and temperatures in turn define the through-flow Mach numbers in the combustor as a function of altitude and flight Mach number.

Other fuels could be investigated in the current facility, either alone or in conjunction with additional fuels premixed in the flow. Aluminum borohydride, a pyrophoric fuel, was studied by Fletcher, et al. (1967) at static pressures as low as 1" Hg (0.04 atm) for use in piloting the combustion of more conventional fuels. "Jet fuel" was burned when it was piloted by aluminum borohydride injected upstream or downstream of the fuel injection point (at the wall) in an air environment. Other fuels were considered, including pentaborane, trimethylaluminum, diethylaluminum hydride, and vinyl-silane. Of these, aluminum borohydride and pentaborane produced the most promising results.

The mechanism by which supersonic combustion is initiated and enhanced by the addition of a hypergolic substance (one which spontaneously ignites in the presence of air) is through localized chemical heat release, which can drive the hydrogen-air system into regions of fast reaction. Silane (SiH_4) is a potential hypergolic additive and Papas (1994) presents preliminary results for

silane/hydrogen-air opposed jet flames as well as a kinetic mechanism for silane oxidation.

References

Ace Glass Corp., Personal Communication (1995)

Aeronautics and Space Engineering Board, *Aeronautical Technologies for the Twenty-First Century*. Washington, D.C.: National Academy Press (1992)

Alpinieri, L.J., "Turbulent Mixing of Coaxial Jets," *AIAA Journal*, 2 (1964) 1560

Anderson, J.D., Jr. *Hypersonic and High Temperature Gas Dynamics*. New York: McGraw-Hill (1989)

Anderson, J.D., Jr. *Introduction to Flight (3rd ed.)*. New York: McGraw-Hill (1989)

Anderson, J.D., Jr. *Modern Compressible Flow with Historical Perspective (2nd ed.)*. New York: McGraw-Hill (1990)

Beckwith, I.E., and Moore, J.A., "An Accurate and Rapid Method for the Design of Supersonic Nozzles," *NACA Technical Note 3322*. (1955)

Beér, J.M., and Chigier, N.A., *Combustion Aerodynamics*. London: Applied Science Publishers (1974)

Billig, F.S., "*Propulsion Systems from Takeoff to High-Speed Flight*," <u>High-Speed Flight Propulsion Systems</u>, Progress in Astronautics and Aeronautics, 137 (1991)

Billig, F.S., "Research on Supersonic Combustion," *Jour. Propulsion and Power* 9, (1993) 499

BMA Silencers, Bulletin 1330-8, Fox Valve Development Corp. Dover, NJ (1994)

Cheng, S.I., Kovitz, A.A., "Theory of Flame Stabilization by a Bluff Body," *Seventh Symposium (International) on Combustion*, The Combustion Institute, (1959) 681

Davis, M.G., McGregor, W.K., Mason, A.A., "OH Chemiluminescent Radiation from Lean Hydrogen-Oxygen Flames," *Jour. Chem. Phys.*, **61** (1974) 1352

Dunn, M.G., Lordi, J.A., Wittliff, C.E., Holden, M.S., "*Facility Requirements for Hypersonic Propulsion System Testing*," High-Speed Flight Propulsion Systems, Progress in Astronautics and Aeronautics, **137** (1991)

Figueira da Silva, L.F., Deshaies, B., "The Influence of Equivalence Ratio and Sorêt Effect on the Ignition of Hydrogen-Air Mixtures in Supersonic Boundary Layers," *Twenty-Fifth Symposium (International) on Combustion*, The Combustion Institute, (1994) 29

Figueira da Silva, L.F., Deshaies, B., Champion, M., "Numerical Study of Ignition Within Hydrogen-Air Supersonic Boundary Layers," *AIAA Journal* **31**, (1993) 884

Fletcher, E.A., "Early Supersonic Combustion Studies at NACA and NASA," *Eleventh Symposium (International) on Combustion*, The Combustion Institute, (1967) 729

Fox Valve Development Corp., Personal Communication with Bob Fritz (1994)

Gaydon, A.G., and Wolfhard, H.G., *Flames: Their Structure Radiation and Temperature (4th ed.)*. New York: Chapman and Hall (1979)

Gaydon, A.G., *The Spectroscopy of Flames*. London: Chapman and Hall (1957)

Glassman, I, *Combustion (2nd ed.)*. Orlando, FL: Academic Press (1987)

Goldstein, R.J., *Fluid Mechanics Measurements*. New York: Springer-Verlag (1983)

Held, T.J., "The Oxidation of Methanol, Isobutene and Methyl tertiary-Butyl Ether," Ph.D. Thesis. Department of Mechanical and Aerospace Engineering, Princeton University, Princeton, New Jersey (1993)

Hidaki, Y. Takahashi, S., Kawano, H., Suga, M., and Gardiner, W.C., "Shock-Tube Measurement of the Rate Constant for Excited $OH(A^2\Sigma^+)$ Formation in the Hydrogen-Oxygen Reaction," *J. Phys. Chem.*, **86** (1982) 1429

Im, H.G., Bechtold, J.K., and Law, C.K., "Analysis of Thermal Ignition in Supersonic Flat-Plate Boundary Layers," *J.Fluid Mech.* **249**, (1993) 99

Im, H.G., Helenbrook, B.T., Lee, S.R., and Law, C.K., "Ignition in the Supersonic Hydrogen/Air Mixing Layer with Reduced Reaction Mechanisms," *J. Fluid Mech.*, **322** (1996) 275

Kaskan, W.E. "Abnormal Excitation of OH in $H_2/O_2/N_2$ Flames," *Jour. Chem. Phys.*, **31** (1959) 944

Kee, R.J., Rupley, F.M., and Miller, J.A., "Chemkin-II: A Fortran Chemical Kinetics Package for the Analysis of Gas-Phase Chemical Kinetics," *Sandia Report SAND89-8009* (1989)

Kee, R.J., Rupley, F.M., and Miller, J.A., "The CHEMKIN Thermodynamic Data Base," *Sandia Report SAND87-8215* (1987)

Kim, T.J., "Gas Phase Kinetic Studies of the Hydrogen - Oxygen and Carbon Monoxide - Hydrogen - Oxygen Systems," M.S.E. Thesis. Department of Mechanical and Aerospace Engineering, Princeton University, Princeton, New Jersey (1994)

Kodak, "Schlieren Photography," *Eastman Kodak Company Publication* (1977)

Kordylewski, W. and Scott, S.K., "The Influence of Self-Heating on the Second and Third Explosion Limits in the O2 + H2 Reaction," *Combustion and Flame*, 57 (1984) 127

Law, C.K., "Mechanisms of Flame Stabilization in Subsonic and Supersonic Flow," *Major Research Topics in Combustion*, New York: Springer-Verlag (1992) 201

Lewis, B. and von Elbe, G., *Combustion, Flames and Explosions of Gases (3rd ed.)*. Orlando, FL: Academic Press (1987)

Lutz, A.E., Kee, R.J., and Miller, J.A., "SENKIN: A Fortran Program for Predicting Homogeneous Gas Phase Chemical Kinetics with Sensitivity Analysis," *Sandia Report SAND87-8248* (1987)

Maas, U. and Warnatz, J., "Ignition Processes in Hydrogen-Oxygen Mixtures," *Combustion and Flame*, 74 (1988) 53

Meyer, J.W., Oppenheim, A.K., "On the Shock-Induced Ignition of Explosive Gases," *Thirteenth Symposium (International) on Combustion*, The Combustion Institute, (1970) 1153

Meyer-Arendt, J.R., *Introduction to Classical and Modern Optics*. Prentice-Hall, New-York (1972)

Mueller, M., Work in progress. (1996)

Munson, B.R., Young, D.F., and Okiishi, T.H., *Fundamentals of Fluid Mechanics*. New York: John Wiley & Sons (1990)

Nicholson, H.M. and Field, J.P., "Some Experimental Techniques for the Investigation of the Mechanism of Flame Stabilization in the Wakes of Bluff Bodies," *Third Symposium (International) on Combustion*, The Combustion Institute, (1949) 44

Niioka, T., Terada, K., Kobayashi, H., Hasegawa, S., "Flame Stabilization Characteristics of Strut Divided into Two Parts in Supersonic Airflow," *Jour. Propulsion and Power* 11, (1995) 112

Pfefferle, L.D., Pfefferle, W.C., "Catalysis in Combustion," *Catal. Rev. Sci. Eng.*, 29 (1987) 219

Pope, A. and Goin, K.L., *High-Speed Wind Tunnel Testing*. New York: John Wiley and Sons, Inc. (1965)

Richmond, J.K., Shreeve, R.P., "Wind-Tunnel Measurements of Ignition Delay Using Shock-Induced Combustion," *AIAA Journal* 5, (1967) 1777

Rubins, P.M. and Rhodes Jr., R.P., "Shock-Induced Combustion with Oblique Shocks: Comparison of Experiment and Kinetic Calculations," *AIAA Journal* 1, (1963) 2778

Schlichting, H., *Boundary Layer Theory (4th ed.)*. New York: McGraw-Hill Book Co. (1960)

Shevell, R.S., *Fundamentals of Flight*. New Jersey: Prentice-Hall (1983)

Slutsky, S., Tamagno, J., and Trentacoste, N., "Supersonic Combustion in Premixed Hydrogen-Air Flows," *AIAA Journal* 3, (1965) 1599

Smits, A.J., Personal communication (1995)

Strahle, W.C., "Theoretical Consideration of Combustion Effects on Base Pressure in Supersonic Flight," *Twelfth Symposium (International) on Combustion*, The Combustion Institute, (1968) 1163

Swithenbank, J., Ewan, B.C.R., Chin, S.B., Shao, L., Wu, Y., "Mixing Power Concepts in Scramjet Engine Design," *Major Research Topics in Combustion*, New York: Springer-Verlag (1992) 531

White, F.M., *Viscous Fluid Flow (2nd ed.)*. New York: McGraw-Hill Book Co. (1991)

Williams, G.C., Hottel, H.C., and Scurlock, A.C., "Flame Stabilization and Propagation in High Velocity Gas Streams," *Third Symposium (International) on Combustion*, The Combustion Institute, (1949) 21

Winterfeld, G., "Stabilization of Hydrogen-Air Flames in Supersonic Flow," *Modern Research Topics in Aerospace Propulsion*, New York: Springer-Verlag (1991) 37

Yetter, R.A., Dryer, F.L. and Golden, D., "Pressure Effects on the Kinetics of High Speed Chemically Reacting Flows," *Major Research Topics in Combustion*, New York: Springer-Verlag (1992) 309

Yetter, R.A., Dryer, F.L. and Rabitz, H., "A Comprehensive Reaction Mechanism for Carbon Monoxide/Hydrogen/Oxygen Kinetics," *Comb. Sci. Tech.*, 79 (1991) 97

Yetter, R.A., Personal communication (1996)

Yetter, R.A., Rabitz, H. and Hedges, R.M., "A Combined Stability - Sensitivity Analysis of Weak and Strong Reactions of Hydrogen/Oxygen Mixtures," *Int. Jour. Chem. Kin.*, 23 (1991) 251

Zucker, R.D., *Fundamentals of Gas Dynamics*. Ohio: Matrix Publishers (1977)

Zukoski, E.E. and Marble, F.E., "Experiments Concerning the Mechanism of Flame Blow-off from Bluff Bodies," *Proc. Gas Dyn. Symp.*, Northwestern Univ., Evaston, Ill., (1956)